이학박사학위논문

Synthesis of Graphene Quantum Dots for Energy Applications

기능화된 그래핀 나노재료의 합성 및 에너지 저장으로의 응용

2015 년 8 월

서울대학교 대학원

화학부 물리화학 전공

문 준 희

Synthesis of Graphene Quantum Dots for Energy Applications

그래핀 양자점 합성 및 에너지 저장으로의 응용

지도교수: 홍 병 희

이 논문을 이학박사 학위논문으로 제출함

2015년 8월

서울대학교 대학원

화학부 물리화학전공

문준희

문준희의 이학박사 학위논문을 인준함

2015년 8월

위 원 장 장두전 ㊞

부위원장 홍병희 ㊞

위 원 조성표 ㊞

위 원 남좌민 ㊞

위 원 박재성 ㊞

Ph. D. Thesis

Synthesis of Graphene Quantum Dots for Energy Applications

Supervisor: Professor Byung Hee Hong

Major: Physical Chemistry

By Joonhee Moon

Department of Chemistry

Graduate School of Seoul National University

2015

Abstract

Synthesis of Graphene Quantum Dots for Energy Applications

Joonhee Moon

Department of Chemistry

The Graduate School Seoul National University

Recently, with the increased demand in energy resources, great efforts have been devoted to developing advanced energy storage and conversion systems. The increasing consumption and the rapid depletion of fossil fuels has driven the major research focus to exploitation and utilization of renewable energy such as wind energy, tidal energy and solar energy for the past few decades. To provide widespread usage of renewable energies, efficient energy storage and conversion technologies are required. Recently, graphene and graphene-based materials have attracted great attention owing to their unique properties of high mechanical flexibility, large surface area, chemical stability, superior electric and thermal conductivities that render them great choices as alternative electrode materials for electrochemical energy storage systems, i.e., lithium batteries, supercapacitors, water splitting systems, and solar systems.

The specific objectives of my thesis are as follow: (1) this dissertation is the results of an effort to develop the solar-to-hydrogen (STH) conversion efficiency using nitrogen doped graphene and graphene quantum sheets as a catalyst of cathode materials for hydrogen evolution reaction (HER) (2) graphene quantum dots with

oxygen rich functional groups were incorporated into sulfur cathode materials of lithium sulfur battery to enhance the battery performance. The main results of my dissertation research can be summarized as follows.

In Part Ⅰ, firstly, a simple one-step method to prepare nitrogen doped graphene quantum sheets (N-GQSs) was introduced by directly applying nitrogen plasma to as-grown graphene on Cu foil. Secondly, monolayer graphene (Gr) and nitrogen doped graphene (N-Gr) were applied as a catalyst on silicon wafer for HER, which strongly shifted toward the anodic direction without a change in the saturation current density as well as exhibits the strong potential as the passivation layer in neutral pH 7. Finally, N-doped graphene quantum sheets were decorated on an optimized silicon nanowires as a catalyst for the solar-driven HER, which can boost the catalytic activity toward the photoelectrochemical HER. The results showed that the N-GQSs electrodes exhibits higher applied bias photon-to-current efficiency (ABPE) than that of any other carbon-based photoelectrochemical HER catalysts reported to date.

In part Ⅱ, to study the role of oxygen functional groups in improving the cyclability, graphene oxide wrapped on sulfur composites were synthesized and used as a cathode electrode in a lithium sulfur battery (Li-S battery). For Further study on structure and functional groups of cathode electrode, graphene quantum dots with oxygen functional groups is found to promote the structural integration of densely packed carbon black (CB) shells surrounding sulfur particles, which enables faster charge transfer and minimal loss of lithium polysulfides through the tightly packed sulfur-carbon morphology and the carbon-sulfur (C-S) bonding. Finally, the

mechanism study of N-GQDs assisted Li-S battery that leads to the excellent cycling and rate performance were thoroughly investigated by detailed electrochemical analysis guided by theoretical modeling.

This dissertation provides the details of my work on all projects related to synthesize and characterization of functionalized graphene and graphene quantum dots for energy system: hydrogen evolution reaction and lithium sulfur batteries. These contents are reported in *Energy Environ. Sci.* 8, 1329 (2015), *Adv. Mater.* 26, 3501 (2014), *Energy Environ. Sci.* 6, 3658 (2013), and Nanoscale (DOI:10.1039/c5nr01951f).

Keywords: graphene, graphene quantum sheets, graphene quantum dots, hydrogen evolution reaction (HER), catalyst, lithium sulfur battery, C-S bonding, nano-sized sulfur

Student Number: 2012-30873

Contents

List of Figures

Chapter 1

Chapter 2

N-GQS is 4.84 ± 0.06 nm. The insets in e and f show selected area diffraction patterns (SAED) of graphene and N-GQS.

Figure 4. (a) Raman spectra and (b) XPS spectra of as-grown graphene and N-GQS. (c, d) Detailed C 1*s* and N 1*s* XPS peaks of N-GQS. (e) UV-vis absorption spectra of N-GQS in dichloromethane. The inset shows a photograph of the N-GQS solution under 365 nm wavelength UV lamp. (f) Photoluminescence (PL) spectra of the N-GQS for different excitation wavelengths (360~440 nm).

Figure 5. SEM images of (a) bare Si and (b) porous Si. Cyclic Voltammetry (CV) of N-GQS on bare Si and porous Si. (c) Photocurrent density-potential (*J-E*) curves for the lightly boron doped p-Si and p-porous Si electrode deposited with N-GQS. N-GQS was introduced by dry transfer on bare Si and by wet transferred on porous Si. Each CV process was performed at a scan rate of 0.005 Vs^{-1}. (d) Electrochemical activity of N-GQS on a Glassy Carbon (GC) electrode with rotating ring disk system. CV data were corrected by iR compensation.

Figure 5. SERS spectra of 1,4-PDI molecules in (a) Si@Au/1,4-PDI, (b) Si@Au/1,4-PDI/Au and (c) Si@Au/1,4-PDI/Au/1,4-PDI systems. The inset shows the Raman band of silicon wafer at 520 cm^{-1} used as an internal reference.

Figure 6. Schematic presentation of 1,4-PDI molecules trapped between two Au nanoparticles. The red part represents the impermeable area for the additional 1,4-PDI molecules into the gap of Au nanoparticle dimer.

Figure 7. (a) FDTD calculation results of the local field intensity ($|E/E_0|^2$) distributions (logarithmic scale) near Au nanoparticle dimer (diameter = 55 nm, gap distance = 1 nm) excited with (a) a parallel-polarized and (b) a perpendicular-

polarized light (wavelength = 632.8 nm) to the dimer axis. (c) The intensity distribution ($|E/E_0|^4$) in the gap of two Au nanoparticles excited with a parallel-polarized light as a function of distance from the center of the gap.

Figure S1. (a, b) AFM surface morphologies of Cu foils annealed at 1,000˚C. (c, d) AFM images of continuous monolayer graphene film grown on Cu by CVD. (e, f) AFM images of N-GQSs converted from monolayer graphene on Cu after N_2-plasma treatment. Scan sizes, 10 x 10 μm^2 for a, c, and e, 1.5 x 1.5 μm^2 for b, d, and f, respectively.

Figure S2. (a-c) AFM images of monolayer graphene on Cu with varying exposure time to N_2-plasma for 0, 8, and 16 sec, respectively. Scan area, 1.5 x 1.5 μm^2. (d) AFM profile of N_2-plasma treated graphene on Cu corresponding to the red box in c. Scan area, 600 x 600 nm^2.

Figure S3. (a) Schematic illustration and photograph images of hydrogen evolution reaction on N-GQSs/Si photocathode.

Chapter 3

Figure 1. Cyclic Voltammetry (CV) of graphene (Gr), N_2-plasma-treated Gr (NGr), Pt, and Pt with NGr on a Si electrode. (a) Photocurrent density-potential (*J-E*) curves for the lightly boron doped p-Si electrode deposited with Gr and NGr. The plasma treatment on Gr was introduced with high purity N_2 gas for 14 sec, which is called NGr-Si. In case of Pt-Si and Pt-NGr-Si electrodes, Pt nanoparticles were deposited on bare Si and NGr-Si by the electroless deposition method, respectively. (b)

Polarization curves of Gr, and NGr on heavily arsenic doped n^+ type Si electrodes under dark condition. Each CV was performed at a scan rate of 0.05 V/sec.

Figure 2. Electrochemical activity of Gr on Glassy Carbon (GC) electrode. (a) CV curve of GC, Gr on GC, NGr on GC, and Pt on GC from rotating disk electrode system. CV data were corrected by iR compensation. (b) Tafel plots were derived from (a) CV data. The 'b' in the inset (mV/decade) and J_0 (A/cm^2) indicate a Tafel slope and an exchange current density, respectively.

Figure 3. (a) Raman spectra and (b) high resolution XPS spectra of N 1s peak of Gr and NGr. The N 1*s* peak is separated into N1 (398.5 eV), N2 (399.9 eV), and N3 (401 eV) which are labeled by green, blue, and red lines. An inset image in (b) represents schematic of NGr. The gray, green, blue, and red spheres indicate the carbon, pyridinic nitrogen, pyrrolic nitrogen, and quaternary nitrogen atoms, respectively. (c-d) High resolution XPS spectra of Si 2*p* region of bare Si, Gr-Si, and NGr-Si electrodes. XPS spectra of each sample (c) before the chronoamperometry test and (d) after the chronoamperometry test at 0 V *vs.* RHE for 10,000 sec. Narrow-scan data of the Si 2*p* region were collected using pass energy of 40 eV and 0.05 eV/step.

Figure 4. The stability test of bare Si, Gr-Si, and NGr-Si photocathodes. CV of Si photocathodes during 300 cycles with a scan rate of 0.05 V/sec at (a) pH 0 and (b) pH 6.8. Polarization curves of each photoelectrodes shifted negatively vs. RHE as the CV operation increased. (c) Chronoamperometry operation of Si photocathodes. The change of normalized photocurrent density (J/ J_{init}) at 0 V vs. RHE of each photoelectrodes with the increase of time at pH 0 (solid line) and pH 6.8 (dash-dotted

line), respectively. J_{init} is the initial current density in the chronoamperometry operation.

Figure S1. Calibration respect to RHE. Current vs. the applied potential respect to Ag/AgCl reference electrode with using (a) Pt foil for Si PEC cell experiment and (b) Pt wire as the counter electrode for RDE experiment.

Figure S2. Resistance of bare Glassy Carbon (GC), Gr on GC, and NGr on GC. Impedance spectroscopy analysis revealed that the resistances of the bare GC, Gr-GC, NGrGC are 7.1 ohm, 7.2 ohm, and 7.4 ohm respectively. Resistances were measured using iR compensation mode in the electrochemical analyzer (CHI 600D, CH Instruments, Inc.).

Figure S3. The logarithm of the exchange current densities calculated by extrapolation to the x-axis. Compared to the bare GC, Gr and NGr catalysts show the high activity for the HER.

Figure S4. Photoelectrochemical performance of NGr-Si photocathode with variation of the amount of Pt solution. (a) Polarization curves of NGr on Si electrode. Each cyclic voltammetry was performed during 4 cycles at a scan rate of 0.05 V/s. The durations of the plasma treatment on Gr were introduced with high purity N2 gas for 4 sec, 10 sec, 14 sec, and 16 sec. For comparison, cyclic voltammogram of Gr without plasma treatment on Si electrode is presented. (b) Representative data from polarization curves of NGr on Si electrode of Figure S4 a

Figure S5. Surface morphology of monolayer Gr and NGrs. (a) AFM images and (b) Raman characterization of a pristine Gr sample as a function of the exposure time to N_2 plasma and the each image was taken the same area measured by AFM. Numbers

on each figure indicate the exposure time. All figures have a size of 6.5 × 6.5 μm_2 (c) Raman spectra of the samples. Numbers on the left side of the left figure indicate the exposure time. Raman peaks are indexed accordingly.

Figure S6. XPS spectra of Gr and NGr. The C 1*s* is 76.78 atomic weight % (at. %) for Gr and 57.17 at. % for NGr, N 1*s* is 0.00 at. % for Gr and 2.20 at. % for NGr, and O 1*s* is 23.22 at. % for Gr and 40.63 at. % for NGr, respectively.

Figure S7. The change of onset potential of bare Si (black line), Gr-Si (red line), and NGr-Si (blue line) electrodes. The onset potential measured from the first CV sweep was a standard, and the difference between the measured onset potential during the CV cycles and the value of the first sweep was investigated; this difference is defined as ΔE – negative shift. The onset potential was measured with increasing the number of cyclic voltammetry in 1M $HClO_4$ (pH 0, dash dot line) and 0.4 M NaH_2PO_4 and 0.6 M Na_2HPO_4 (pH 6.8, solid line) electrolytes, respectively.

Figure S8. The change of photocurrent density at 0 V vs. RHE of bare Si (black line), Gr-Si (red line), and NGr-Si (blue line) electrodes with the increase of time at (a) pH 0 (1M HClO4) and (b) pH 6.8 (0.6 M NaH_2PO_4 and 0.4 M Na_2HPO_4), respectively. At pH 0, NGr-Si electrode shows a spiky plot during a chronoamperometry test because hydrogen bubbles stick to hydrophobic surfaces until sudden bursts occur.

Figure S9. The stability test of bare Si, Gr-Si, and NGr-Si photocathodes. CV results of Si photocathodes during 300 cycles with a scan rate of 0.05 V/sec at (a) pH 0, (b) pH 3.8, and (c) pH 6.8. Polarization curves of each photoelectrodes were shifted negatively vs. RHE as the number of cycles increased.

Figure S10. The stability test of bare Si, Gr-Si, and NGr-Si photocathodes. CV results of Si photocathodes during 300 cycles with a scan rate of 0.05 V/sec at (a) pH 0, (b) pH 3.8, and (c) pH 6.8. Polarization curves of each photoelectrodes were shifted negatively vs. RHE as the number of cycles increased.

Figure S11. Chronoamperometry test of bare Si, NGr-Si, and Pt-NGr-Si photocathodes at pH 6.8. (a) The change of photocurrent density at 0 V *vs.* RHE of bare Si (black line), NGr-Si (red line), and Pt-NGr-Si (blue line) electrodes with the increase of time at pH 6.8. (b) The change of normalized photocurrent density (J/ Jinit) at 0 V *vs.* RHE of each photoelectrodes with the increase of time at pH 6.8.

Chapter 4

Figure 1. Schematic of N-doped graphene quantum sheets (N-GQSs) decorated on a Si nanowire (SiNW) photocathode electrode. Photons absorbed by the SiNWs generate minority carriers (electrons), which drift to the semiconductor/electrolyte interface, where $2H^+$ is reduced to H_2; the N-GQSs serve as electrocatalysts for hydrogen production. The gray, green, blue, and red spheres in the schematic of N-GQSs represent the carbon, pyrrolic nitrogen, quaternary nitrogen, and pyridinic nitrogen atoms, respectively. The average diameter of the N-GQSs is 5 nm, as determined from a TEM image.

Figure 2. SEM images of SiNW arrays on p-silicon substrate obtained by metal assisted chemical etching method. (a) Cross-section and (b) top-view. (c) Dark-field TEM images of N-GQSs on p-SiNWs. (d) High-resolution TEM image shows Moiré pattern created by N-GQS in silicon lattices.

Figure 3. Cyclic voltammograms of N-doped graphene quantum sheets (N-GQSs) on silicon photocathodes. (a) Photocurrent density-potential (*J-E*) curves for a lightly boron-doped planar p-Si electrode and Si nanowire deposited with N-GQSs. The Si nanowire was fabricated using a metal-catalyzed electroless method. (b) Polarization curves of N-GQS on heavily arsenic-doped n^+-type Si electrodes under dark conditions.

Figure 4. Electrochemical activity of graphene monolayer and N-GQSs on glassy carbon (GC) electrodes in a rotating disk electrode system. (a) Cyclic voltammograms (CV) of a graphene monolayer on GC, N-GQSs on GC, Pt/C on GC. CV data obtained compensating for ohmic drop (iR) losses are also plotted (dashed curves). (b) Tafel plots derived from the CV data in (a).

Figure 5. Summary of the experimental data for Si and glassy carbon (GC) electrodes. (a) The photoelectrochemical performance of p-type Si-based photoelectrodes. 'Onset potential' and 'ABPE' indicate the potential at -1 mA/cm^2 *vs.* RHE and the applied bias photon-to-current efficiency, respectively; 'bare' indicates the performance of the bare electrode without deposited catalyst. (b) Electrochemical performance of N-GQSs on GC electrode and other HER catalysts determined using rotating disk electrode system. J_0 indicates that the exchange current density. References can be found in the supporting information (Tables S2 and S3).

Figure 6. Comparison of the electrochemical activity of Si nanowire and N-GQSs on Si nanowire. (a) Mott-Schottky plots from capacitance measurement as a function of potential *vs.* RHE under dark condition. (b) Nyquist plot for Si

nanowire and N-GQSs on Si nanowire at 0 V *vs.* RHE under dark condition. (c) The transient curve of the photocurrent from Si nanowire and N-GQSs on Si nanowire when the light was turned on and turned off at 0 V vs. RHE.

Figure S1. (a) AFM image of nitrogen plasma treated GQSs on Cu foil. Scan size, 600 x 600 nm^2. (b) TEM image of N-GQSs. (c) Histogram showing the size distribution of N-GQSs. (d) Raman spectra of graphene (black) and N-GQSs (red) and (e) detailed N 1*s* XPS spectra of N-GQSs. (f) UV-vis absorption of the N-GQSs in dichloromethane. The inset shows a photograph of the N-GQSs solution under 365 nm wavelength UV lamp.

Figure S2. SEM mapping images of N-GQSs decorated on Si nanowires. (a,b) Colour images of all displayed with three elements; C (red), Si (green), and O (blue).

Figure S3. (a) Bright-field and (b) dark-filed TEM images of N-GQSs dispersed on p-SiNWs. (c) Selected area diffraction patterns (SAED) gives p-SiNWs are well etched toward [001] direction. GQS pattern is hardly observed due to the strong silicon lattice.

Figure S4. Photoelectrochemical performance of Si photocathode (a) Polarization curves of various Si electrodes without depositing any catalyst. Si nanowire were made by metal-catalyzed electroless method. Each of the etching time is 20 min, 30 min, 120 min, and 180 min. Each cyclic voltammetry was performed during 2 or 4 cycles at a scan rate of 5 mV/s. (b) Polarization curves of various Si electrodes deposited with N-GQSs catalyst.

Figure S5. SEM images of cross-sectional views of p-type (100) Si wafers etched in 5 M HF and 0.015 M $AgNO_3$ solution at different etching times. The etching times

are (a) 20 min, (b) 30 min, (c) 120 min, and (d) 180 min.

Figure S6. (a) Schematic illustration and photograph images of hydrogen evolution reaction on N-GQSs/Si photocathode

Figure S7. Calibration respect to RHE. Current vs. the applied potential respect to Ag/AgCl reference electrode with using (a) Pt foil for Si PEC cell experiment and **(b)** Pt wire as the counter electrode for rotating disk electrode (RDE) experiment.

Chapter 5

Figure 1. Introduction to the Li/S battery. (a) The theoretical energy density of different rechargeable battery systems based on active materials only. The units are Wh kg^{-1} and Wh L^{-1} for gravimetric and volumetric energy density, respectively. M = $Ni_{1/3}Mn_{1/3}Co_{1/3}$ for the $LiMO_2$–graphite system. For projected $LiMO_2$–silicon cell, the specific capacity for the cathode and anode are 250 and 3000 mAh g^{-1}, respectively. The density is 4.8 g cm^3 for $LiMO_2$, and the capacity per volume is 2200 mAh L^{-1} for silicon after considering the necessary space for volume expansion. (b) The voltage profile and chemistry of sulfur cathode in the organic electrolyte.

Chapter 6

Figure 1. (a) Schematic illustration and (b) scanning electron microscopy (SEM) image of GO-S/CB composites. (c) Transmission electron microscopy (TME) image and (d) high resolution TEM image of GO-S/CB. (e) Scanning-TEM (STEM) image and (f-h) C, S, and O energy-dispersive S-ray spectroscopy (EDS) maps of the GO-S/CB composites.

Figure 2. (a) FTIR spectra of GO-S/CB and S/CB. The peaks correspond to the various functional groups in GO-S/CB and S/CB. (b) O 1*s* XPS spectra and (c) Raman spectra of GO-S/CB and S/CB.

Figure 3. X-ray diffraction (XRD) patterns and Thermogravimetric analysis (TGA). (a) XRD spectra of S/CB and GO-S/CB on Al foil current collector and (b) TGA spectra collected in N_2 atmosphere with a heating rate of 10℃/min showing the S content of the GO-S electrodes.

Figure 4. Electrochemical characterization of S/CB and GO-S/CB cathodes. Voltage profiles for (a) S/CB and (b) GO-S/CB plotted from 1^{st} to 20^{th} cycles at 0.5 *C*. (c) Cycling performance and (d) Coulombic efficiency of S/CB and GO-S/CB at 0.5 C for 100 cycles.

Figure 5. Cyclic Voltammetry peaks of (a) S/CB and (b) GO-S/CB cathodes at 0.03 mVs^{-1} scan rate.

Figure 6. (a) Rate performance and (b) Coulombic efficiency of S/CB and GO-S/CB composites from 0.1 *C* up to 1 *C*.

Figure 7. Electrochemical Impedance Spectroscopy (EIS) plots of S/CB and GO-S/CB (a) before and (b) after cycles. The symmetry cell of Li metal is plotted in Fig. (a) grey dots.

Figure S1. SEM images of (a) GO-S/CB and (b) S/CB composites. The insets show the magnified images of GO-S/CB and S/CB, respectively.

Figure S2. (a) Fourier transform infrared spectroscopy (FTIR) spectra of CB and GO. Strong peaks attributed to the characteristic vibrational mode of oxygen functional groups. X-ray photoelectron spectroscopy of CB and GO. (b) C 1*s* peaks

and (c) O 1*s* peaks.

Chapter 7

Figure 1. Material characterization of GQDs-S/CB and S/CB composites. a,b, High-resolution TEM images of GQDs. The inset in Fig. 2b shows a histogram of the GQDs size distribution. c, FT-IR spectra of GQDs and CB. The peaks in this figure correspond to the various functional groups in the GQDs and CB. SEM images of d, GQDs-S, and g, GQDs-S/CB. e, HRTEM images of the GQDs-S composites and GQD pattern (yellow circle). A Moiré pattern (red circle) is clearly visible in these TEM images, which is created by a superposition of the GQDs and S crystalline lattices, and f, Raman spectrum of GQDs-S composites, which shows that the GQDs are formed on the sulphur particles. The strong peaks at 218.16 and 472.75 cm^{-1} arise from sulphur, and the D (disorder) and G (graphitic) peaks arise from the GQDs. Schematic diagrams show the structure, h, and the magnified structure, i, of GQDs-S/CB.

Figure 2. Schematic diagrams and SEM images of S/CB and GQDs-S/CB in a Li-S battery. a,b, Schematic configuration of S/CB and GQDs-S/CB employed as a cathode in a Li-S battery. The sulphur (yellow) is wrapped with carbon black (S/CB) and compactly covered with graphene quantum dots and carbon black (GQDs-S/CB), respectively. Polysulphides were dissolved into solvent and the color changed to orange. c,d, SEM images of GQDs-S/CB and S/CB.

Figure 3. Electrochemical properties of S/CB and GQDs-S/CB electrodes. a, Schematic illustration of the discharge profile of a conventional Li-S battery. High

order-polysulphides (S_n^{2-}, n=8-4) and low order-polysulphides (S_n^{2-}, n=2-1) are abbreviated as HO-PSs and LO-PSs. The onset potential (*U*) and the capacity (*Q*) in the dissolution and precipitation regime are noted, which facilitates the analysis of the electrochemical properties of each sample. b, Rate performance of the GQDs-S/CB and S/CB at 0.1 *C* to 10 *C*. c, cycling performance and Coulombic efficiency at 0.5 *C* of both samples for 100 cycles. d,f, Onset potential as a function of cycle number and e,g, capacity as a function of rate and capacity as a function of cycle number.

Figure 4. High resolution C 1*s* X-ray photoemission spectroscopy (XPS) and computational calculations a, S and GQDs-S composites before cycling. b, C 1*s* and c, S 2*p* high resolution spectra of the S/CB and GQDs-S/CB electrodes after 20 cycles. Each spectrum was fitted with functions corresponding to different valencies of carbon and sulphur (dashed line) and the sum of those fitted curves (red line) is consistent with the raw data (black solid line). d, C 1*s* spectra of CB and GQDs/CB electrodes in Li_2S_8 catholyte. e, Raman spectra showing C-S bond formation within the samples. f, XRD spectra of GQDs/CB and CB electrodes in in a Li_2S_8 catholyte. g, A plot of the relative energies for the reactant and product in binding of polysulphides to GQDs, versus the sulphur chain length. The functional groups on GQDs enhance the binding of polysulphides to the carbon due to the substitution of -OH (C-OH) to Sn^{2-}. Yellow, red, white, and gray represents S, O, H, and C atoms, respectively.

Figure 5. TEM and SEM images of nano-sized sulphur on GQDs electrode in Li_2S_8 catholyte after 20 cycles. a,TEM image of nano-sized sulphur in GQDs materials.

The aggregate seen in the TEM is mainly comprised of GQDs, and sulphur is identified as the small darker particles. b, GQDs (yellow circle) covered on nano-sized sulphur particles, c, HRTEM image that shows the lattice fringes of the nano-sized sulphur and GQDs. d, The FFT image of the HRTEM image in c. The two bright spots represent Bragg spots for the sulphur particles, and the other spots are GQDs Bragg spots. e, SEM image of the GQDs electrode in the catholyte after cycling. f-h, C, S, and O energy-dispersive X-ray (EDX) spectroscopy maps of the GQDs electrode.

Figure S1. Scanning electron microscopy and energy-dispersive X-ray spectroscopy characterization of the GQDs-S composites. SEM images of the GQS-S composites, and C, S, and O EDX maps of the GQDs-S composites.

Figure S2. Scanning transmission electron microscopy and EDX characterization of the GQDs-S/CB composites. TEM images of the GQS-S/CB composites, and C, S, and O EDX maps of the GQDs-S/CB composites.

Figure S3. X-ray diffraction (XRD) patterns and Thermogravimetric analysis (TGA). XRD of sulphur, GQDs-S, and GQDs-S/CB composites a, and TGA collected in N_2 atmosphere with a heating rate of 10℃/min b, the S content of the cathode.

Figure S4. X-ray photoelectron spectroscopy of S/CB, and GQDs-S/CB particles. a, C 1*s* peaks, b, S 2*p* peaks, and c, O 1*s* peaks of S/CB and GQDs-S/CB particles.

Figure S5. a, Cycling performance and b, discharge profile of GQDs-S/CB, modified S/CB, and S/CB at 0.05 *C* for 100 cycles. The GQDs-S/CB electrode shows superior cycle retention compared to S/CB and modified S/CB, which indicates that

the surfactant alone does not prevent dissolution of the sulphide discharge-products into the electrolyte.

Figure S6. Charge-discharge profiles of a, S/CB and b, GQDs-S/CB at 0.5 *C* for 100 cycles.

Figure S7. Rate performance of a, S/CB and b, GQDs-S/CB from 0.1 *C* up to 10 *C*.

Figure S8. Relative ratios of dissolution/precipitation regime capacity (Q_2/Q_1). a, Cycling performance up to 100 cycles. b, Rate performance from 0.1 *C* to 10 *C*.

Figure S9. Electrochemical impedance spectroscopy (EIS). Lithium/sulphur cells a, as-prepared, b, fully charged, and c, discharged state after 20 cycles. Insets show the high-frequency range. The equivalent circuit model used to analyze the Nyquist plots d, charge-discharge states.

Figure S10. High resolution C 1*s* X-ray photoelectron spectroscopy a,b, C 1 *s* spectrum of the S/CB and GQDs-S/CB electrodes after 20 cycles in the di scharged state. Each spectrum has been fitted with peaks for different bonde d carbon (dashed line) and the sum of the fitting curves (red line) is consist ent with the raw data (black solid line).

Figure S11. SEM images of GQDs-S/CB and S/CB cathode electrodes after electrochemical cycling. a,b, GQDs-S and S electrodes after cycling.

Figure S12. SEM images and Raman spectra of lithium anodes after cycling against S/CB and GQDs-S/CB electrodes. a,d, SEM images after 20 cycles. b,e, Sulphur energy-dispersive X-ray spectroscopy maps. c,f, Raman spectra. The S peaks are assigned to 156, 221, 473 cm^{-1}, Li_2S to 378 cm^{-1}, and S^{2-} to 746 cm^{-1} (ref. 2). No peaks are present in the cell containing GQDs-S/CB.

Figure S13. High resolution S 2*p* X-ray photoelectron spectroscopy and cycl e performance. a,b, S 2*p* spectrum of the CB and GQDs electrodes, in the charge state, after 20 cycles. These electrodes were cycled in the Li_2S_8 cath olyte. Each spectrum was fitted with functions corresponding to different valencies of sulphur (dashed line) and the sum of these fitted curves (red line) is consistent with the raw data (black solid line). c, Cycle retention of GQDs/CB and CB el ectrodes in Li_2S_8 catholyte over 100 cycles.

Figure S14. The relative energies for the reactant and product in binding of polysulphides to GQDs. The functional groups enhance the binding of polysulphides to carbon due to substitution of –OH (C-COOH) for S_n^{2-}. Yellow, red, white, and gray represents S, O, H, and C atoms, respectively.

Figure S15. TEM images of nano-sized sulphur on a CB electrode in Li_2S_8 catholyte after 20 cycles. a, Bright field STEM image of the CB electrode. b-d, Energy-dispersive X-ray spectroscopy maps of C, S, and O of the CB electrode in the Li_2S_8 catholyte. e, SEM image of the CB electrode in the Li_2S_8 catholyte after cycling. f-h, C, S, and O EDX maps of the GQDs electrode.

Figure S16. HRTEM (high-resolution transmission electron microscopy) images of nano-sized sulphur on GQDs electrode in Li_2S_8 catholyte after 20 cycles. a, TEM image of nano-sized sulphur in the GQD electrode. b, The FFT of the selected region in image, a. The ring pattern of graphene quantum dots. c, Magnification of nano-sized sulphur in image a shows the lattice fringes of sulphur and GQDs. d, The FFT of the selected area in image, c.

List of Tables and Schemes

Chapter 1

Chapter 2

Chapter 3

Chapter 4

Chapter 7

Table S1. Summary of XPS quantitative values of each elements in Figure S4

Table S2. Summary of numerical values of each component (U_1, U_2, Q_1, Q_2, and Q_{total}) with selected cycles for S/CB at 0.5 *C*

Table S3. Summary of numerical values of each component (U_1, U_2, Q_1, Q_2, and Q_{total}) with selected cycles for GQDs-S/CB at 0.5 *C*

Table S4. Summary of numerical values of each component (U_1, U_2, Q_1, Q_2, and Q_{total}) with various C-rates for S/CB

Table S5. Summary of numerical values of each component (U_1, U_2, Q_1, Q_2, and Q_{total}) with various C-rates for GQDs-S/CB

Chapter 1

General Introduction

Hydrogen evolution reaction

The hydrogen production from water under solar energy is considered as one of renewable energy sources and important environmental-issues. However, the development of efficient photoelectrodes and related co-catalyst for water splitting is still challenges in hydrogen production. Considering the thermodynamic potential, a single-component semiconductor with a higher band gap than 1.23V can simultaneously generate hydrogen and oxygen gas from water as well as its band structure is in their proper positions. However, overall water splitting by one single-component semiconductor is still hampered by the poor kinetics in although several semiconductor have band-edge positions that are appropriate for the photoelectrochemical reduction of water. Overcoming this kinetic limitation requires a stronger driving force. Until now, the solar-to-hydrogen conversion efficiency of single-component semiconductor is still under 5%[1], which stimulates photoelectrochemical cells to be separated as cathode and anode electrodes as well as co-catalyst for water splitting also became one of the most important and challenging issues for photoelectrochemical hydrogen production. A critical requirement for outstanding catalysts in a photoelectrochemical cell is not only the ability to boost the kinetics of a chemical reaction but also durability against electrochemical and photoinduced degradation.[12]

General description of HER and catalyst for HER

The oxidation reaction in the electrolysis of water is:[12]

$O_2 + 4e^- + 4H^+ \leftrightarrow 2H_2O$ $E_{anodic} = 1.23\ V - 0.059(pH)\ V\ (vs.\ NHE)$ (1)

while the reduction reaction is:

$4e^- + 4H^+ \leftrightarrow 2H_2$ $E_{cathodic} = 0\ V - 0.059(pH)\ V\ (vs.\ NHE)$ (2)

Where, NHE is the Normal Hydrogen Energy and the standard potential is dependent on pH ($E_{half} = E - 0.059(pH)$ vs NHE). In these two equations, the thermodynamic potential of water splitting ($E^o_{cell} = 1.23V$) is observed by subtracting (2) from (1). Kinetically, however, when a voltage of 1.23V is applied, electrolysis occurs with difficulty, which results in no current flow. In this situation, additional potential is needed to drive a reaction at a certain rate, which is called overpotential, η. Meanwhile, if a current of i_c flows at the cathode, the same current of i_a must flow at the anode to complete the circuit. Because of this, both electrodes (anode and cathode) need the overpotential. Figure 1 shows current to potential curve for the water-splitting reaction. The red line and blue line indicates oxidation and reduction reaction of water electrolysis, respectively. The overpotential at the cathode and anode is written η_c and η_a, respectively. Therefore, total applied potential, E_{appl}, is:[12]

$$E_{appl}=1.23V+\eta_c+\eta_a \quad (3)$$

Higher overpotential requires higher total applied voltage. Using an electrocatalyst for water splitting can reduce the overpotential required for electrolysis of water.

The hydrogen evolution reaction can be written as:

$$H^+ + e^- \rightarrow 1/2H_2 \quad (4)$$

Its standard potential is 0 V vs. NHE and the potential is dependent on pH (E = 0 V – 0.059(pH) vs NHE). Mechanistically, for the HER in acidic solution, the following possible reaction steps have been suggested.[16]

$$H_3O^+ + e^- \rightarrow H_{ads} + H_2O \quad (5)$$

$$H_{ads} + H_3O^+ + e^- \rightarrow H_2 + H_2O \quad (6)$$

$$H_{ads} + H_{ads} \rightarrow H_2 \quad (7)$$

where H_{ads} is the adsorbed hydrogen atom on the surface. Eq. (5) is a discharge step (the Volmer reaction), eq. (6) is a desorption step (the Heyrovsky reaction), and eq. (7) is a recombination step (the Tafel reaction). Therefore, two different pathways for HER can occur. A combination of eq. (5) and (7) step is known as the Volmer-Tafel mechanism. In this mechanism, protons from the solution are discharged on the surface, forming adsorbed hydrogen atoms. Then, two adjacent adsorbed hydrogen atoms combine to form molecular hydrogen. The combination of eq. (5) and (6) is known as the Volmer-Heyrovsky mechanism. A proton from the electrolyte solution is discharged on the catalyst surface to form an adsorbed hydrogen atom. This step is followed by combination with another proton and electron to form molecular hydrogen. However, for the reaction to proceed at a sufficient rate, it needs to be catalyzed on an electrode surface. Possible candidates for an HER catalyst include various metals such as Pt, Pd, and Ru as well as metal oxide, carbon, and enzymes with active centers. Using Pt catalyst for HER, equations (8) – (10) can be described as follows:[2]

$$Pt + H^+ + e- \rightarrow H\text{-}Pt \qquad \text{Volmer reaction} \quad (8)$$

$2(H\text{-}Pt) \rightarrow H_2 + 2Pt$ Tafel reaction (9)

$H\text{-}Pt + H^+ + e^- \rightarrow H_2 + Pt$ Heyrovsky reaction (10)

HER activity of the catalyst can be characterized by representative parameters; the exchange current density and the bond energy of hydrogen adsorbed to the catalyst.[3] During hydrogen evolution, a current I can be described as:[4]

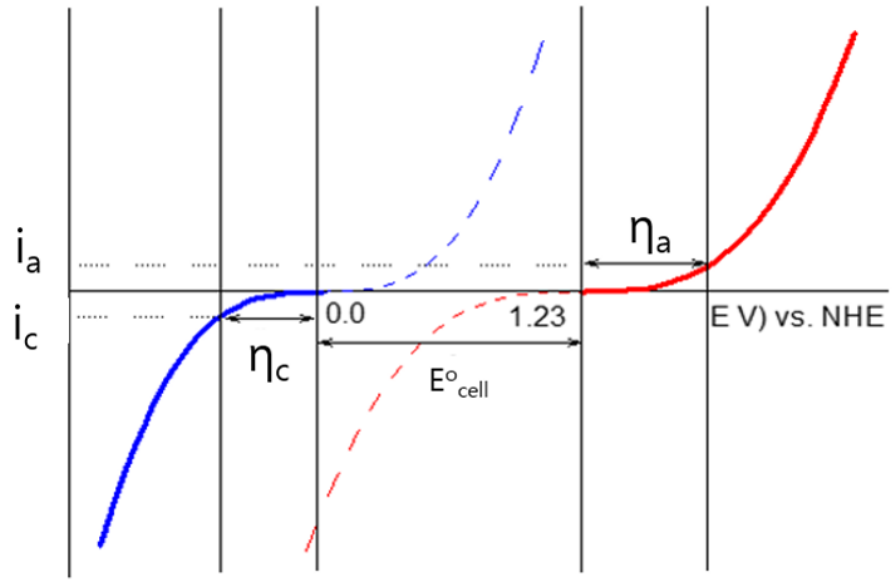

Figure 1. Schematic of the current to potential curve of water splitting reaction

Carbon based HER electrocatalysts

The design of the carbon-based catalysts can represent an important research direction in the search for non-precious, environmentally benign, and corrosion resistant catalysts. In particular, graphene possesses excellent transmittance and superior intrinsic carrier mobility,[5] thus there have been several attempts to use graphene as a catalyst. It has been reported that the reduced graphene oxide (rGO) containing catalytic active materials exhibited an improved activity in HERs as well as oxygen evolution reactions (OERs) or oxygen reduction reactions (ORRs).[6] However, in most cases, the role of carbon materials is limited to an electrical conducting substrate or a supporter that enhances the performance of other decorated active catalysts. Recently, new possibilities have been investigated that monolayer graphene acts as an electrocatalyst for efficient HER.[7] Uk Sim et al., reported that monolayer graphene acts as a catalyst for hydrogen evolution reaction on Si-electrode and boost their catalytic activity by plasma treatment in N_2-ambient.[7] Plasma treatment induces the abundant defects and the incorporation of nitrogen atom in graphene structure, which can act as catalytic sites on graphene. Monolayer graphene containing nitrogen impurities exhibits a remarkable increase in the exchange current density and leads to significant anodic shift of the onset current from a Si-electrode. The electro-catalytic activity of the carbon-based catalyst was much lower than other metal-based catalysts, but the HER

activity of carbon catalyst has increased gradually. The J_0 of monolayer graphene is also comparable to that of the other non-noble metal catalyst, nanoparticulate MoS_2.[7,8,9] J_0 can be accurately calculated by considering the number of active sites. For example, the J_0 of MoS_2 for the HERs is experimentally measured to be 1.3×10^{-7} to 3.1×10^{-7} $A/cm^2_{geometric}$.[9]Active sites of MoS_2 nanoparticle for HER are known to be edge sites of MoS_2 nanoparticle.[10] For the direct site-to-site comparison between MoS_2 nanoparticle and Pt catalyst, T. Jaramillo *et al*. have measured an exchange current per site of MoS_2 combined with STM analysis.[9] The exchange current per site is then multiplied by the site density of Pt for a fair comparison to the transition metal catalyst, resulting in the exchange current density of 7.9×10^{-6} A/cm^2. This value is still similar to exchange current density of monolayer graphene (2.7×10^{-6} A/cm^2). To sum up, while the representative carbon-based catalyst, graphene, has the catalytic activity for HER, the identification and quantification of the active sites of the single monolayer graphene should be further investigated for comparative study.

Recently, a metal-free carbon catalyst doped with nitrogen and phosphorous showed good activity for HER (Figure 2 (c) - (d)). Co-activated N and P heteroatom, which is adjacent to C atom in the graphene matrix, could affect its valence orbital energy levels to enhance reactivity for HER. Graphitic-carbon nitride with nitrogen-doped graphene also shows enhanced

HER activity with similar low overpotential and Tafel slope compared to some well-developed metallic catalysts. Through the density functional theory calculations, it is known that intrinsic chemical and electronic coupling of graphitic C_3N_4 and N-doped graphene synergistically promotes the proton adsorption and reduction kinetics. Table 1 summarizes a selection of experimental values of exchange current for the hydrogen evolution on carbon-based catalysts.

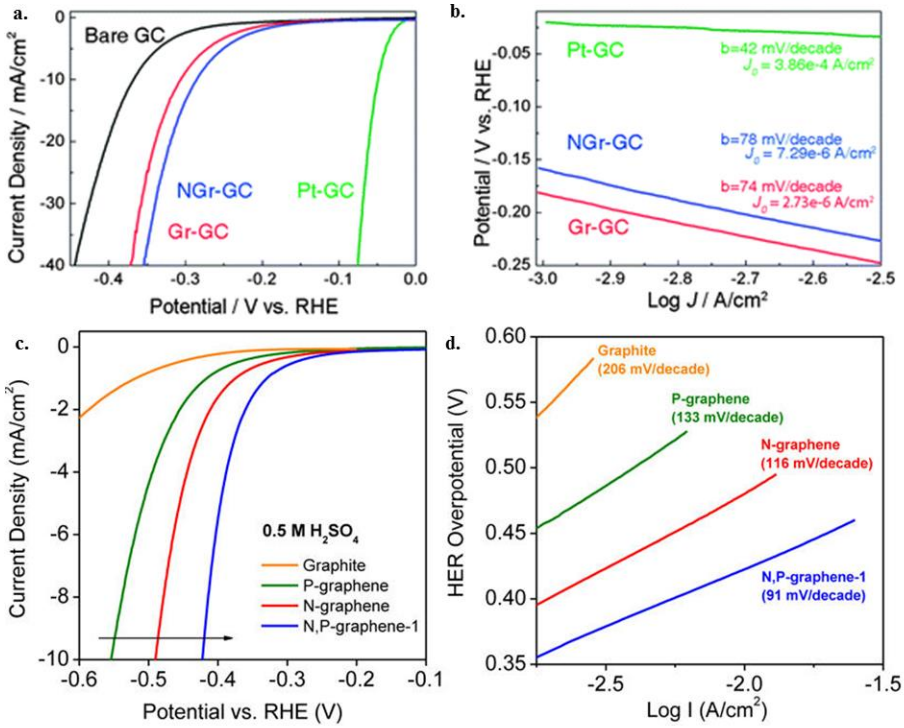

Figure 2. Electrochemical properties and chemical structure of graphene based electrodes (a) CV curve of GC, Gr on GC, NGr on GC, and Pt on GC from a rotating disk electrode system. (iR corrected) (b) Tafel plots were derived from (a) CV data. (c, d) HER polarization curves and the corresponding Tafel plots of N- and/or P-doped graphene electrocatalysts. Reprinted with permission (a), (b) from ref. Copyright 2013 The Royal Society of Chemistry and (c), (d) from ref. [116] Copyright 2014 American Chemical Society.

Catalyst/Substrate (adhesive)	Loading method	Electrolyte	Activity			Ref. (Year)
			Tafel Slope (mV/dec)	TOFs (S^{-1})	Exchange current –log(j_0) (A/cm^2)	
Monolayer graphene	CVD grown graphene	1M HClO4	(75)	N/A	7.57	(2013)
N doped Gr	Annealing mixed precursors	0.5M H_2SO_4 0.1M KOH	(116) (143)	N/A	7.15 9.93	(2014)
P doped Gr	Annealing mixed precursors	0.5M H_2SO_4 0.1M KOH	(133) (159)	N/A	8.05 10.79	(2014)
N,P doped Gr	Annealing mixed precursors	0.5M H_2SO_4 0.1M KOH	(91) (145)	N/A	6.62 9.40	(2014)
g-C_3N_4@NG/GC (Nafion)	Exfoliation & Polycondensation	0.5M H_2SO_4	(51.5)	N/A	6.46	(2014)

Table 1. Selection of experimental values of Tafel slope and exchange current for the hydrogen evolution on carbon based catalyst system. Loading method and electrolyte used are described.

References

1. A. Kudo, Y. Miseki, *Chemical Society Reviews* **2009**, *38*, 253-278.
2. J. Larminie, A. Dicks, M. S. McDonald, *Fuel cell systems explained, Vol. 2*, Wiley New York, **2003**.
3. H. Wolfschmidt, O. Paschos, U. Stimming, in *Fuel Cell Science*, John Wiley & Sons, Inc., **2010**, pp. 1-70.
4. B. E. Conway, G. Jerkiewicz, *Electrochimica Acta* **2000**, *45*, 4075-4083.
5. K. Novoselov, A. K. Geim, S. Morozov, D. Jiang, M. K. I. Grigorieva, S. Dubonos, A. Firsov, *Nature* **2005**, *438*, 197-200.
6. aY. Liang, Y. Li, H. Wang, J. Zhou, J. Wang, T. Regier, H. Dai, *Nature Mater.* **2011**, *10*, 780-786; bJ.-D. Qiu, G.-C. Wang, R.-P. Liang, X.-H. Xia, H.-W. Yu, *J. Phys. Chem. C* **2011**, *115*, 15639-15645; cQ. Xiang, J. Yu, M. Jaroniec, *Chem. Soc. Rev.* **2012**, *41*, 782-796.
7. U. Sim, T.-Y. Yang, J. Moon, J. An, J. Hwang, J.-H. Seo, J. Lee, K. Y. Kim, J. Lee, S. Han, B. H. Hong, K. T. Nam, *Energy Environ. Sci.* **2013**, *6*, 3658-3664.
8. J. Kibsgaard, Z. Chen, B. N. Reinecke and T. F. Jaramillo, *Nat Mater*, **2012**, 11, 963-969.
9. T. F. Jaramillo, K. P. Jørgensen, J. Bonde, J. H. Nielsen, S. Horch, I. Chorkendorff, *Science* **2007**, *317*, 100-102.
10. Y. Li, H. Wang, L. Xie, Y. Liang, G. Hong, H. Dai, *Journal of the American Chemical Society* **2011**, *133*, 7296-7299.
11. Y. Zheng, Y. Jiao, L. H. Li, T. Xing, Y. Chen, M. Jaroniec, S. Z. Qiao, *ACS Nano* **2014**, *8*, 5290-5296.
12. U. Sim, K. Jin, S. Oh, D. Jeong, J. Moon, J. Oh, K. T. Nam, *Handbook of Clean Energy Systems*, 2015.

Part Ⅰ

N-doped Graphene for Hydrogen Evolution Reaction (HER)

Chapter 2

One-step synthesis of N-doped graphene quantum sheets from monolayer graphene by nitrogen plasma

Introduction

Recently, graphene quantum dots (GQDs) has been attracting much attention in bioimaging, light-emitting, and photovoltaic applications[1–3] due to its unique optical properties depending on size and functional edge as well as the accessibility to solution chemistry.[4–6] This has stimulated tremendous efforts to develop various synthesizing methods such as hydrothermal cutting,[7] patterning by nanolithography,[8] and electrochemical scissoring of graphene sheets,[9] as well as bottom up synthesis by wet chemistry to produce GQDs with different sizes and functionalities.[6] Usually, these methods require strongly acidic environment or time-consuming multi-step processes, which is a drawback for more efficient synthesis of high-quality GQDs. Moreover, in order to be used for various optoelectronic and energy applications, GQDs often need to be fabricated as a thin-film structure on a solid interface. However, the GQDs in aqueous solvent are hardly processible because they are unstable in aqueous environment. In addition, preparing GQD films from aqueous dispersion is challenging because spin coating or drop-casting method doesn't provide enough control over thickness and uniformity as well as it requires rigid and flat surface rather than flexible or conformal substrates. Plasma treatment is one of the facile ways to tune the intrinsic properties of graphene, and previously, oxygen plasma was applied to prepare chemically functionalized graphene showing uniform photoluminescence and Raman spectral changes originated from its defective structures.[10,11] On the other hand, chemical doping is an effective way to tune the optical, chemical, and electronic properties of graphene.[12] Likewise, the band-gap of GQDs can be engineered by changing size, shape, edge-, and surface

functionalities,[6,13,14] leading to tunable photoluminescence with higher intensity. In particular, the functional modification with nitrogen could offer more active sites needed for higher catalytic activities, which is important for various energy applications.[9] Herein, we introduce a simple one-step method to prepare large-scale N-doped GQSs by directly applying nitrogen plasma to as-grown graphene on Cu, which can be transferred as a film like layer or easily dispersed in an organic solvent. Moreover, we confirm that the N-GQSs transferred on flat Si and porous Si can be a good photoelectrochemical catalyst for hydrogen evolution reaction (HER). Atomic force microscopy (AFM) and transmission electron microscopy (TEM) images show that the average size of N-GQSs is 4.84 nm, and the substitution of carbon with nitrogen is evidenced by Raman spectroscopy and X-ray photoelectron spectroscopy (XPS). The unique optical properties of N-GQSs were confirmed by absorption and photoluminescence spectra, showing strong emission with the maximum wavelength of 430 nm when excited by 365 nm radiation source (Xe lamp).

Experimental

Synthesis of graphene quantum sheets

In the first step of graphene synthesis, a copper foil was put into a quartz reactor in the CVD system and then heated to 1000℃ with flowing H_2 at 70 mTorr. Additionally, the sample was annealed for 20 min without changing the condition. The gas mixture of H_2 and CH_4 was flowed with rates of 5 and 50 SCCM for 30 min under 8 Torr. Finally, the sample was rapidly cooled down to room temperature with flowing H_2. After growth, in order to remove graphene on one of the sides of Cu foil, graphene on Cu was placed into the plasma chamber (SNTEK). The chamber pressure was pumped down to 50 mTorr, and O_2 gas was introduced into the chamber by applying a radio-frequency (13.56 MHz) forward power of 100 W for 10 s. In addition, to make N-GQS on the front side of Cu, low density N_2-plasma was produced by applying 10 W power. The N_2 flow rate was 20 SCCM and the working pressure of the chamber was 120 mTorr. Under these conditions, the N_2 plasma treatments were performed for 14 s to test the electrochemical reaction of the graphene surface. Finally, poly(methyl methacrylate) (PMMA) was spincoated on graphene and then copper foil was removed in 0.1 M ammonium persulfate solution. After washing with deionized water, the graphene was transferred onto the Si substrate and then PMMA was removed in acetone for 30 min.

Characterization

Raman spectra were obtained with a Renishaw micro-Raman spectroscope with an excitation wavelength of 514.5 nm, an Ar laser. The spot diameter was approximately 2 mm with a 50x objective lens. The oxygen plasma treatment (SNTEK) was carried out with a 100 W radio-frequency (rf) power for 13 s under 140 mTorr and the nitrogen plasma was accelerated with a 10 W rf power for several exposure times (14 s) under 120 mTorr. XPS spectra were collected by AXIS Ultra DLD (Kratos. Inc) using a monochromatic Al K (1486.6 eV), 150 W source at Korea Basic Science Institute (KBSI). Narrow-scan data were collected using a pass energy of 40 eV and 0.05 eV per step.

Calibration with respect to relative hydrogen electrode

The Ag/AgCl/3 M NaCl electrode (BASi) was used as the reference electrode. Pt foil (2 cm x 2 cm x 0.1 mm, 99.997% purity, Alfa Aesar) was used as the counter electrode. In the case of RDE experiment, Pt wire (0.1 mm diameter, Dr Bob's cell) was used as the counter electrode. It was carefully calibrated with respect to the reversible hydrogen electrode (RHE) in an aqueous 1 M perchloric acid solution (Sigma Aldrich) with high purity H_2 saturation at 25℃. The RHE was calibrated to between -0.201 V and -0.203 V vs. the Ag/AgCl reference electrode. The potential was controlled using a potentiostat (CHI 600D, CH Instrument) at a scan rate of 5 mV s^{-1}.

Results and Discussion

First, the monolayer graphene was synthesized by using 10 × 10 cm^2 Cu foils as catalytic substrates in 1000℃ quartz reactor with flowing 50 sccm CH_4 and 5 sccm H_2 for 30 min under 8 Torr.[13] Next, the N-GQSs were prepared by irradiating nitrogen plasma (10 W RF power with varying exposure time under 120 mTorr) to as-grown CVD graphene on Cu as shown in Figure 1. Finally, the N-GQSs were transferred using conventional polymer-assisted dry-transfer methods on a target substrate after removing Cu by 0.1 M aqueous ammonium persulphate etchant.[15] Alternatively, the floating N-GQSs after removing Cu without PMMA can be dispersed into common organic solvent such as dichloromethane using solvent extraction techniques.

The AFM images in Figure 2 a-d show the gradual increase of surface roughness with increasing nitrogen plasma treatment time, indicating that the as-grown graphene on Cu is directly converted N-GQSs. The AFM height profile of N_2-plasma treated graphene for 16 sec shows the average height of 1.64 ± 0.06 nm (Figures S1 and S2).

Figure 3 a-b show the N-GQSs film directly transferred from Cu to a SiO_2 substrate after coating with poly(methyl methacrylate) (PMMA) layer. The PMMA can be easily removable by acetone. Figure 3 c-d show the N-GQDs drop-cased ontoa SiO_2 substrate from the suspension in dichloromethane. The atomic structures of N-GQSs were investigated by high-resolution transmission electron microscopy (HRTEM) as shown in Figure. 3e-g. The sample was prepared by drop-drying the N-GQSs solution on a graphene-supported TEM grid.[16]

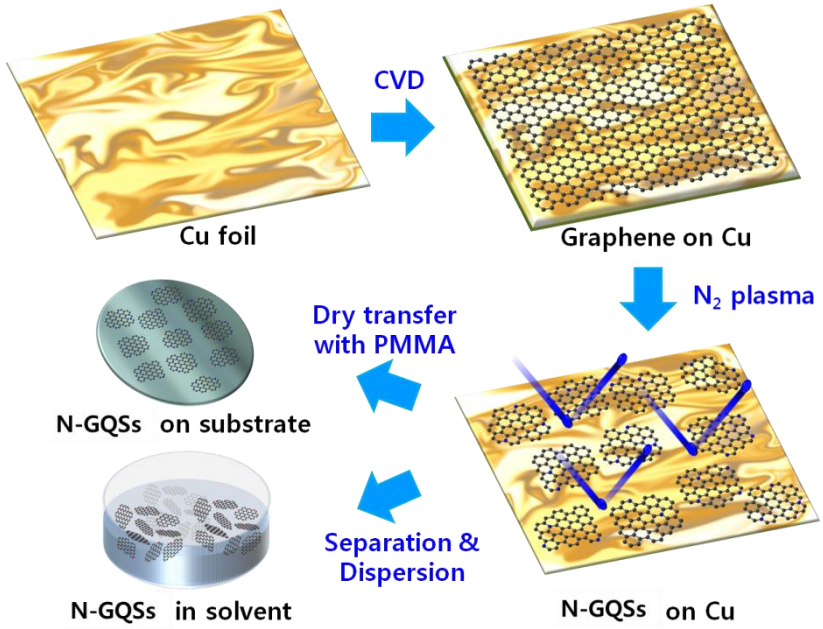

Figure 1. Schematic illustration of N-GQSs fabrication processes.

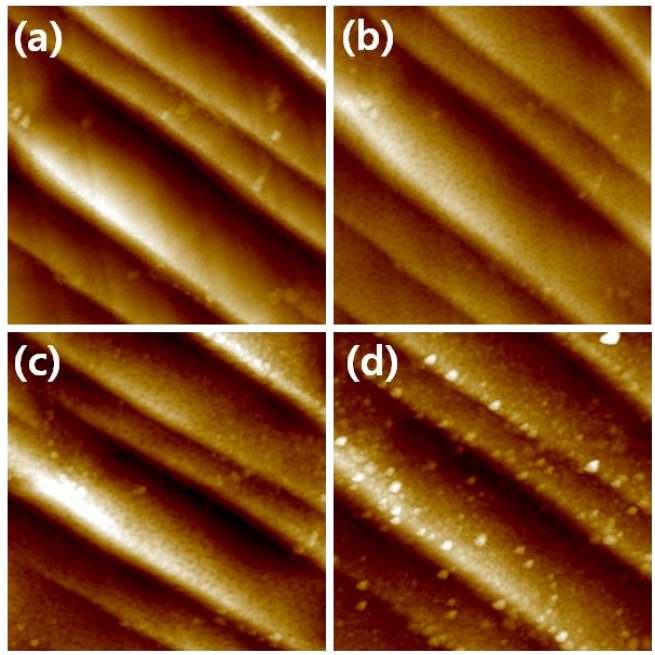

Figure 2. (a-d) AFM images of graphene on Cu surface after exposure to nitrogen plasma for 0, 2, 4, and 6 sec, respectively. Scan sizes, 1.5 x 1.5 μm^2. The AFM images were obtained from a fixed position.

Most of N-GQSs show a size distribution from 3 to 7 nm with an average value of 4.84 nm (Figure 3 h). The clear atomic lattice structure shown in Figure 3 g indicates that the N-GQSs are highly crystalline.

After exposure to nitrogen plasma, the D peaks related structural defects at the edges of graphene were signifi cantly increased in Raman spectra (Figure 4 a).[17,18] On the other hand, the shift of D and 2D peaks indicates that the graphene is doped with nitrogen atoms.[19] X-ray photoelectron spectroscopy (XPS) measurements were performed to determine the chemical composition of N-GQSs (Figure 4 b-d). No N 1*s* peak was observed in monolayer graphene. The strong C 1*s* peak at 284.8 eV corresponding to sp^2 carbon indicates that the conjugated honeycomb lattices are mostly maintained after N_2-plasma treatment. We suppose that the oxygen related sub peaks such as C-O (286.6 eV), C=O (288.3 eV), and O-C=O (289 eV) are originated from the reaction of unstable N-GQS edges or defects with oxygen when exposed to air. The C-N bond peak at 285.2 eV in C 1*s* spectrum (Figure 4 c) as well as the pridinic (398.5 eV) and pyrrolic (399.9 eV) peaks in N 1*s* spectrum (Figure 4 d) indicate that nitrogen-to-carbon ratio is ～2.7%. The UV-vis absorption spectrum of the N-GQSs shows an absorption band with a peak maximum (λ_{max}) at 270 nm (Figure 4 e). The PL spectrum exited at 370 nm shows a strong peak at λ_{max} = 430 nm. Thus, the N-GQDs emitted intense blue luminescence under 365 nm wavelength irradiation by UV lamp (Figure 4 e, inset). We found that the λ_{max} in PL spectra is almost invariable with varying excitation wavelength from 360 nm to 420 nm.

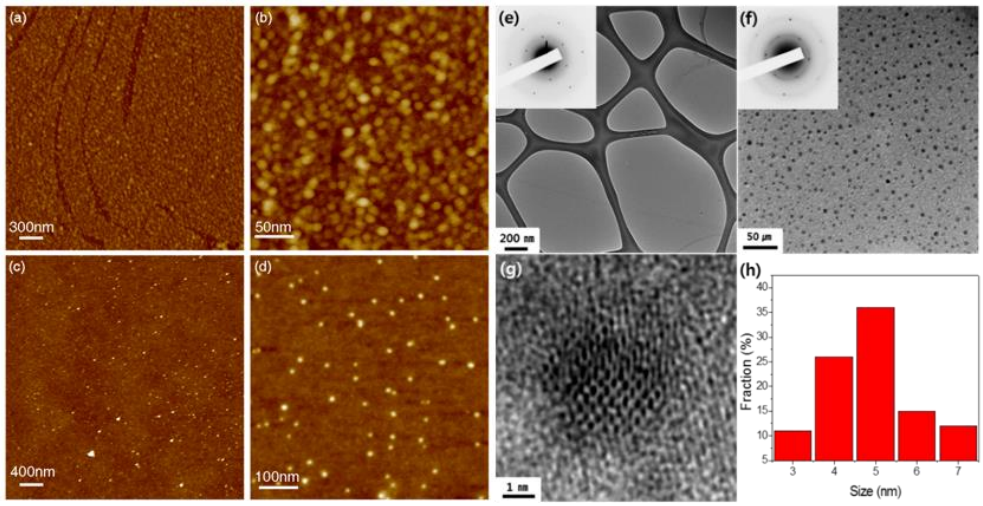

Figure 3. (a, b) AFM images of the N-GQSs transferred to a SiO_2 substrate using polymer-support layer (PMMA). (c, d) AFM images of N-GQS drop-casted from solution to a SiO_2 substrate. Scan sizes, 10 x 10 m^2 for a and c, 1.5 x 1.5 m^2 for b and d, respectively. See Supporting Information of detailed AFM analyses (Figure. S1 and S2). (e) TEM image of monolayer graphene supported by holely carbon grids. (f, g) Low and high-resolution TEM images of N-GQSs on a graphene-supported grid. (h) Histogram showing the size distribution of N-GQS and the average size of N-GQS is 4.84 ± 0.06 nm. The insets in e and f show selected area diffraction patterns (SAED) of graphene and N-GQS.

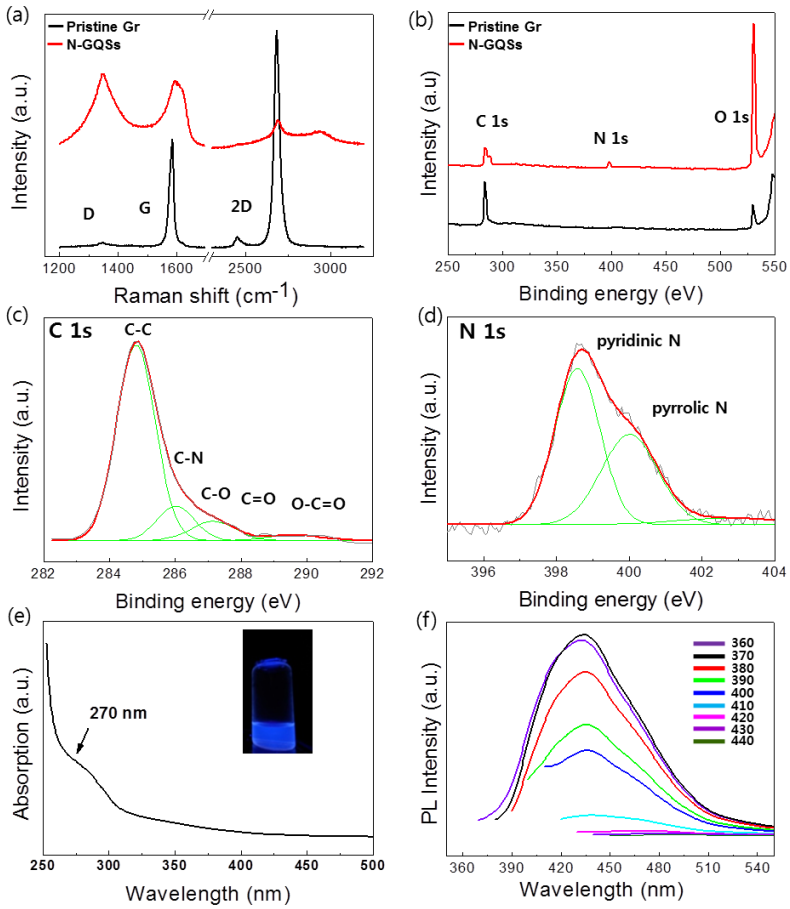

Figure 4. (a) Raman spectra and (b) XPS spectra of as-grown graphene and N-GQS. (c, d) Detailed C 1*s* and N 1*s* XPS peaks of N-GQS. (e) UV-vis absorption spectra of N-GQS in dichloromethane. The inset shows a photograph of the N-GQS solution under 365 nm wavelength UV lamp. (f) Photoluminescence (PL) spectra of the N-GQS for different excitation wavelengths (360~440 nm).

Recently, graphene based catalyst becomes an attractive candidate for photoelectrochemical reaction.[20,21] **Figure 5** demonstrates the catalyst application of N-GQSs on a flat bare Si and a porous Si substrates for hydrogen production. The scanning electron microscopy (SEM) images in Figure 5 a-b show the cross section of a bare Si and a porous Si and each inset shows the top-view of the sample. To evaluate the photocathodic behavior, N-GQSs were loaded on a bare Si with the dry transfer and on a porous Si with the solution drop-casting. The photocurrent density was measured as potential sweep from 0.4 V to –0.8 V *vs*. Reversible Hydrogen Electrode (RHE) in a three electrode cell. A light source of a 300 W Xe lamp (100 mW cm^{-2}) with an Air Mass 1.5 Global condition filter was illuminated on the samples in an aqueous 1 M perchloric acid solution (pH 0) (Figure S3). Interestingly, the N-GQSs exhibit the superior catalytic activity for HER. As shown in Figure 5 c, the photocurrent density-potential (*J*–*E*) curve of N-GQSs/bare Si dramatically is shifted approximately ~0.35 V toward positive potential compared to that of the bare Si as well as the onset potential of N-GQSs also positively shifted by 0.29 V (Table S1). Compared to bare Si, porous Si exhibits enhanced limiting current density and positive shift of onset potential ascribed to light trapping effect. In N-GQSs on a porous Si substrate, the positive shift in 0.09 V of the onset potential also shows higher activity for HER compared to that of a porous Si. Figure 5 d shows the electrocatalytic activity of N-GQSs, CV curves of the samples were obtained without illumination with rotating disk electrode (RDE) system. For the working electrode, N-GQSs were transferred to a glassy carbon tip which is inert in aqueous solution. The *J*–*E* curves were swept from 0.1 V to –0.35 V and the onset potential were

obtained –5 mA cm^{-2} of HER current density of as-grown graphene and N-GQSs (Table S1). The onset potential of N-GQSs is –0.22 V with respect to RHE, which has positive shift by 0.07 V compared to that of as-grown graphene. This result is similar to the photoelectrochemical behavior of the *J*–*E* curves, a positive shift in the overall *J*–*E* curve induced by N-GQSs. From the above results, we conclude that the N-GQSs show the superior electrocatalytic effect for hydrogen production when combined with Si photocathodes with arbitrary morphologies.

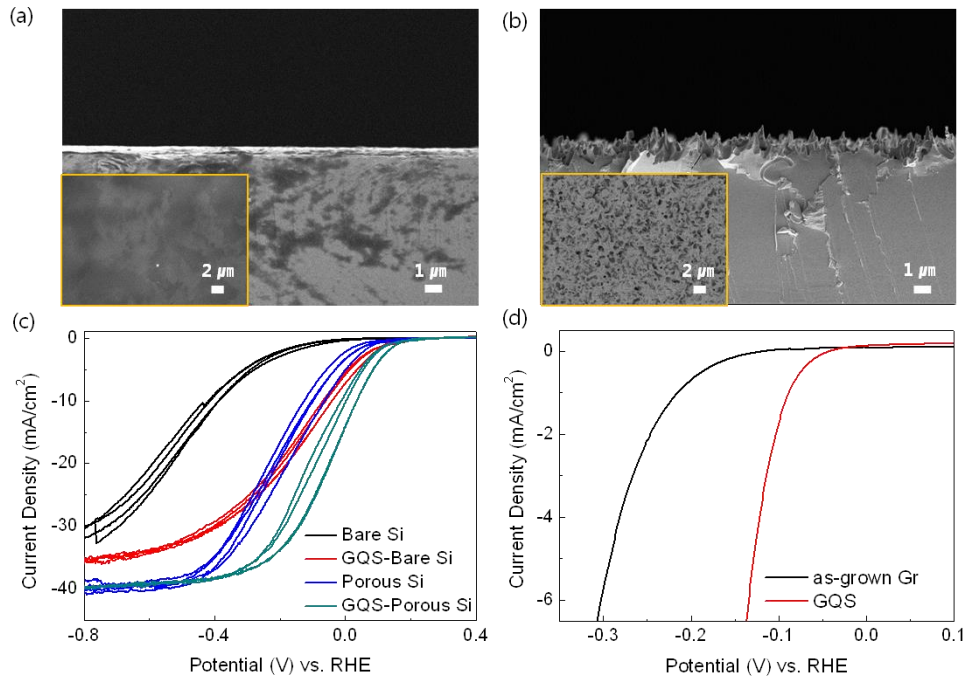

Figure 5. SEM images of (a) bare Si and (b) porous Si. Cyclic Voltammetry (CV) of N-GQS on bare Si and porous Si. (c) Photocurrent density-potential (*J-E*) curves for the lightly boron doped p-Si and p-porous Si electrode deposited with N-GQS. N-GQS was introduced by dry transfer on bare Si and by wet transferred on porous Si. Each CV process was performed at a scan rate of 0.005 Vs^{-1}. (**d**) Electrochemical activity of N-GQS on a Glassy Carbon (GC) electrode with rotating ring disk system. CV data were corrected by iR compensation.

Conclusions

In summary, we have demonstrated the formation of N-doped GQSs from as-grown monolayer graphene on Cu using nitrogen plasma. Various spectroscopic analyses including AFM, TEM, XPS, Raman, and PL indicate the direct formation of high-quality N-GQSs from CVD graphene. The N-GQSs can be transferred onto an arbitrarily shaped photocathode surface to enhance the catalytic activity for photoelectrochemical hydrogen evolution, which would be also useful for various display, energy, and biological applications.

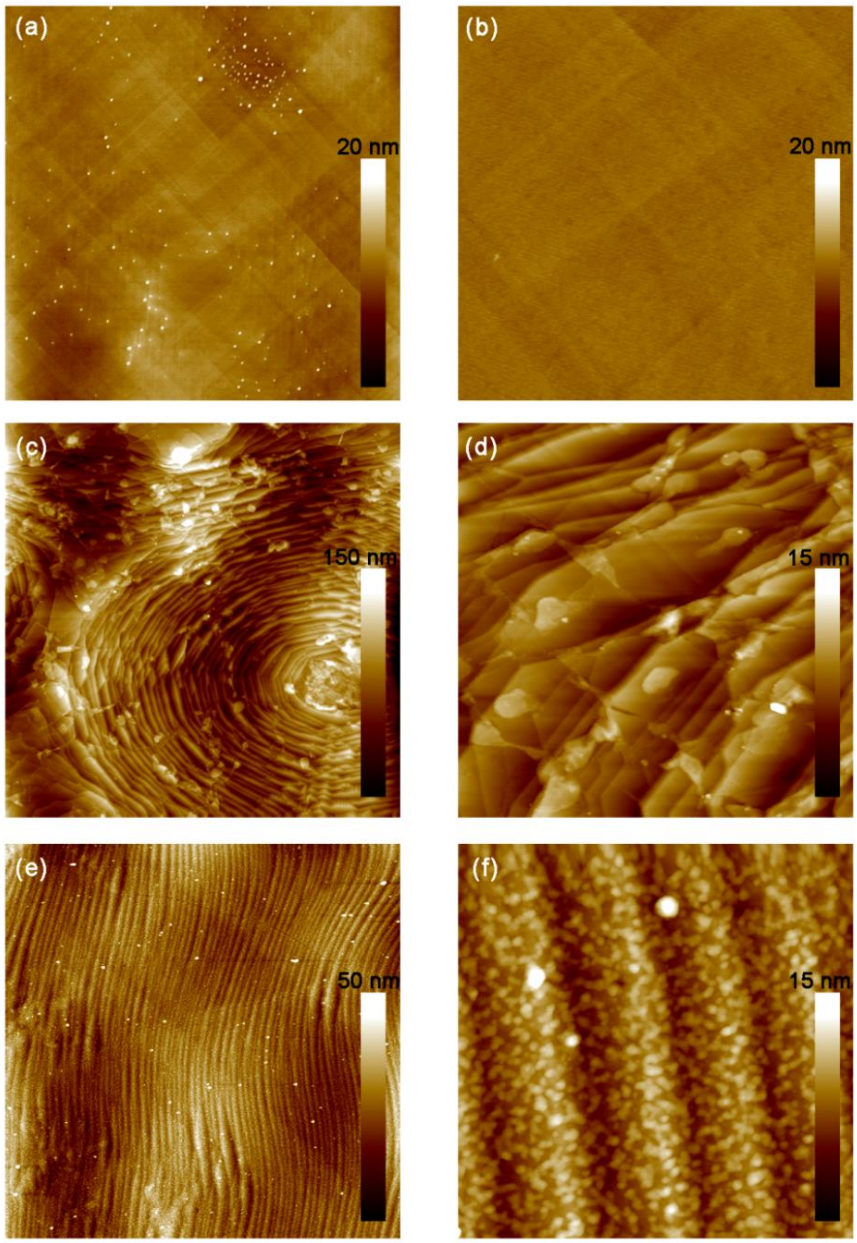

Figure S1. (a, b) AFM surface morphologies of Cu foils annealed at 1,000˚C. (c, d) AFM images of continuous monolayer graphene film grown on Cu by CVD. (e, f) AFM images of N-GQSs converted from monolayer graphene on Cu after N_2-plasma treatment. Scan sizes, 10 x 10 μm^2 for a, c, and e, 1.5 x 1.5 μm^2 for b, d, and f, respectively.

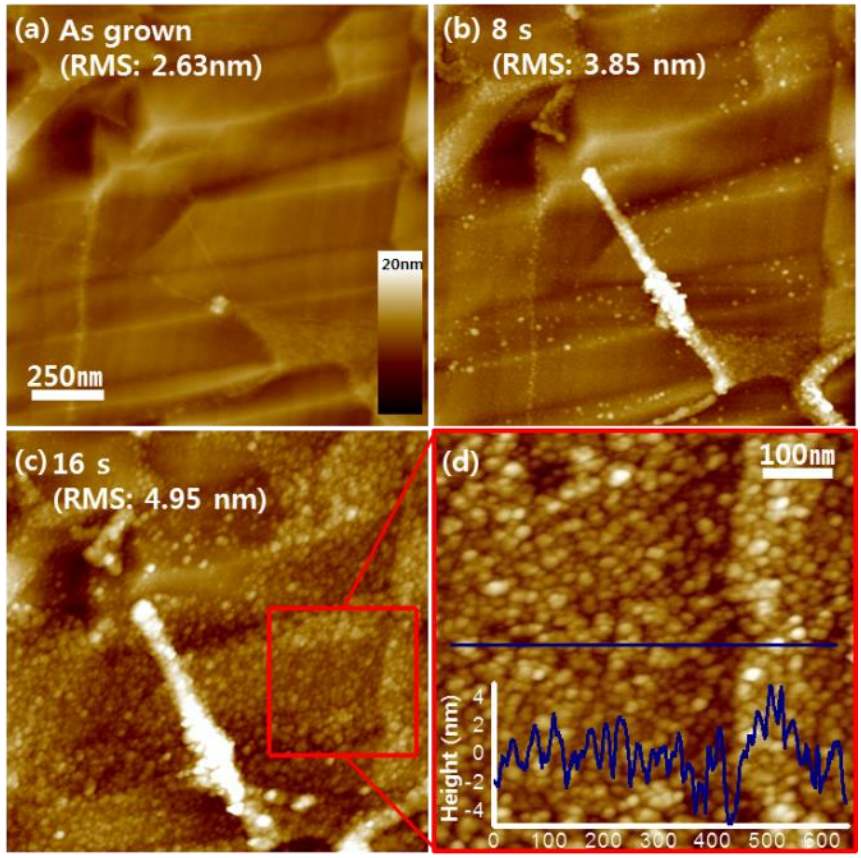

Figure S2. (a-c) AFM images of monolayer graphene on Cu with varying exposure time to N_2-plasma for 0, 8, and 16 sec, respectively. Scan area, 1.5 x 1.5 μm^2. (d) AFM profile of N_2-plasma treated graphene on Cu corresponding to the red box in c. Scan area, 600 x 600 nm^2.

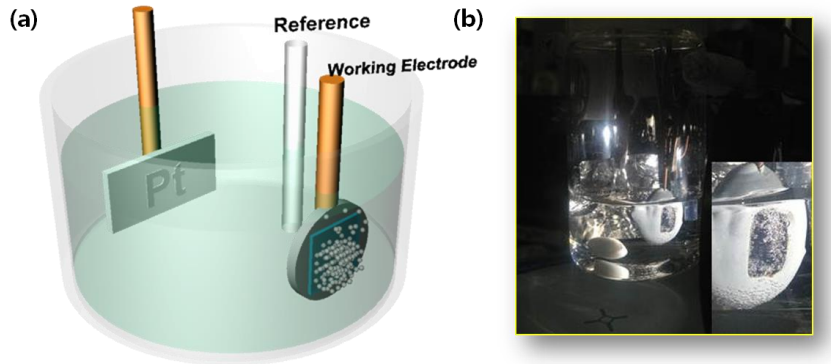

Figure S3. (a) Schematic illustration and photograph images of hydrogen evolution reaction on N-GQSs/Si photocathode.

Table S1. Summary of the experimental data for Si and glassy carbon (GC) electrodes.

condition	Electrode	Onset potential [E (V) at -1mA/cm^2]	[E (V) at -5mA/cm^2]
Under illumination (p type Si)	Bare Si	-0.17	-0.29
	Porous Si	0.07	-0.03
	GQS monolayer Si	0.12	0.01
	GQS solution-porous Si	0.16	0.08
RDE (Glassy carbon) under dark condition	Bare Si	-0.24	-0.33
	As grown Gr-Si	-0.21	-0.29
	GQS-Si	-0.08	-0.22

This value was calculated from the consideration of the following reference; Y. W. Chen, J. D. Prange, S. Dühnen, Y. Park, M. Gunji, C. E. Chidsey and P. C. McIntyre, Nature Mater., 2011, 10, 539-544.

References

1. X. Geng, L. Niu, Z. Xing, R. Song, G. Liu , M. Sun, G. Cheng, H. Zhong, Z. Liu, Z. Zhang, L. Sun, H. Xu, L. Lu, L. Liu, *Adv. Mater.* **2010**, *22*, 638.
2. D. I So , B. W. Kwon, D. H. Park, W. Seo, Y. Yi, B. Adgadi, C. Lee, W. K. Choi, *Nature Nanotech*. **2012**, *7*, 465.
3. a) J. K. Kim , M. J. Park , S J. Kim , D. H. Wang , S.-P. Cho , S. Bae , J. H. park , B. H. Hong , *Acs Nano* **2013** , *7* , 7207 ; b) X. Yan , X. Cui , B. Li , L. Li , *Nano Letters* **2010**, *10*, 1869.
4. S. Kim, S. W. Hwang, M. Kim, D. Y. Shin, D. H. Shin, C. O. Kim, S. B. Yang, J. H. Park, E. Hwang, S. Choi, G. Ko, S. Sim, C. Sone, H. J. Choi, S. Bae, B. H. Hong, *Acs Nano* **2012**, *6*, 8203.
5. S. H. Jin, D. H. Kim, G. H. Jun, S. H. Hong, S. Jeon, *ACS Nano* **2013**, *7*, 1239.
6. X. Yan, X. Cui, L. Li, *J. Am. Chem. Soc.* **2010**, *132*, 5944.
7. D. Pan, J. Zhang, Z. Li, M. Wu, *Adv. Mat.* **2010**, *22*, 734.
8. J. Lee, K. Kim, W. I. Park, B. Kim, J. H. Park, T. Kim, S. Bong, C. Kim, G. Chae, M. Jun, Y. Hwang, Y. S. Jung, S. Jeon, *Nano Letters* **2012**, *12*, 6078.
9. Y. Li, Y. Zhao, H. Cheng, Y. Hu, G. Shi, L. Dai, L. Qu, *J. Am. Chem. Soc.* **2012**, *134*, 15.
10. T. Gokus, R. R. Nair, A. Bonetti, M. Bohmler, A. Lombardo, K. S. Novoselov, A. K. Geim, A. C. Ferrari, A. Hartschuh, *ACS Nano* **2009**, *3*, 3963.
11. D. C. Kim, D.-Y. Jeon, H.-J. Chung, Y. Woo, J. K. Shin, S. Seo, *Nanotechnology* **2009**, *20*, 375703.
12. C. Hu, Y. Liu, Y. Yang, J. Cui, Z. Huang, Y. Wang, L. Yang, H. Wang, Y. Xiao, J. Rlong, *J. Mater. Chem. B* **2013**, *1*, 39.
13. X. Yan, B. Li, X. Cui, K. Wei, L. Li, *J. Phys. Chem. Lett.* **2011**, *2*, 1119.
14. H. Tetsuka, R. Asahi, A. Ngoya, K. Okamoto, I. Tajima, R. Ohta, A. Okamoto, *Adv. Mater.* **2012**, *24*, 5333.
15. S. Bae, H. Kim, Y. Lee, X. Xu, J. Park, Z. Yi, J. Balakrishnan, T. Lei, H. R. Kim, Y. I. Song, Y. Kim, K. S. Kim, B. Ozyilmaz, J. Ahn, B. H. Hong, S. Iijima, *Nature Nanotech*. **2010**, *5*, 574.

16. S. Horischi, T. Gotou, M. Fujiwara, *Appl. Phys. Lett.* **2004**, *84*, 2403.
17. A. C. Ferrari, J. C. Meyer, V. Scardaci, C. Casiraghi, M. Lazzeri, F. Mauri, S. Piscanec, D. Jiang, K. S. Novoselov, S. Roth, A. K. Geim, *Phys. Rev.* **2006**, *97*, 187401.
18. a) A. Ferrari, J. Robertson, *Phys. Rev. B* **2001**, *64*, 075414; b) C. Casiraghi, S. Pisana, K. S. Novoselov, A. K. Geim, A. C. Ferrari, *Appl. Phys. Lett.* **2007**, *91*, 233108.
19. L. G. Bulusheva, A. V. Okotrub, I. A. Kinloch, A. G. Kurenya, A. G. Kudashov, X. Chen, H. Song, *Phys. Stat. Sol. (b)* **2008**, *245*, 1971.
20. U. Sim, T. Yang, J. Moon, J. An, J. Hwang, J. Seo, J. Lee, K. Y. Kim, X. Han, B. H. Hong, K. T. Nam, *Energy Environ. Sci.* **2013**, *6*, 3658.
21. A. C. Nielander, M. J. Bierman, N. Petrone, N. C. Strandwitz, S. Ardo, F. Yang, J. Hone, N. S. Lewis, *J. Am. Chem. Soc.* **2013**, *135*, 17246.

Chapter 3

N-doped monolayer graphene catalyst on silicon photocathode for hydrogen production

Introduction

The discovery of efficient catalysts represents one of the most important and challenging issues for the implementation of photoelectrochemical hydrogen production.[1] A critical requirement for outstanding catalysts in a photoelectrochemical cell (PEC) is not only the ability to boost the kinetics of a chemical reaction but also durability against electrochemical and photoinduced degradation.[2] Generally, precious metals, such as platinum, exhibit superior performance in these requirements; however, the unavoidable weaknesses of precious metals are the economic aspects because of the high-price.[1] Therefore, there has been an intense search for efficient, durable, and inexpensive alternative catalysts.[2,3] Here, we demonstrate that monolayer graphene can catalyze the hydrogen evolution reaction (HER); thus, monolayer graphene can enhance the performance of silicon (Si) photocathodes through a significant decrease in the overpotential. The catalytic activity can be improved in N-doped and defect-abundant graphene that was prepared by treatment with N_2 plasma. Furthermore, surface passivation with a transparent monolayer graphene catalyst allows the Si photocathode to work efficiently and stably in neutral water by suppressing oxidation.

A PEC is the most promising system to sustainably produce hydrogen fuel; a PEC requires semiconductor photoelectrodes that generate electron–hole pairs with absorbed photons and stimulate charge transfer to a semiconductor–aqueous interface.[1] To improve the kinetics of charge transfer, heterogeneous catalysts are added to the surface of a semiconductor.[4] Many attempts to develop highly efficient catalysts have had limited success; the development of an earth-abundant catalyst

that operates at pH 7 with a low overpotential is still a challenge.[2,5] In PEC, negative effects from catalysts should be considered: (1) reflection by the overlaid catalyst, (2) an unfavorable band structure such as a Schottky barrier (3) photocorrosion, and (4) recombination sites at the interface.[6,7] Therefore, to design catalysts for photoelectrochemical water splitting, the optical properties, stability and interfacial issues must be comprehensively considered. The design of carbon-based catalysts represents an important research direction in the search for non-precious, environmentally benign, and corrosion resistant catalysts. Especially, graphene possesses excellent transmittancy and superior intrinsic carrier mobility;[8] thus there have been several attempts to use graphene as a catalyst. It has been reported that reduced graphene oxide (rGO) containing catalytic active materials exhibited improved activity in HERs, oxygen evolution reactions (OERs), and oxygen reduction reactions (ORRs).[9–11] However, in most cases, the role of carbon materials is limited to an electrical conducting substrate or a support that enhances the performance of other decorated active catalysts. In this study, we investigated new possibilities for monolayer graphene as an electrocatalyst for efficient HER and found that nitrogen doping and defects achieved through treatment with N_2 plasma improved the catalytic activity. To the best of our knowledge, there is no prior report on the application of monolayer graphene to hydrogen production.

As a proof of concept, the Si photocathode was employed to investigate the catalytic activity of graphene and the effect of nitrogen doping in photoelectrochemical HER. Si is the most promising photocathode material due to the small band gap of 1.12 eV and precise controllability;[12] however, it cannot be

durably operated in aqueous electrolytes because of surface oxidation.[13] Therefore, passivation of Si surface is essential for the durable operation of the Si photocathode in neutral water.[13] Monolayer graphene on Si acts as a passivation layer against surface oxidation without attenuating the photon incidence.

Experimental

Synthesis of graphene

A monolayer graphene was grown on Cu foil by chemical vapor deposition (CVD) and then transferred to a SiO_2 surface. In the first step of graphene synthesis, a copper foil was put into a quartz reactor in the CVD system and then heated to 1000 ℃ with flowing H_2 at 70 mTorr. Additionally, the sample was annealed for 20 min without changing the condition. The gas mixture of H_2 and CH_4 was flowed with rates of 5 and 50 SCCM for 30 min under 8 Torr. Finally, the sample was rapidly cooled down to room temperature with flowing H_2. After growth, in order to remove graphene on one of the sides of Cu foil, graphene on Cu was placed into the plasma chamber (SNTEK). The chamber pressure was pumped down to 50 mTorr, and O_2 gas was introduced into the chamber by applying a radio-frequency (13.56 MHz) forward power of 100 W for 10 s. In addition, to make vacancy sites and N-doping graphene on the front side of Cu, low density N_2-plasma was produced by applying 10 W power. The N_2 flow rate was 20 SCCM and the working pressure of the chamber was 120 mTorr. Under these conditions, the plasma treatments were performed with various exposure times from 0 to 16 s of N_2 plasma to test the electrochemical reaction of the graphene surface. Finally, poly(methyl methacrylate) (PMMA) was spincoated on graphene and then copper foil was removed in 0.1 M ammonium persulfate solution. After washing with deionized water, the graphene was transferred onto the Si substrate and then PMMA was removed in acetone for 30 min.

Preparation of Si photocathode

In order to establish an ohmic contact between copper wire and the unpolished side (back side) of the Si wafer, a gallium–indium eutectic alloy was incorporated followed by the silver paste. The epoxy was used to insulate and protect the back contact of Si except for the intended illumination area (0.25 cm^2) of the Si front side. Gr was transferred to the Si surface from Cu foil. PMMA was spin-coated on Gr and then the copper foil was removed in an ammonium persulfate solution. After washing with deionized water, Gr was transferred onto the Si substrate and then PMMA was removed in acetone for 30 min. Electrochemical measurements Electrochemical measurements were performed in a three-electrode cell using an electrochemical analyzer (CHI 600D, CH Instruments, Inc.). Pt foil was used as the counter electrode and Ag/AgCl/3 M NaCl electrode was used as the reference electrode. The reference electrode was carefully calibrated with respect to RHE in an aqueous 1 M perchloric acid solution with high purity H_2 saturation at 25℃ (Fig. S1†). The RHE was calibrated to between -0.201 V and -0.203 V *vs.* the Ag/AgCl reference electrode. To evaluate the photoelectrochemical behavior, visible light from a 300 W Xe lamp was illuminated onto the substrate with the light intensity of 100 mW cm^{-2} using an Air Mass 1.5 Global condition glass filter. The RDE system was purchased from EG&G PARC Inc and Glass Carbon tip for RDE measurement (dia. 3 mm) was purchased from BASi. The Pt catalyst mixed with 5 wt% Nafion was synthesized from the literature method.16 The Pt catalyst ink of 10 uL was loaded on GC and dried at 110℃. RDE measurement was performed at a rotating speed of 1000 rpm with a scan rate of 5 mV s^{-1}.

Calibration with respect to relative hydrogen electrode

The Ag/AgCl/3 M NaCl electrode (BASi) was used as the reference electrode. Pt foil (2 cm x 2 cm x 0.1 mm, 99.997% purity, Alfa Aesar) was used as the counter electrode. In the case of RDE experiment, Pt wire (0.1 mm diameter, Dr Bob's cell) was used as the counter electrode. It was carefully calibrated with respect to the reversible hydrogen electrode (RHE) in an aqueous 1 M perchloric acid solution (Sigma Aldrich) with high purity H_2 saturation at 25℃. The RHE was calibrated to between -0.201 V and -0.203 V vs. the Ag/AgCl reference electrode (Fig. S1†). Since the potential difference between Ag/AgCl and RHE is dependent on electrolyte pH, temperature, and so on, the potential was carefully measured before each set of measurement and the measurement was conducted at least three times for each condition. The potential was controlled using a potentiostat (CHI 600D, CH Instrument) at a scan rate of 5 mV s^{-1}.

Characterization

Raman spectra were obtained with a Renishaw micro-Raman spectroscope with an excitation wavelength of 514.5 nm, an Ar laser. The spot diameter was approximately 2 mm with a 50 x objective lens. The oxygen plasma treatment (SNTEK) was carried out with a 100 W radio-frequency (rf) power for 13 s under 140 mTorr and the nitrogen plasma was accelerated with a 10 W rf power for several exposure times (0 to 16 s) under 120 mTorr. XPS spectra were collected by AXIS Ultra DLD (Kratos. Inc) using a monochromatic Al K (1486.6 eV), 150 W source at Korea Basic Science Institute (KBSI). Narrow-scan data were collected using a pass energy of 40 eV and 0.05 eV per step.

Results and Discussion

Monolayer graphene (Gr) was grown on Cu foil through chemical vapor deposition (CVD) and was transferred to p-type Si wafer. To evaluate the photocathodic behavior of Gr loaded on a Si (Gr-Si) electrode, a current density measurement was performed as the potential was swept from 0.4 V to -1.0 V vs. Reversible Hydrogen Electrode (RHE) in a three electrode cell. A light source of a 300 W Xe lamp illuminated the Si photoelectrode with a light intensity of 100 mW/cm^2 with an Air Mass 1.5 Global condition filter in an aqueous 1 M perchloric acid solution (pH 0).

In measurements of the photoelectrochemical performance, Gr exhibites catalytic activity for HER. As shown in Figure 1a, the current density of the bare Si increases gradually from -0.2 V vs. curve is shifted by approximately 0.2 V toward the positive potential. The onset potential is defined as the potential at the photocurrent density of -1 mA/cm^2. The onset potential of Gr-Si is 0.01 V vs. RHE, and this potential is a positive shift by 0.18 V compared to that of bare Si (-0.17 V vs. RHE). Figure 1b also shows dark current densities of heavily arsenic doped n^+ type Si electrodes. In the dark condition, the positive shift in 0.14 V of the onset potential (-0.49 V vs. RHE for Gr-Si) also shows higher activity for HER compared to that of the bare Si (-0.63 V vs. RHE). This result indicates that monolayer Gr acts as an effective catalyst for HER on the Si photocathode.

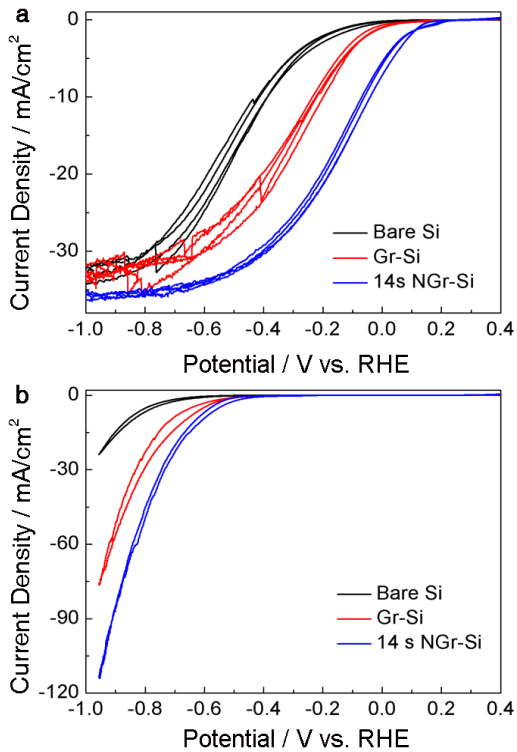

Figure 1. Cyclic Voltammetry (CV) of graphene (Gr), N_2-plasma-treated Gr (NGr), Pt, and Pt with NGr on a Si electrode. (a) Photocurrent density-potential (*J-E*) curves for the lightly boron doped p-Si electrode deposited with Gr and NGr. The plasma treatment on Gr was introduced with high purity N_2 gas for 14 sec, which is called NGr-Si. In case of Pt-Si and Pt-NGr-Si electrodes, Pt nanoparticles were deposited on bare Si and NGr-Si by the electroless deposition method, respectively. (b) Polarization curves of Gr, and NGr on heavily arsenic doped n^+ type Si electrodes under dark condition. Each CV was performed at a scan rate of 0.05 V/sec.

To investigate the electrocatalytic activity of Gr, we measured cyclic voltammetry (CV) without illumination with a rotating disk electrode (RDE). To fabricate the working electrode, Gr was transferred to a glassy carbon (GC) tip that is inert in aqueous solution. As shown in Figure 2a, in *J-E* curves of the RDE measurements, the current density from the electrolysis of water exponentially increases after the onset as the potential is swept from 0 V to -0.5 V. To compare the onset potential for the HER in the RDE system, the potential to attain -5 mA/cm^2 of HER current density was measured for bare GC and for Gr-GC. The potential to attain -5 mA/cm^2 of HER current density is -0.33 V for the bare GC. Similar to the behavior of the photocurrent response for the Gr-Si electrode, a positive shift in the overall J-E curve is also observed for Gr-GC. The potential for Gr-GC at -5 mA/cm^2 is -0.28 V vs. RHE; this potential is shifted positive by 50 mV compared to that for the bare GC. This result means that the Gr monolayer has electrocatalytic activity for HER regardless of substrate materials.

To quantitatively gain more insight into the catalytic activity of Gr, the *J-E* curves in Figure 2a is converted into a plot of the potential as a function of the logarithm of *J*; this plot is called a Tafel plot. The measured potentials are corrected for the ohmic potential drop (iR) losses that originated from the resistance of the interface between the substrate and the electrolyte. Analyzing the impedance spectroscopy reveals that the resistances of the bare GC and Gr-GC are 7.1 and 7.2 ohm, respectively (Figure S2). The Tafel plot provides two parameters to estimate the electrocatalytic activity: the Tafel slope and the exchange current density. The Tafel slope is defined to be a measure of the

potential increase required to increase the resulting current by 1 order of magnitude.[14] The bare GC shows a Tafel slope of 85 mV/decade, and Gr-GC exhibited a 9 mV/decade lower Tafel slope (74 mV/decade) than that of bare GC. For the comparison with the well-known catalyst, Pt particles were deposited on GC and the electro-catalytic activity was analysed. The applied potential to obtain -5 mA/cm^2 is -0.04 V vs. RHE, that is shifted positively by 0.24 V compared to that of Gr-GC. The Tafel slope of Pt-GC is 42 mV/decade, which is a 32 mV/decade lower than that of Gr-GC. In case of 2D MoS_2 catalyst, the potential to attain -5 mA/cm^2 is -0.19 V vs. RHE and the Tafel slope was 60 mV/decade when deposited as a mixture with Nafion on GC.[15]

The Tafel slope is an inherent property of the catalyst that is determined by the rate-limiting step for HER. Mechanistically, for the HER in acidic solution, the following possible reaction steps have been suggested:[16]

$$H_3O^+ + e^- \rightarrow H_{ads} + H_2O \quad (1)$$

$$H_{ads} + H_3O^+ + e^- \rightarrow H_2 + H_2O \quad (2)$$

$$H_{ads} + H_{ads} \rightarrow H_2 \quad (3)$$

where H_{ads} is the adsorbed H. (1) is a discharge step (the Volmer reaction), (2) is a desorption step (the Heyrovsky reaction), and (3) is a recombination step (the Tafel reaction). The value of the Tafel slope also relates to the adsorbed hydrogen coverage (θ_H) on the surface of electrode. If the recombination of adsorbed hydrogen (the Tafel reaction) is the rate-determining step for the HER and if the coverage is very high ($\theta_H \approx 1$), the measured Tafel slope is 30 mV/decade. However, if the electrochemical desorption step (the Heyrovsky reaction) is the

rate-determining step, a Tafel slope of 40 ~ 118 mV/decade is measured and is dependent of the value of θ_H (0 ~ 1).[17] The observed Tafel slope of ~80 mV/decade in the current work indicates that the kinetics of the HER on bare GC and Gr-GC electrodes is determined by the Heyrovsky reaction because θ_H has an intermediate value.

The exchange current density (J_0) is defined to be the current density at zero overpotential. The catalytic effect originates from improving the rate of charge transfer at the interface between the electrode and electrolyte or from lowering the activation energy barrier for a chemical reaction; these catalytic effects are represented by J_0. The higher J_0 indicates that electron transfer or the adsorption/desorption of protons at the electrode/electrolyte can occur more easily with a lower kinetic barrier. From the Tafel plot, J_0 can be obtained by extrapolating the plot in Figure 2b and extracting the current density at 0 V vs. RHE. The Gr-GC electrode shows an enhanced J_0 of 2.73×10^{-6} A/cm^2, which is higher than the J_0 of bare GC (1.63×10^{-6} A/cm^2) (Figure S3). The J_0 of the monolayer Gr is also compared with that of the nanoparticulate MoS_2. The accurate J_0 can be calculated by considering the number of active sites. For example, the J_0 of MoS_2 for the HERs is experimentally measured to be 1.3×10^{-7} to 3.1×10^{-7} A/cm$^2_{geometric}$.[18] Active sites of MoS_2 nanoparticle for HER are known to be edge sites of MoS_2 nanoparticle.[16,18] For the direct site-to-site comparison between MoS_2 nanoparticle and Pt catalyst, T. Jaramillo *et al*. have measured an exchange current per site of MoS_2 combined with STM analysis.[18] The exchange current per site is then multiplied by the site density of Pt for a fair comparison

to the transition metal catalyst, resulting in the exchange current density of 7.9×10^{-6} A/cm^2. This value is still similar to exchange current density of Gr (2.7×10^{-6} A/cm^2). We are currently investigating to identify and quantify the active sites of the single monolayer Gr. From the Tafel analysis, Gr has the catalytic activity for the HER compared to that of the nanoparticulate MoS_2.

The catalytic activity of Gr can be further enhanced by generating more active sites. We expected that treatment with N_2 plasma would induce nitrogen doping and abundant defects in graphitic carbon structure and that these doping and defect sites could be catalytic sites for the HER. In a previous study, Dai's group showed that introducing nitrogen dopants and defect sites in a CNT-Gr composite facilitated an improvement in electrocatalytic activity for ORR.[19] The surface of the as-grown Gr on Cu foil was modified with a N_2 plasma in a reactive ion etcher (RIE), and the catalytic activities of the N_2-plasma-treated Gr (NGr) were measured for various durations of the plasma treatment.

The N_2-plasma treatment improved the catalytic activity of Gr. We optimized the duration of the plasma treatment, and obtained the best-performing Gr at the duration of 14 sec (Figures 1a and S4). As shown in Figure 1a, an additional positive shift of the onset potential is observed for NGr under illumination. The onset potential for NGr-Si is 0.12 V vs. RHE, and this onset potential is enhanced by more than 0.11 V compared to that for Gr-Si. In comparison to bare Si with the onset of -0.17 V vs. RHE, the onset potential is shifted positively by 0.29 V. The more significant enhancement by Gr and NGr is detected at a current density of -10 mA/cm^2. To obtain -10 mA/cm^2 of

photocurrent, potentials of -0.42 V, -0.21 V, and -0.04 V vs. RHE are needed for bare Si, Gr-Si, and NGr-Si, respectively. The potential for -10 mA/cm^2 is shifted to the anodic direction by 0.38 V for NGr-Si compared with bare Si. The cathodic current from NGr-Si rises rapidly at potentials more negative than the onset potential and at current densities less than -5 mA/cm^2. In the dark condition, NGr-Si also shows the positive shift in 50 mV (-0.44 V vs. RHE) compared to the Gr-Si (Figure 1b), which results in the photovoltage of 0.56 V by depositing NGr on bare Si (Table S1). For comparing the catalytic activity of NGr with that of the best catalyst, the CV of Si with electroless-deposited Pt (Pt-Si) is also measured (Figure S5). The onset of Pt-Si is 0.24 V vs. RHE, and the potential to obtain -10 mA/cm^2 is 0.11 V vs. RHE, which is the positive shift in 0.12 V vs. RHE compared to that of the NGr-Si electrode. NGr-Si is also compared to the Si electrode decorated with an earth abundant catalyst, Ni.[20] The Ni-Si electrode shows solar-to-hydrogen (STH) conversion efficiency of 0.4% with the onset potential of 0.34 V vs. RHE and *J* at 0 V vs. RHE of 10 mA/cm^2. NGr-Si shows the onset potential (0.12 V vs. RHE) and *J* at 0 V vs. RHE (-5.5 mA/cm^2). Consequently, the STH conversion efficiency (+0.16%) is achieved by using the NGr catalyst (Table S1). The NGr-Si is also compared with Si electrode with MoS_2 catalyst. The Photocurrent density at 0 V vs. RHE of NGr on the Si electrode is much higher (-5.5 mA/cm^2) than the reported value of MoS_2(approximately -0.5 mA/cm^2).[21]

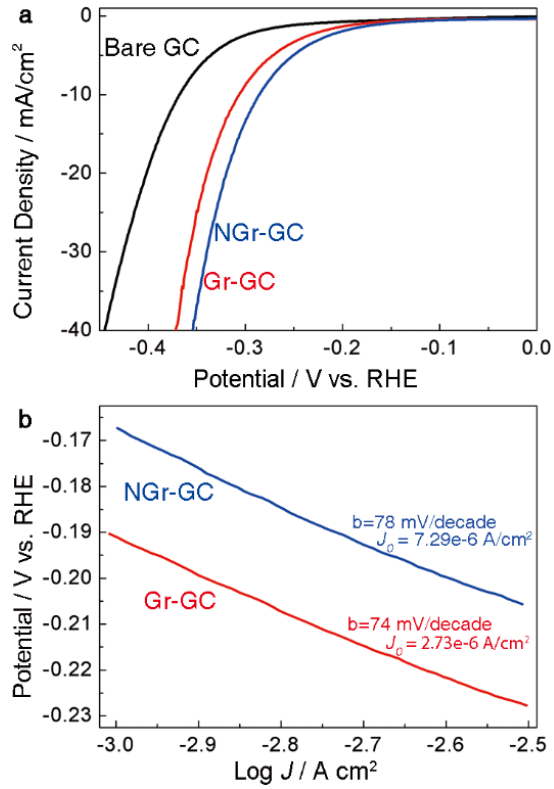

Figure 2. Electrochemical activity of Gr on Glassy Carbon (GC) electrode. (a) CV curve of GC, Gr on GC, NGr on GC, and Pt on GC from rotating disk electrode system. CV data were corrected by iR compensation. (b) Tafel plots were derived from (a) CV data. The 'b' in the inset (mV/decade) and J_0 (A/cm^2) indicate a Tafel slope and an exchange current density, respectively.

An additional positive shift in the onset potential by NGr is also observed in the RDE measurements. The potential to attain current density of -5 mA/cm^2 is -0.26 V vs. RHE; this value is 70 mV larger than that of the bare GC (-0.33 V vs. RHE) and is 20 mV larger than that of the Gr-GC (-0.28 V vs. RHE). The improvement in the catalytic activity with NGr is also confirmed by the comparison of J_0 in the Tafel plot (Figure 2b). The J_0 of NGr-GC is 7.29×10^{-6} A/cm^2, which is approximately 2.8 times of Gr-GC. This is a comparable value with that of the nanoparticulate MoS_2 (7.9×10^{-6} A/cm^2).[18]

In Figure 3, we describe the changes in chemical states of Gr after N_2 plasma treatments of various durations. AFM images for the surface of NGr with N_2 treatment for 14 sec show that plenty of defects and edges were generated in the Gr, while that of monolayer Gr was smooth (Figure S7). In the Raman spectra (Figure 3a), the generation of defects and edges by the N_2 treatment is also identified. In the Raman spectra of pristine Gr, the D peak is due to the breathing modes of six-atom rings, which comes from transverse optical phonons around *K* or *K′* point in the first Brillouin zone. It involves an intervalley double resonance process. The absence of a significant D peak is the evidence of the good crystallization of the single Gr layer. Normally, the D peak is negligibly weak in pristine Gr, but the peak still exists approximately 2% of the G peak. However, after the plasma treatment, the intensity of the D peak significantly increases and the D′ peak at ~1620 cm^{-1} is activated by intravalley double resonance process, i.e., connecting two points belong to the same cone around *K* or *K′*. Moreover, the D + G combination mode at ~2950 cm^{-1} requires defects for

its activation.[22] Thus, these changes in the Raman spectra indicate the formation of abundant edge and defective sites in NGr.

Additionally, the spectral features of monolayered Gr are observed in the Raman spectra. Before the plasma treatment, the G to 2D intensity ratio of ~0.5 and a symmetric 2D band are found at ~1580 cm^{-1} and at ~2670 cm^{-1}.[23] These features are caused by the G band from the in-plane vibrational mode and the 2D band from double resonance scattering, respectively.[24,25] Thus, they can be observed when Gr is successfully formed in a single-layer.

The plasma treatment induces not only the formation of many defect sites but also nitrogen doping in Gr. The chemical states of the nitrogen dopant were identified from the high resolution N 1*s* spectra from X-ray photoelectron spectroscopy (XPS, Figure 3b and S8). No obvious distinct nitrogen peak is observed for Gr, whereas nitrogen peaks for NGr are observed at pyridinic (398.5 eV), pyrrolic (399.9 eV), and a small number of quaternary nitrogen (401 eV) sites with a concentration of ~ 2.2 at.%. Inset in Figure 3b shows a schematic diagram of the bonding configurations for nitrogen in NGr. The passivation effect of Gr was also investigated. CV of Si photocathodes was measured during 300 cycles with a scan rate of 0.05 V/sec (Total operation time of each electrodes is about 20,000 sec) in pH 0 and pH 6.8. As shown in Figure 4a and 4b, CV curves of all electrodes shift negatively vs. RHE as the CV cycle increases, but bare Si shows the largest negative shift even in much lower cycles. As a key parameter determining the passivation performance of Gr and NGr against the surface oxidation of Si, the changes in onset potentials were

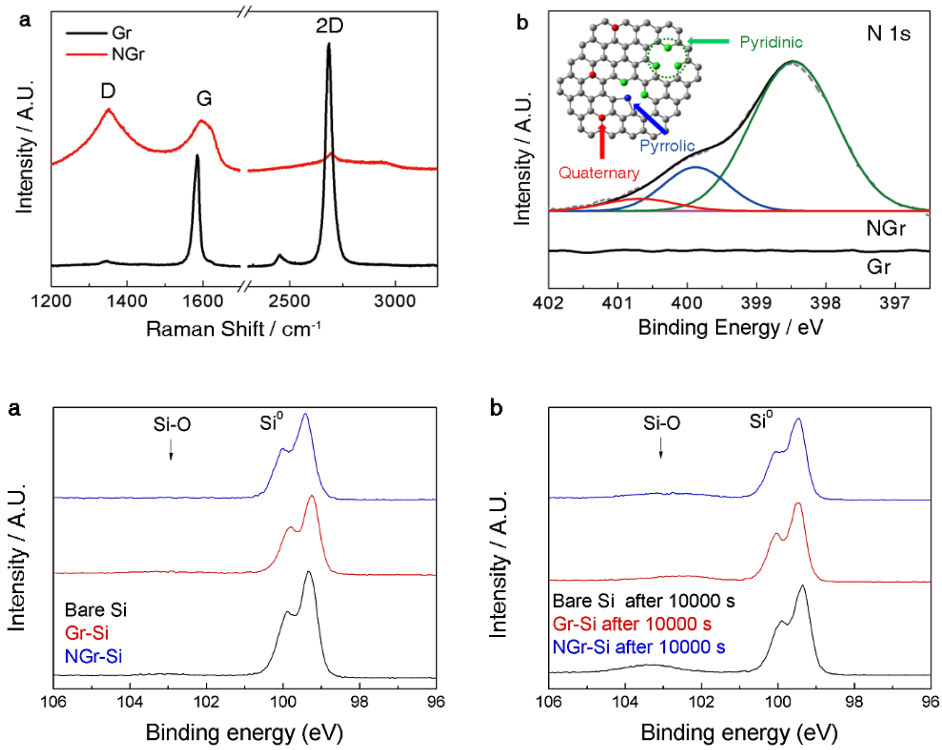

Figure 3. (a) Raman spectra and (b) high resolution XPS spectra of N 1s peak of Gr and NGr. The N 1*s* peak is separated into N1 (398.5 eV), N2 (399.9 eV), and N3 (401 eV) which are labeled by green, blue, and red lines. An inset image in (b) represents schematic of NGr. The gray, green, blue, and red spheres indicate the carbon, pyridinic nitrogen, pyrrolic nitrogen, and quaternary nitrogen atoms, respectively. (c-d) High resolution XPS spectra of Si 2*p* region of bare Si, Gr-Si, and NGr-Si electrodes. XPS spectra of each sample (c) before the chronoamperometry test and (d) after the chronoamperometry test at 0 V *vs.* RHE for 10,000 sec. Narrow-scan data of the Si 2*p* region were collected using pass energy of 40 eV and 0.05 eV/step.

measured (Figure S9). At pH 0, the Gr-Si and NGr-Si electrodes shows only shifts in the onset potential of 0.1 V and 0.035 V, respectively, while the onset potential of the bare Si electrode shifts negatively by 0.38 V within 100 cycles (Figure S9). At pH 6.8, both the Gr-Si and NGr-Si electrodes shows the negative shift of less than 0.24 V in the onset potential, whereas the onset potential of the bare Si sharply decreases and is saturated at a value of approximately -1.1 V vs. RHE within only 30 cycles.

A chronoamperometray test of the bare Si, Gr-Si, and NGr-Si was also performed at 0 V vs. RHE (Figure S10) and the current densities normalized by their initial values were displayed as a function of time in Figure 4c. Gr-Si and NGr-Si also shows the suppressed degradation of the performance in the photocurrent density compared to that of the bare Si at both pH 0 and pH 6.8 condition. The performance of the bare Si completely fails only after 1,000 sec (Figure 4c and S10) at pH 6.8. The NGr-Si electrode maintains more than 30% of the normalized current and -4.8 mA/cm^2 (pH 0) even at 10,000 sec. Thus, from the change of the onset potential and current density at 0 V vs. RHE, it is known that Gr and NGr suppresses the degradation of the photoelectrochemical performance by the oxidation of Si surface.

To confirm the passivation effect of Gr and NGr on Si surface, the surface state of Si was investigated before and after the chronoamperometry test at 0 V vs. RHE for 10,000 sec. (Figure S14). XPS spectra of bare Si, Gr-Si, and NGr-Si were measured in the Si $2p_{3/2}$ region. The Si peak can be assigned at 99.3 eV, and SiO_2 peak can be assigned at 103.3 eV.[26] From XPS spectra of bare Si, the peak

of Si-O increases after the chronoamperometry test. In case of Gr-Si and NGr-Si samples, after the long-term test, there is only slight increase in the Si-O peak. These results indicate that graphene suppresses the oxidation of Si surface during the photoelectrolysis.

To further enhance the electro-catalytic activity of Gr, Pt nanoparticles were electrodeposited onto the NGr-Si (Pt-NGr-Si). We also expected that the passivation effect of Gr to suppress the Si oxidation during the photoelectrolysis could make the synergistic advantage with other catalysts. As a proof of concept, Pt was chosen to investigate those effects. The catalytic activity of Pt-NGr-Si was significantly enhanced compared to that of NGr-Si as shown in Figure S5. From a CV measurement, the onset of Pt-NGr-Si is 0.35 V vs. RHE at -1 mA/cm^2, and the potential to reach -10 mA/cm^2 is 0.25 V vs. RHE. The STH conversion efficiency is increased to 3.05 %. As expected, the long-term stability was also achieved by combining Pt and Gr as demonstrated in Figure S12 and Figure S13. The chronoamperometry test showed that Pt-NGr-Si is maintained the stable current density of -4.7 mA/cm^2 and -4.0 mA/cm^2 respectively at pH 3.8 and 6.8 even after 8,000 sec.

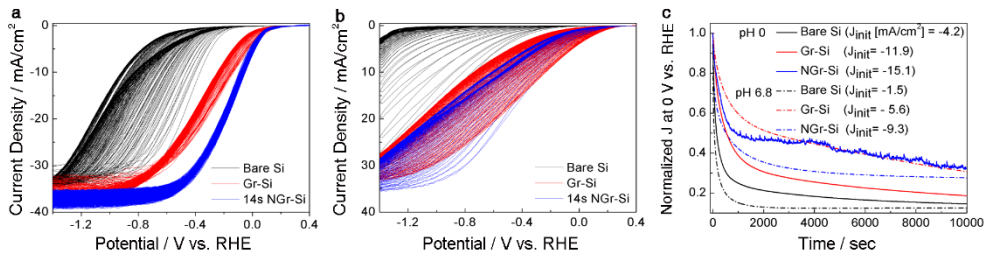

Figure 4. The stability test of bare Si, Gr-Si, and NGr-Si photocathodes. CV of Si photocathodes during 300 cycles with a scan rate of 0.05 V/sec at (a) pH 0 and (b) pH 6.8. Polarization curves of each photoelectrodes shifted negatively vs. RHE as the CV operation increased. (c) Chronoamperometry operation of Si photocathodes. The change of normalized photocurrent density (J/ J_{init}) at 0 V vs. RHE of each photoelectrodes with the increase of time at pH 0 (solid line) and pH 6.8 (dash-dotted line), respectively. J_{init} is the initial current density in the chronoamperometry operation.

Conclusions

We have presented the N-doped monolayer graphene catalyst that enhanced the PEC performance of a Si-photocathode. The onset potential for photocurrent from the Si was significantly shifted toward the anodic direction without a change in the saturation current density. NGr has excellent catalytic activity for photoelectrochemical HER on the Si photocathode and is the passivation layer that maintains higher onset potential and current density even at neutral pH. Our approach in this study exploits a strategy to develop metal-free carbon-based catalysts with high efficiency and durability for solar-driven hydrogen fuel production.

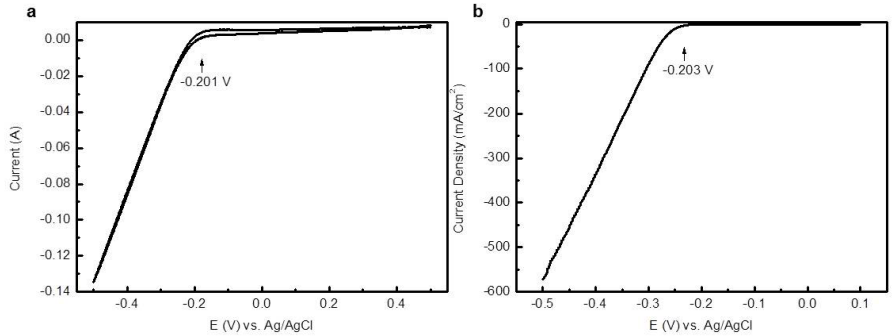

Figure S1. Calibration respect to RHE. Current vs. the applied potential respect to Ag/AgCl reference electrode with using (a) Pt foil for Si PEC cell experiment and (b) Pt wire as the counter electrode for RDE experiment.

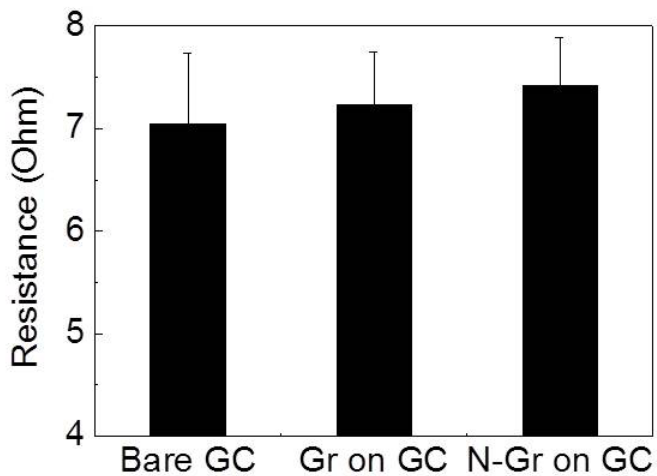

Figure S2. Resistance of bare Glassy Carbon (GC), Gr on GC, and NGr on GC. Impedance spectroscopy analysis revealed that the resistances of the bare GC, Gr-GC, NGrGC are 7.1 ohm, 7.2 ohm, and 7.4 ohm respectively. Resistances were measured using iR compensation mode in the electrochemical analyzer (CHI 600D, CH Instruments, Inc.).

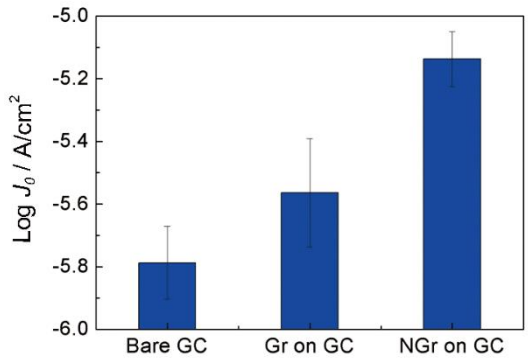

Figure S3. The logarithm of the exchange current densities calculated by extrapolation to the x-axis. Compared to the bare GC, Gr and NGr catalysts show the high activity for the HER.

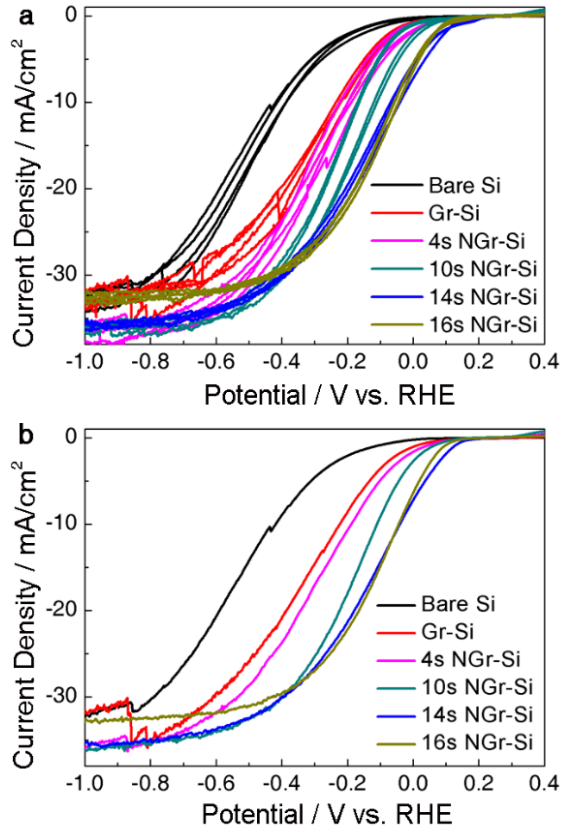

Figure S4. Photoelectrochemical performance of NGr-Si photocathode with variation of the amount of Pt solution. (a) Polarization curves of NGr on Si electrode. Each cyclic voltammetry was performed during 4 cycles at a scan rate of 0.05 V/s. The durations of the plasma treatment on Gr were introduced with high purity N2 gas for 4 sec, 10 sec, 14 sec, and 16 sec. For comparison, cyclic voltammogram of Gr without plasma treatment on Si electrode is presented. (b) Representative data from polarization curves of NGr on Si electrode of Figure S4 a

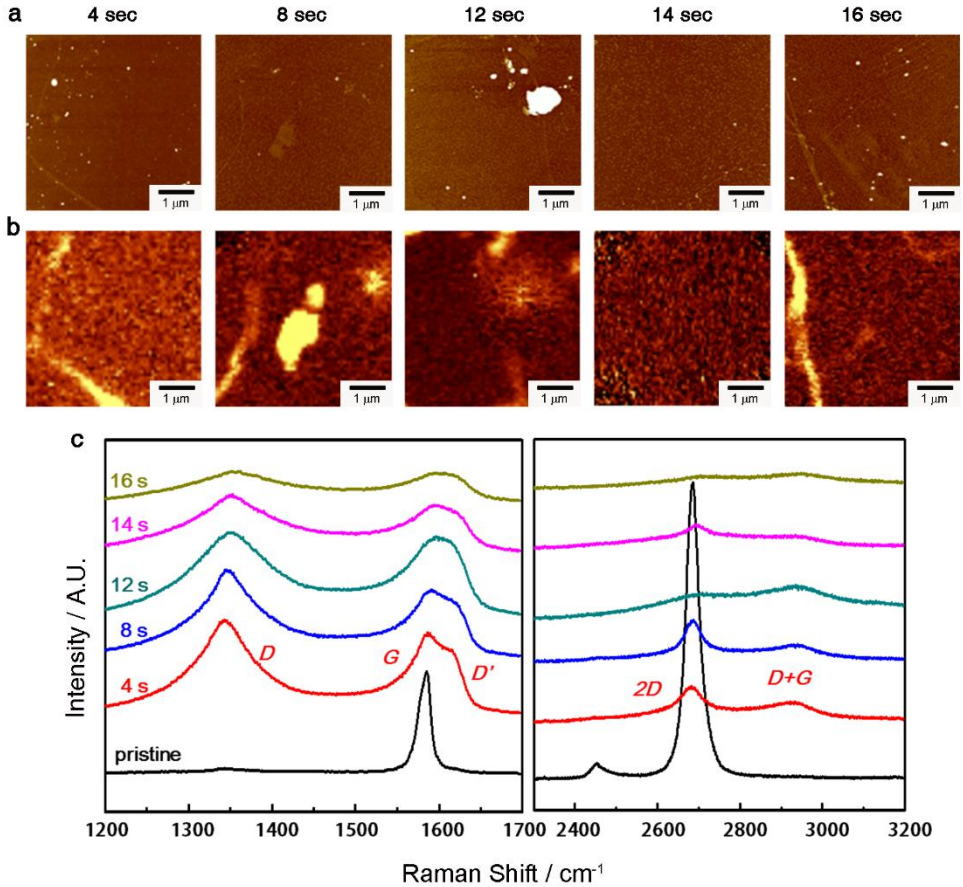

Figure S5. Surface morphology of monolayer Gr and NGrs. (a) AFM images and (b) Raman characterization of a pristine Gr sample as a function of the exposure time to N_2 plasma and the each image was taken the same area measured by AFM. Numbers on each figure indicate the exposure time. All figures have a size of 6.5 × 6.5 μm_2 (c) Raman spectra of the samples. Numbers on the left side of the left figure indicate the exposure time. Raman peaks are indexed accordingly.

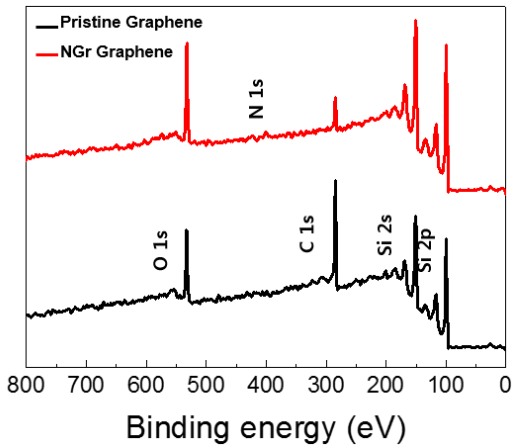

Figure S6. XPS spectra of Gr and NGr. The C 1*s* is 76.78 atomic weight % (at. %) for Gr and 57.17 at. % for NGr, N 1*s* is 0.00 at. % for Gr and 2.20 at. % for NGr, and O 1*s* is 23.22 at. % for Gr and 40.63 at. % for NGr, respectively.

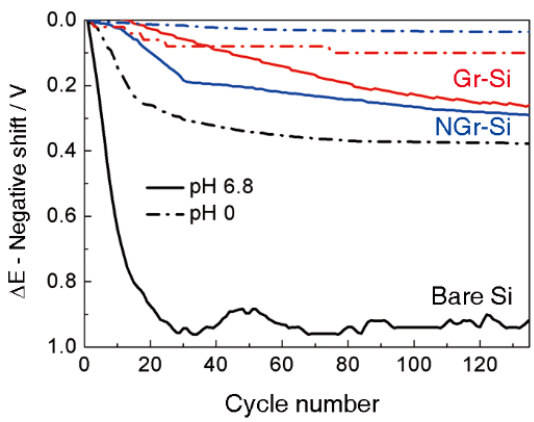

Figure S7. The change of onset potential of bare Si (black line), Gr-Si (red line), and NGr-Si (blue line) electrodes. The onset potential measured from the first CV sweep was a standard, and the difference between the measured onset potential during the CV cycles and the value of the first sweep was investigated; this difference is defined as ΔE – negative shift. The onset potential was measured with increasing the number of cyclic voltammetry in 1M $HClO_4$ (pH 0, dash dot line) and 0.4 M NaH_2PO_4 and 0.6 M Na_2HPO_4 (pH 6.8, solid line) electrolytes, respectively.

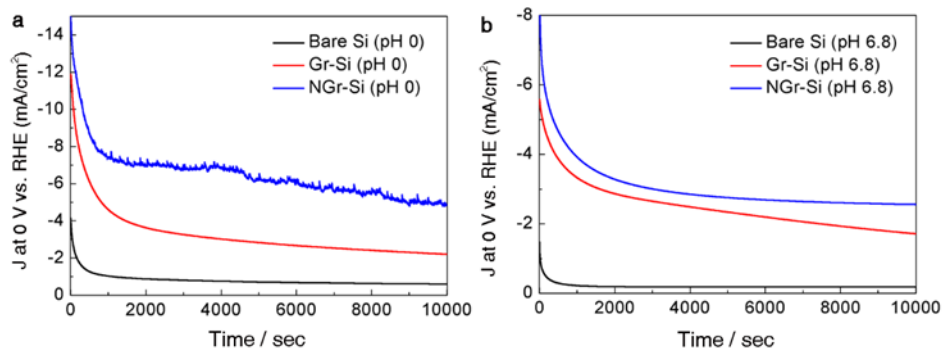

Figure S8. The change of photocurrent density at 0 V vs. RHE of bare Si (black line), Gr-Si (red line), and NGr-Si (blue line) electrodes with the increase of time at (a) pH 0 (1M HClO4) and (b) pH 6.8 (0.6 M NaH_2PO_4 and 0.4 M Na_2HPO_4), respectively. At pH 0, NGr-Si electrode shows a spiky plot during a chronoamperometry test because hydrogen bubbles stick to hydrophobic surfaces until sudden bursts occur.

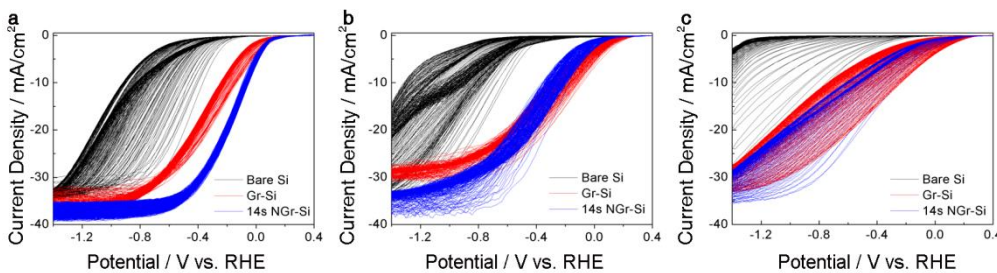

Figure S9. The stability test of bare Si, Gr-Si, and NGr-Si photocathodes. CV results of Si photocathodes during 300 cycles with a scan rate of 0.05 V/sec at (a) pH 0, (b) pH 3.8, and (c) pH 6.8. Polarization curves of each photoelectrodes were shifted negatively vs. RHE as the number of cycles increased.

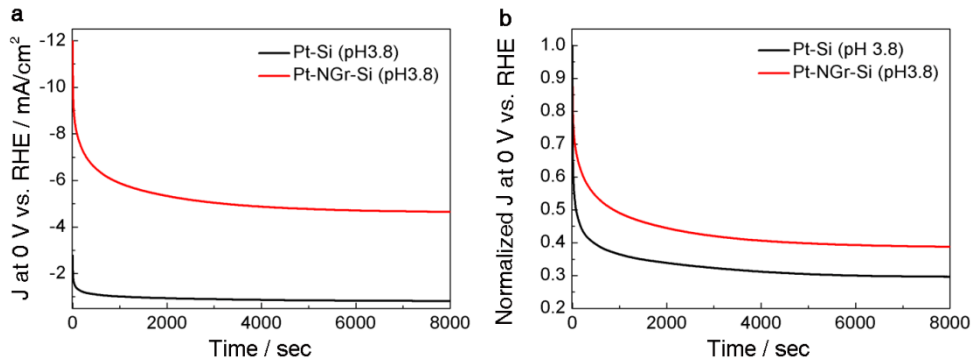

Figure S10. The stability test of bare Si, Gr-Si, and NGr-Si photocathodes. CV results of Si photocathodes during 300 cycles with a scan rate of 0.05 V/sec at (a) pH 0, (b) pH 3.8, and (c) pH 6.8. Polarization curves of each photoelectrodes were shifted negatively vs. RHE as the number of cycles increased.

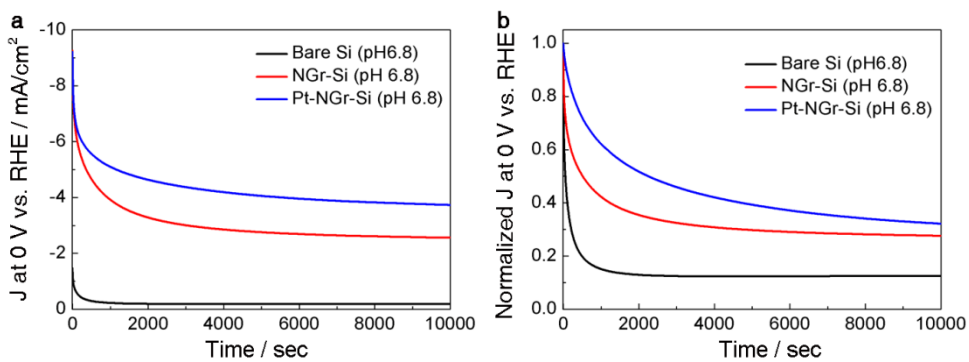

Figure S11. Chronoamperometry test of bare Si, NGr-Si, and Pt-NGr-Si photocathodes at pH 6.8. (a) The change of photocurrent density at 0 V *vs.* RHE of bare Si (black line), NGr-Si (red line), and Pt-NGr-Si (blue line) electrodes with the increase of time at pH 6.8. (b) The change of normalized photocurrent density (J/ Jinit) at 0 V *vs.* RHE of each photoelectrodes with the increase of time at pH 6.8.

Table S1. Summary of the experimental data for Si and Glassy Carbon (GC) electrodes.

Condition	Electrode	Onset potential [E (V) at -1 mA/cm^{-2}]	E (V) at -5 mA/cm^{-2}	E (V) at -10 mA/cm^{-2}	Solar-to-Hydrogen Conversion Efficiency (%)
Under illumination (p type Si)	Bare Si	-0.17	-0.29	-0.42	0.02
	Gr--Si	0.01	-0.13	-0.21	0.04
	14s NGr-Si	0.12	0.02	-0.04	0.16
	Pt-Si	0.24	0.16	0.11	1.19
	Pt-NGr-Si	0.35	0.29	0.25	3.05
Under dark condition (n^+ type Si)	Bare Si	-0.63	-0.78	-0.85	
	Gr-Si	-0.49	-0.61	-0.69	
	14s NGr-Si	-0.44	-0.55	-0.62	
Photovoltage*	Bare Si	0.46			
	Gr-Si	0.50			
	14s NGr-Si	0.56			
RDE (GC) under dark condition	Bare GC	-0.24	-0.33	-0.37	
	Gr-GC	-0.18	-0.28	-0.31	
	14s NGr-GC	-0.16	-0.26	-0.29	
	Pt-GC	-0.02	-0.04	-0.05	

The photovoltage is defined as the difference between the onset potential under the dark and illumination condition. This value was calculated from the consideration of the following reference; Y. W. Chen, J. D. Prange, S. Dühnen, Y. Park, M. Gunji, C. E. Chidsey and P. C. McIntyre, Nature Mater., 2011, 10, 539-544. (Ref. 5 in the main article)

References

1. A. Heller, E. Aharon-Shalom, W. A. Bonner and B. Miller, *J. Am. Chem. Soc.*, 1982, **104**, 6942-6948.
2. Y. Hou, B. L. Abrams, P. C. K. Vesborg, M. E. Björketun, K. Herbst, L. Bech, A. M. Setti, C. D. Damsgaard, T. Pedersen, O. Hansen, J. Rossmeisl, S. Dahl, J. K. Nørskov and I. Chorkendorff, *Nature Mater.*, 2011, **10**, 434-438.
3. S. Y. Reece, J. A. Hamel, K. Sung, T. D. Jarvi, A. J. Esswein, J. J. H. Pijpers and D. G. Nocera, *Science*, 2011, **334**, 645-648.
4. A. Kudo and Y. Miseki, *Chem. Soc. Rev.*, 2009, **38**, 253-278.
5. Y. W. Chen, J. D. Prange, S. Dühnen, Y. Park, M. Gunji, C. E. Chidsey and P. C. McIntyre, *Nature Mater.*, 2011, **10**, 539-544.
6. R. N. Dominey, N. S. Lewis, J. A. Bruce, D. C. Bookbinder and M. S. Wrighton, *J. Am. Chem. Soc.*, 1982, **104**, 467-482.
7. U. Sim, H.-Y. Jeong, T.-Y. Yang and K. T. Nam, *J. Mater. Chem. A*, 2013, **1**, 5414-5422.
8. K. Novoselov, A. K. Geim, S. Morozov, D. Jiang, M. K. I. Grigorieva, S. Dubonos and A. Firsov, *Nature*, 2005, **438**, 197-200.
9. Y. Liang, Y. Li, H. Wang, J. Zhou, J. Wang, T. Regier and H. Dai, *Nature Mater.*, 2011, **10**, 780-786.
10. J.-D. Qiu, G.-C. Wang, R.-P. Liang, X.-H. Xia and H.-W. Yu, *J. Phys. Chem. C*, 2011, **115**, 15639-15645.
11. Q. Xiang, J. Yu and M. Jaroniec, *Chem. Soc. Rev.*, 2012, **41**, 782-796.
12. M. G. Walter, E. L. Warren, J. R. McKone, S. W. Boettcher, Q. Mi, E. A. Santori and N. S. Lewis, *Chem. Rev.*, 2010, **110**, 6446-6473.
13. F.-M. Liu, B. Ren, J.-W. Yan, B.-W. Mao and Z.-Q. Tian, *J. Electrochem. Soc.*, 2002, **149**, G95-G99.
14. A. J. Bard and L. R. Faulkner, *Electrochemical methods: fundamentals and applications*, Wiley, New York, 1980.
15. J. D. Benck, Z. Chen, L. Y. Kuritzky, A. J. Forman, and T. F. Jaramillo, *ACS Catal*., 2013, **2**, 1916-1923

16. Y. Li, H. Wang, L. Xie, Y. Liang, G. Hong and H. Dai, *J. Am. Chem. Soc.*, 2011, **133**, 7296-7299.
17. B. Conway and B. Tilak, *Electrochim. acta*, 2002, **47**, 3571-3594.
18. T. F. Jaramillo, K. P. Jørgensen, J. Bonde, J. H. Nielsen, S. Horch and I. Chorkendorff, *Science*, 2007, 317, 100-1024075-4083.
19. Y. Li, W. Zhou, H. Wang, L. Xie, Y. Liang, F. Wei, J.-C. Idrobo, S. J. Pennycook and H. Dai, *Nature Nanotech.*, 2012, **7**, 394-400.
20. J. R. McKone, E. L. Warren, M. J. Bierman, S. W. Boettcher, B. S. Brunschwig, N. S. Lewis and H. B. Gray, *Energy Environ. Sci*., 2011, **4**, 3573-3583.
21. P. D. Tran, S. S. Pramana, V. S. Kale, M. Nguyen, S. Yang Chiam, S. K. Batabyal, L. H. Wong, J. Barber, and J. Loo, *Chem. Eur. J.*, 2012, **18**, 13994-13999.
22. L. G. Cancado, A. Jorio, E. H. Martins, F. Stavale, C. A. Achete, R. B. Capaz, M. V. O. Moutinho, A. Lombardo, T. S. kulmala, and A. C Ferrari, *Nano Letters*, 2011, **11**, 3190.
23. A. Ferrari and J. Robertson, *Phys. Rev. B*, 2001, **64**, 075414.
24. C. Casiraghi, S. Pisana, K. S. Novoselov, A. K. Geim and A. C. Ferrari, *Appl. Phys. Lett.*, 2007, 91, 233108.
25. X. Li, W. Cai, J. An, S. Kim, J. Nah, D. Yang, R. Piner, A. Velamakanni, I. Jung, E. Tutuc, S. K. Banerjee, L. Colombo and R. S. Ruoff, *Science*, 2009, **324**, 1312-1314.
26. C.D. Wagner, W. M. Riggs, L. E. Davis, J. F. Moulder and G. E. Muilenberg, *Handbook of X-ray Photoelectron Spectroscopy*, Perkin-Elmer Corporation, USA, 1979.

Chapter 4

N-doped graphene quantum sheets on silicon nanowire photocathodes for hydrogen production

Introduction

The development of sustainable energy sources is an urgent issue because of the current level of energy consumption.[1] Renewable and sustainable energy sources must be developed because the present energy sources have several disadvantages such as CO2 emission and limited deposits of fossil fuels.[2] Photoelectrochemical hydrogen production using solar energy represents an important and environmentally friendly technology with no carbon emissions.[3] The development of efficient and cheap photoelectrodes for water splitting is one of the fundamental challenges in hydrogen production.[4] Despite the intriguing advances in controlling the nanostructural interface and newly discovered material compositions for photoelectrodes, sluggish kinetic issues associated with a high overpotential remain some of the most difficult issues that need to be resolved.[5,6] Intense research into efficient, durable, and inexpensive hydrogen evolution reaction (HER) catalysts has been undertaken to solve the kinetic problem.[7–10] In general, precious metals such as platinum exhibit superior performance as HER catalysts; however, the unavoidable disadvantage of precious metals is their high cost.[11] A critical requirement for producing outstanding catalysts in a photoelectrochemical cell is not only the ability to boost the kinetics of the electrochemical reaction but also the ability to resist electrochemicaland photoinduced degradation. Herein we demonstrate that the combination of controlling a nanostructure of the photoelectrode and using a carbon-based hydrogen evolution catalyst represents a significant step toward enhancing the applied bias photon-to-current efficiency (ABPE). In the present work, a 430 mV decrease in overpotential was achieved using graphene quantum sheets on a silicon

nanowire, which exhibited an enhanced effect comparable to that of platinum catalysts. Furthermore, the current density at the reversible potential *vs.* a reversible hydrogen electrode (RHE) exhibited a 101-fold enhancement relative to the current density achieved with planar silicon substrates. The thermodynamic potential of water splitting is 1.23 V, which is observed by subtracting the reduction reaction and oxidation reaction in the photoelectrochemical reaction of water. At the anode, the oxidation reaction in the electrolysis of water is:

$$O_2 + 4e^- + 4H^+ \leftrightarrow 2H_2O, \quad E_{anodic} = 1.23\ V - 0.059(pH)\ V\ (vs.\ NHE) \quad (1)$$

whereas the reduction reaction at the cathode is:

$$4e^- + 4H^+ \leftrightarrow 2H_2, \qquad E_{cathodic} = 0\ V - 0.059(pH)\ V\ (vs.\ NHE) \qquad (2)$$

where, NHE is the normal hydrogen electrode and the standard potential is dependent on pH ($E_{half} = E - 0.059(pH)$ vs NHE). Kinetically, however, when a voltage of 1.23 V is applied, electrolysis is difficult to induce, which results in no current flow. In this situation, a higher potential, which is referred to as the overpotential, η, is needed to drive the reaction at a certain rate. Moreover, if a current i_c flows at the cathode, a current i_a of the same magnitude must flow at the anode to complete the circuit, which requires the overpotential at both electrodes. The overpotentials at the cathode and anode are denoted as η_c and η_a, respectively. Therefore, the total applied potential, E_{appl}, is

$$E_{appl} = 1.23\ V + \eta_c + \eta_a \qquad (3)$$

A higher overpotential requires a higher total applied voltage. Using an electrocatalyst for water splitting can reduce the overpotential required for the electrolysis of water.

In an effort to reduce the overpotential for the water splitting reaction, various catalysts have been deposited onto photoelectrode materials. Previously reported HER catalysts include pure metals, metal composites/alloys, compounds such as nonmetallic elements, and molecular catalysts.[4,5,12-16] Among metal-based catalysts, Pt, Pd, and Ru are near the top of the volcano plot, exhibiting high catalytic activity toward the HER.[7] For example, Pt nanoparticles on p-type Si nanowires in aqueous electrolyte solutions can enhance the onset potential by approximately 0.42 V.[17] In view of economic issues, recent progress has been concentrated on the incorporation of metal nanoparticles into earth-abundant elements rather than on the use of noble metals alone.[11] Nonprecious metal catalysts and catalysts that are abundant in nature have also exhibited high activity toward the HER. Binary structures such as MoS_2, Mo_2N, Mo_2C, and Ni_2P and bimetallic compounds such as Co-Mo-N and Ni-Mo have been suggested as catalysts with high HER activity.[12,18-21] However, the rigorous and precise tuning of the composition of $A_xB_yM_z$ compounds, controlling the active sites in catalysts for the HER, and nanostructuring make optimization of the properties of catalysts for the HER difficult. Moreover, when deposited with catalysts, the saturation current density and the current density at a reversible potential vs. RHE significantly decrease because of light scattering by catalysts on the surface of the photoelectrodes.

To solve the problems associated with previously developed catalysts, carbon-based catalysts may represent an important research direction in the search for low-cost, environmentally friendly, and corrosion-resistant catalysts.

Among carbon-based catalysts, graphene, in particular, possesses excellent transmittance and superior intrinsic carrier mobility; thus, several attempts have been made to use graphene as a catalyst.[22] Co-activated N and P heteroatoms adjacent to C atoms in the graphene matrix can affect such catalysts' valence orbital energy levels and thereby enhance their reactivity toward the HER.[23] Graphitic-carbon nitride combined nitrogen-doped graphene also exhibits enhanced HER activity, with HER properties similar to those of well-established metallic catalysts.[24] Reduced graphene oxide containing catalytic active materials has exhibited improved activity in oxygen reduction reactions and oxygen evolution reactions as well as in the HER.[25-28] However, in most cases, the role of carbon materials is limited to an electrically conducting substrate or a supporter that increases the HER activity of other decorated active catalysts. Recently, we suggested that monolayer graphene deposited onto a planar Si electrode acts as an efficient HER electrocatalyst and that N_2 plasma treatment enhances its catalytic activity.[29] In this study, we further investigated N_2-plasma-treated graphene quantum sheets deposited on the Si nanowire photocathodes as efficient HER electrocatalyst.

Controlling the surface structure of Si represents another important approach to improving photoelectrochemical performance. Si, one of the most abundant elements in the Earth's crust, can be used both as a photocathode and a photoanode for photochemical water splitting because its bandgap (1.12 eV) allows for the absorption of a significant portion of the solar spectrum.[30,31] However, the small band bending between the conduction band edge and the H^+/H_2 redox level of aqueous

electrolytes limits the photoelectrochemical performance of Si relative to that of Si/non-aqueous solvent systems.[5] The application of an external potential or the use of catalysts is necessary for efficient operation under solar irradiation. To overcome this problem, a porous structure or a nanostructure can increase the current density of Si photoelectrodes by increasing the number of effective reaction sites between the Si semiconductor and the liquid electrolyte junction as well as by reducing the reflection of incident light.[6,32] A nanowire structure can increase the efficiency due to the orthogonalization of the direction of incident light absorption and charge carrier collection.[33] Therefore, the combination of an optimized Si nanowire photocathode and a graphene quantum sheet catalyst can boost the catalytic activity toward the photoelectrochemical HER.

Experimental

Synthesis of graphene quantum sheets

A copper foil (10 × 10 cm^2) was inserted into a quartz tube and then heated to 1,000℃ min with flowing 5 sccm H_2. After reaching 1,000℃, the sample was annealed for 20 min under the same condition. The gas mixture of 50 sccm CH_4 and 5 sccm H_2 was flowed for 30 min at a pressure of 8 Torr. After growth, the monolayer graphene on back-side of copper was removed by oxygen plasma (100 W RF power, 12 sec). Next, the N-GQSs were prepared by being irradiate with nitrogen plasma (10 W RF power, 12 sec) to graphene on front-side of copper foil. Finally, the N-GQSs were floated on a 0.1 M ammonium persulfate etchant to remove the Cu substrate. After the Cu was removed, the floating N-GQSs were dispersed in a common organic solvent such as dichloromethane by solvent extraction.[48]

Preparation of Si nanowire (SiNW) photocathode

Boron-doped (p-type) single-crystal Si wafers (4-inch diameter, 500-mm thickness, doped to achieve a resistivity of 10-15 cm, oriented along the (100) plane were purchased from Namkang Co. Ltd. $AgNO_3$ powder (99.5%) and HF (48–51 wt%) were purchased from Sigma Aldrich, and concentrated nitric acid solution (70 wt%) was purchased from Daejung Chemical. The wafers were cut into 1 cm^2 pieces and successively cleaned in acetone, 2-propanol and deionized water for 10 min under sonication.

Each of the Si nanostructures was fabricated by the metal-catalyzed electroless etching method in a 20 mL aqueous solution of $AgNO_3$ (0.015 M) and HF (5 M) for

an etching times of 20 min, 30 min, 120 min, or180 min (Figure S5). Excess Ag residues that could be contaminated during the electroless etching were removed by washing with 70% nitric acid solution for two hours.

A SiNW photocathode was fabricated by establishing an ohmic contact at the back side of a Si substrate. After a native oxide layer was removed on the Si surface using HF, gallium-indium eutectic alloy was loaded onto the surface, followed by the application of silver conductive paste a copper wire; the resulting assembly was then dried at 100ºC. To insulate and protect the back contact of the Si substrate, epoxy was applied over the entire sample except for the area that was illuminated on the front side. After the bare Si cell was fabricated, N-GQSs were transferred onto the Si surface via drop-casting.

Electrochemical measurements

Photoelectrochemical measurements were performed in a three-electrode cell using an electrochemical analyzer (CHI 760E, CH Instruments, Inc.). Schematic illustration and photograph images of hydrogen evolution reaction on N-GQSs/Si photocathode are shown in Figure S6. Pt foil and Pt wire were used as the counter electrode, and a Ag/AgCl/3 M NaCl electrode was used as the reference electrode. The reference electrode was carefully calibrated with respect to RHE at 25℃ in an aqueous 1 M perchloric acid solution saturated with high purity H_2. The RHE was calibrated to between -0.201 V and -0.203 V vs. the Ag/AgCl reference electrode (Figure S7). To evaluate the photoelectrochemical behavior, visible light from a 300 W Xe lamp was illuminated onto the substrate with a light intensity of 100 mW/cm^2 using a glass Air Mass 1.5 Global filter. For the

electrochemical study, the Rotating Disk Electrode (RDE) system was purchased from PINE, Inc., and a glass carbon tip was used for the RDE measurements (dia. 5 mm). For comparison, 10 uL of Pt catalyst ink mixed with 5 wt% Nafion was loaded onto the GC and dried at 110^{o}C. RDE measurements were performed at a rotation speed of 1,000 rpm and at a scan rate of 5 mV/sec.

Characterization

Raman spectra were collected using a Renishaw micro-Raman spectrometer with an excitation wavelength of 514.5 nm emitted from an Ar laser. The spot diameter was ~2 μm, and a 50× objective lens was used. Oxygen plasma treatment (SNTEK) was carried out at a radio-frequency (rf) power of 100 W for 13 sec under a pressure of 140 mTorr for back side of graphene on Cu and the nitrogen plasma was accelerated at an rf power of 10 W over an exposure time of 12 sec under a pressure of 120 mTorr on graphene.

Results and Discussion

Measurements of photoelectrochemical performance show that N-doped graphene quantum sheets (N-GQSs) on a Si photoelectrode exhibit catalytic HER activity. Fig. 1 shows a schematic of hydrogen production on N-GQSs on Si nanowire arrays (SiNWs) in an acid solution under irradiation. Photons absorbed by the SiNWs generate minority carriers (electrons), which drift to the semiconductor/electrolyte interface where $2H^+$ is reduced to H_2; the N-GQSs serve as electrocatalysts for hydrogen production. In the schematic of the N-GQSs, gray, green, blue, and red spheres represent carbon, pyrrolic nitrogen, quaternary nitrogen, and pyridinic nitrogen atoms, respectively, based on high resolution X-ray photoelectron spectrum (XPS) measurements. The transmission electron microscopy (TEM) image and a size-distribution histogram indicate that the average diameter of the N-GQSs is 5 nm (Fig. S1). N-GQSs were transferred to p-type silicon nanowires via drop-casting. The N-GQSs were converted from monolayer graphene on Cu foil using nitrogen plasma. After exposure to nitrogen plasma, the nano-sized GQSs were distributed on the Cu foil and were subsequently characterized by atomic force microscopy (AFM); the strong D peak of the sheets, which is related to the structural defects at the edges of graphene, was identified in the Raman spectrum. In addition, the doping of the GQSs with ~2.9% nitrogen was determined by the N 1*s* XPS spectrum, and the UV-vis absorption spectrum of the N-GQSs revealed an absorption band with a peak at 275 nm, as shown in Fig. S1. The well-aligned SiNW arrays serve as an anti-reflector that enhances light absorption in the structure and increases the overall surface area; the N-GQSs act as electrocatalysts for hydrogen evolution.

The top-view and cross-sectional scanning electron microscopy (SEM) images of the N-GQSs on SiNWs are shown in Fig. 2a and b. The SiNWs exhibited an average diameter of ~400 nm, and lengths of up to ~5 μm. To determine the crystallinity, orientation, and morphology of the N-GQSs on SiNWs, TEM analyses were performed. The selected area electron diffraction pattern, with an incident beam axis of [11-0] (Fig. S3), indicated that a single-crystalline SiNW was well aligned along the [001] direction; the thickness fringes, brightness and dark line pattern indicate that the SiNW was etched as a column with angled edges, as shown in Fig. 2c. Moreover, the N-GQSs, which measured approximately 7 nm in diameter, were uniformly placed on the SiNWs, as indicated by dark-field TEM imaging (Fig. 2c); moreover, the formation of the N-GQSs was verified by high-resolution TEM (HRTEM). The HRTEM image shows the Moiré pattern created by the superposition of the mismatched crystalline lattices of the N-GQSs and SiNWs, as shown in Fig. 2d. The lattice plane spacing of p-Si was observed to be 3.1 Å, which corresponds to the silicon (100) plane (JCPDS, no. 24-1402). The Moiré pattern (6.2 Å) indicates mixed translational and rotational geometry. The corresponding spacing of the fringes was calculated as follows:[34]

$$a_m = (a_{GQS} \times a_{Si}) / \sqrt{a_{GQS}^2 + a_{Si}^2 - 2a_{GQS}a_{Si}\cos(\alpha_{GQS} - \alpha_{Si})} \quad (4)$$

where a_m is the *d*-spacing of the Moiré pattern, a_{GQS} is the *d*-spacing of the N-GQS, and a_{si} is the *d*-spacing of Si. On the basis of Eq. (4), the placement of an N-GQS on a SiNW with a 20 degree tilt was verified by the relation between the Moiré fringe spacing and the Si lattice plane.

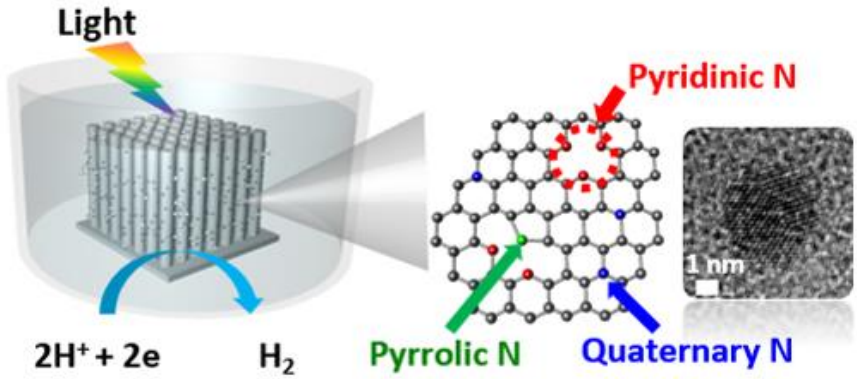

Figure 1. Schematic of N-doped graphene quantum sheets (N-GQSs) decorated on a Si nanowire (SiNW) photocathode electrode. Photons absorbed by the SiNWs generate minority carriers (electrons), which drift to the semiconductor/electrolyte interface, where $2H^+$ is reduced to H_2; the N-GQSs serve as electrocatalysts for hydrogen production. The gray, green, blue, and red spheres in the schematic of N-GQSs represent the carbon, pyrrolic nitrogen, quaternary nitrogen, and pyridinic nitrogen atoms, respectively. The average diameter of the N-GQSs is 5 nm, as determined from a TEM image.

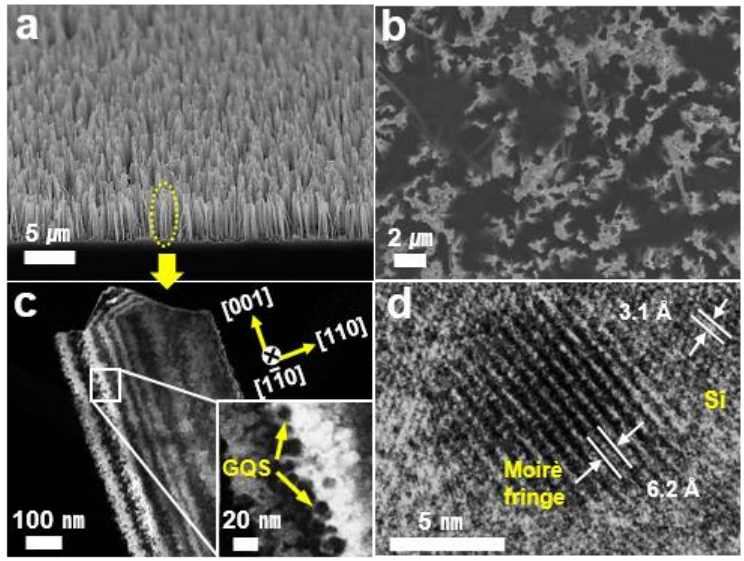

Figure 2. SEM images of SiNW arrays on p-silicon substrate obtained by metal assisted chemical etching method. (a) Cross-section and (b) top-view. (c) Dark-field TEM images of N-GQSs on p-SiNWs. (d) High-resolution TEM image shows Moiré pattern created by N-GQS in silicon lattices.

To investigate the dependence of Si photoelectrode on its nanostructure, Si substrates of various nanostructures were fabricated by silver metal-assisted chemical etching.[35] Normal boron-doped p-type (100) Si substrates were immersed in an aqueous solution of 0.015 M silver nitrate and 5 M hydrofluoric acid. Continuous Si oxidation by the galvanic reduction of Ag^+ ions and the ensuing dissolution of silicon oxide by HF resulted in the [100] directional etching of the Si substrates. The etching time was varied among 20 min, 30 min, 120 min, and 180 min. Depending on the etching time, different Si nanostructures were observed as characterized by SEM (Figure S5). When the etching time was shorter than 120 min, a porous nanostructure was observed. The transition of the surface structure from a porous to a nanowire structure occurred when the Si substrates were etched for 120 min. After this stage, the length of the nanowires was observed to increase with increasing etching time. Representative images of the SiNWs are shown in Figures 2a and 2b.

For the evaluation of the photocathodic behavior of the nanostructured Si electrodes, the current density was measured as the potential was swept from 0.4 V to -1.0 V *vs.* RHE in a three-electrode cell. A 300 W Xe lamp illuminated the Si photoelectrode with a light intensity of 100 mW/cm^2 through an Air Mass 1.5 Global filter in an aqueous 1 M perchloric ($HClO_4$) acid solution (pH 0). Because the applied potential of the Si working electrode was negative (cathodic), the magnitude of the current density increased and saturated at a specific value of the applied potential. The current density at the saturation point is called the limiting current density or the saturation current density. As shown in Figure 3a

and Figure S4, the current density of the planar Si continued to increase until the length of the nanowires reached 5 μm as the surface became increasingly nanostructured. The limiting current density of bare planar Si was approximately -33 mA/cm^2. The surface area of the nanostructured Si substrate was greater than that of the planar structure. The reflectance of incident light could be reduced by the nanostructured Si surface. Although the surface of planar Si reflects approximately one quarter of incident light, photon absorption is enhanced at the nanostructured surface because of its low reflectance. Nanostructured silicon wires have been reported to exhibit a light trapping effect,[36] which can enhance the current level for hydrogen production when the length of the Si nanowires is optimized to exhibit strong broadband optical absorption.[37] The nanowire structure also has the advantage of inducing the orthogonalization of light absorption and charge-carrier collection.[33] Thus, the minority carriers generated by incident solar light can move to the lateral side of each nanowire and participate in the hydrogen evolution reaction more quickly than in the planar structure. To calculate the photovoltage of the Si photoelectrode, the dark current density was also measured. The photovoltage is defined as the difference between the onset potential under the dark and illuminated conditions. Figure 2b shows the dark current densities of representative Si electrodes. The dark current density of the nanostructured electrodes was also greater than that of the planar Si substrate. The nanostructured photoelectrode (0.59 V of photovoltage) exhibited a positive shift in photovoltage of 0.13 V relative to that of the planar Si electrode (0.46 V of photovoltage) as shown in Table S1.

In measurements of the photoelectro-catalytic performance, N-GQSs on SiNWs exhibited catalytic activity toward the HER. As shown in Figure 3a, the current density of the N-GQSs/planar Si structure increased gradually from -0.2 V *vs.* RHE and was saturated at approximately -35 mA/cm^2 below -0.8 V *vs.* RHE at negative applied potentials. This current density is higher than that of planar Si without N-GQSs. Interestingly, measurements of the N-GQSs/planar Si structure showed that the overall current density-potential (*J-E*) curve was shifted by approximately 0.2 V toward positive potentials compared to that of planar Si without N-GQSs. The onset potential is defined as the potential at a photocurrent density of -1 mA/cm^2. The onset potential of N-GQSs/planar Si was 0.13 V *vs.* RHE, representing a positive shift of 0.30 V compared to the onset potential of bare Si (-0.17 V *vs.* RHE). Figure 3b also shows the dark current densities of the heavily arsenic-doped n^+-type Si electrodes. In the dark condition, the positive shift in the onset potential of 0.21 V (-0.44 V *vs.* RHE for N-GQSs/planar Si) also shows higher than that of planar Si (-0.63 V vs. RHE for planar Si).

When incorporated into the nanostructured photoelectrode system, the N-GQSs exhibited much higher catalytic activity than that of the planar photoelectrode system. The onset potential of the N-GQSs/Si nanowire electrode was 0.26 V *vs.* RHE, which is 0.09 V higher than that of the Si nanowire without a catalyst (0.17 V *vs.* RHE). Both the increased onset potential and the current density at the reversible potential (0 V *vs.* RHE) showed an enhanced ABPE of 2.29%, which is greater than that of the bare Si nanowire system (0.91%). ABPE is the applied bias photon-to-current efficiency:[38]

$$ABPE = [j_{ph}\ (mA/cm^2) \times (V_{redox} - V_b)\ (V) / P_{in}\ (mW/cm^2)]_{AM\ 1.5\ G} \times 100\ (\%)\ (5)$$

where, j_{ph} is the photocurrent density obtained under an applied bias V_b, V_{redox} is the redox potential for hydrogen production (0 V), V_{bias} is the externally applied bias potential that is often necessary to achieve reasonable photocurrents, and P_{light} is the intensity of the incident light for AM 1.5 G condition (~100 mW/cm^2).The enhanced photocatalytic performance indicates a synergistic effect between the N-GQSs and Si nanowire structures; moreover, the N-GQSs act as effective HER catalysts on the Si photocathode. Compared to previously reported carbon-based catalysts on Si system, the N-GQSs/Si nanowire system exhibits a higher ABPE.

To investigate the electrocatalytic activity of the N-GQSs, we measured cyclic voltammetry using a rotating disk electrode (RDE) system. To fabricate the working electrode, an N-GQSs solution was transferred to a glassy carbon (GC) tip that was inert in an aqueous solution. As shown in Figure 4a, in the *J-E* curves obtained by the RDE measurements, the current density associated with the water splitting reaction exponentially increased after the onset point as the potential was swept from 0.1 V to -0.45 V. For comparison with the potential for the HER in the RDE system, the potential required to attain -5 mA/cm^2 of HER current density was measured for graphene monolayer/GC, N-GQSs/GC, and Pt/GC systems. Also for comparison, the RDE of a graphene monolayer without plasma treatment was measured. The potential required to attain -5 mA/cm^2 of HER current density was -0.32 V *vs.* RHE for the graphene monolayer without plasma treatment. The potential for the N-GQSs/GC electrode at -5 mA/cm^2 was -0.22 V *vs.* RHE; this potential was positively

(anodically) shifted by 100 mV relative to that for the monolayer graphene. This result indicates that the N-GQSs and monolayer graphene exhibit electrocatalytic activity toward the HER.

To gain further quantitative insight into the catalytic activity of the N-GQSs, the *J-E* curves in Figure 4a were converted into plots of the potential as a function of the logarithm of *J*. This potential-log *J* plot is called a Tafel plot. The measured potentials were corrected for the iR losses that originated from the resistance of the interface between the electrode and the electrolyte. Analysis of the impedance spectra revealed that the resistances of the graphene monolayer and N-GQSs/GC were 7.5 and 8.0 Ω, respectively. The Tafel plot provides two parameters for estimating the electrocatalytic activity: the Tafel slope and the exchange current density. The Tafel slope is defined to be a measure of the potential increase required to increase the resulting current by one order of magnitude. The graphene monolayer exhibited a Tafel slope of 75 mV/decade, and the N-GQSs/GC exhibited a slope of 45 mV/decade, 30 mV lower than that of the graphene monolayer. For comparison with a well-known catalyst, Pt particles were deposited onto GC and the electro-catalytic activity of the resulting electrode was measured. The applied potential required to obtain -5 mA/cm^2 was -0.04 V *vs.* RHE, which represents a positive shift of 0.18 V relative to that of the N-GQSs/GC electrode. The Tafel slope of Pt-GC was 42 mV/decade, which is similar to that of the N-GQSs/GC. For previously reported carbon-based catalysts, the potential required to attain -5 mA/cm^2 was -0.5 V *vs.* RHE for N-doped graphene and -0.3 V *vs.* RHE for graphitic C_3N_4,

respectively.[23,24] The Tafel slope was reported to be 116 mV/decade for N-doped graphene and 51.5 mV/decade for graphitic C_3N_4 when deposited as a mixture with Nafion or carbon black on GC, respectively.

The Tafel slope provides an indication of which reaction steps are possible in the HER among the following:[39]

$$H_3O^+ + e^- \rightarrow H_{ads} + H_2O \quad \text{Volmer reaction} \quad (6)$$

$$H_{ads} + H_3O^+ + e^- \rightarrow H_2 + H_2O \quad \text{Heyrovsky reaction} \quad (7)$$

$$H_{ads} + H_{ads} \rightarrow H_2 \quad \text{Tafel reaction} \quad (8)$$

where H_{ads} is adsorbed H, (6) is a discharge step, (7) is a desorption step, and (8) is a recombination step. Considering the adsorbed hydrogen coverage (θ_H) on the surface of an electrode, if the recombination of adsorbed hydrogen (the Tafel reaction) is the rate-determining step for the HER and if the coverage is very high ($\theta_H \approx 1$), the measured Tafel slope will be 30 mV/decade. However, if the electrochemical desorption step (the Heyrovsky reaction) is the rate-determining step, a Tafel slope of 40-118 mV/decade is measured and is dependent of the value of θ_H (0-1).[40] The observed Tafel slope of 45 mV/decade in the present work indicates that the kinetics of the HER on the graphene monolayer/GC and N-GQS/GC electrodes is determined by the Heyrovsky reaction.

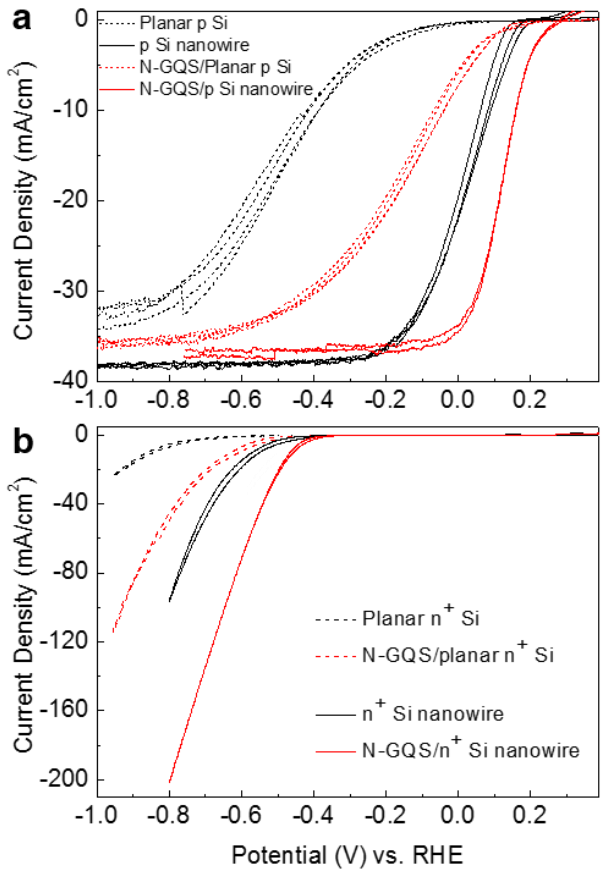

Figure 3. Cyclic voltammograms of N-doped graphene quantum sheets (N-GQSs) on silicon photocathodes. (a) Photocurrent density-potential (*J-E*) curves for a lightly boron-doped planar p-Si electrode and Si nanowire deposited with N-GQSs. The Si nanowire was fabricated using a metal-catalyzed electroless method. (b) Polarization curves of N-GQS on heavily arsenic-doped n^+-type Si electrodes under dark conditions.

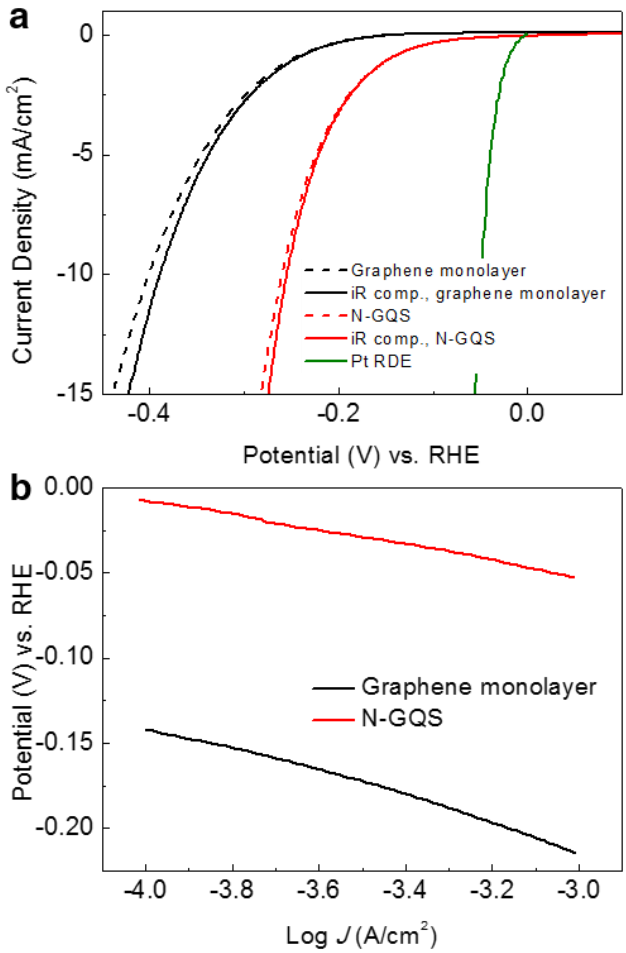

Figure 4. Electrochemical activity of graphene monolayer and N-GQSs on glassy carbon (GC) electrodes in a rotating disk electrode system. (a) Cyclic voltammograms (CV) of a graphene monolayer on GC, N-GQSs on GC, Pt/C on GC. CV data obtained compensating for ohmic drop (iR) losses are also plotted (dashed curves). (b) Tafel plots derived from the CV data in (a).

The exchange current density (J_0) of the N-GQSs catalyst was also analyzed. During hydrogen evolution, the current I can be described the following equation:[7]

$$I=-e(r^{+}-r^{-}) \quad (8)$$

where $r^{+}-r^{-}$ is the net rate of the electron transfer between the oxidation ($4e^{-} + 4H^{+} \leftarrow 2H_2$) and the reduction ($4e^{-} + 4H^{+} \rightarrow 2H_2$) from Eq. (2). The exchange current is the sum of the forward and backward rates when Eq. (2) is in equilibrium. The ability of a given material to catalyze the HER is usually measured by J_0, which is the rate of hydrogen evolution per surface area at the electrode potential when the reaction is at equilibrium. The J_0 is also defined as the current density at zero overpotential. The catalytic effect originates from improvement of the rate of charge transfer at the interface between the electrode and electrolyte or from a decrease in the activation energy barrier for a chemical reaction; these catalytic effects are represented by J_0. A high value of J_0 indicates that electron transfer or the adsorption/desorption of protons at the electrode/electrolyte can occur more easily, with a lower kinetic barrier. The value of J_0 can be obtained by extrapolating the Tafel plot in Figure 4b and extracting the current density at 0 V *vs.* RHE. The N-GQSs/GC electrode exhibited an enhanced J_0 of 7.1×10^{-5} A/cm^2, which was 26.3 times greater than the J_0 of monolayer graphene on GC (2.7×10^{-6} A/cm^2). The J_0 of the N-GQSs was also compared with that of other carbon-based catalysts (Table S3). The reported carbon-based catalysts exhibited a lower J_0 than that of our N-GQSs electrode. In addition, a metal-free carbon catalyst doped with nitrogen and

phosphorous exhibited a J_0 of 2.4×10^{-7} A/cm^2 and a graphitic C_3N_4 catalyst with nitrogen-doped graphene exhibited 3.5×10^{-6} A/cm^2 of J_0.[23,24]

Figure 5 summarizes the experimental data for the Si and GC electrodes. As shown in Figure 5b, our N-GQSs catalyst exhibited a lower Tafel slope and a higher J_0 compared to those of other reported carbon-based HER catalysts. Moreover, considering its role as a co-catalyst on the photoelectrode, the N-GQSs/Si nanowire system exhibited better photoelectrochemical performance in terms of ABPE and onset potential than any other reported catalyst/photoelectrode system (Figure 5a). Using only a non-metal carbon-based catalyst without incorporating a noble catalyst, the ABPE was increased to 2.29% by the combination of the nanostructured photoelectrode and N-GQSs catalyst. The good HER activity of the N-GQSs is attributed to abundant defects introduced by the plasma treatment. Moreover, high-resolution XPS result show that N-sites are classified into pyridinic (2.07 at%), pyrrolic (0.45 at%), and a small number of quaternary nitrogen (0.16 at%), which acts as the good catalytic sites for HER (Figure S1 e). Previous report also suggested that N-doping on graphene could significantly improve the HER by providing additional active sites[23] and theoretical computation shows favorable N-sites for H adsorption.[41] We are under investigation various N-sites with density functional theory for the precise mechanism on HER.

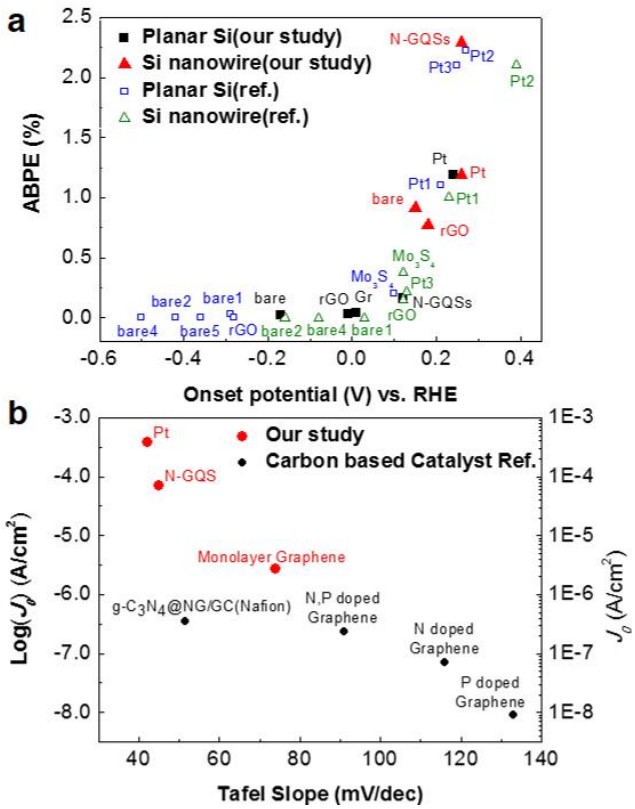

Figure 5. Summary of the experimental data for Si and glassy carbon (GC) electrodes. (a) The photoelectrochemical performance of p-type Si-based photoelectrodes. 'Onset potential' and 'ABPE' indicate the potential at -1 mA/cm^2 *vs.* RHE and the applied bias photon-to-current efficiency, respectively; 'bare' indicates the performance of the bare electrode without deposited catalyst. (b) Electrochemical performance of N-GQSs on GC electrode and other HER catalysts determined using rotating disk electrode system. J_0 indicates that the exchange current density. References can be found in the supporting information (Tables S2 and S3).

To further study the electrochemical performance of the N-GQSs/Si electrode, capacitance, impedance, and transient photoresponse measurements were performed, the results of which are shown in Figure 6. Capacitance measurements of the N-GQSs/Si nanowire and bare Si nanowire electrodes were performed as the potential was swept from 0.6 V to -0.5 V *vs.* RHE in a three-electrode cell without illumination. On the basis of the capacitance results, the flat band potential of the Si nanowire and N-GQSs/Si nanowire electrodes were calculated using the Mott-Schottky relation:[42]

$$1/C_{sc}^2 = 2(E - E_{fb} - kT/e)/(e\varepsilon\varepsilon_0 N) \qquad (9)$$

where C_{sc} is the capacitance of the space charge region, ε is the dielectric constant of the semiconductor, ε_0 is the permittivity of free space, N is the donor density (electron donor concentration for an n-type semiconductor or hole acceptor concentration for a p-type semiconductor), E is the applied potential, and E_{fb} is the flat band potential. Figure 6a shows the typical Mott-Schottky plots for a p-type silicon semiconductor. The donor density was calculated from the slope, and the E_{fb} was determined by extrapolation to a capacitance of zero. On the basis of these relations, the N-GQSs/Si nanowire electrode exhibited an E_{fb} of 0.13 V *vs.* RHE, whereas the E_{fb} of the bare Si nanowires was 0.02 V vs. RHE, as shown in Figure 6a. According to the equation: $E_b = E - E_{fb}$, the applied potential determines the magnitude of band bending (E_b) in the semiconductor and E_{fb}.[43] As E_{fb} increases positively, the absolute value of E_b increases because the applied potential, E is always negative under the cathodic reaction for proton reduction. Higher band bending at the interface between the electrode and electrolyte promotes faster charge

separation of generated electrons and holes.[44] The possibility of charge recombination or surface trapping at sub-band gap energy levels may also be diminished. The higher E_{fb} of the N-GQSs/SiNW electrode relative to that of the bare SiNW electrode appears to have augmented the extent of band bending at the depletion region of the semiconductor near the solid/solution interface because of the relationship between E_b and E_{fb}. Moreover, the doping density of bare SiNW and N-GQSs/SiNW is also calculated from Mott-Schottky relationship. Using the Eq. (9), the bare SiNW shows the donor density of 4.46×10^{15} /cm^3, which corresponds to the resistivity of $10^0 \sim 10^1$ ohm×cm for boron doped p-Si.[45] The N-GQSs/SiNW electrodes shows the donor density of 5.74×10^{15} /cm^3. From the donor density results, N-GQSs deposited on SiNW showed slight increase of the donor density, which might change the electrochemical property at the semiconductor/liquid interface. Zheng *et al.* reported that N dopant adjacent to C atom in a graphene matrix act as an electron acceptor through the analysis of the natural bond orbital population.[23] Likewise, N dopant on GQSs might also act as an active catalytic site for HER.

Impedance measurements were also performed to study the enhanced electrochemical properties of the N-GQSs/SiNW system. Under an illumination intensity of 100 mW/cm^2 with a frequency of 10^3-1 Hz and an amplitude of 5 mV in a three electrode system, electrochemical impedance spectroscopy was performed at 0 V *vs.* RHE. Figure 6b shows a Nyquist plot representing a typical impedance result. In Figure 6b, the N-GQSs/SiNW electrode shows two semicircles that are smaller than those exhibited by the Si nanowire electrode.

On the basis of the results gathered from these two semicircles, two capacitance elements can be assigned: the capacitance of the charge depletion layer in the semiconductor and the capacitance of the double layer at the semiconductor/electrolyte interface. In the high-frequency region, the charge transfer process in the depletion layer of the semiconductor dominates, whereas charge transfer across the double layer at the semiconductor/electrolyte interface is dominant in the low-frequency region.[46] In the case of the N-GQSs/SiNW electrodes, the two semicircles indicating charge transfer processes in the double layers at the solid/solution interface and in the depletion region of the semiconductor are smaller than those of the bare SiNWs. The smaller semicircle in the low frequency range means that the charge transfer resistance of the N-GQSs/SiNW in the double layer is lower than that of bare SiNW. The charge transfer resistance is also related with a kinetic barrier energy for the faradaic reactions across the double.[46] Thus, N-GQSs might promote the faradaic reactions by reducing the charge transfer resistance across the double layer. Similar charge transfer mechanism of the hydrogen production was also reported using reduced graphene oxide catalyst.[28] From the result of smaller semicircle in the high frequency range, the charge transfer resistance of the semiconductor depletion layer in the N-GQSs/SiNW is also lower than that of the bare SiNW. The charge transfer resistance in the semiconductor depletion layer is also correlated with higher photocurrent response because of the higher band bending in the depletion layer.[44, 47]

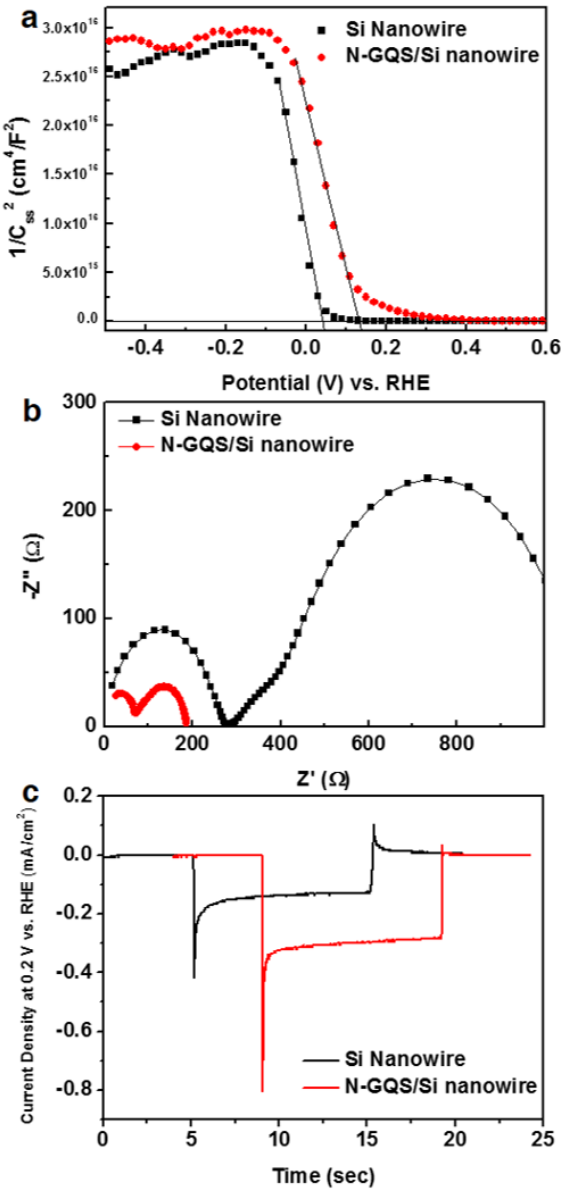

Figure 6. Comparison of the electrochemical activity of Si nanowire and N-GQSs on Si nanowire. (a) Mott-Schottky plots from capacitance measurement as a function of potential *vs.* RHE under dark condition. (b) Nyquist plot for Si nanowire and N-GQSs on Si nanowire at 0 V *vs.* RHE under dark condition. (c) The transient curve of the photocurrent from Si nanowire and N-GQSs on Si nanowire when the light was turned on and turned off at 0 V vs. RHE.

Transient photoresponse measurements were also performed to determine the factors enhancing the photoelectrochemical performance of the N-GQSs/SiNW electrodes; the results are shown in Figure 6c. The transient behavior of the N-GQSs/SiNW and bare Si nanowire electrodes was measured at 0.2 V *vs.* RHE using a chopped illumination system. Figure 6c shows the transient behavior of the N-GQSs/Si and bare Si electrodes without a catalyst. The light was turned on and turned off after 10 sec while the potential was maintained at 0.2 V *vs.* RHE. At the moment of the light was turned on, the current density reached a peak, which is referred to as the initial photocurrent density (J_{in}). The J_{in} values of the N-GQSs/Si nanowire and bare Si nanowire electrodes were -0.80 mA/cm^2 and -0.42 mA/cm^2, respectively. The current density then saturated, and the saturated photocurrent density (J_{st}) under illumination was -0.30 mA/cm^2 for the N-GQSs/Si nanowire electrode and -0.13 mA/cm^2 for the bare Si nanowire electrode. At the moment the light was turned off, the current density again showed an oscillating plot, and the current density at the peaks was designated as J_{off}. The J_{off} values of the N-GQSs/Si nanowire and Si nanowire electrodes were is -0.02 mA/cm^2 and -0.12 mA/cm^2, respectively. The high $J_{st}/J_{in,\ \text{N-GQSs}}$ ratio of 0.375 and small J_{off} of the N-GQS/Si nanowire electrode suggest that fewer carriers were trapped and that less recombination occurred at the surface state of the electrode surface, in comparison with those of the surface state of the bare Si nanowire sample ($J_{st}/J_{in,\ \text{bare}}$ = 0.309). Together, the capacitance and impedance results indicate that the N-GQSs/Si nanowire electrode can contribute to charge separation by inducing favorable band bending and boosting the charge transfer rate, which enhance the electrode's HER performance. To summarize, the

results obtained from the capacitance, impedance, and transient photoresponse measurements indicate that the N-GQSs/SiNW electrode enhances the HER activity by reducing the possibility of charge recombination and lowering the kinetic barriers for the HER at the interface between the Si semiconductor and electrolyte solution.

Conclusions

We fabricated N-doped graphene quantum sheets (N-GQSs) as a catalyst for the solar-driven hydrogen evolution reaction on Si nanowire photocathodes. The onset potential for the Si nanowire photocurrent was significantly shifted toward the anodic direction without a change in the saturation current density. N-GQSs exhibited excellent catalytic activity for the photoelectrochemical HER on Si nanowire photocathodes. The results showed that the N-GQSs electrodes exhibited a ABPE of 2.29%, which is higher than that of any other carbon-based photoelectrochemical HER catalysts reported to date. Our approach in this study involved a strategy for developing metal-free carbon-based catalysts with high efficiency for solar-driven hydrogen fuel production.

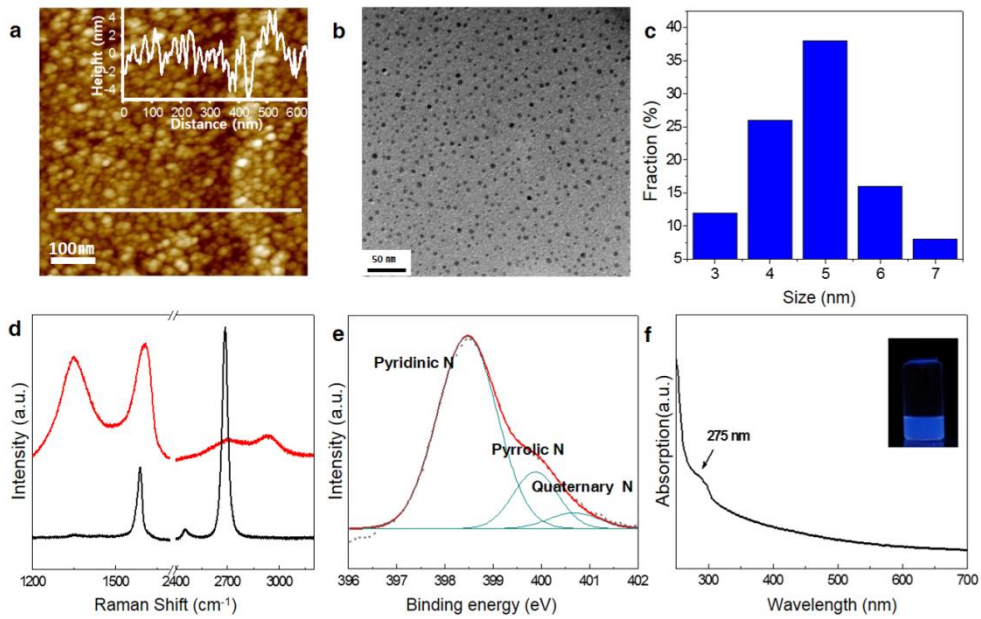

Figure S1. (a) AFM image of nitrogen plasma treated GQSs on Cu foil. Scan size, 600 x 600 nm^2. (b) TEM image of N-GQSs. (c) Histogram showing the size distribution of N-GQSs. (d) Raman spectra of graphene (black) and N-GQSs (red) and (e) detailed N 1*s* XPS spectra of N-GQSs. (f) UV-vis absorption of the N-GQSs in dichloromethane. The inset shows a photograph of the N-GQSs solution under 365 nm wavelength UV lamp.

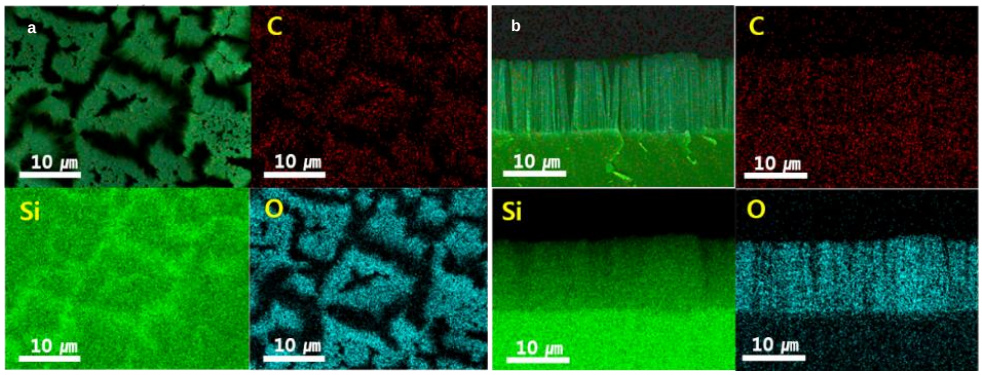

Figure S2. SEM mapping images of N-GQSs decorated on Si nanowires. (a,b) Colour images of all displayed with three elements; C (red), Si (green), and O (blue).

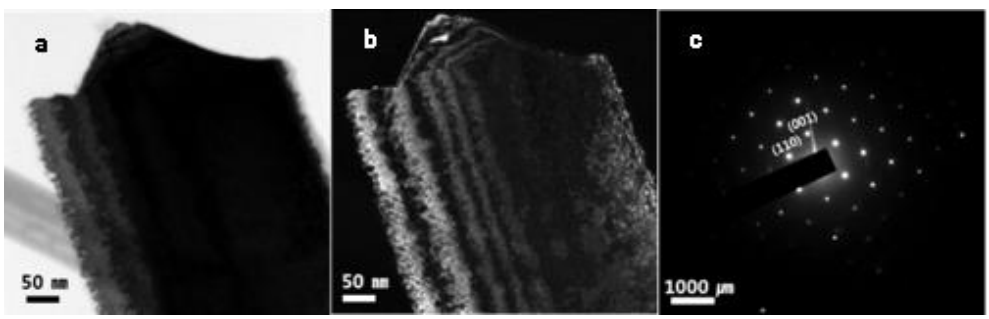

Figure S3. (a) Bright-field and (b) dark-filed TEM images of N-GQSs dispersed on p-SiNWs. (c) Selected area diffraction patterns (SAED) gives p-SiNWs are well etched toward [001] direction. GQS pattern is hardly observed due to the strong silicon lattice.

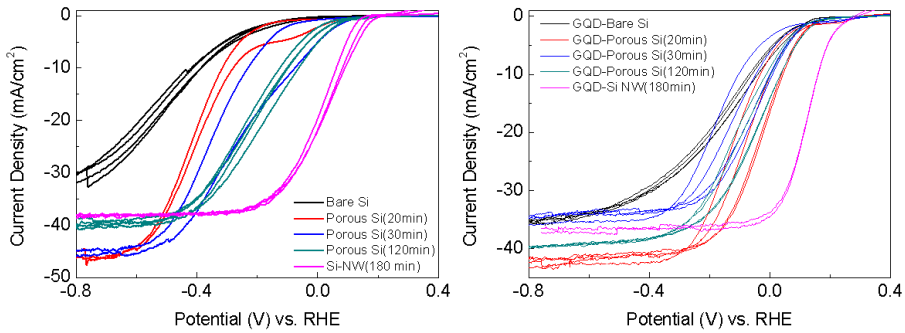

Figure S4. Photoelectrochemical performance of Si photocathode (a) Polarization curves of various Si electrodes without depositing any catalyst. Si nanowire were made by metal-catalyzed electroless method. Each of the etching time is 20 min, 30 min, 120 min, and 180 min. Each cyclic voltammetry was performed during 2 or 4 cycles at a scan rate of 5 mV/s. (b) Polarization curves of various Si electrodes deposited with N-GQSs catalyst.

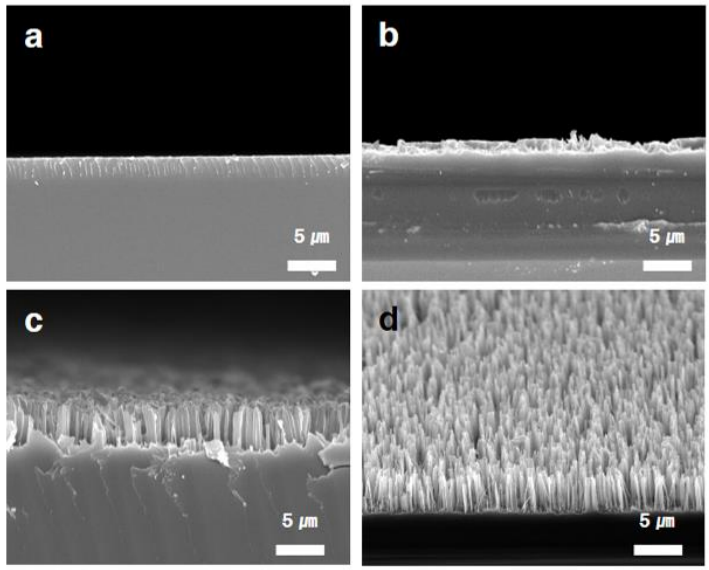

Figure S5. SEM images of cross-sectional views of p-type (100) Si wafers etched in 5 M HF and 0.015 M $AgNO_3$ solution at different etching times. The etching times are (a) 20 min, (b) 30 min, (c) 120 min, and (d) 180 min.

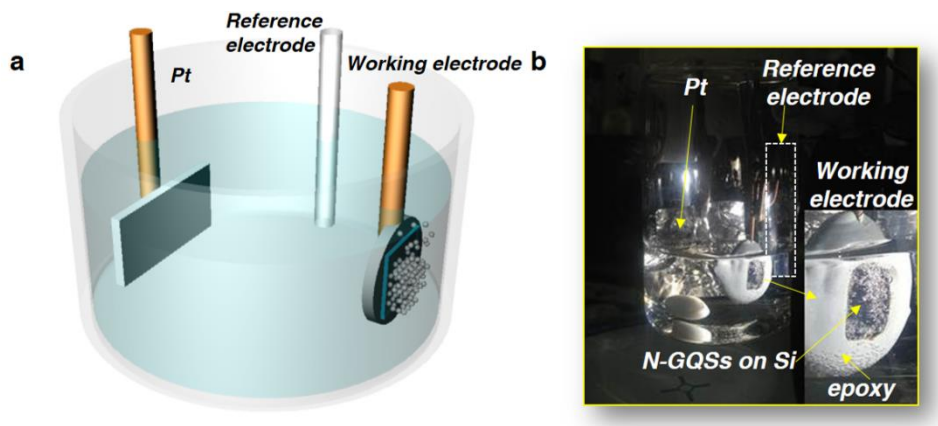

Figure S6. (a) Schematic illustration and photograph images of hydrogen evolution reaction on N-GQSs/Si photocathode

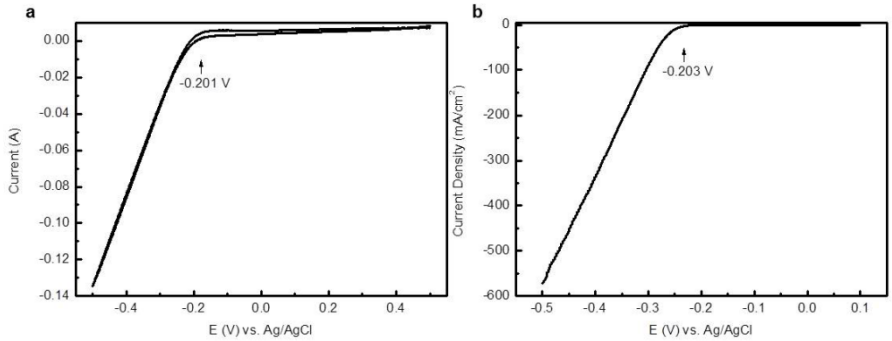

Figure S7. Calibration respect to RHE. Current vs. the applied potential respect to Ag/AgCl reference electrode with using (a) Pt foil for Si PEC cell experiment and (b) Pt wire as the counter electrode for rotating disk electrode (RDE) experiment.

Table S1. Summary of the experimental data of Si and Glassy Carbon (GC) electrodes.

Condition	Electrode	Onset potential [E (V) at -1 mA/cm^2]	E (V) at -5 mA/cm^2	E (V) at -10 mA/cm^2	Current density at reversible potential vs. RHE [mA/cm^2 at 0 V vs. RHE]	ABPE$^{\#}$ (%)
Under illumination (p type Si)	Planar Si	-0.17	-0.29	-0.42	0.34	0.02
	Si NW	0.17	0.12	0.09	21.61	0.91
	N-GQSs/ planar Si	0.13	0.03	-0.04	6.78	0.16
	N-GQSs/ Si NW	0.26	0.19	0.16	34.49	2.29
Under dark condition (n^+ type Si)	Planar Si	-0.63	-0.78	-0.85		
	Si NW	-0.42	-0.51	-0.56		
	N-GQSs/ planar Si	-0.44	-0.55	-0.62		
	N-GQSs/ Si NW	-0.37	-0.42	-0.45		
Photovoltage*	Planar Si	0.46				
	Si NW	0.59				
	N-GQSs/ planar Si	0.57				
	N-GQSs/ Si NW	0.63				
RDE analysis	Graphene/ GC	-0.20	-0.32	-0.37		
	N-GQSs/ GC	-0.11	-0.22	-0.25		
	Pt/GC	-0.02	-0.04	-0.05		

* The photovoltage is defined as the difference between the onset potential under the dark and illumination condition.

ABPE is the applied bias photon-to-current efficiency

Table S2. Summary of the photoelectrochemical data of various catalysts on p-type Si electrodes.

Catalyst	Synthesis and Loading method	Electrolyte	Activity			Ref. (Year)
			Onset Potential vs. RHE (V)	ABPE (%)	E (V) at -5 mA/cm^2	
Planar Si (our study)						
without catalyst (bare)		1M $HClO_4$	-0.17	0.02	-0.42	
Graphene (Gr)	CVD grown graphene & transfer	1M $HClO_4$	0.01	0.04	-0.21	
N-doped graphene quantum sheets (N-GQSs)	CVD grown graphene, plasma treatment, GQSs solution & drop casting	1M $HClO_4$	0.12	0.16	-0.04	
Pt	Nanoparticle by metal catalyzed electroless method	1M $HClO_4$	0.24	1.19	0.11	
Reduced graphene oxide (rGO)	Hummers' method & drop casting	1M $HClO_4$	-0.01	0.03	-0.20	
Si nanowire(our study)						
bare		1M $HClO_4$	0.15	0.91	0.13	
rGO	Hummers' method & drop casting	1M $HClO_4$	0.18	0.77	0.13	
N-GQSs	CVD grown graphene, plasma treatment, GQSs solution & drop casting	1M $HClO_4$	0.26	2.29	0.19	
Pt	Nanoparticle by metal catalyzed electroless method	1M $HClO_4$	0.26	1.19	0.19	
Planar Si(Ref.)						
bare[1]		0.2 M potassium hydrogen phthalate (KHP) with 0.5 M K_2SO_4, buffered to pH 4.5 using KOH.	-0.29*	0.03	-0.423*	[1](2011)
Pt[1]	Nanoparticle by metal catalyzed electroless method		0.21*	1.1	0.15*	
rGO	Hummers' method & drop casting	H_2SO_4 solution containing 0.5 M K_2SO_4 (pH = 1.8)	-0.28*	~0*	-0.49*	[2](2013)
bare[2]		H_2SO_4 and 0.5 M K_2SO_4 (pH 1)	-0.42*	~0*	-0.55*	[3](2012)
Pt[2]	Nanoparticle by metal catalyzed		0.27*	~2.22*	0.2*	

	electroless method					
Pt[3]	Nanoparticle by metal catalyzed electroless method	0.5 M aq. K_2SO_4 adjusted to pH ~ 2 using H_2SO_4	0.25*	2.1	0.2*	[4](2011)
bare[4]		1M $HClO_4$	-0.5*	~0*	-0.07*	[5](2011)
Mo_3S_4	Molecular cluster synthesis & drop casting		0.1*	~0.2*	0.04*	
bare[5]		0.5M H_2SO_4	-0.36*	~0*	-0.54*	[6](2011)
Si nanowire(Ref.)						
bare[1]		0.2 M KHP with 0.5 M K_2SO_4, buffered to pH 4.5 using KOH.	0.03	0	N/A	[1](2011)
Pt[1]	Nanoparticle by metal catalyzed electroless method		0.23*	1	0.16*	
bare[2]	Nanoparticle by metal catalyzed electroless method	H_2SO_4 and 0.5 M K_2SO_4 (pH 1)	~-0.16*	~0*	~-0.3*	[3](2012)
Pt[2]			~0.39*	~2.1*	~0.33*	
Pt[3]	Nanoparticle by metal catalyzed electroless method	0.5 M aq. K_2SO_4 adjusted to pH ~ 2 using H_2SO_4	0.13*	0.21	0.04*	[4](2011)
bare[4]		1M $HClO_4$	-0.08*	~0*	-0.22*	[5](2011)
Mo_3S_4	Molecular cluster synthesis & drop casting		0.12*	~0.38*	0.08*	
rGO	Hummers' method & drop casting	H_2SO_4 solution containing 0.5 M K_2SO_4 (pH = 1.8)	0.12*	0.15*	-0.04*	[2](2013)

*: Values were measured and extrapolated by our group referring to the figures and data from the references. The onset potential is defined as the potential at a photocurrent density of -1 mA/cm^2.

Table S3. Summary of the electrochemical data of RDE system for various catalysts on GC electrodes.

Catalyst/Substrate (adhesive)	Loading method	Electrolyte	Activity			Ref. (Year)
			Tafel Slope (mV/dec)	Exchange current J_0 (A/cm^2)	Exchange current $\log(J_0)$ (A/cm^2)	
Our Study						
Monolayer Graphene	CVD grown graphene	1M $HClO_4$	74	2.7E-6	-5.57	
N-GQSs	CVD grown graphene and plasma treatment	1M $HClO_4$	45	7.1E-5	-4.15	
Pt	Annealing from mixed precursors	1M $HClO_4$	42	3.86E-4	-3.41	
Carbon based catalyst (Ref.)						
N doped Graphene	Annealing from mixed precursors	0.5M H_2SO_4	116	7.04E-8	-7.15	[7](2014)
P doped Graphene	Annealing from mixed precursors	0.5M H_2SO_4	133	8.97E-9	-8.05	[7](2014)
N, P doped Graphene	Annealing from mixed precursors	0.5M H_2SO_4	91	2.4E-7	-6.62	[7](2014)
graphitic-C_3N_4@N-graphene/glassy carbon (Nafion)	Exfoliation & Polycondensation	0.5M H_2SO_4	51.5	3.5E-7	-6.46	[8](2014)

References

1. J. R. McKone, E. L. Warren, M. J. Bierman, S. W. Boettcher, B. S. Brunschwig, N. S. Lewis and H. B. Gray, Energy & Environmental Science, 2011, 4, 3573-3583.
2. Z. Huang, P. Zhong, C. Wang, X. Zhang and C. Zhang, ACS Applied Materials & Interfaces, 2013, 5, 1961-1966.
3. I. Oh, J. Kye and S. Hwang, Nano Letters, 2011, 12, 298-302.
4. S. W. Boettcher, E. L. Warren, M. C. Putnam, E. A. Santori, D. Turner-Evans, M. D. Kelzenberg, M. G. Walter, J. R. McKone, B. S. Brunschwig, H. A. Atwater and N. S. Lewis, Journal of the American Chemical Society, 2011, 133, 1216-1219.
5. Y. Hou, B. L. Abrams, P. C. K. Vesborg, M. E.Björketun, K. Herbst, L. Bech, A. M. Setti, C. D. Damsgaard, T. Pedersen, O. Hansen, J. Rossmeisl, S. Dahl, J. K. Nørskov and I. Chorkendorff, Nat Mater, 2011, 10, 434-438.
6. J. Oh, T. G. Deutsch, H.-C. Yuan and H. M. Branz, Energy & Environmental Science, 2011, 4, 1690- 1694.
7. Y. Zheng, Y. Jiao, L. H. Li, T. Xing, Y. Chen, M. Jaroniec and S. Z. Qiao, ACS Nano, 2014, 8, 5290- 5296. 8. Y. Zheng, Y. Jiao, Y. Zhu, L. H. Li, Y. Han, Y. Chen, A. Du, M. Jaroniec and S. Z. Qiao, Nat Commun, 2014, 5.

References

1. J. A. Turner, *Science*, 2004, **305**, 972–974.
2. N. S. Lewis and D. G. Nocera, *Proc. Natl. Acad. Sci.* U. S. A., 2006, **103**, 15729–15735.
3. M. G. Walter, E. L. Warren, J. R. McKone, S. W. Boettcher, Q. Mi, E. A. Santori and N. S. Lewis, *Chem. Rev.*, 2010, **110**, 6446–6473.
4. T. R. Cook, D. K. Dogutan, S. Y. Reece, Y. Surendranath, T. S. Teets and D. G. Nocera, *Chem. Rev.*, 2010, **110**, 6474–6502.
5. S. W. Boettcher, E. L. Warren, M. C. Putnam, E. A. Santori, D. Turner-Evans, M. D. Kelzenberg, M. G. Walter, J. R. McKone, B. S. Brunschwig, H. A. Atwater and N. S. Lewis, *J. Am. Chem. Soc.*, 2011, **133**, 1216–1219.
6. U. Sim, H.-Y. Jeong, T.-Y. Yang and K. T. Nam, *J. Mater. Chem. A*, 2013, **1**, 5414–5422.
7. J. K. Nørskov, T. Bligaard, A. Logadottir, J. R. Kitchin, J. G. Chen, S. Pandelov and U. Stimming, *J. Electrochem. Soc.*, 2005, **152**, J23–J26.
8. T. F. Jaramillo, J. Bonde, J. Zhang, B.-L. Ooi, K. Andersson, J. Ulstrup and I. Chorkendorff, *J. Phys. Chem. C*, 2008, **112**, 17492–17498.
9. Y. Hou, A. B. Laursen, J. Zhang, G. Zhang, Y. Zhu, X. Wang, S. Dahl and I. Chorkendorff, *Angew. Chem., Int. Ed.*, 2013, **52**, 3621–3625.
10. Y. Yan, B. Xia, Z. Xu and X. Wang, *ACS Catal.*, 2014, **4**, 1693–1705.
11. C. Chen, Y. Kang, Z. Huo, Z. Zhu, W. Huang, H. L. Xin, J. D. Snyder, D. Li, J. A. Herron, M. Mavrikakis, M. Chi, K. L. More, Y. Li, N. M. Markovic, G. A. Somorjai, P. Yang and V. R. Stamenkovic, *Science*, 2014, **343**, 1339–1343.
12. J. R. McKone, E. L. Warren, M. J. Bierman, S. W. Boettcher, B. S. Brunschwig, N. S. Lewis and H. B. Gray, *Energy Environ. Sci.*, 2011, **4**, 3573–3583.
13. B. Marsen, B. Cole and E. L. Miller, *Sol. Energy Mater. Sol. Cells*, 2008, **92**, 1054–1058.
14. M. W. Kanan, Y. Surendranath and D. G. Nocera, *Chem. Soc. Rev.*, 2009, **38**, 109–114.
15. A. Kudo and Y. Miseki, *Chem. Soc. Rev.*, 2009, **38**, 253–278.

16. J. Ran, J. Zhang, J. Yu, M. Jaroniec and S. Z. Qiao, *Chem. Soc. Rev.*, 2014, **43**, 7787–7812.
17. I. Oh, J. Kye and S. Hwang, *Nano Lett.*, 2011, **12**, 298–302.
18. D. H. Youn, S. Han, J. Y. Kim, J. Y. Kim, H. Park, S. H. Choi and J. S. Lee, *ACS Nano*, 2014, **8**, 5164–5173.
19. R. K. Shervedani and A. Lasia, *J. Electrochem. Soc.*, 1998, **145**, 2219–2225.
20. B. Cao, G. M. Veith, J. C. Neuefeind, R. R. Adzic and P. G. Khalifah, *J. Am. Chem. Soc.*, 2013, **135**, 19186–19192.
21. S. Chen, J. Duan, Y. Tang, B. Jin and S. Zhang Qiao, *Nano Energy*, 2015, **11**, 11–18.
22. K. S. Novoselov, A. K. Geim, S. V. Morozov, D. Jiang, M. I. Katsnelson, I. V. Grigorieva, S. V. Dubonos and A. A. Firsov, *Nature*, 2005, **438**, 197–200.
23. Y. Zheng, Y. Jiao, L. H. Li, T. Xing, Y. Chen, M. Jaroniec and S. Z. Qiao, *ACS Nano*, 2014, **8**, 5290–5296.
24. Y. Zheng, Y. Jiao, Y. Zhu, L. H. Li, Y. Han, Y. Chen, A. Du, M. Jaroniec and S. Z. Qiao, *Nat. Commun.*, 2014, **5**.
25. Y. Liang, Y. Li, H. Wang, J. Zhou, J. Wang, T. Regier and H. Dai, *Nat. Mater.*, 2011, **10**, 780–786.
26. J.-D. Qiu, G.-C. Wang, R.-P. Liang, X.-H. Xia and H.-W. Yu, *J. Phys. Chem. C*, 2011, **115**, 15639–15645.
27. Q. Xiang, J. Yu and M. Jaroniec, *Chem. Soc. Rev.*, 2012, **41**,782–796.
28. Z. Huang, P. Zhong, C. Wang, X. Zhang and C. Zhang, *ACS Appl. Mater. Interfaces*, 2013, **5**, 1961–1966.
29. U. Sim, T.-Y. Yang, J. Moon, J. An, J. Hwang, J.-H. Seo, J. Lee, K. Y. Kim, J. Lee, S. Han, B. H. Hong and K. T. Nam, *Energy Environ. Sci.*, 2013, **6**, 3658–3664.
30. Y. Hou, B. L. Abrams, P. C. K. Vesborg, M. E. Bj¨orketun, K. Herbst, L. Bech, A. M. Setti, C. D. Damsgaard, T. Pedersen, O. Hansen, J. Rossmeisl, S. Dahl, J. K. Nørskov and I. Chorkendorff, *Nat. Mater.*, 2011, **10**, 434–438.
31. Y. W. Chen, J. D. Prange, S. D¨uhnen, Y. Park, M. Gunji, C. E. D. Chidsey, P. C. McIntyre, *Nat. Mater.*, 2011, **10**, 539–544.

32.J. Oh, T. G. Deutsch, H.-C. Yuan and H. M. Branz, *Energy Environ. Sci.*, 2011, **4**, 1690–1694.

33.B. M. Kayes, H. A. Atwater and N. S. Lewis, *J. Appl. Phys.*, 2005, **97**.

34.D. B. Williams, Carter and C. Barry, Transmission Electron Microscopy, Springer, 2009.

35. K. Peng, H. Fang, J. Hu, Y. Wu, J. Zhu, Y. Yan and S. Lee, Chem.–Eur. J., 2006, **12**, 7942–7947.

36.E. Garnett and P. Yang, *Nano Lett.*, 2010, **10**, 1082–1087.

37.L. Tsakalakos, J. Balch, J. Fronheiser, M.-Y. Shih, S. F. LeBoeuf, M. Pietrzykowski, P. J. Codella, B. A. Korevaar, O. V. Sulima, J. Rand, A. Davuluru and U. Rapol, *J. Nanophotonics*, 2007, **1**, 013552.

38.Z. Chen, T. F. Jaramillo, T. G. Deutsch, A. Kleiman-Shwarsctein, A. J. Forman, N. Gaillard, R. Garland, K. Takanabe, C. Heske, M. Sunkara, E. W. McFarland, K. Domen, E. L. Miller, J. A. Turner and H. N. Dinh, *J. Mater. Res.*, 2010, **25**, 3–16.

39.L. R. F. Allen and J. Bard, John Wiley & Sons, Inc., 2001, 864.

40.B. E. Conway and G. Jerkiewicz, *Electrochim. Acta*, 2000, **45**, 4075–4083.

41.Y. Fujimoto and S. Saito, *J. Appl. Phys.*, 2014, **115**, 153701.

42.A. W. Bott, *Curr. Sep.*, 1998, **17**, 87–91.

43.K. Gelderman, L. Lee and S. W. Donne, *J. Chem. Educ.*, 2007, **84**, 685.

44.N. S. Lewis, *J. Electrochem. Soc.*, 1984, **131**, 2496–2503.

45.R. E. Hummel, Electronic Properties of Materials, Springer, 4th edn, 2011.

46.D. Merki, H. Vrubel, L. Rovelli, S. Fierro and X. Hu, *Chem. Sci.*, 2012, **3**, 2515–2525.

47.T. Lopes, L. Andrade, H. A. Ribeiro and A. Mendes, Int. *J. Hydrogen Energy*, 2010, **35**, 11601–11608.

48.J. Moon, J. An, U. Sim, S.-P. Cho, J. H. Kang, C. Chung, J.-H. Seo, J. Lee, K. T. Nam and B. H. Hong, *Adv. Mater.*,2014, **26**, 3501–3505.

Part Ⅱ

Oxygen-rich functionalized graphene for lithium sulfur battery

Chapter 5

General introduction of lithium sulfur battery

Lithium sulfur battery

Rechargeable batteries with superior performance are desired to solve imminent energy and environmental issues.[1–3] Lithium ion batteries have become dominant in the market as the state-of-the-art energy storage devices in portable and smart devices, such as cell phone, cameras and laptops, due to high energy density and log cycle life. However, the specific capacity and energy density become insufficient to meet the increased energy-demanding applications including electric vehicles and grid-level energy storage.[4,5] To solve these challenges, many researchers try to find an advanced batteries system with superior performance over current technologies.

The Li/S battery is an attractive and promising candidate among emerging battery technologies.[6] The concept of utilizing elemental sulfur as a cathode electrode material was introduced by Herbet and Ulam in 1960s.[7,8] In Li/S battery cell, elemental sulfur and lithium are used as the positive and negative electrodes, respectively, and the overall reaction during discharge can be described as

$$S_8 + 16Li^+ + 16e \rightarrow 8Li_2S \text{ (cathode)}$$

$$16Li \rightarrow 16Li^+ + 16e^- \text{ (anode)}$$

Sulfur and lithium have theoretical specific capacities of 1673 and 3861 mAh g^{-1}, respectively and the average voltage of the full cell is 2.15 V. The Li/S battery system supply a theoretical energy density of 2500 Wh kg^{-1} or 2800 Wh L^{-1},[4,9] which is 5 times higher than that of current lithium ion batteries (500 Wh kg^{-1}), as shown in Figure 1a.

The common Li/S battery architecture is comprised of a positive electrode of sulfur, carbon additives and binder, and a metallic lithium anode separated by an

organic electrolyte. In the organic liquid electrolyte. Figure 1b shows a typical charge-discharge profile in a Li/S cell. During the discharge process, two voltage plateaus at 2.4 and 2.15 V, which corresponded to the reduction of high-order lithium polysulfides (Li_2S_x, $4 \leq x$) and low-order lithium polysulfide (Li_2S_x, $x \leq 4$), are observed. During charging cycle, two plateaus at 2.2 and 2.5 V appear. Based on the phase transition mechanism, the discharge procedure goes through two stages.[10,11] The reaction of elemental sulfur with Li forms high-order lithium polysulfide, which dissolve in the liquid electrolyte.

$$S_8 + 2Li^+ + 2e^- \rightarrow Li_2S_8$$

$$3Li_2S_8 + 2Li^+ + 2e^- \rightarrow 4\,Li_2S_6^-$$

$$Li_2S_8 + 2Li^+ + 2e^- \rightarrow 2Li_2S_4$$

In the second steps, insoluble Li_2S_2 and Li_2S are formed and they precipitate out at the cathode. The corresponding voltage is lower, as indicated by the long plateau at 2.1 V.

$$Li_2S_4 + 2Li^+ + 2e^- \rightarrow 2Li_2S_2$$

$$Li_2S_2 + 2Li^+ + 2e^- \rightarrow 2Li_2S$$

The reaction of first plateau has fast or moderate kinetics, while the second reaction of converting Li_2S_2 to Li_2S is difficult and is impeded by slow solid-state diffusion. Consequently, the voltage drops rapidly once Li_2S covers the whole electrode, resulting in the termination of discharge. The summary of the reaction sequence of the sulfur cathode and the corresponding electrochemical profile is shown in Figure 1b.

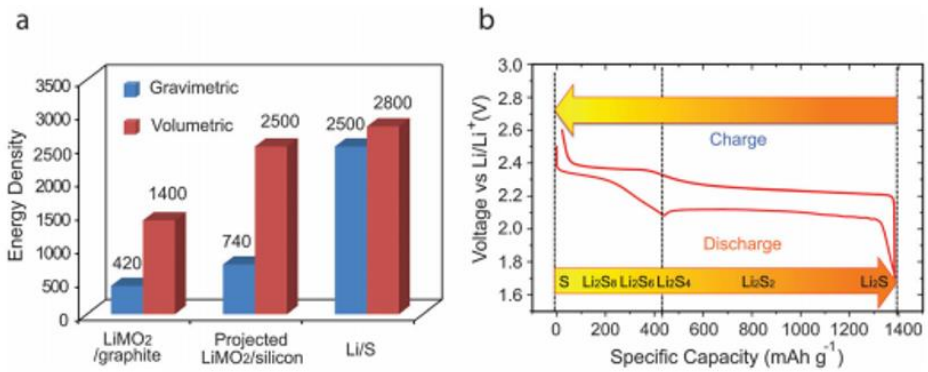

Figure 1. Introduction to the Li/S battery. (a) The theoretical energy density of different rechargeable battery systems based on active materials only. The units are Wh kg^{-1} and Wh L^{-1} for gravimetric and volumetric energy density, respectively. M = $Ni_{1/3}Mn_{1/3}Co_{1/3}$ for the $LiMO_2$–graphite system. For projected $LiMO_2$–silicon cell, the specific capacity for the cathode and anode are 250 and 3000 mAh g^{-1}, respectively. The density is 4.8 g cm^3 for $LiMO_2$, and the capacity per volume is 2200 mAh L^{-1} for silicon after considering the necessary space for volume expansion. (b) The voltage profile and chemistry of sulfur cathode in the organic electrolyte. This is referred by Yi's group.

Previous challenges and Studies

Rechargeable Li/S batteries have significant attention when considering the high specific energy density and low price. However, there is still have challenges to commercialize. The first problem is related to the volume change of sulfur particles during battery operation. Sulfur has a density of 2.03 g cm^3, while Li_2S (low-order polysulfide) is lighter (1.66 g cm^3), which leads to the volume expansion (80%) when sulfur is fully converted to Li_2S. This volume change causes fast capacity fading due to the pulverized structure of active materials. Second, the poor electrical conductivity of sulfur (10^{-28} $S \cdot cm^{-1}$) and Li_2S ($\geq 10^{14}$ ohm·cm),[12] which results in sluggish kinetics of the sulfur cathode. Moreover, the ionic insulating nature of sulfur leads to low active material utilization. Once a thin low-order polysulfide layer completely covers the whole electrode, further lithiation will be largely hampered and the voltage decreases rapidly. Third, the polysulfides are intermediates produced during the electrochemical reduction of sulfur which are highly soluble in the electrolyte. These soluble species diffused from the sulfur cathode to the lithium anode driven by the concentration and gradually passivating the anode. The low-order polysulfide can move back to the cathode and oxidized to high-order polysulfide. This parasitic process takes place continuously, creating an internal "shuttle" phenomenon. The polysulfide shuttle usually leads to an irreversible loss of sulfur in cathode, which results in low Coulombic efficiency.[4,9,14] and fast capacity fading. Moreover, the dissolution and precipitation process alters the morphology of the cathode in each cycle, which induces strain inside the electrode and degrades the cycle life.[13] Besides challenges related to the sulfur cathode, the use of lithium metal

anodes results in safety concerns and energy density penalties due to the use of excess lithium;[15,16] these concerns warrant careful examination in the future.

To solve these challenges, many researches have been focused on the rational design of the electrode structure. Based on previous reports in the past several years, the ideal sulfur electrode structure should have the following characteristics:[17,18] first, sufficient space for sulfur volumetric expansion during battery operation; second, small dimensions of the active material to avoid pulverization; third, short transport pathways for both electrons and Li ions for high capacity and power capability; forth, physically and chemically trapping the high-order polysulfide; fifth, additional electrolyte additives to cover the lithium surface to minimize the shuttle effect. These characteristics allow to develop various sulfur structures which can be divided into several categories, such as graphene-sulfur composites, nano-sized carbon-sulfur composites, conductive polymer-sulfur composites, etc.

References

1. J. M. Tarascon and M. Armand, *Nature*, 2001, **414**, 359-367.
2. M. Armand and J.-M. Tarascon, *Nature*, 2008, **451**, 652-657.
3. M. S. Whittingham, *Chem. Rev.*, 2004, **104**, 4271-4301.
4. X. L. Ji and L. F. Nazar, *J. Mater. Chem.*, 2010, **20**, 9821-9826.
5. M. Z. Jacobson, *Energy Environ. Sci.*, 2009, **2**, 148-173.
6. P. G. Bruce, S. A. Freunberger, L. J. Hardwick and J.-M. Tarascon, *Nat. Mater.*, 2012, **11**, 19-30.
7. D. Herbert and J. Ulam, U.S. Patent, 3043896, 1962.
8. J. R. Birk and R. K. Steunenberg, *Adv. Chem. Ser.*, 1975, 186-202.
9. Y. V. Mikhaylik and J. R. Akridge, *J. Electrochem. Soc.*, 2004, **151**, A1969-A1976
10. K. Kumaresan, Y. Mikhaylik and R. E. White, *J. Electrochem. Soc.*, 2008, **155**, A576-A582.
11. H. Yamin and E. Peled, *J. Power Sources*, 1983, **9**, 281-287.
12. Y. Yang, G. Y. Zheng, S. Misra, J. Nelson, M. F. Toney and Y. Gui, *J. Am. Chem. Soc.*, 2012, **134**, 15387-15394.
13. R. Elazari, G. Salitra, Y. Talyosef, J. Grinblat, C. ScordilisKelley, A. Xiao, J. Affinito and D. Aurbach, *J. Electrochem. Soc.*, 2010, **157**, A1131-A1138.
14. S. Joongpyo, K. A. Striebel and E. J. Cairns, *J. Electrochem. Soc*., 2002, **149**, A1321-A1325.
15. C. Brissot, M. Rosso, J. N. Chazalviel and S. Lascaud, *J. Power Sources*, 1999, **81**, 925-929.
16. X. H. Liu, L. Zhong, L. Q. Zhang, A. Kushima, S. X. Mao, J. Li, Z. Z. Ye, J. P. Sullivan and J. Y. Huang, *Appl. Phys. Lett.*, 2011, **98**, 183107
17. G. Zheng, Y. Yang, J. J. Cha, S. S. Hong, and Y. Cui, *Nano Lett.*, 2011, **11**, 4462-4467.
18. Y. Yang, G. Zheng, and Y. Cui, *Chem. Soc. Rev.* 2013, **42**, 3018-3032.

Chapter 6

An electrochemical approach to graphene oxide coated sulfur for long cycle life

Introduction

There has been a growing demand for studies on eco-friendly and alternative energy sources to replace fossil fuels and natural gas. Lithium-based rechargeable batteries with both high volume and gravimetric energy have received significant attention as green power sources for portable electronics including mobile phones and laptops.[1-3] However, state-of-the-art lithium rechargeable battery systems must be substantially improved to satisfy the ever-increasing energy demands of current electric vehicles for both high energy and power density.[1-3] The low specific capacity of cathode materials (~ 150 mAh/g for layered oxides and ~ 170 mAh/g for $LiFePO_4$) compared to those of the anode materials (370 mAh/g for graphite and 4200 mAh/g for silicon[4]) has spurred many researchers to develop new high capacity cathode materials.

Among many candidates, sulfur is one of the most promising materials that can overcome the aforementioned issues. Elemental sulfur has a theoretical specific capacity of 1675 mAh/g,[5,6] which is approximately five times higher than that of conventional $LiCoO_2$ cathode materials. Furthermore, sulfur has other noticeable advantages[7] as its resource is abundant, and it is inexpensive and environmentally friendly. These advantages are expected to play pivotal roles in commercializing as a next generation battery system that has a high specific energy.

However, the poor electronic conductivity of elemental sulfur (~1×10^{-30} S/cm at room temperature) limits its utilization as an active material for sulfur

electrodes[8]. During charging and discharging, the sulfur cathode is converted into lithium polysulfides (Li_2S_8, Li_2S_6, Li_2S_4 2.15-2.4 V and Li_2S_2, Li_2S ≤2.1 V)[8,9] dissolved in liquid organic electrolytes and deposited on lithium metal electrodes and separators, which causes irreversible loss of polysulfides. Recently, Y. V. Mikhaylik *et al.* reported that high order polysulfides generated at the sulfur electrode in charge state diffuse to the lithium anode where they react directly with the lithium metal in a parasitic reaction to recreate the low order polysulfides. Those species diffuse back to the surfur cathode to regenerate the higher forms of polysulfide, thus creating a shuttle mechanism.[10] These losses of an active material leads to low Coulombiv efficiency, poor rechargeability, and rapie fading of the capacity.[8-12] Thus, extensive research studies have been conducted in an attempt to overcome the above mentioned problems. In fact, the effots have been focuesed on enhancing the electrical conductivity of sulfur by combinding it with various conducting materials such as porous carbon,[13-15] one dimensional carbon,[16,17] graphene oxide (GO),[18-20] and conductive polymers.[21] In particular, the GO-based materials showed enhanced electrochemical properties because GO-sulfur composites are capable of preventing the shuttle of polysulfides. However, the role of oxygen functional groups in such improvement has still not been completely understood yet.

In this work, GO wrapped sulfur (GO-S) composites were prepared and decorated with carbon black (CB), and then utilized as a cathode electrode in a lithium sulfur battery (Li-S battery). The structural properties of the cathode electrode were characterized *via* transmission electron microscopy (TEM), scanning

electron microscopy (SEM), and Raman spectroscopy. In addition, the chemical properties were determined by using Fourier transform infrared spectroscopy (FTIR) and X-ray photoelectron spectroscopy (XPS). The cyclic performance and Coulombic efficiency was analysed using various electrochemical measurement techniques.

Experimental

Synthesis: GO used in this paper was synthesized by Hummer's method.[22] Graphite power (10 g) was prepared in a flask in an ice bath. 7.6 g $NaNO_3$ was added into the flask which was filled with 338 ml H_2SO_4 under stirring condition until homogenized. In addition, 45 g of $KMnO_4$ was gradually put into the system over 1 h under magnetic stir. The solution was removed from the ice bath after 2 h and was further stirred for 5 days. Then viscous slurry was obtained and then added to 600 ml aqueous solution over 1 h and H_2O_2 (30 wt.%) (5 ml) was added into the mixture with stirring system over 1 day. The brown colour mixture was rinsed with deionized water using centrifuge system for several times. Finally, the GO aqueous solution was obtained and dried with vacuum evaporator.[17]

GO (~4 mg/ml) was dispersed in deionized water and sonicated for 1 h. GO has hydrophilic properties from oxygen functional group, which made GO was easily dispersed in water. In order to increase the conductivity of the core-shell material, carbon black nanoparticles (Super P, ~ 40 nm in diameter, CB, 40 mg) were loaded on the graphene oxide (GO) by simple sonication method. The mixture in the flask was sonicated for 1 h for a homogeneous suspension. For GO-S/CB composites, 1.5 g of $Na_2S_2O_3$ powder was dissolved in 250 ml deionized water and hydrochloric acid was added to the solution with a magnetic stirring, which turns to be yellow colour from sulfur. To decorate GO/CB on sulfur particles, Triton TX-100 aqueous solution was poured into the flask while the system was heated up to ~ 70°C in an oil bath. After 20 min at ~ 70°C, the

prepared GO/CB suspension was added into the flask and kept for 20 min under vigorous magnetic stirring. Then, the system was cooled down to room temperature and the resultant product was collected and rinsed several times by centrifuge. The product was dried in a vacuum system.

Cell Assembly and Electrochemical Measurement: The GO-S composites were mixed with Super P (type of carbon black) and polyvinyldifluoride (PVDF), with mass ration of 60:20:20, in N-Methylpyrrolidone (NMP) solvent to produce electrode slurry. The slurry was loaded onto a current collector, an aluminium foil, using a doctor blade technique, and then dried for 3 h to form a working electrode. After dehydration, it was pressed by a roll press machine and then, it was dried again for 12 h. The loading level of total material was ~ 1-1.2 mg/cm^2. 2032 type coin cells were used for the battery type and Li metal foil for the counter electrode. The electrolyte was 1.0 M lithium bis-trifluoro-methane sulfonylimide (LITFSI) in 1,3-dioxolane (DOL) and 1,2-dimethoxyethane (DME) (volume ratio 1:1). In addition, it should be noted that $LiNO_3$ was used as an additive in the electrolyte to enhance the cycle stability of the Li-S cell. The coin cells were assembled in an Ar-filled glove box. The galvanostatic charge-discharge experiment was performed with a WBC3000 cycler (WonA Tech, Korea) at room temperature (RT). The coin cells were cycled at a constant current density of 835 mA/g (0.5 *C*) on cycling performance or various constant current density from 0.1 *C* to 1 *C* on rate performance with the voltage range of 1.7-2.8 V *vs.* Li/Li$^+$. All the specific capacity values were based on the mass of elemental sulfur. The Cyclic voltammetry (CV) was operated from 1.5 V to 3.0 V at 0.03

mV/s scan rate, which can be converted to the constant current of 0.1 *C*-rate. The Electrochemical Impedance Spectroscopy (EIS) was recorded by applying an AC voltage of 0.005 V in the frequency range from 100,000 to 0.05 Hz.

Material Characterization: The charge-discharge capacity of the Li-S cell was calculated by the sulfur content of the electrode matrix and the weight ratio of sulfur to carbon in the composite electrode was measured by thermogravimetric analysis (TGA: SDT Q600). TGA measurements were conducted in a nitrogen atmosphere from room temperature to 600°C at a heating rate of 5°C/min. X-ray diffraction pattern was obtained using High Power XRD from Rigaku Corp. with Cu K_α radiation (λ) 0.15418 nm (model: D-MAX2500-PC). The diffraction data was recorded in the 2θ range of 20-80° with a step of 4°/min. To determine the surface morphology, field-emission scanning electronic microscopy (FE-SEM) was performed (AURIGA, Carl Zeiss).

Results and Discussion

The GO-S/CB composites were synthesized with a help of surfactants in order to increase the surface affinity between GO and sulfur. The surfactant is also useful to control the grain size in a manner similar to that of conventional sulfur particles. The GO contained both hydrophobic aromatic and hydrophilic regions which interact with carbon black (Super P, average particle size ~50 nm, CB), and polysulfides, respectively. The schematic illustration in Fig. 1(a) shows a sulfur particle tightly packed with GO sheets. The SEM images of GO-S/CB show a few micron-sized sulfur particles well covered with GO and CB (Fig. 1(b) and Fig. S1(a)), while the surface of the sulfur particles are partially exposed in the S/CB electrode as shown in Fig. S1(b). The fringes and Moiré patterns in the TEM images (Figs. 1(c,d)) imply that the sulfur particles are compactly wrapped with GO and CB. The corresponding GO-S/CB composites were characterized using scanning transmission electron microscopy (STEM) and energy dispersive X-ray spectroscopy (EDS). The elemental EDS mapping for carbon (orange), sulfur (blue), and oxygen (magenta) clearly shows that GO-S/CB forms a core-shell structure with oxygen-rich functional groups (Figs. 1(e-h)).

The surfaces of the GO-S/CB and the S/CB electrodes were characterized *via* Fourier transform infrared spectroscopy (FTIR), X-ray photoelectron spectroscopy (XPS), and Raman spectroscopy, as shown in Fig. 2. The FTIR spectrum of GO-S/CB shows various configurations of oxygen in the structure including the vibration modes of -OH, C=O, C-O, and C-O-C at 3434 cm^{-1}, 1725 cm^{-1}, 1024–1180 cm^{-1}, and

1200 cm^{-1}, respectively; the peak at 1629 cm^{-1} results from the sp^2-hybridized C=C in-plane stretching.[23] Moreover, the O 1*s* spectra obtained from XPS exhibit significantly higher intensity of the peak at 533.0 eV (C-OH) in GO-S/CB, compared to that of the S/CB. These results noticeably match with the FTIR and XPS spectra of each carbon material (GO and CB) as shown in Fig. S2. The Raman spectra exhibit typical of carbon peaks; i.e., two strong peaks at 1350 cm^{-1} for the D band and at 1590 cm^{-1} for the G band, which stem respectively from structural defects and the in-plane vibrational mode.[24] The Raman spectrum in the inset of Fig. 2(c) shows a peak corresponding to sulfur only.[25] The sulfur peak was not observed for both samples, implying that the sulfur particles are surrounded by carbon materials.

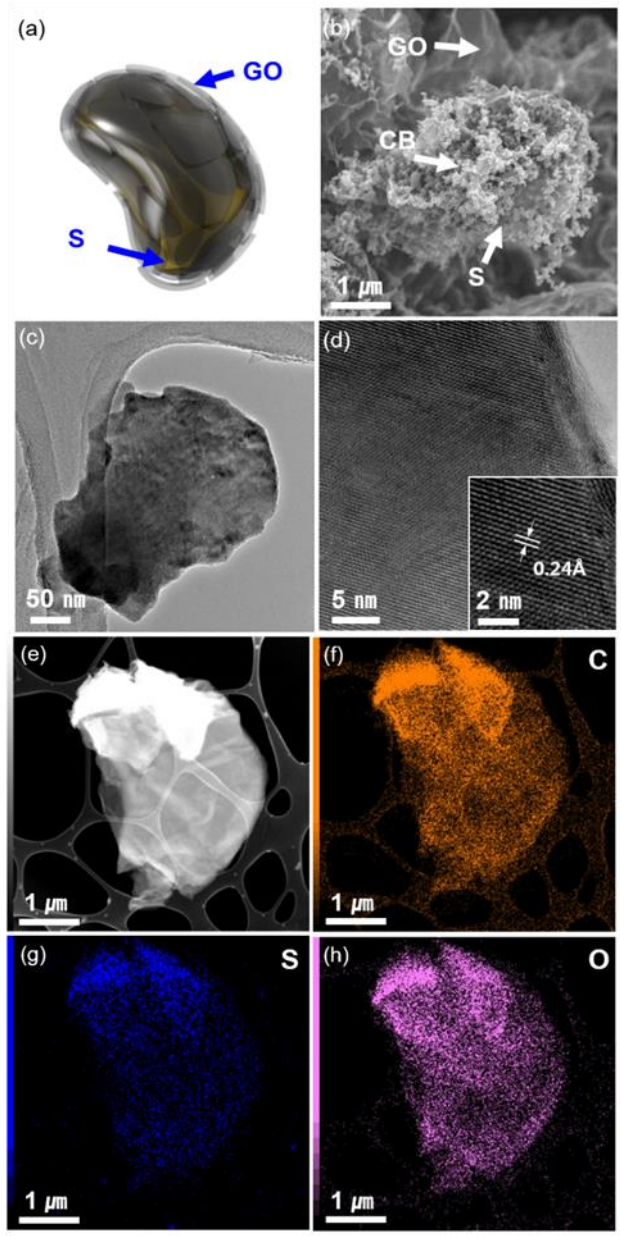

Figure 1. (a) Schematic illustration and (b) scanning electron microscopy (SEM) image of GO-S/CB composites. (c) Transmission electron microscopy (TME) image and (d) high resolution TEM image of GO-S/CB. (e) Scanning-TEM (STEM) image and (f-h) C, S, and O energy-dispersive S-ray spectroscopy (EDS) maps of the GO-S/CB composites.

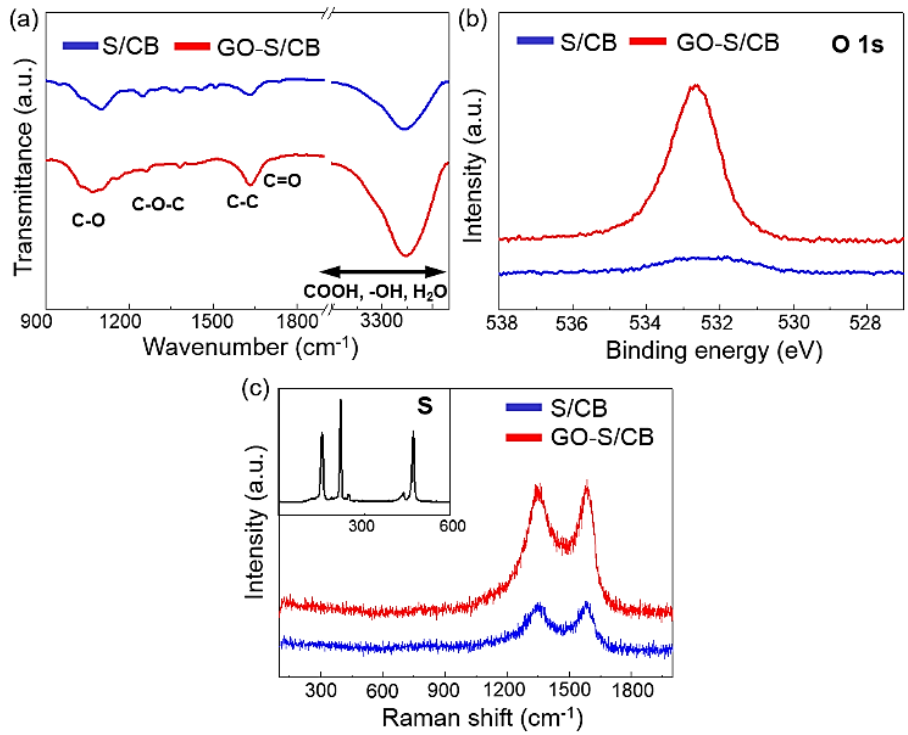

Figure 2. (a) FTIR spectra of GO-S/CB and S/CB. The peaks correspond to the various functional groups in GO-S/CB and S/CB. (b) O 1*s* XPS spectra and (c) Raman spectra of GO-S/CB and S/CB.

Figure 3(a) shows the X-ray diffraction (XRD) patterns measured from the S/CB and GO-S/CB composites on the Al foil. The positions of the peaks corresponding to sulfur particles all occurred at the standard Bragg position of the orthorhombic phase with the space group Fddd (JCPDS 24-0733: S_8)[26] and no traces of other impurities were detected. The amount of GO in the GO-S composite was quantified *via* TGA analysis. Fig. 3(b) represents the TGA results of the GO-S composite from 40 to 600℃ under a nitrogen atmosphere, and the weight loss was shown approximately up to 84wt.%. The loss of the sulfur-conducting material composite results mainly from the evaporation of sulfur at temperatures of ~170-250℃. Furthermore, the continuous and steady weight loss of the second stage above 370°C is estimated to be 6 wt.%. The sulfur content of the GO-S composite was adjusted to 90 wt.% during the preparation process.

Fig. 4(a) and (b) show conventional charge-discharge profiles of the S/CB and the GO-S/CB as a lithium sulfur battery. The cell is discharged and charged at 0.5 C rate (835 mA/g) for 20 cycles, which is sufficient for revealing variations and tendencies in the electrochemical behavior. In the discharge profiles, two-step plateaus were generated at 2.4 V and 2.1 V due to the dissolution of sulfur to soluble high-order polysulfide and the precipitation of low-order polysulfide to lithium sulfide (Li_2S_8, Li_2S_6, Li_2S_4 2.15-2.4 V and Li_2S_2, Li_2S ≤2.1 V).[8,9] In this paper, we designated three regions, Q_1, Q_2 and ΔV, which facilitate the explanation of the electrochemical properties of GO-S/CB cathode electrode. Q_1 and Q_2 indicate

capacity of the dissolution and the precipitation regions, respectively and the ΔV means of overpotential between discharge and charge reactions.

In the Q_1 region, the sulfur particles as reactants are initially dissolved into electrolyte, and then, the reactants are reduced to the long-chain sulfides (S_n^{2-},n=8-4) in the liquid phase (dissolved state). In this regime, the lithium/polysulfide ions can easily move, leading to the fast kinetics of the reaction. However, those liquid mechanism leads to irreversible loss of soluble polysulfides due to diffusion from the polysulfide into the bulk electrolyte.[9] In the Q_2 region, long-chain polysulfides are converted to short-chain polysulfides (S_n^{2-},n=4-1), and then finally produced the lithium sulfide (Li_2S) (precipitated state); the kinetics of this reaction are sluggish owing to the formation of lithium polysulfides, driving the high reversible cycle retention of capacity.[9] In charge processes, the reverse reactions aforementioned occur. Q_1, Q_2, and ΔV provide insight into the origins of the unique reaction mechanism of the materials. The GO-S/CB exhibits the constant Q_1 capacity retention with increasing cycle number, while the capacity of S/CB is continuously fading due to irreversible loss of polysulfide, which represents that GO can play a key role in reserving polysulfides.

Moreover, the slowly decreasing Q_2 value of the GO-S/CB, compared to the rapidly decreasing value of S/CB indicates that GO provides reversible reaction sites with polysulfide. Previous studies assert that the oxygen-rich carbon matrix promotes the interaction of carbon with sulfides.[18,19,27] Thus, we believe that the increased electrochemical performance of GO stems from physical wrapping and chemical surface modification. The cycling performance and Coulombic efficiency

of S/CB and GO-S/CB composites were measured at 0.5 *C* rate (1 *C* rate = 1,675 mA/g) for 100 cycles, as shown in Figs. 4(c) and (d); respective initial capacities of 1003.5 mAh/g and 1142.7 mAh/g were obtained for S/CB and GO-S/CB at the first cycle. At the relatively fast *C*-rate, GO as a conducting agent supports electrical contact with sufur, which shows the discharge capacities of ~723.7 mAh/g (GO-S/CB) and ~307.3 mAh/g (S/CB) at 100th cycle, respectively. The fading capacity of the S/CB may be attributed to its Coulombic efficiency, i.e., the S/CB exhibits a low charge/discharge ratio in the initial cycle, but the Coulombic efficiency increased gradually due to the shuttle mechanism stemming from the irreversible loss of the polysulfide into electrolyte. This loss indicates that the structure of the S/CB does not trap the soluble polysufide.[10]

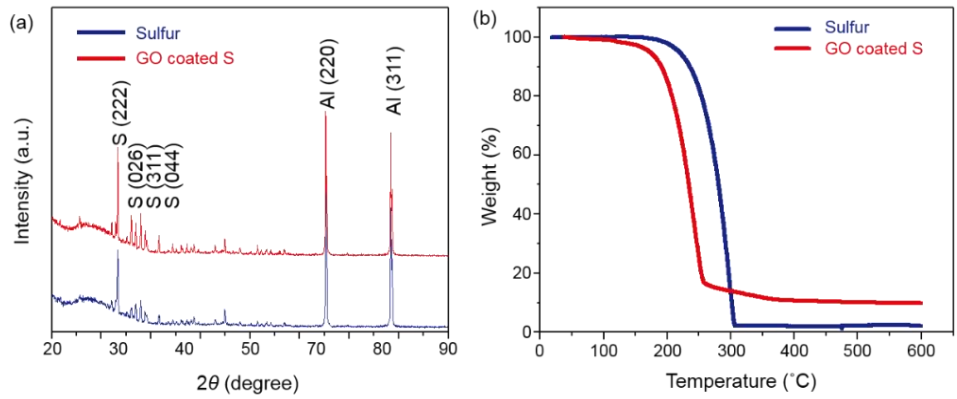

Figure 3. X-ray diffraction (XRD) patterns and Thermogravimetric analysis (TGA). (a) XRD spectra of S/CB and GO-S/CB on Al foil current collector and (b) TGA spectra collected in N_2 atmosphere with a heating rate of 10℃/min showing the S content of the GO-S electrodes.

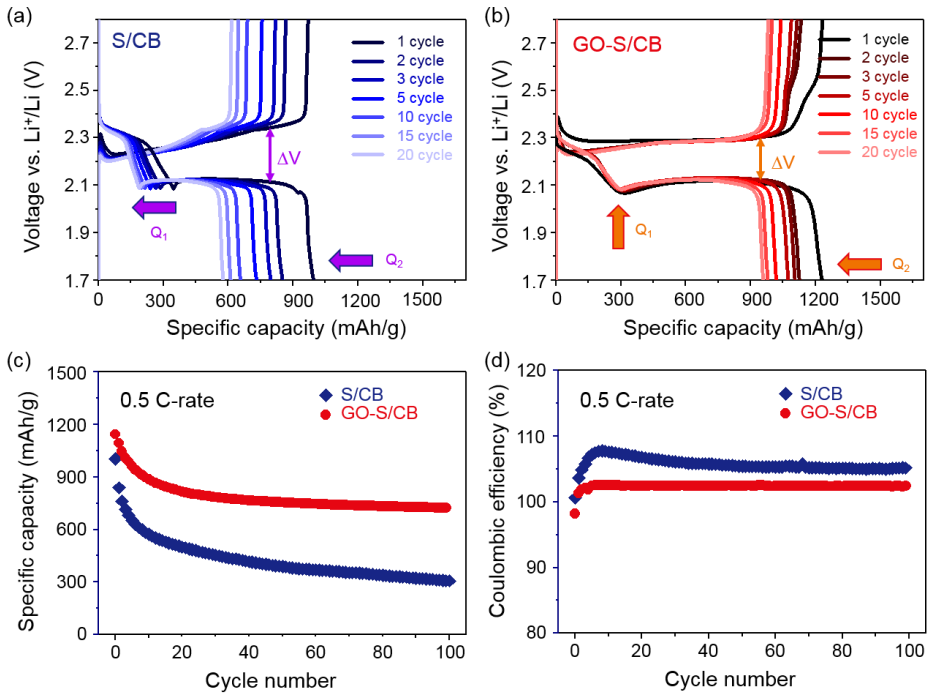

Figure 4. Electrochemical characterization of S/CB and GO-S/CB cathodes. Voltage profiles for (a) S/CB and (b) GO-S/CB plotted from 1st to 20th cycles at 0.5 *C*. (c) Cycling performance and (d) Coulombic efficiency of S/CB and GO-S/CB at 0.5 *C* for 100 cycles.

The overpotential (ΔV) was estimated from the reaction potential of the charge/discharge profile (Figs. 4(a and b)). In Fig. 5, the cyclic voltammetry (CV) results provide a detailed view of the reaction potential including that of the oxidized and reduced polysulfides. To exclude the effect of mass transfer of an ion in the electrolyte, a scan rate of CV at 0.03 mVs^{-1} was converted to the approximately 0.1 *C* rate. Moreover, to facilitate electrochemical analysis, we designated the first and second reactions of the anodic and cathodic scan as O_2 and O_1, and R_1 and R_2, respectively; i.e. solid-state sulfur (S_8) is converted to polysulfide in R_1 region and liquid-state sulfide forms solid-state sulfur in the O_1 area. In the R_2 and O_2 regions, liquid-state sulfide is converted to solid Li_2S, and Li_2S is dissolved in polysulfide, respectively. The R_2 of S/CB and GO-S/CB exhibits similar reaction potential. In contrast, the R_1 reaction of GO-S/CB exhibits a 0.3 V higher potential shift than that of S/CB, indicative of the superior electrical contact between sulfur and the conducting agent. In the anodic scan, however, the O_1 and O_2 peaks of GO-S/CB are shifted toward more negative potentials than those of S/CB. This phenomenon is consistent with the improved electrical contact of GO-S/CB, while the increased hysteresis of charge/discharge of S/CB stems from electrical contact loss. In addition, the higher intensity and sharper peaks of GO-S/CB indicate better reaction kinetics at each step, compared to those of the S/CB.

Rate capability tests were conducted at various *C*-rates (0.1 *C* to 1 *C*), as shown in Fig. 6. The GO-S/CB exhibits superior stability of rate performance in the higher *C*-rate condition, which concurs with the Coulombic efficiency

resulting from the irreversible loss of dissolved polysulfide with increasing current. On the other hand, the Coulombic efficiency of S/CB is significantly influenced by the constant current scale in Fig. 6(b). After a rate of 1 *C*, the Coulombic efficiency is still sharply reduced even after recovery up to 0.1 *C*, which implies that the severe active-material loss at high constant results from an unstable structure. This result also indicates that the accumulated sulfide has a significant influence on the successive cycling performance; i.e., the so-called shuttle phenomena. Thus, our results suggest that GO improves the electrical conductivity and physical stability of the cathode materials during battery operation.

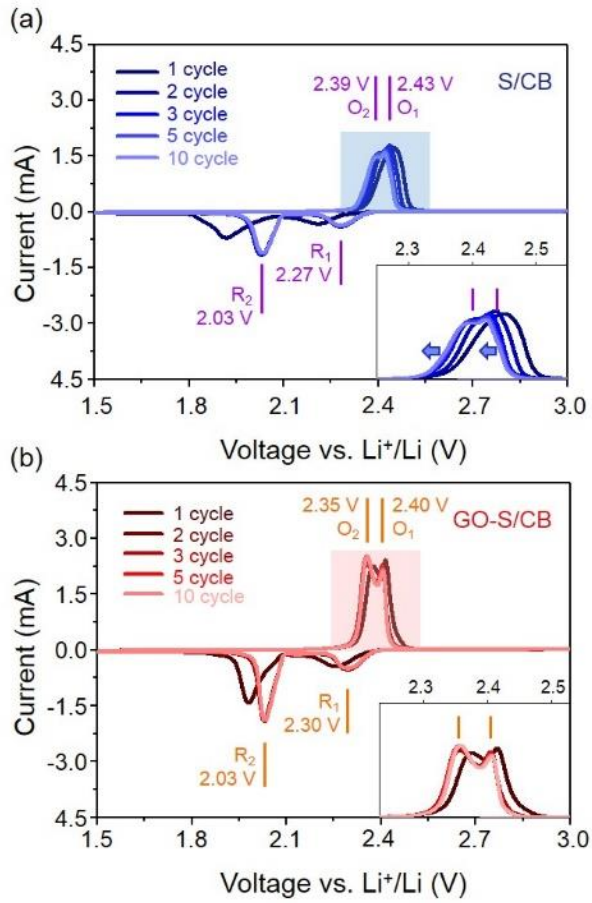

Figure 5. Cyclic Voltammetry peaks of (a) S/CB and (b) GO-S/CB cathodes at 0.03 mVs^{-1} scan rate.

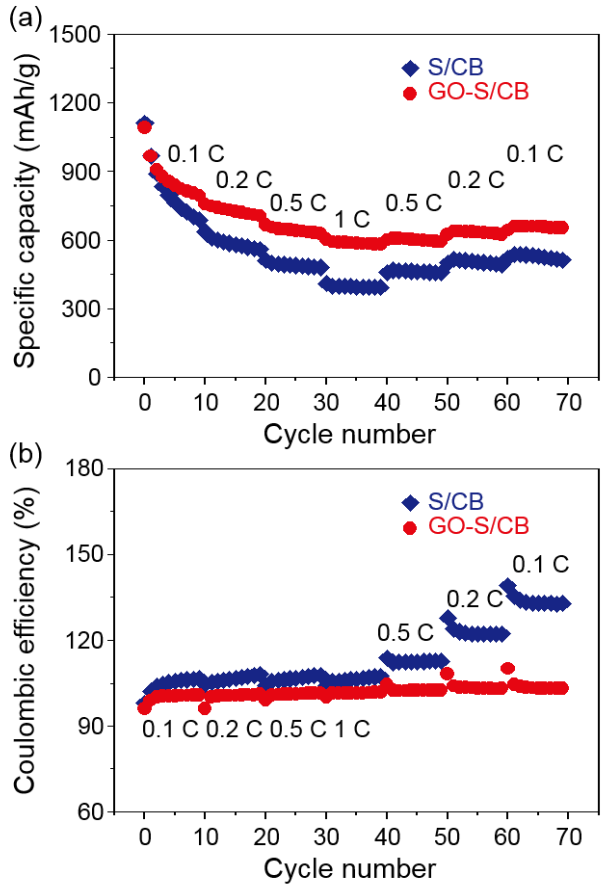

Figure 6. (a) Rate performance and (b) Coulombic efficiency of S/CB and GO-S/CB composites from 0.1 *C* up to 1 *C*.

The electrochemical impedance spectroscopy (EIS) spectra (Fig. 7) represents the structural stability and electrical conductivity of the cathode electrodes before and after battery operation. The Nyquist plots are composed of a semi-circle in the high-frequency region, which is related to contact and charge transfer resistance, and a short inclined line in the low-frequency regions; this line results from ion diffusion in the cathode.[29] In order to measure the precise EIS property of the cathode electrode, a symmetric type cell with lithium metal is positioned in a parallel configuration (grey dots), and the effect of lithium metal on the EIS spectra was determined. Prior to cycling, the semi-circle corresponding to GO-S/CB is smaller than its S/CB counterpart. This indicates that the electrical conductivity of the former is higher than that of the latter. Moreover, after battery operation, the diameters of both semi-circles increase owing to the formation of a passivation layer, increased resistance of the electrolyte, modified surface roughness, and so forth. The semi-circle corresponding to GO-S/CB is, however, still smaller than that of S/CB, which indicates that the GO aid in increasing the conductivity and structural stability during battery operation.

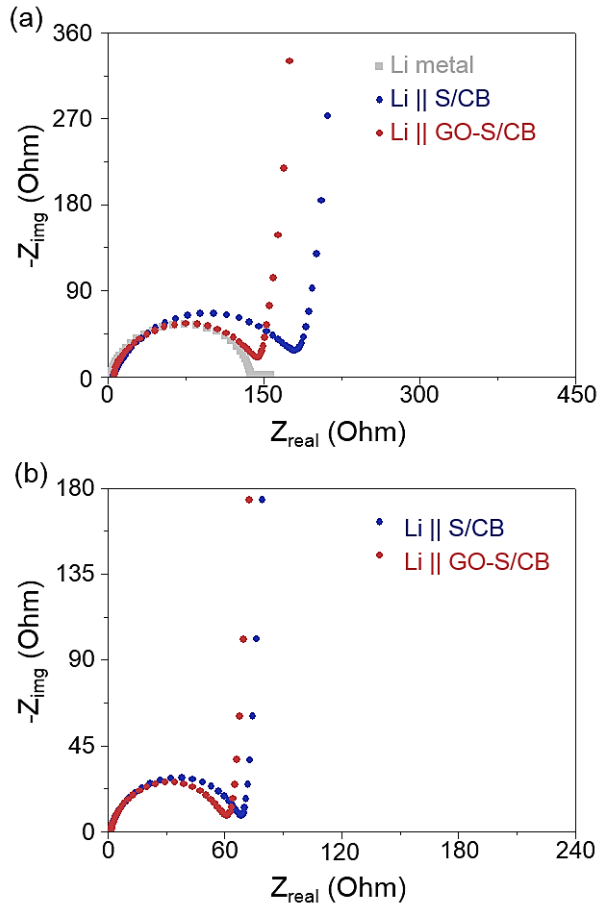

Figure 7. Electrochemical Impedance Spectroscopy (EIS) plots of S/CB and GO-S/CB (a) before and (b) after cycles. The symmetry cell of Li metal is plotted in Fig. (a) grey dots.

Conclusions

In summary, we have synthesized GO-S/CB composites that micron-sized sulfur particles are encapsulated by GO sheets. The structural properties and chemical properties of GO-S/CB composites were characterized by various microscopic and spectroscopic techniques. Various electrochemical analyses were conducted to elucidate the role of GO that has rich oxygen functional groups and its effect on the electrochemical properties. The charge-discharge profiles revealed the significantly enhanced cycling and rate performance of the GO-S/CB electrode, indicating that GO plays a key role in trapping dissolved polysulfide and in improving electronic conductivity. Moreover, the Columbic efficiency of the GO-S/CB electrode prevents capacity fading stemming from the dissolution and precipitation of polysulfide, and also promotes homogeneous electron flows. In addition, EIS spectra indicate that the GO-S/CB electrode has a higher electrical conductivity before/after battery cycling than the S/CB electrode, implying that the structure of the GO-S/CB electrode is maintained during battery operation. Thus, we expect that the incorporation of GOs would make an important step forward to the practical applications of Li-S batteries in the future.

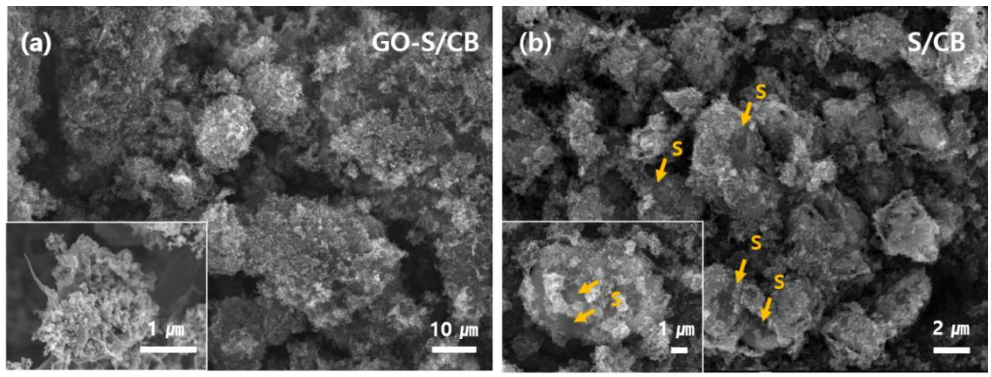

Figure S1. SEM images of (a) GO-S/CB and (b) S/CB composites. The insets show the magnified images of GO-S/CB and S/CB, respectively.

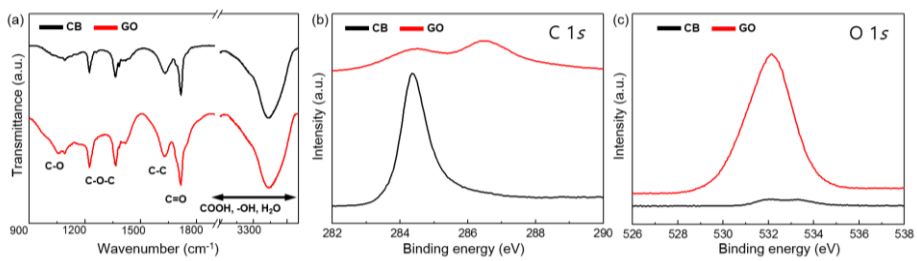

Figure S2. (a) Fourier transform infrared spectroscopy (FTIR) spectra of CB and GO. Strong peaks attributed to the characteristic vibrational mode of oxygen functional groups. X-ray photoelectron spectroscopy of CB and GO. (b) C 1*s* peaks and (c) O 1*s* peaks.

References

1. N. Choi, Z. Chem, S. A. Freunberger, X. Ji, Y.-K. Sun, K. Amine, G. Yushin, L. F. Nazar, J. Cho and P. G. Bruce, *Angew. Chem., Int. Ed.*, 2012, **51**, 9994.

2. Y.-K. Sun, Z. Chen, H.-J. Noh, D.-J. Lee, H.-G. Jung, Y. Ren, S. Wang, C. S. Yoon, S.-T. Myung and K. Amine, *Nat. Mater.*, 2012, **11**, 942.

3. M. Armand and J.-M. Tarascon, *Nature*, 2008, **451**, 652.

4. C. K. Chan, H. Peng, G. Liu, K. McIlwrath, X. F. Zhang, R. A. Huggins and Y. Cui, *Nat. Nanotechnol.*, 2008, **3**, 31.

5. J. Kim, D.-J. Lee, H.-G. Jung, Y.-K. Sun, J. Hassoun and B. Scrosati, *Adv. Funct. Mater.*, 2013, **23**, 1076.

6. J. Wang, J. Yang, C. Wan, K. Du, J. Xie and N. Xu, *Adv. Funct. Mater*. 2003, **13**, 487.

7. W. J. Chung, J. J. Griebel, E. T. Kim, H. Yoon, A. G. Simmonds, H. J. Ji, P. T. Dirlam, R. S. Glass, J. J. Wie, N. A. Nguyen, B. W. Guralnick, J. Park, A. Somogy, P. Theato, M. E. Mackey, Y.-E. Sung, K. Char and J. Pyun, *Nat. Chem.*, 2013, **5**, 518.

8. Y. Yang, G. Zheng and Y. Cui, *Chem. Soc. Rev.*, 2013, **42**, 3018.

9. Y.-S. Su, Y. Fu, T. Cochell and A. Manthiram, *Nat. Commun.*, 2013, **4**, 2985.

10. Y. V. Mikhaylik and J. R. Akridge, *J. Electrochem. Soc.*, 2004, **151**, A1969.

11. R. Elazari, G. Salitra, A. Garsuch, A. Panchenko and D. Aurbach, *Adv. Mater.*, 2011, **23**, 5641.

12. S. S. Zjang and J. A. Read, *J. Power Sources*, 2012, **200**, 77.

13. C. D. Liang, N. J. Dudney and J. Y. Howe, Chem. Mater., 2009, 21, 4724.

14. N. Jayaprakash, J. Shen, S. S. Moganity, A. Corona and L. A. Archer, *Angew. Chem., Int. Ed.*, 2011, **50**, 5904.

15. J. L. Wang, J. Yang, J. Y. Xie, N. X. Xu and Y. Li, *Electrochem. Commun.*, 2002, **4**, 499.

16. G. Zheng, Y. Yang, J. J. Cha, S. S. Hong and Y. Cui, *Nano Lett.*, 2011, **11**, 4462.

17. W. Ahn, K.-B. Kim, K.-N. Jung, K.-H. Shin and C.-S. Jin, *J. Power Sources*, 2012, **202**, 394.

18. H. Wang, Y. Yang, Y. Liang, J. T. Robinson, Y. Li, A. Jackson, Y. Cui and H. Dai, *Nano Lett.*, 2011, **11**, 2644.

19. L. Ji, M. Rao, H. Zheng, L. Zhang, Y. Li, W. Duan, J. Guo, E. J. Cairns and Y. Zhang, *J. Am. Chem. Soc.*, 2011, **133**, 18522.

20. J. Liu, Y. L. Cao, X. L. Li, I. A. Aksay, J. Lemmon, Z. M. Nie and Z. G. Yang, *Phys. Chem. Chem. Phys.*, 2011, **13**, 7660.

21. C. D. Dimitrakopoulos and P. R. L. Malenfant, *Adv. Mater.*, 2002, **14**, 99.

22. W. S. Hummers Jr. and R. E. Offeman, *J. Am. Chem. Soc.*, 1958, **80**, 1339.

23. M. Acik, G. Lee, C. Mattevi, A. Pirkle, R. M. Wallace, M. Chhowalla, K. Cho and Y. Chabal, *J. Phys. Chem. C*, 2011, **115**, 19761.

24. L. G. Cancado, K. Takai, T. Enoki, M. Endo, Y. A. Kim, H. Mizusaki, A. Jorio, L. N. Coelho, R. Magalhäes-Paniago and M. A. Pimenta, *Appl. Phys. Lett.*, 2006, **88**, 163106.

25. J.-T. Yeon, J.-Y. Jang, J.-G. Han, J. Cho, K. T. Lee and N.-S. Choi, J. *Electrochem. Soc.*, 2012, **159**, A1308.

26. Joint Committee in Powder Diffraction Standards (JCPDS), International Center of Diffraction Data, Swarthmore, PA.

27. X. Ji, K. T. Lee and L. F. Nazar, *Nat. Mater.*, 2009, **8**, 500.

28. J. Brückner, S. Thieme, H. T. Grossmann, S. Dörfler, H. Althues and S. Kaskel, *J. Power Sources*, 2014, **268**, 82.

29. Z. Dung, Z. Zhang, Y. Lai, J. Liu, J. Li and Y. Liu, *J. Electrochem. Soc.*, 2013, **160**, A553.

Chapter 7

Graphene Quantum Dots: Induces C-S Bonding Suitable for High Sulphur/Shulphide Utilization

Introduction

Rechargeable lithium ion batteries (LIBs) are widely used for various applications such as portable devices, bio-medical implants, and electric vehicles because of their high energy and power density [1-4]. However, current LIBs based on graphite-transition metal oxide electrode couples have nearly reached a ceiling in their storage capability due to their electrical and crystal structural limitations. Therefore, breakthroughs with new energy storage systems that can surpass current performance barrier of LIBs should be brought about in a timely manner. Recently, systems that can operate by electrochemical transformation of sulphur (S_8) to lithium sulphide (Li_2S) have attracted great attention because elemental lithium and sulphur can be directly utilized as an anode and a cathode, respectively[5]. Sulphur (S_8) generated from petroleum refinement[6] is an ideal choice for a cathode due to its low cost, environmental friendliness, and high theoretical specific capacity (1,675 mAh/g, 16 electron process) when it is fully transformed to Li_2S (refs 6-9). However, three main barriers limit the efficient use of sulphur as a cathode: the deleterious electrochemically induced volume expansion of lithiated from S_8 to Li_2S (~80%), the poor electronic conductivity of S_8 (~1×10^{-30} S/m) and Li_2S (~1×10^{-14} S/m), and the irreversible loss of intermediate LiPSs into the electrolyte[5,10,11]. This loss of LiPSs during cycling is responsible for the poor cycle stability, low sulphur utilization, and polysulphide-shuttle mechanism[5]. To overcome these problems, various carbonaceous materials have been integrated into the sulphur cathode matrix to take advantage of their physical properties to prevent LiPSs dissolution into the electrolyte[12-14], sorption properties[15-17], and high electronic conductivity[18-19]. In

particular, graphene oxide (GO)-sulphur composites have been reported as a new approach to prevent the loss of LiPSs by adsorption and wrapping properties of GO (refs 20-23). However, these systems were found to have poor structural integrity[24] between S and GO, which allows LiPSs to be readily lost by repeated electrochemical cycling. Furthermore, these studies focused on the characteristics of as-prepared GO-S composites, which limits understanding of the role of functional groups during battery operation.

Herein, we introduce nano-sized GQDs (an average particle size of ~4 nm) with oxygen functional groups[25-27] that assemble with sulphur and carbon black (CB) to form a tightly packed structure, which provides fast charge conduction pathways while minimizing the irreversible loss of LiPSs. Oxygen functional groups also serve to preserve dissolved LiPSs by the formation of C-S bonds (the so called sulphiphilic property), as confirmed by density functional theory (DFT) calculations, whereby high sulphur/sulphide utilization is achieved even at high current densities. In order to study the mechanism of the enhanced electrochemical performance, the contribution of dissolution and precipitation to the electrochemical performance was carefully considered.

Experimental

Synthesis of graphene quantum dots.

Carbon fibers were placed into a mixture of H_2SO_4 and HNO_3. The solution was sonicated for 2 h, and then stirred for 24 h. The solution was then refluxed at 90℃ for 48 h with vigorous stirring. The mixture was cooled and diluted with deionized water, and the pH was adjusted to 8 with Na_2CO_3. The final product was dialyzed for 5 days and then filtered. Finally, the GQDs aqueous solution was concentrated.

Synthesis of GQDs-S composites.

1.5 g of $Na_2S_2O_3$ powder (Sigma-Aldrich) was dissolved in 250 ml deionized water, and this solution was stirred with 10 ml hydrochloric acid. The GQDs-S core-shell composites were synthesized by heating up to ~80℃, and then added 10 ml Triton TX-100 (Sigma-Aldrich, average mol wt.% 625) to the solution for 20 min. The prepared GQDs (80 mg in 20 ml D.I. water) solution was added and vigorously stirred in this flask for 20 min. A carbon black suspension (40 mg in 20 ml D.I. water) was then injected into this mixture and was stirred vigorously for 30 minutes. Then, the solution was cooled to room temperature and the collected products were rinsed several times. Finally the GQDs-S/CB composites were dried under vacuum evaporator.

Cell fabrication and electrochemical measurement.

The electrodes were fabricated from slurries that contained 60 wt.% sulphur, 20 wt.% conducting agents and 20 wt.% polyvinylidene fluoride (pvdf) binder dispersed in N-methyl-2-pyrrolidone (2 ml). The prepared slurry was cast onto an aluminum foil using a doctor blade method. The prepared electrodes were transferred to an Ar-filled

glove box and were assembled in a 2032 type coin cell. The mass loading of all samples was ~1 mg of active material. The electrolyte was 1.0 M LiTFSI (lithium bis-trifluoromethanesulfonimide) and 0.1 M $LiNO_3$ (lithium nitrate) with DOL (dioxolane) and DME (dimethyl ether) 1:1 volume ratio (Panax Etec, Korea). The separator was supplied from SK Innovation Corporation (Korea), and lithium metal was used as a counter electrode. Electrochemical properties were measured with a WBCS3000 cycler (Won-A Tech, Korea). The voltage window for electrochemical measurements was fixed between 1.7 – 2.8 V vs. Li^+/Li (all the voltages below are vs. Li^+/Li). The Carbon or GQDs electrodes were fabricated similarly to the aforementioned procedures from slurries that contained 80 wt.% contents of carbon (carbon-only, and carbon black:GQDs=1:1) and 20 wt.% polyvinylidene fluoride (pvdf) binder dispersed in N-methyl-2-pyrrolidone (2 ml). Li_2S_8 catholyte was prepared by using Li_2S and S_8 powders which were inserted into the same electrolyte condition according to the stoichiometric ratio. In order to analyze the cycled electrodes the coin cells were opened in an Ar-filled glove box. All the samples were analyzed after rinsing with copious amounts of DOL/DME.

Characterization.

XRD was performed on a (Rigaku, D-MAX2500-PC) operating with Cu Ka radiation (λ=1.5406 Å) at 40 kV and 200 mA. TEM was performed on a (JEOL JEM-2100F). XPS was performed on a AXIS Ultra DLD (Kratos.Inc) using a 150 W monochromatic Al K (1486.6 eV) source at the Korea Basic Science Institute (KBSI). High resolution data was collected using a pass energy of 40 eV and 0.05 eV step. Raman spectra was obtained with a Renishaw micro-Taman spectroscope with an

excitation wavelength of 514.5 nm. The spot diameter was approximately 2 μm.

Computational methods.

We carried out density functional theory (DFT) calculations for optimizing structures and analyzing frequencies. Conventional B3LYP exchange-correlation functional[39] was used for the DFT calculations. B3LYP is a hybrid-GGA exchange-correlation functional, which means size-consistency problem can't be considered. To more precisely describe the anion systems, we used a 6-31++G(d) basis set which added diffuse functions to all atoms. All structures in this paper are optimized which is confirmed by frequency analysis. GAUSSIAN 09 package[40] is used for all calculations.

Results and Discussion

To study the physical/chemical properties of GQDs, various microscopic and spectroscopic analytical tools were employed. High resolution transmission electron microscope (HRTEM) images were collected to study the morphology of the GQDs (Figs. 1a and 1b). The GQDs are highly crystalline and show an average size of 4.11 (±0.55) nm (the inset of Fig. 1b). Oxygen-rich functional groups on the edge of the GQDs where non-bonding carbons exist were identified by Fourier-transform infra-red (FTIR) spectroscopy (Fig. 1c). Strong peaks attributed to the characteristic vibrational modes of oxygen functional groups (–OH at 3,434 cm^{-1}, C=O at 1,725 cm^{-1}, C-O in 1,024-1,180 cm^{-1}, and C-O-C at 1,200 cm^{-1}) can be observed in GQDs, while the peak at 1,629 cm^{-1} results from sp^2-hybridized C=C (in-plane stretching)[28]. These oxygen-functional groups of GQDs can strongly bond to sulphur *via* electrostatic interaction.

The GQDs-S composites were prepared by GQDs and S that is chemically reduced from $Na_2S_2O_3$. It should be noted that surface of sulphur was mediated by a surfactant (see the details in the Method section). The scanning electron microscopy (SEM) and TEM images in Figs. 1d and 1e show the morphology of the GQDs-S. Several micron-sized sulphur particles are homogeneously coated with GQDs. The uniform distribution of GQDs on the sulphur surface is confirmed by energy dispersive X-ray spectroscopy (EDX) mapping of C, O, and S (Fig. S1). The graphitic characteristic of GQDs-S was established by Raman spectroscopy (Fig. 1f), where the peaks for carbon (D and G at 1,350 and 1,590 cm^{-1}, ref. 29) and sulphur (the four characteristic peaks below 600 cm^{-1})[30] can be clearly resolved.

The GQDs-S/carbon black (CB, average particle size of ~50 nm) composite structures were prepared from GQDs-S and CB *via* van der Waals interaction[20]. Experimental details can be found in the Methods section. The SEM image of GQDs-S/CB, Fig. 1g, presents that CBs are tightly bound to the GQDs-S composites. Scanning transmission electron microscopy (STEM)-EDX was used to determine the compositional distribution of C, O, and S in the GQDs-S/CB composite and shows that C, O, and S is homogeneously distributed throughout the composite structure (Fig. S2). X-ray diffraction (XRD) analysis of the GQDs-S/CB composite structures reveals high S crystallinity and phase purity (Fig. S3a) and the composition of GQDs-S/CB was estimated by thermogravimetric analysis (TGA) (Fig. S3b) to be 70 : 20 : 10 (wt.%) in S : CB : GQD. X-ray photoelectron spectroscopy (XPS), Fig. S4, analyzed the surface of the GQDs-S/CB composite and the results of the quantitative analysis are displayed in Table S1. The XPS results indicate higher intensity of C=O (286.7 eV in C 1*s* and 530.9 eV in O 1*s*) and C-OH (533 eV in O 1*s*) for GQDs-S/CB compared to S/CB due to the surfactant and oxygen functional group of the GQDs[31]. Meanwhile negligible S 2*p* signal was detected since the GQDs-S are covered with CB in the GQDs-S/CB structure (see S 2*p* in GQDs-S/CB *vs*. S/CB). The schematic illustration in Figs. 1h and 1i, shows the GQDs distributed on a sulphur particle, which can strongly bond to CB, leading to a densely coated GQDs-S/CB composite structure.

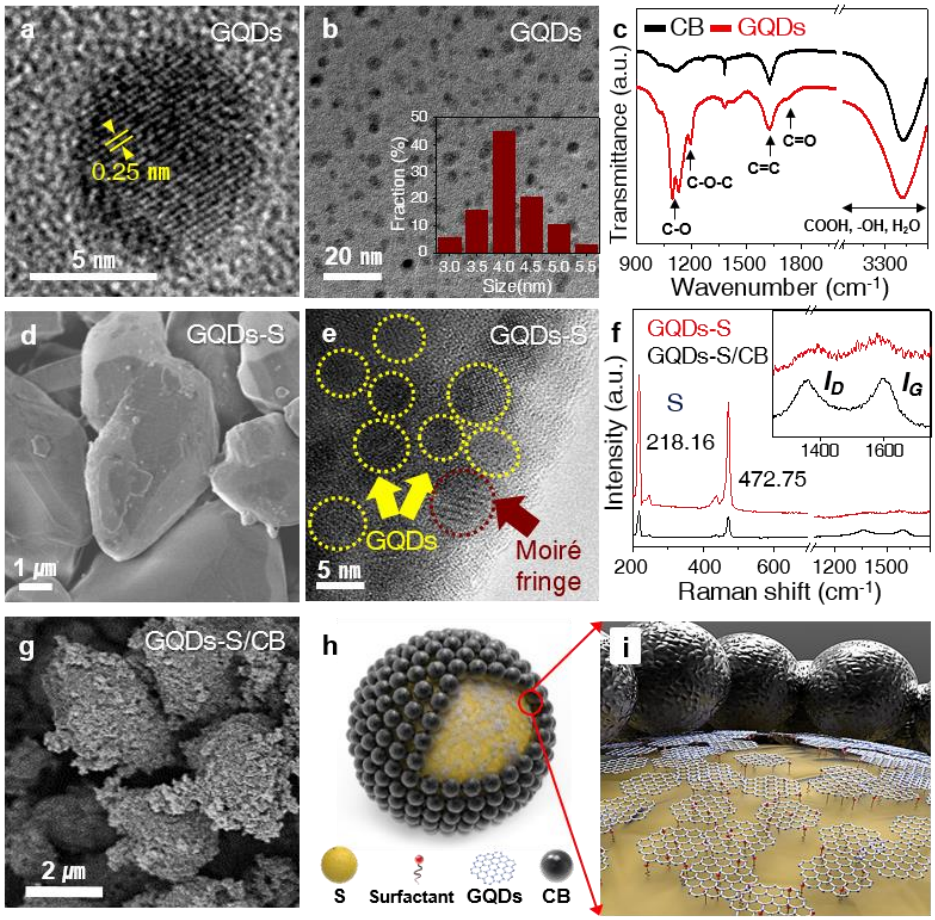

Figure 1. Material characterization of GQDs-S/CB and S/CB composites. a,b, High-resolution TEM images of GQDs. The inset in Fig. 2b shows a histogram of the GQDs size distribution. c, FT-IR spectra of GQDs and CB. The peaks in this figure correspond to the various functional groups in the GQDs and CB. SEM images of d, GQDs-S, and g, GQDs-S/CB. e, HRTEM images of the GQDs-S composites and GQD pattern (yellow circle). A Moiré pattern (red circle) is clearly visible in these TEM images, which is created by a superposition of the GQDs and S crystalline lattices, and f, Raman spectrum of GQDs-S composites, which shows that the GQDs are formed on the sulphur particles. The strong peaks at 218.16 and 472.75 cm^{-1} arise from sulphur, and the D (disorder) and G (graphitic) peaks arise from the GQDs. Schematic diagrams show the structure, h, and the magnified structure, i, of GQDs-S/CB.

The schematic illustration in Fig. 2a depicts a conventional Li-S battery, where the anode is made of a metallic lithium, and the cathode is a composite of sulphur and CB. The structure of the cathode has a large impact on the irreversible loss of LiPSs into the electrolyte during battery operation. Herein, GQDs are introduced at the S/CB cathode, as shown in Fig. 2b. The GQDs contain both hydrophobic aromatic and hydrophilic defect regions, which can interact with CBs (ref. 20) and S_8, respectively. Scanning electron microscopy (SEM) images (Figs. 2c and 2d) confirm that the GQDs-S/CB composite electrodes are densely packed with CBs, which should increase electrochemical performance by highly preserving LiPSs in the geometric structure of GQDs-S/CB, while the surface of the sulphur particles are partially exposed in S/CB electrode. The exposure of S_8 to the electrolyte leads to the severe loss of electrochemically generated LiPSs followed by the degradation of the electrochemical performance.

The discharge profile in Fig. 3a illustrates a schematic model of possible reaction pathways that occur in a conventional Li-S battery. In the upper plateau region, elemental sulphur (S_8) is gradually reduced to the soluble sulphide anion (S_8^{2-}). Then, continuous reduction leads to the conversion of dissolved S_8^{2-} to S_n^{2-} (n = 6, 4) [32]. Since these high-order LiPSs (HO-LiPSs, (S_n^{2-}, n=8-4)) reactions are generated in the liquid electrolyte, the loss of active materials can occur simultaneously with this electrochemical reaction. The summation of the upper plateau and slope regions can be defined as the dissolution regime. Once the composition of S_4^{2-} is reached, low-order LiPSs (LO-LiPSs, (S_n^{2-}, n=2-1)) are converted to Li_2S through the reduction of S_4^{2-} (lower plateau region, defined as

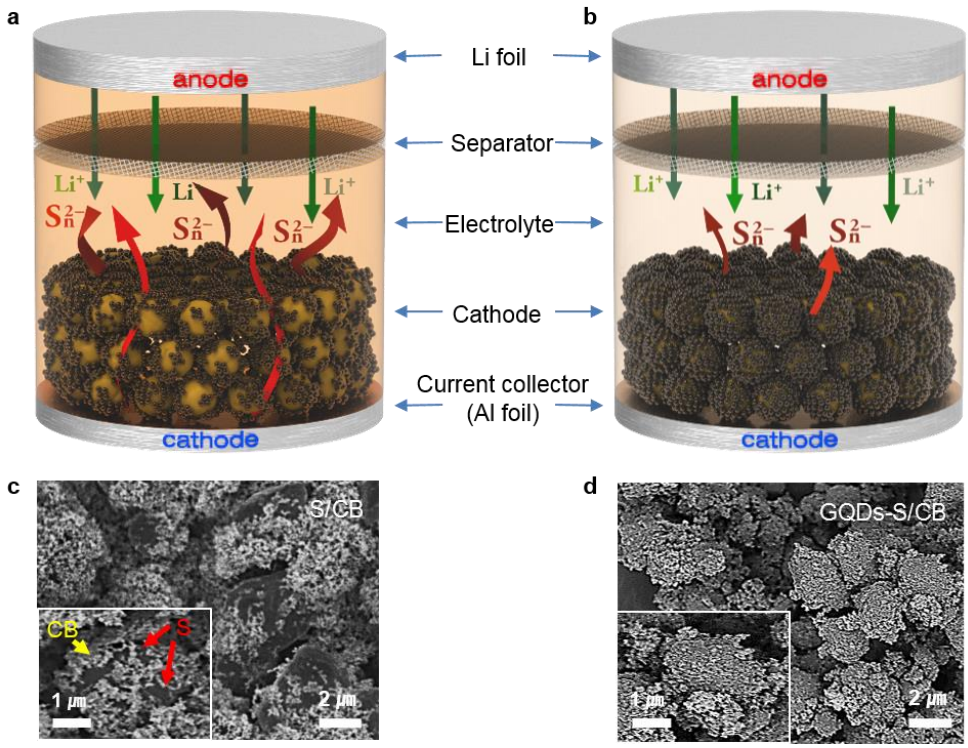

Figure 2. Schematic diagrams and SEM images of S/CB and GQDs-S/CB in a Li-S battery. a,b, Schematic configuration of S/CB and GQDs-S/CB employed as a cathode in a Li-S battery. The sulphur (yellow) is wrapped with carbon black (S/CB) and compactly covered with graphene quantum dots and carbon black (GQDs-S/CB), respectively. Polysulphides were dissolved into solvent and the color changed to orange. c,d, SEM images of GQDs-S/CB and S/CB.

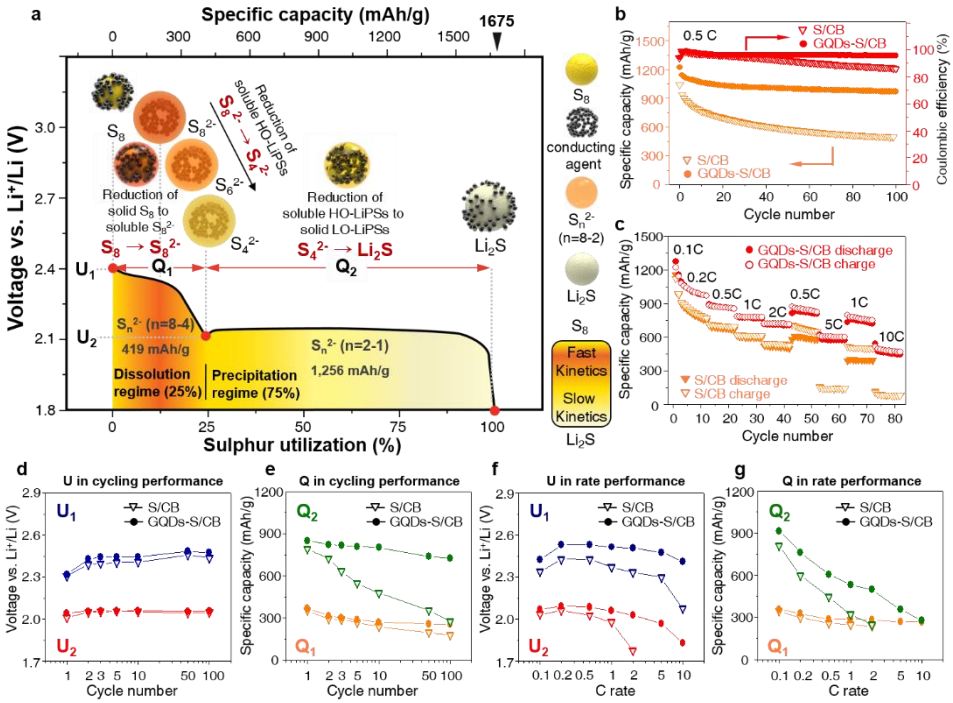

Figure 3. Electrochemical properties of S/CB and GQDs-S/CB electrodes. a, Schematic illustration of the discharge profile of a conventional Li-S battery. High order-polysulphides (S_n^{2-}, n=8-4) and low order-polysulphides (S_n^{2-}, n=2-1) are inscribed the HO-PSs and LO-PSs as abbreviation. The onset potential (*U*) and the capacity (*Q*) in the dissolution and precipitation regime are noted, which facilitates the analysis of the electrochemical properties of each sample. b, Rate performance of the GQDs-S/CB and S/CB at 0.1 *C* to 10 *C*. c, cycling performance and Coulombic efficiency at 0.5 *C* of both samples for 100 cycles. d,f, Onset potential as a function of cycle number and e,g, capacity as a function of rate and capacity as a function of cycle number.

precipitation regime). Finally, Li_2S results from the complete reduction of S_8, which induces ~80% (compared to S_8) theoretical volume expansion. Representative points U_1, U_2, Q_1, and Q_2 are marked in the profile, where U_1 and U_2 indicate the onset reaction potentials of the dissolved and precipitated species, respectively, while Q_1 and Q_2 are the capacities corresponding to dissolution and precipitation regime, respectively. Q_1 is 419 mAh/g estimated from the reaction, S_8 (*s*) + $4Li^+ + 4e^- \leftrightarrow 2Li_2S_4$ (*l*). Meanwhile, Q_2 is 1,256 mAh/g which is achieved by the reduction of higher order to lower order polysulphides, $2Li_2S_4$ (*l*) + $12Li^+ \leftrightarrow 8Li_2S$ (*s*). Four parameters (U_1, U_2, Q_1, and Q_2) and the Q_2/Q_1 ratio (= 3) will be evaluated to understand the battery performance[32].

The cycling performance was tested at 0.5 *C*-rate (1 *C* = 1,675 mA/g assuming the reaction, $S_8 + 16Li^+ + 16e^- \leftrightarrow 8Li_2S$) in Fig. 3b. GQDs-S/CB composites exhibit superior cyclability and Coulombic efficiency compared to S/CB. A discharge capacity of ~1,000 mAh/g was achieved after 100 cycles while S/CB showed only 459.57 mAh/g. The capacity *vs*. voltage profiles at selected cycles are presented in Fig. S6. The electrochemical properties of modified sulphur (surfactant coated sulphur) covered with CBs were also measured to study the effect of the surfactant on the electrochemical performance (Fig. S5). Modified S/CB exhibits lower initial capacity but slightly better retention than S/CB because the surfactant on the surface of S partially protect the loss of HO-LiPSs (refs 15,20). Figure 3c presents the rate capabilities of GQDs-S/CB and S/CB from 0.1 *C* to 10 *C* (see Fig. S7 for the capacity *vs*. voltage profiles at the different rate steps). The GQDs-S/CB shows excellent rate properties in comparison with S/CB. In Fig. S8, a capacity of 540.17 mAh/g at 10 *C*

was achieved (42% *vs*. capacity at *C*/10) in GQDs-S/CB. In contrast, only 120.35 mAh/g was achieved at 10 *C* (10% *vs*. that at *C*/10) in S/CB.

The onset potentials (U_1 and U_2) and capacities (Q_1 and Q_2) of GQDs-S/CB and S/CB are presented in Figs. 3d-3g, which were derived from the capacity *vs*. voltage profiles (Figs. S6 and S7). These values are tabulated in Tables S2-5. Firstly, these parameters are studied to analyse the electrochemical differences between GQDs-S/CB and S/CB. In the first cycle, U_1 of GQDs-S/CB is 2.33 V, which is slightly higher than that of S/CB, 2.31 V, owing to the lowered interface resistance. The better carbon coverage in GQDs-S/CB leads to faster electron transfer kinetics (Fig. 3d). Electrochemical impedance spectroscopy (EIS) quantified the interfacial resistance, as shown in Fig. S9. The radius of the smaller sized semi-circle (100 kHz – 1 Hz) is proportional to summation of the initial resistance and the charge transfer resistance (R_{int} + R_{ct}) based on the equivalent circuit in Fig S9a (ref. 33). The U_2 value is also slightly higher in GQDs-S/CB, which indicates that HO-LiPSs are easily reduced to LO-LiPSs. After the first cycle, a slight increase of U_1 and U_2 was observed for both samples due to the decrease in overpotential resulting from the rearrangement of micron-sized sulphur[33]. U_1 and U_2 of both GQDs-S/CB and S/CB follow the same trend during 100 cycles which confirms that there is no significant change of onset potential after the first cycle.

In contrast, Q_1 and Q_2 show quite different behaviour as shown in Fig. 3e. For the first cycle, higher Q_1 and Q_2 are observed in GQDs-S/CB (Q_1 = 370.9 mAh/g and Q_2 = 853.24 mAh/g) compared to the S/CB (Q_1 = 354.86 mAh/g and Q_2 = 793.35 mAh/g) due to the enhanced electrical contact by the densely packed sulphur-carbon

structure. However, the Q_2/Q_1 ratios are low in both GQDs-S/CB (Q_2/Q_1 = 2.30) and S/CB (Q_2/Q_1 = 2.24). Such low Q_2/Q_1 ratio for the first cycle can be attributed to the irreversible initial loss of HO-LiPSs, inefficient precipitation of LO-LiPSs, and electrolyte decomposition was followed by formation of solid electrolyte interphase (SEI). Q_1 and Q_2 values gradually decrease with extended cycling in S/CB. While the Q_1 values show relatively slow decay, severe fading of Q_2 is observed, which indicates the precipitation reaction is highly impeded by the loss of active sites. Whereas, the Q_1 and Q_2 values are maintained for GQDs-S/CB even after 100 cycles through minimized loss of active species and preservation of active sites for facile reactions. The Q_2/Q_1 ratios in GQDs-S/CB are found to be 2.94 and 2.81, at the 10th cycle and the 100th cycle, respectively, which are close to the theoretical value (=3), while Q_2/Q_1 ratios of S/CB are 1.96 and 1.55, at the 10th and 100th cycle, respectively. Such high Q_2/Q_1 ratios strongly support that the redox reaction between S_8 and Li_2S can occur very reversibly owing to highly efficient electrode structure driven by GQDs. The GQDs can aid in capturing the PSs during the electrochemical reaction, which will be discussed in detail later. In addition, the EIS study, Fig. S9 b,c, and associated discussion to support PSs capture by GQDs can be found in supplemental section.

The U_1 and U_2 values are also derived from the rate capability tests as shown in Fig. 3f. The GQDs-S/CB electrode shows slightly higher U_1 and U_2 values than S/CB at a relatively low rate (< 0.2 *C*). However, the U_1 and U_2 values of the S/CB electrodes significantly decrease at a rate above the 0.5 *C* rate while the U_1 and U_2 values of the GQDs-S/CB electrodes remain more stable. The higher U_1 and U_2 in

GQDs-S/CB confirm that the GQDs increase the electrical conductivity of the material, whereby overpotentials that are required to initiate the dissolution (U_1) and precipitation (U_2) reactions are decreased. It should be noted that the tendency of U_1 and U_2 are similar because these values are related to the electrical contact of S_8 and HO-LiPSs, respectively. On the contrary, different behaviours are observed in Q_1 and Q_2, particularly, under the higher current density as shown in Fig. 3g. The reaction kinetics for formation of HO-LiPSs is fast; thus, Q_1 is less affected by high current density[34]. However, a significant decrease is revealed in Q_2 at higher current density, which is attributed to the slow reduction due to the low electrical conductivity of LO-LiPSs or limited reaction sites. The Q_2/Q_1 ratios in S/CB are 2.36 and 1.27, at 0.1 *C* and 2 *C* rate, respectively, while higher Q_2/Q_1 ratios, 2.55 (at 0.1 *C*) and 1.75 (at 2 *C*), can be achieved in GQDs-S/CB. The larger Q_2/Q_1 ratio in GQDs-S/CB indicate superior capacity retention is available through the facile charge transfer and preserved reaction sites, which leads to faster reaction kinetics of LO-LiPSs (higher Q_2) as well as lower overpotential (higher U_1 and U_2).

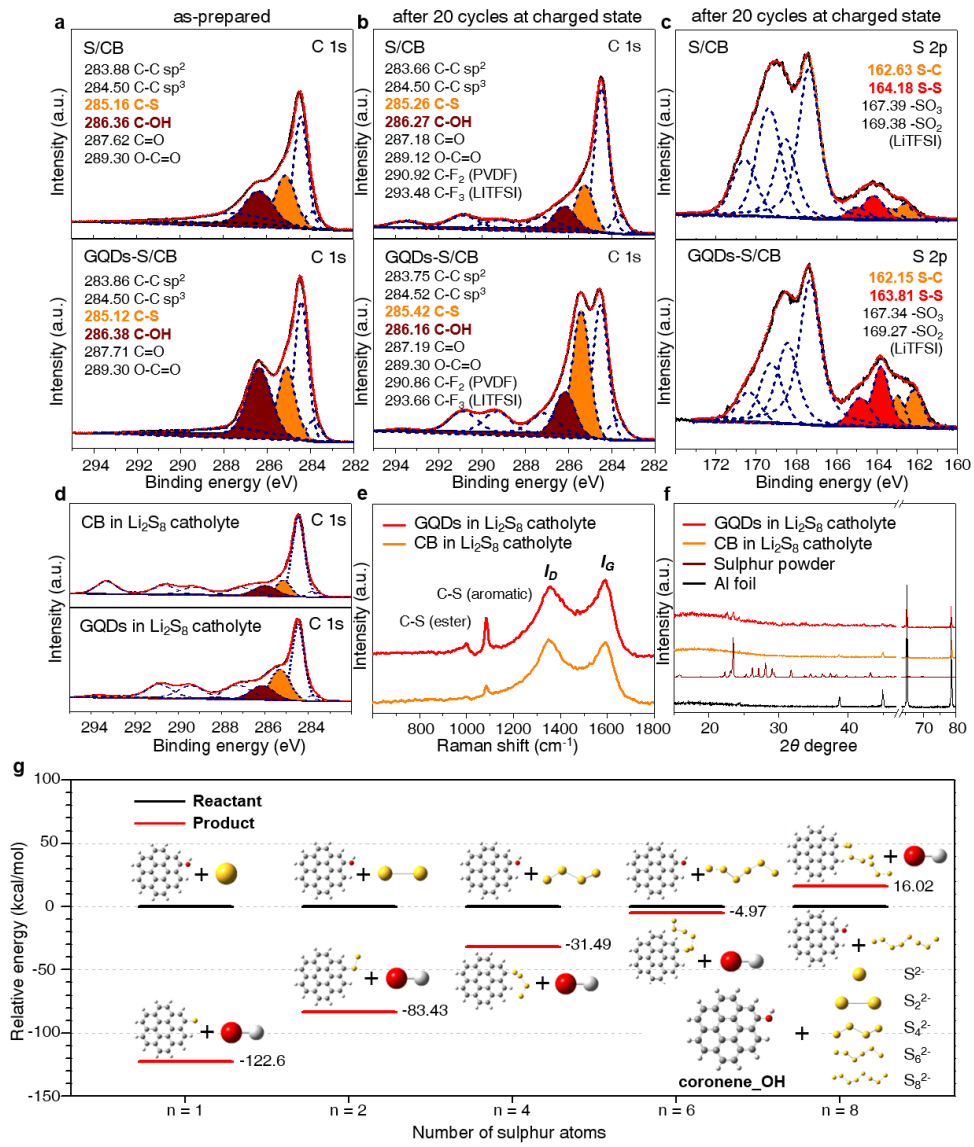

Figure 4. High resolution C 1*s* X-ray photoemission spectroscopy (XPS) and computational calculations a, S and GQDs-S composites before cycling. b, C 1*s* and c, S 2*p* high resolution spectra of the S/CB and GQDs-S/CB electrodes after 20 cycles. Each spectrum was fitted with functions corresponding to different valencies of carbon and sulphur (dashed line) and the sum of those fitted curves (red line) is consistent with the raw data (black solid line). d, C 1*s* spectra of CB and GQDs/CB electrodes in Li_2S_8 catholyte. e, Raman spectra showing C-S bond formation within

the samples. f, XRD spectra of GQDs/CB and CB electrodes in in a Li_2S_8 catholyte. g, A plot of the relative energies for the reactant and product in binding of polysulphides to GQDs, versus the sulphur chain length. The functional groups on GQDs enhance the binding of polysulphides to the carbon due to the substitution of -OH (C-OH) to Sn^{2-}. Yellow, red, white, and gray represents S, O, H, and C atoms, respectively.

The chemical bonding states of S/CB and GQDs-S/CB electrodes were characterized by XPS (Fig. 4a-c). The C 1*s* spectra of the as-prepared electrodes (Fig. 4a) exhibit peaks at 283.8 eV and 284.5 eV attributed to sp^2 and sp^3 hybridized carbons[35], respectively, while the peak at 285.3 eV corresponds to C-S bonding[36]. The peak at 286.2 eV is assigned to C-OH bonding, which is more intense in the GQDs-S/CB than S/CB because the GQDs have a high density of OH surface functional groups. The two peaks that correspond to carbonyl and carboxyl groups are located at 287.0 eV and 289.0 eV, respectively. The C 1*s* spectra of the S/CB electrode obtained from the charged and discharged stages, after the 20th cycle (Figs. 4b and S10), shows negligible intensity loss for the C-OH (286.27 eV) and C-S (285.26 eV) peaks. However, for the GQDs-S/CB electrode, the hydroxyl peak (286.2 eV) decreases noticeably while a C-S peak (285.4 eV) becomes prominent in the charged state. The change in the bonding nature indicates that hydroxyl groups in the GQDs can facilitate the formation of C-S bonds during cycling. These C-S bonds can provide the reaction sites to fully reduce HO-LiPSs to LO-LiPSs, thus the Q_2/Q_1 ratio is stable at ~2.9 even after 100 cycles as shown in Fig. S8. The C-F_2 peak at ~291.0 eV and C-F_3 peak at ~293.0 eV are originated from the binder (polyvinylidene fluoride, PVDF) and electrolyte salt (lithium bis(trifluoromethane)-sulfonimide , LiTFSI), respectively[37].

The S 2*p* spectra in Fig. 4c, collected after 20 cycles, also support the formation of C-S bonding discussed above. The C-S bonding peak (162.63 eV) in S 2*p* is assigned to a lower binding energy than the S-S (164.0 eV) bonding[26], which has correlated with C-S bonding in C 1*s* peak. The intensity in the GQDs-S/CB electrode

is higher than that in the S/CB. The S-S bonding peaks at ~164.0 eV are ascribed to the crystalline sulphur in the electrode[31]. The higher S-S peak intensity of GQDs-S/CB compared to S/CB indicates that more elemental sulphur is formed by adsorption of sulphur onto the GQDs. The adsorption processes prevents irreversible loss of the active material into the electrolyte by formation of nano-sized sulphur that is chemically favorable to bond to the GQDs as discussed later. The peaks at 167.0 eV and around 170.0 eV are attributed to sulphate, SO_2, from LiTFSI (ref. 37) and oxidized polysulphide species, SO_3, respectively.

The SEM images, Fig. S11 and S12, of both anodes and cathodes after 20 cycles, respectively, were taken of GQDs-S/CB and S/CB electrodes. Due to the thick SEI layer formation, the SEM images of the cathodes, Fig. S11, show flattened morphologies. Interestingly, homogenous surfaces can be observed in GQDs-S/CB, while, segregation of carbon is observed in the CB/S electrode. . This morphological difference is driven by the tightly packed structure of GQDs-S/CB during battery operation. A clean surface is observed on the GQDs-S/CB anode while the CB/S anode exhibits S and Li_2S particles on the surface (as confirmed by EDX and Raman spectroscopy as shown in Fig. S12). These sulphur and LiPSs deposits result from the loss of active materials from the cathode side during repeated cycling.

To further investigate the intrinsic surface interaction at the interface between GQDs and CB, GQDs/CB and CB electrodes without sulphur were prepared and electrochemically cycled in Li_2S_8 catholyte (Fig. 4d). The cycle retention of GQDs/CB is over 90% during 100 cycles while CB exhibits a capacity retention below 80% (Fig. S13c). After cycling the GQDs/CB electrode, the C 1*s* and S 2*p*

XPS spectra (Figs. 4d and S13a,b) show higher S-S and C-S peaks compared with CB. Furthermore, Raman peaks for C-S aromatic bonding at 1,086 cm^{-1} and for C-S esteric bonds at 997 cm^{-1} are more intense for the GQDs/CB electrodes[38]. The carbon peaks at 1,590 cm^{-1} and 1,350 cm^{-1} are assigned to the G and D bands of carbon, respectively (Fig. 4e). XRD of the GQDs/CB electrodes also confirms nano-sized crystalline sulphur (Fig. 4f), which strongly supports that PSs are adsorbed on the oxygen functional groups of GQDs. DFT calculations were performed to clarify the formation of C-S bonding between the GQDs and sulphur species. The calculation is based on the following reaction:

$$\text{coronene\_OH} + S_n^{2-} \rightarrow (\text{coronene\_}S_n)^- + OH^- \qquad (n=1, 2, 4, 6, 8)$$

This model is used to represent the terminal edges of the GQDs (ref. 39), with one of the edges replaced by a hydroxyl group, "coronene_OH." A coronene is a polycyclic aromatic hydrocarbon comprising six peri-fused benzene rings with the chemical formula of $C_{24}H_{12}$. The relative energies calculated by DFT for the reactants and products indicate that replacing the terminal hydroxyl group by a sulphur dianion results in a lower energy state. The relative energies are shown in Fig. 4g, where it is clear that the energies of the product decrease when sulphur dianions are replaced with the terminal hydroxyl group. The lower energy of the products (S_n^{2-}, n = 1, 2, 4, and 6) can provide a driving force for the reaction, thereby the formation of C-S bonds are favourable. However, the small sulphur dianions normally exist in the form of a solid crystal combined with lithium cations, such as Li_2S that cannot easily participate in C-S bonding[5]. In addition, sulphur dianions

become unstable as the sulphur chain length is shortened due to the Coulombic repulsion. Meanwhile, large sulphur dianion chains (n>6) tend to disassemble into smaller chains[40]. Thus, it is speculated that the major participants in the reaction are S_2^{2-}, S_4^{2-} and S_6^{2-} ions. In addition, the same DFT calculation was performed for carboxyl group terminated coronene (coronene_COOH) (Fig. S14), showing similar results toacoronene_OH group. Our results highlight the crucial role in the formation of C-S bonds through terminal oxygen-functional groups present on the edge of GQDs.

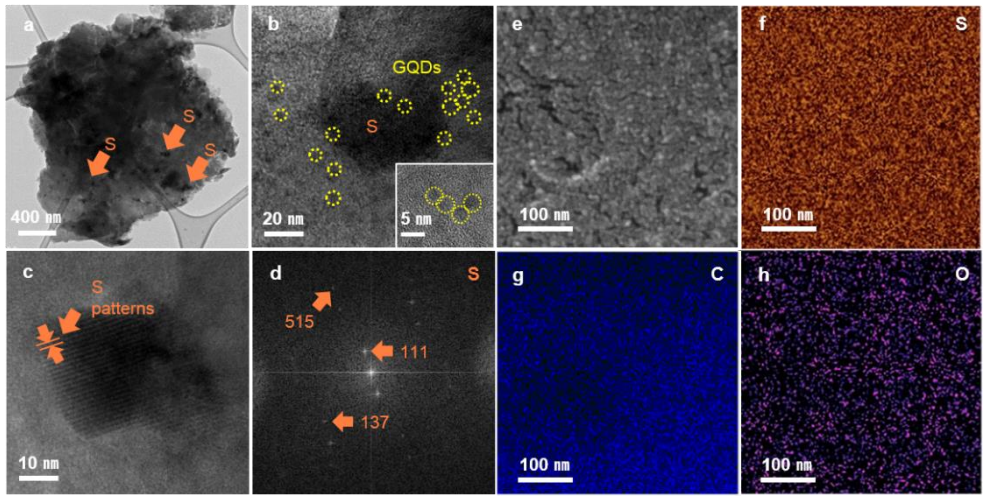

Figure 5. TEM and SEM images of nano-sized sulphur on GQDs electrode in Li_2S_8 catholyte after 20 cycles. a,TEM image of nano-sized sulphur in GQDs materials. The aggregate seen in the TEM is mainly comprised of GQDs, and sulphur is identified as the small darker particles. b, GQDs (yellow circle) covered on nano-sized sulphur particles, c, HRTEM image that shows the lattice fringes of the nano-sized sulphur and GQDs. d, The FFT image of the HRTEM image in c. The two bright spots represent Bragg spots for the sulphur particles, and the other spots are GQDs Bragg spots. e, SEM image of the GQDs electrode in the catholyte after cycling. f-h, C, S, and O energy-dispersive X-ray (EDX) spectroscopy maps of the GQDs electrode.

TEM images were obtained from the GQDs/CB and CB electrodes after 20 (dis)charge cycles in Li_2S_8 catholyte. While only a small number of sulphur particles were observed on the CB electrode (Fig. S15), many nano-sized sulphur particles can be observed on the GQD electrode in Figs. 5a-d. Nano-sized sulphur particles were covered with GQDs, which was confirmed by their lattice fringes corresponding to (111) planes. In addition, the indices of bright spots on the fast Fourier transform (FFT) image indicate sulphur is single crystalline and crystallizes in the orthorhombic structure of the alpha phase (JCPDS, No. 08-0247)[41]. The broad ring patterns in the FFT image indicate the presence of multiple GQDs with different orientations in Fig. S16. The SEM-EDX analysis of the GQDs also indicates that nano-sized sulphur particles are adsorbed onto the GQDs (Figs. 5e-h). On the other hand, the CB electrode contains a low sulphur density (Fig. S15.) This observation implies that the oxygen functional groups in the GQDs induce preferred nucleation of sulphur onto the GQDs. Thus, sulphur can easily be adsorbed/desorbed on the GQDs as predicted by the aforementioned DFT calculation.

Conclusion

In summary, we have designed GQDs-S/CB composites as a high-performance cathode material for Li-S batteries. The nano-sized GQDs induce a tightly packed structure *via* charge interaction with S and CB, which results in enhanced conductivity by shortened electron conduction paths. Furthermore, C-S bonding is generated *in-situ* during the operation of the battery, which originates from the high functional-edge density of the GQDs. Thus, loss of active materials into the electrolyte is minimized. The adsorption of nano-sized sulphur particles onto the GQD interfaces by C-S bonding was confirmed by TEM, and further supported by XPS and Raman analysis and DFT calculations. The GQDs-S/CB composites significantly improve cycling and rate performances, with high reversible capacities at both high and low current density. This excellent cycling behavior was demonstrated through the analysis of discharge profiles. We believe that our results provide a new avenue for material scientists to tailor oxygen-rich functional groups of nano-sized carbon for the application in various batteries.

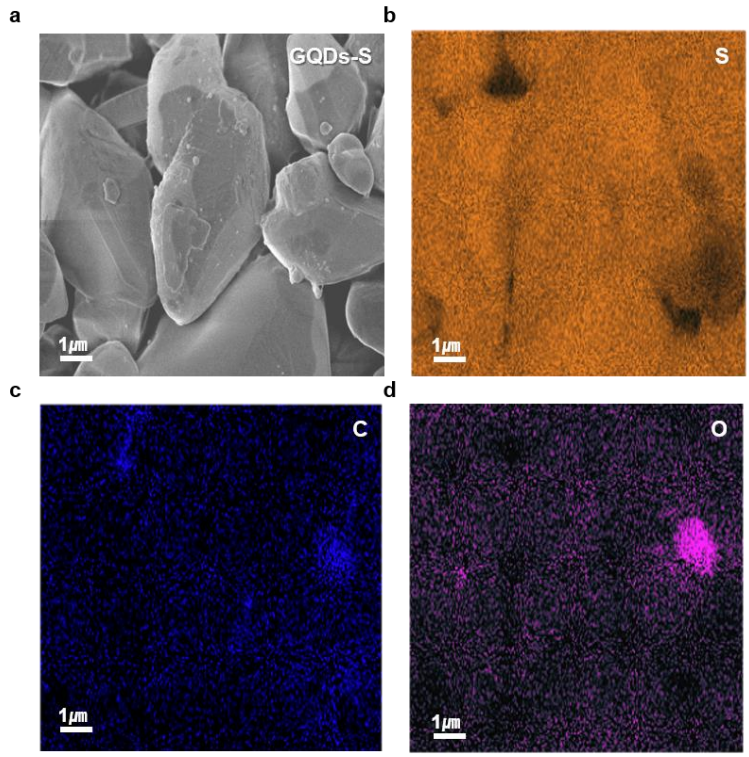

Figure S1. Scanning electron microscopy and energy-dispersive X-ray spectroscopy characterization of the GQDs-S composites. SEM images of the GQS-S composites, and C, S, and O EDX maps of the GQDs-S composites.

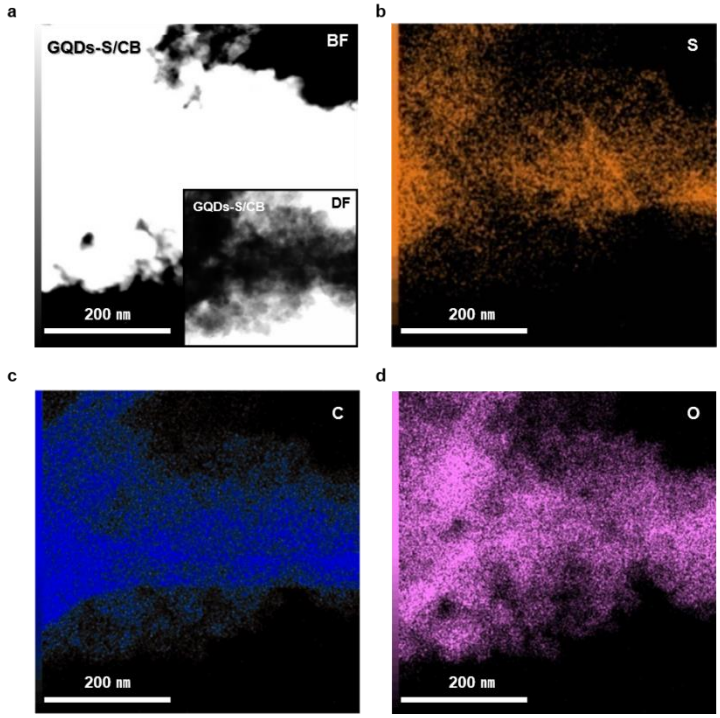

Figure S2. Scanning transmission electron microscopy and EDX characterization of the GQDs-S/CB composites. TEM images of the GQS-S/CB composites, and C, S, and O EDX maps of the GQDs-S/CB composites.

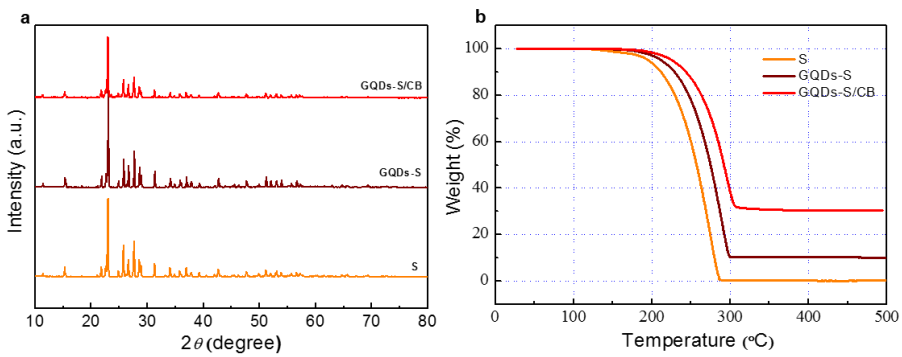

Figure S3. X-ray diffraction (XRD) patterns and Thermogravimetric analysis (TGA). XRD of sulphur, GQDs-S, and GQDs-S/CB composites a, and TGA collected in N_2 atmosphere with a heating rate of 10℃/min b, the S content of the cathode.

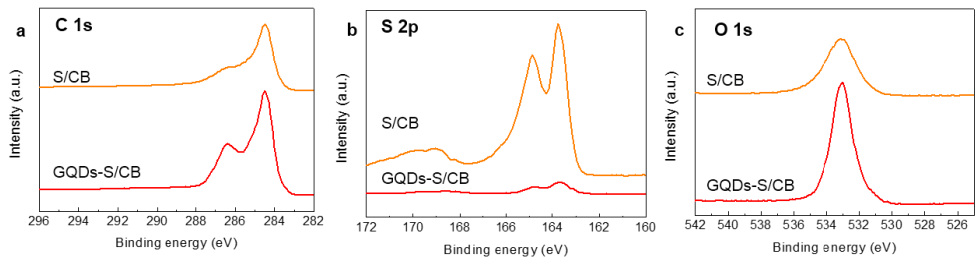

Figure S4. X-ray photoelectron spectroscopy of S/CB, and GQDs-S/CB particles. a, C 1*s* peaks, b, S 2*p* peaks, and c, O 1*s* peaks of S/CB and GQDs-S/CB particles.

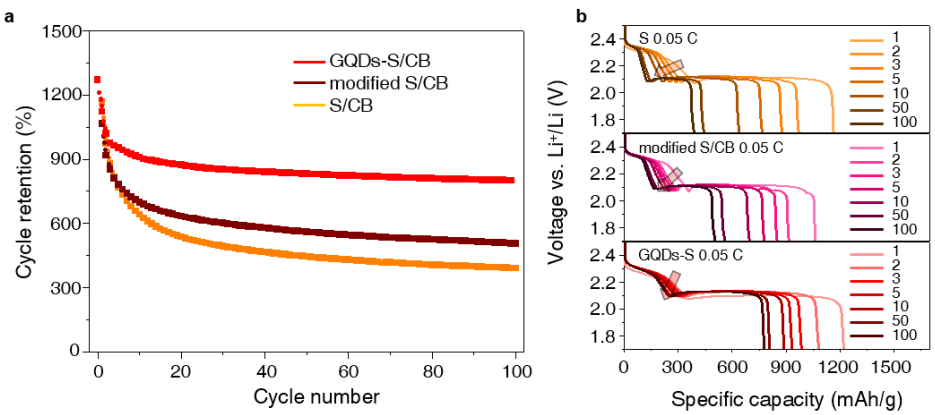

Figure S5. a, Cycling performance and b, discharge profile of GQDs-S/CB, modified S/CB, and S/CB at 0.05 *C* for 100 cycles. The GQDs-S/CB electrode shows superior cycle retention compared to S/CB and modified S/CB, which indicates that the surfactant alone does not prevent dissolution of the sulphide discharge-products into the electrolyte.

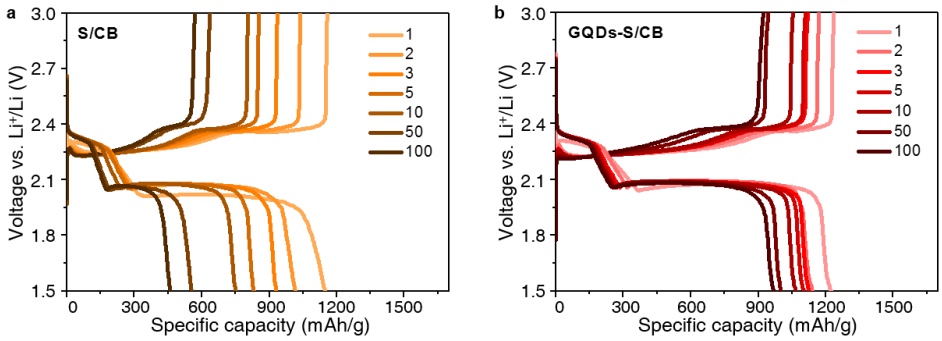

Figure S6. Charge-discharge profiles of a, S/CB and b, GQDs-S/CB at 0.5 *C* for 100 cycles.

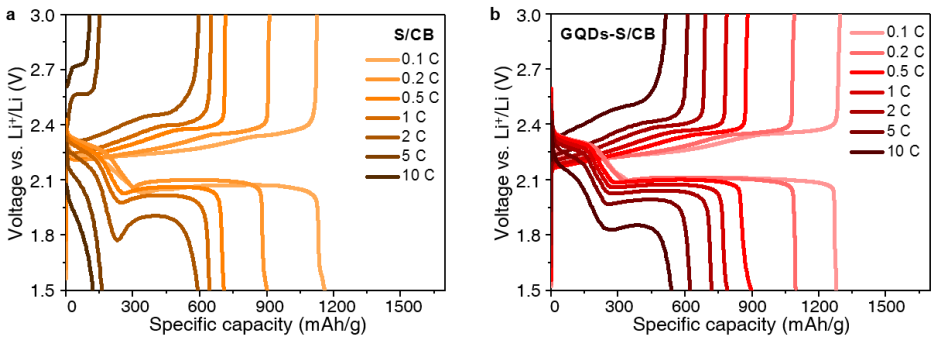

Figure S7. Rate performance of a, S/CB and b, GQDs-S/CB from 0.1 *C* up to 10 *C*.

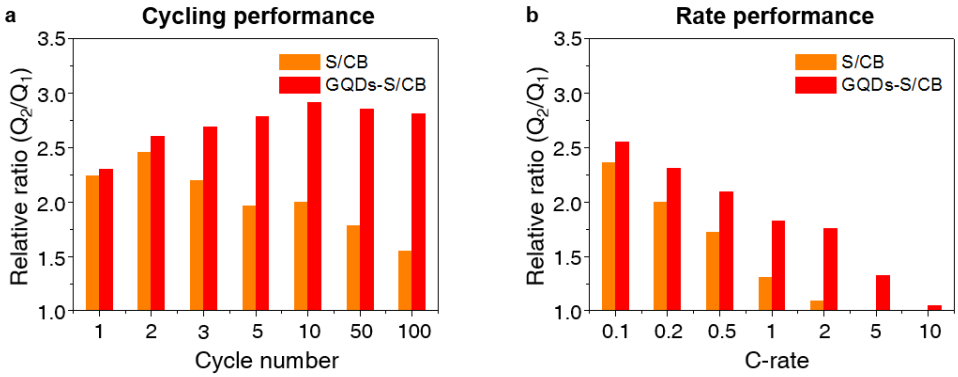

Figure S8. Relative ratios of dissolution/precipitation regime capacity (Q_2/Q_1). a, Cycling performance up to 100 cycles. b, Rate performance from 0.1 *C* to 10 *C*.

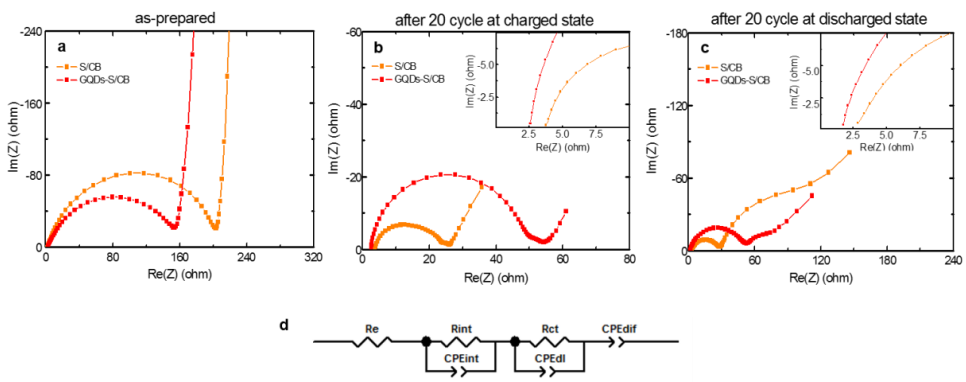

Figure S9. Electrochemical impedance spectroscopy (EIS). Lithium/sulphur cells a, as-prepared, b, fully charged, and c, discharged state after 20 cycles. Insets show the high-frequency range. The equivalent circuit model used to analyze the Nyquist plots d, charge-discharge states.

Electrochemical impedance spectroscopy (EIS) was used to analyze the interfacial resistance of the active material, the solution, and the carbon conducting agents, as shown in Fig. S9. The Warburg element (WO) is converted to a CPE_{diff} term while the other terms were fixed for the fitting process. The constant phase element (CPE) is normally used in modelling impedance data in place of a capacitor to compensate for non-ideal behaviour of the electrode (e.g. roughness or porosity at the electrode surface, ideal semi-circle n=1). R_e is relative to the resistance of the electrolyte, and the ratio R_{int}/CPE_{int} is related to the resistance and capacitance of the interphase contact of the sulphur electrode. In a Nyquist diagram R_e occurs in the high frequency (HF) region (100 kHZ-1kHz). In middle frequency (MF) (1kHz–1Hz) region, the ration R_{ct}/CPE_{dl} is related to the charge transfer resistance and capacitance at the interface between the active materials, the conducting agent, and the electrolyte. The term CPE_{diff}, the diffusion impedance, related to the Li-ion diffusion process, occurs in low frequency (LF, 1Hz-100mHz)[1]. EIS was also performed in the charged/discharged states at the 20th cycle, Figs. S9b and S9c, to examine the conductivities of both electrodes in these states. At high frequency (> 100 Hz), where the EIS response is associated with Rint/Cint, the GQDs-S/CB shows a larger semi-circle compared to that of S/CB owing to the higher concentration of active material. Despite the higher population of active materials, the GQDs-S/CB electrodes exhibit a smaller semi-circle than S/CB at intermediate frequency region (100 Hz – 1 Hz). This semi-circle is related to Rct/Cdl, which suggests that the GQDs-S/CB electrode has higher structural stability and lower electrical resistance compared to the S/CB electrode. These observations support that the GQDs-S/CB prohibit dissolution of HO-LiPSs into the electrolyte and facilitate electron transfer between the conducting agent and active materials.

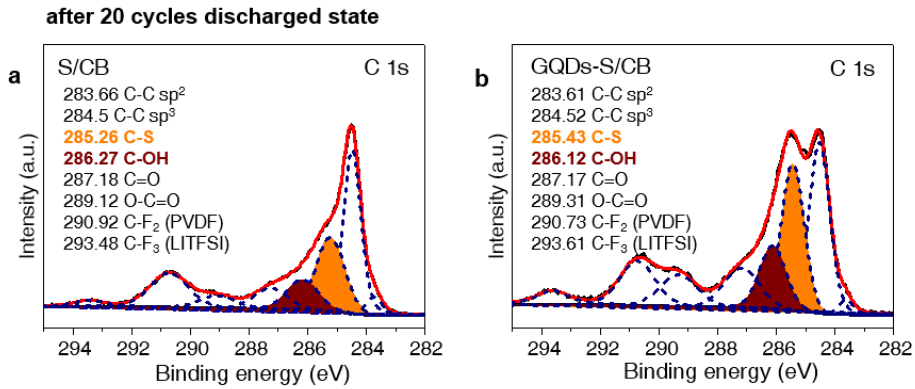

Figure S10. High resolution C 1*s* X-ray photoelectron spectroscopy a,b, C 1*s* spectrum of the S/CB and GQDs-S/CB electrodes after 20 cycles in the discharged state. Each spectrum has been fitted with peaks for different bonded carbon (dashed line) and the sum of the fitting curves (red line) is consistent with the raw data (black solid line).

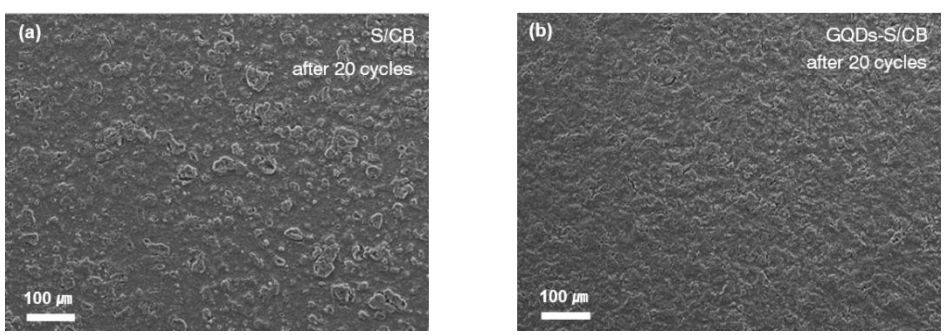

Figure S11. SEM images of GQDs-S/CB and S/CB cathode electrodes after electrochemical cycling. a,b, GQDs-S and S electrodes after cycling.

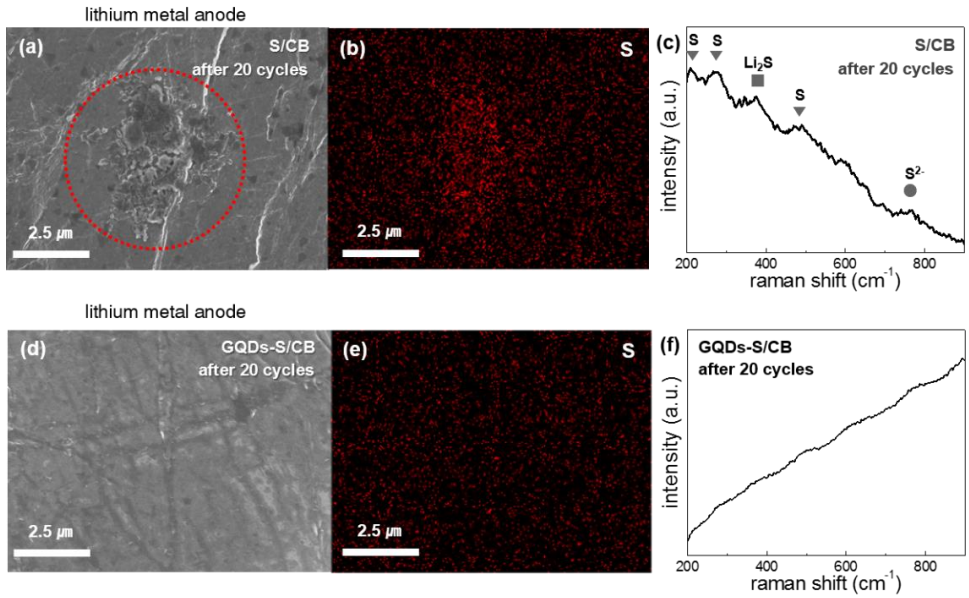

Figure S12. SEM images and Raman spectra of lithium anodes after cycling against S/CB and GQDs-S/CB electrodes. a,d, SEM images after 20 cycles. b,e, Sulphur energy-dispersive X-ray spectroscopy maps. c,f, Raman spectra. The S peaks are assigned to 156, 221, 473 cm^{-1}, Li_2S to 378 cm^{-1}, and S^{2-} to 746 cm^{-1} (ref. 2). No peaks are present in the cell containing GQDs-S/CB.

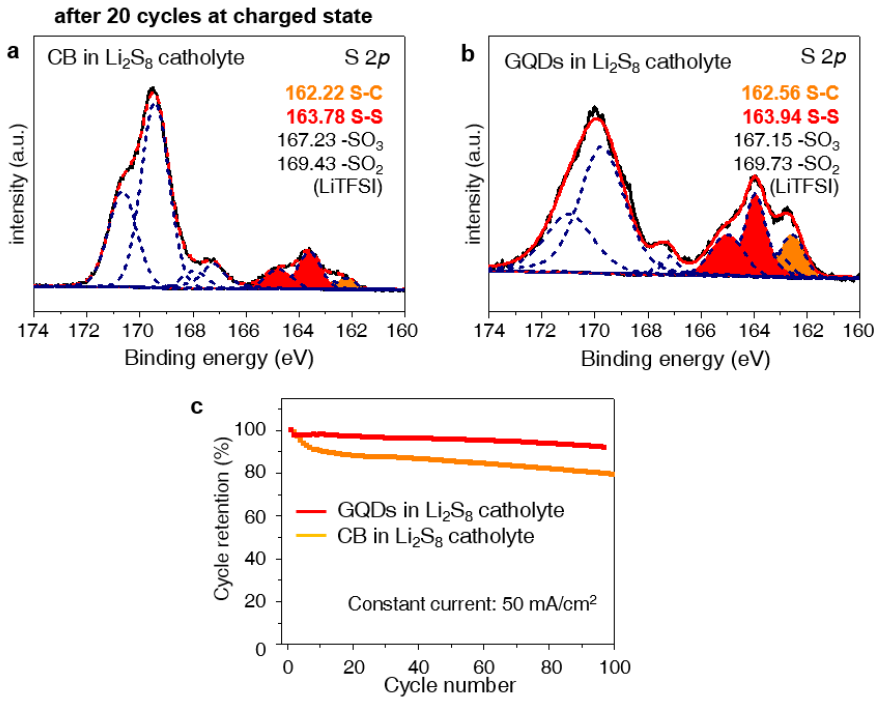

Figure S13. High resolution S 2*p* X-ray photoelectron spectroscopy and cycl e performance. a,b, S 2*p* spectrum of the CB and GQDs electrodes, in the charge state, after 20 cycles. These electrodes were cycled in the Li_2S_8 cath olyte. Each spectrum was fitted with functions corresponding to different valencies of sulphur (dashed line) and the sum of these fitted curves (red line) is consistent with the raw data (black solid line). c, Cycle retention of GQDs/CB and CB el ectrodes in Li_2S_8 catholyte over 100 cycles.

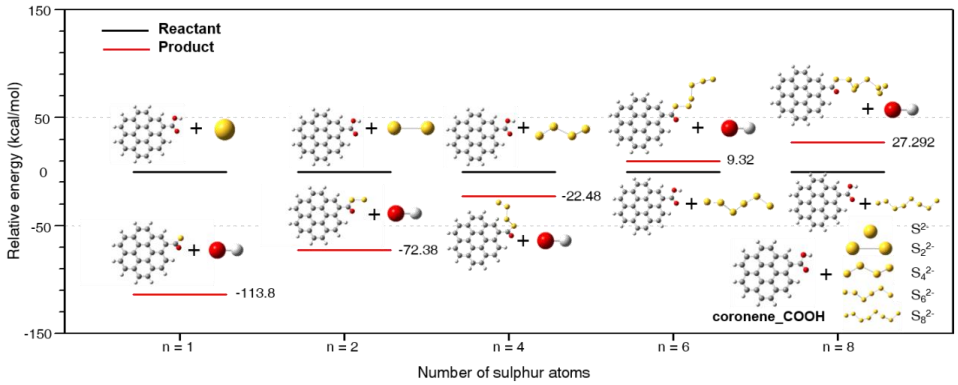

Figure S14. The relative energies for the reactant and product in binding of polysulphides to GQDs. The functional groups enhance the binding of polysulphides to carbon due to substitution of –OH (C-COOH) for S_n^{2-}. Yellow, red, white, and gray represents S, O, H, and C atoms, respectively.

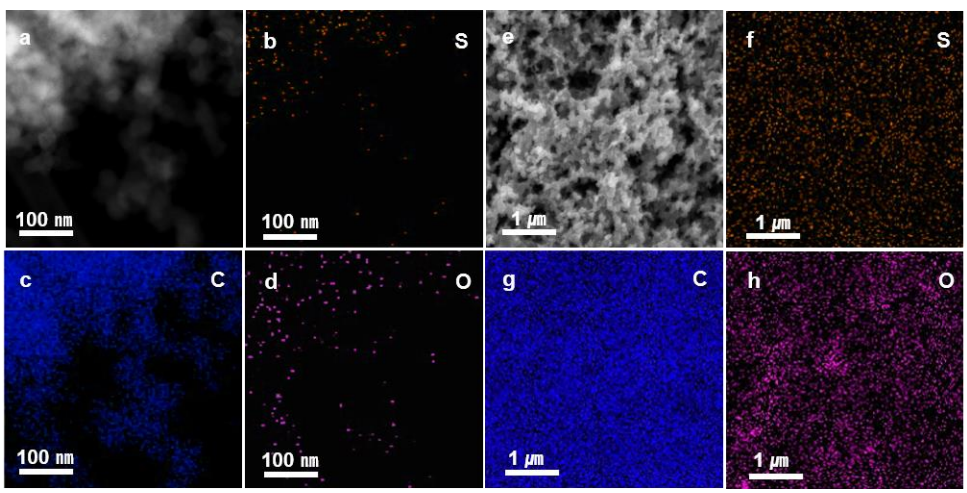

Figure S15. TEM images of nano-sized sulphur on a CB electrode in Li_2S_8 catholyte after 20 cycles. a, Bright field STEM image of the CB electrode. b-d, Energy-dispersive X-ray spectroscopy maps of C, S, and O of the CB electrode in the Li_2S_8 catholyte. e, SEM image of the CB electrode in the Li_2S_8 catholyte after cycling. f-h, C, S, and O EDX maps of the GQDs electrode.

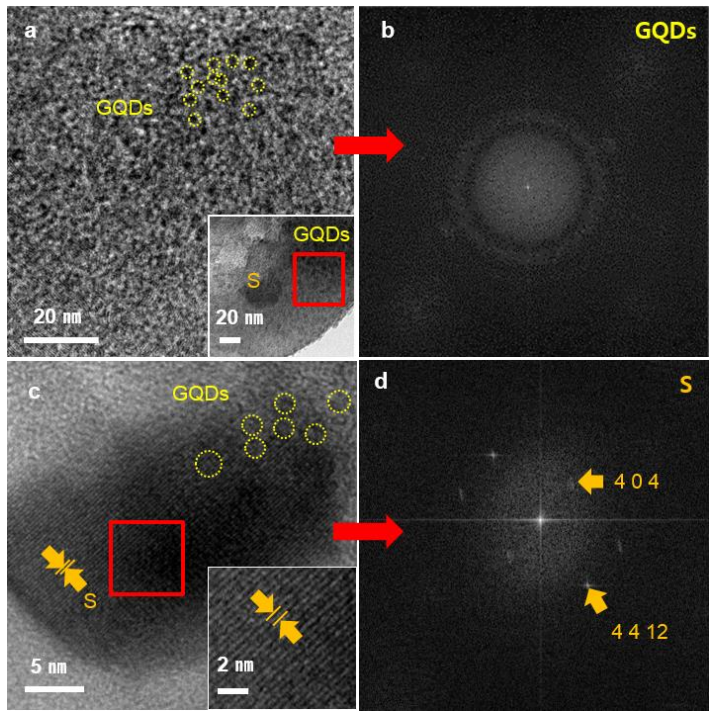

Figure S16. HRTEM (high-resolution transmission electron microscopy) images of nano-sized sulphur on GQDs electrode in Li_2S_8 catholyte after 20 cycles. a, TEM image of nano-sized sulphur in the GQD electrode. b, The FFT of the selected region in image, a. The ring pattern of graphene quantum dots. c, Magnification of nano-sized sulphur in image a shows the lattice fringes of sulphur and GQDs. d, The FFT of the selected area in image, c.

References

1. Armand, M. and Tarascon, J. -M. Building better batteries. *Nature* **451,** 652-657 (2008).
2. Goodenough, J. B., Park, K. -S. The Li-ion rechargeable battery: a perspective. *J. Am. Chem. Soc.***135**, 1167-1176 (2013).
3. Marom, R., et al. A review of advanced and practical lithium battery materials. *J. Mater. Chem.* **21**, 9938-9954 (2011).
4. Cabana, J., et al. Beyond intercalation-based Li-ion batteries: the state of the art and challenges of electrode materials reacting through conversion reactions. *Adv. Mater.* **22**, E170-E192 (2010)
5. Manthiram, A., Fu, Y. and Su, Y.-S. Challenges and prospects of lithium-sulphur batteries. *Acc. Chem. Res.* **46**, 1125-1134 (2013).
6. Chung, W. J., Griebel, J. J., et al. The use of elemental sulfur as an alternative feedstock for polymeric materials. *Nat. Chem.* **5**, 518-524 (2013).
7. Bruce, P. G., Freunberger, S. A., Hardwick, L. J., Tarascon, J. -M. Li-O_2 and Li-S batteries with high energy storage. *Nat. Mater.* **11**, 19-29 (2012).
8. Choi, N. -S., et al. Challenges facing lithium batteries and electrical double-layer capacitors capacitors. *Angew. Chem. Int. Ed.* **51**, 9994-10024 (2012).
9. Simmonds, A. G., Griebel, J. J., Park, J., et al. Inverse vulcanization of elemental sulfur to prepare polymeric electrode materials for Li-S batteries. *ACS Macro Letters* **3**, 229-232 (2014).
10. Mikhaylik, Y. V., Akridge, J. R., Polysulfide shuttle study in the Li/S battery system, *J. Electrochem. Soc.*, **151**, A1969-A1976 (2004).
11. Elazari, R., Salitra, G., Garsuch, A., Panchenko, A., Aurbach, D. Sulphur-impregnated activated carbon fiber cloth as a binder-free cathode for rechargeable Li-S batteries. *Adv. Mater.* **23**, 5641-5644 (2011).
12. Su, Y. and Manthiram, A. Lithium-sulphur batteries with a microporous carbon paper as a bifunctional interlayer. *Nat. Comm.* **3** 1166-1171 (2012).
13. Zhang, C., et al. Confining sulfur in double-shelled hollow carbon spheres for lithium-sulfur batteries. *Angew. Chem. Int. Ed.* **51**, 9592-9595 (2012).

14. Zhou, G. and et al. A graphene-pure sulfur sandwich structure for ultrafast long-life lithium-sulfur batteries. *Adv. Mater.* **26**, 625-631 (2014).
15. Ji, X., Lee, K. T., and Nazar, L. F. A Highly ordered nanostructured carbon-sulphur cathode for lithium-sulphur batteries. *Nat. Mater.* **8**, 500-506 (2009).
16. Xin, S. et al. Smaller sulphur molecules promise better lithium-sulphur batteries. *J. Am. Chem. Soc.* **134**, 18510-18513 (2012).
17. Schuster, J., He, G. et al. Spherical ordered mesoporous carbon nanoparticle with high porosity for lithium-sulphur batteries. *Angew. Chem. Int. Ed.* **51**, 3591-3595 (2012).
18. Ji, L., Aloni, S., Wang, L., Cairns, E. J., Zhang, U. Porous carbon nanofiber-sulphur composite electrodes for lithium/sulphur cells. *Energy Environ. Sci.* **4**, 5053-5059 (2011).
19. Guo, J., Xu, Y., and Wang, C. sulphur-impregnated disordered carbon nanotubes cathode for lithium sulphur batteries. *Nano Letters* **11,** 4288-4294 (2011).
20. Wang, H. et al. Graphene–wrapped sulphur particles as a rechargeable lithium-sulphur battery cathode material with high capacity and cycling stability. *Nano Letters* **11**, 2644-2647 (2011).
21. Ji, L., Rao, M. et al. Graphene oxide as a sulphur immobilizer in high performance lithium/sulphur cells. *J. Am. Chem. Soc.* **133**, 18522-18525 (2011).
22. Zu, C., Manthiram, A. Hydroxylated graphene-sulphur nanocomposites for high-rate lithium-sulphur batteries. *Adv. Energy Mater.* **3**, 1008-1012 (2013).
23. Evers, S., Nazar, L. F. Graphene-enveloped sulphur in a one pot reaction: a cathode with good coulombic efficiency and high practical sulphur content. *Chem. Commun.* **48,** 1233-1235 (2012).
24. Fu, Y. and Manthiram, A. Orthorhombic bipyramidal sulphur coated with polypyrrole nanolayers as a cathode material for lithium-sulfur batteries. *J. Phsy. Chem. C* **116**, 8910-8915 (2012).
25. Peng, J. et al. Graphene quantum dots derived from carbon fibers. *Nano Letters* **12**, 844-846 (2012).

26. Ritter, K. A., Lyding, J. W. The influence of edge structure on the electronic properties of graphene quantum dots and nanoribbons. *Nat. Mater.* **8**, 235-242 (2009).
27. Pan, D., Zhang, J., Li, Z., Wu, M. Hydrothermal route for cutting graphene sheets into blue-luminescent graphene quantum dots. *Adv. Mater.* **22**, 734-738, (2010).
28. Acik, M., Lee, G., Mattevi, C, Pirkle, A., Wallace, R. M., et al. The role of oxygen during thermal reduction of graphene oxide studied by infrared absorption spectroscopy. *J. Phys. Chem. C* **115**, 19761-19781 (2011).
29. Gokus, T., Nair, R. R., Bonetti, A., Bohmler, M., Lombardo, A., Noboselov, et al. Making graphene luminescent by oxygen plasma treatment. *ACS Nano* **3**, 3963-3968 (2009).
30. Yeon, J., Jang, J. et al. Raman spectroscopy and X-ray diffraction studies of sulphur composite electrodes during discharge and charge. *J. Electrochem. Soc.* **159**, A1308-A1314 (2012)
31. John F. Moulder, William F. Stickle, Peter E. Sobol, Kenneth D. Bomben. Handbook of X-ray photoelectron spectroscopy (Physical Electronics, Inc., 1995).
32. Su, Y.-S., Fu, Y., Cochell, T., and Manthiram, A. A strategic approach to recharging lithium-sulphur batteries for long cycle life. *Nat. Comm.* **4**, 2985-2992 (2013).
33. Deng, Z., Zhang, Z. et al. Electrochemical impedance spectroscopy study of a lithium/sulphur battery: modelling and analysis of capacity fading. *J. Electrochem. Soc*. **4**, A553-A558 (2013)
34. Bruckner, J., Soren T. et al. Lithium sulphur batteries: influence of C-rate, amount of electrolyte and sulphur loading on cycle performance. *J. Power Sources* **268**, 82-87 (2014).
35. S. Kaciulis Spectroscopy of carbon: from diamond to nitride films. *Surf. Interface Anal.* **44**, 1155-1161 (2012).
36. Kummer, K., Vyalikh, D. V., High-resolution photoelectron spectroscopy of self-assembled mercaptohexanol monolayers on gold surfaces. *J. Electron. Spectrosc. Relat. Phenom.* **163**, 59-64 (2008).

37. Juhye Song, Sung Jun Lee et al. Thermal reactions of lithiated and delithiated sulphur electrodes in lithium-sulfur batteries. *ECS Electrochemistry Letters* **3** (4) A26-A29 (2014).
38. Socrates, G. Infrared and Raman characteristic group frequencies tables and charts: *Sulphur and Selenium compounds* Ch.16 (John Wiley & Sons Ltd, Third edition, 2001).
39. Song, J., Xu. T. et al. Nitrogen-doped mesoporous carbon promoted chemical adsorption of sulphur and fabrication of high-areal-capacity sulphur cathode with exceptional cycling stability for lithium-sulphur batteries. *Adv. Func. Mater*. **24**, 1243-1250 (2014).
40. Berghof, V., Sommerfeld, T., and Cederbaum, L. S. Sulfur cluster dianions. *J. Phys. Chem. A*, **102**, 5100-5105 (1998).
41. Abrahams, S. C. The crystal and molecular structure of orthorhombic sulfur, *Acta Cryst*. **8**, 661-671 (1955).
42. Stephens, P. J., Devlin, F. J., Chabalowski, C. F., Frisch, M. J. Ab Initio calculation of vibrational absorption and circular dichroism spectra using density functional force fields. *J. Phys. Chem.* **98**, 11623-11627 (1994).
43. Gaussian 09, Frisch, M. J., Trucks, G. W., Schlegel, H. B., Scuseria, G. E., et al. Gaussian, Inc., Wallingford CT, 2009.

Abstract (Korean)

최근 에너지 자원에 대한 수요가 증가함에 따라 새로운 에너지 장치 및 변환 시스템 개발에 대한 노력이 끊임 없이 진행되어 왔다. 급격히 증가된 소비 속도와 빠른 화석연료의 고갈은 지난 수십년간 많은 재생에너지, 풍력에너지, 조력에너지, 그리고 태양 에너지에 관한 연구가 집중되게 되었다. 한편, 재생에너지에 대한 폭넓은 사용을 제공하기 위해 효과적인 에너지 장치 및 변환기술 개발이 요구되는 실정이다. 최근 그래핀 및 그래핀 기반 복합물질은 높은 기계적 구부러짐, 넓은 표면적, 우수한 화학적 안정성, 높은 전기 및 열 전도도 특성으로 인해 많은 관심을 받고 있으며, 전기화학적 에너지 저장장치 즉, 리튬 배터리, 슈퍼캐페시터, 물분해 시스템 및 태양광 시스템에 관한 대체 전극 물질로서의 연구되고 있다.

본 학위논문은 다음과 같다. 1장에서는 질소 도핑된 그래핀 및 그래핀 양자시트를 사용하여 수소 생산반응 전극의 촉매로사용하여 우수한 물분해효율 향상에 대한 결과 및 그에 대한 메커니즘을 규명하는 것이다. 2장에서는 산소기능기를 다량 함유하고 있는 나노 사이즈의 그래핀 양자점을 황 물질에 포함하여 코어 셀 구조를 합성하고 이를 리튬 황 배터리의 양극 물질로 활용하여 고성능 및 고용량 배터리를 구현한 연구이다. 본문의 주요 결과는 다음과 같다.

Part 1, 첫째, 화학기상증착법에 의하여 촉매층 상 (구리 박막)에서 형성된 단층 그래핀에 질소 플라즈마를 인가하여 질소 도핑된 그래핀 양자 시트 (N-doped graphene quantum sheet, N-GQSs)를 간단히 제작하는 방법을 처음으로 발견하였다. 둘째, 단층의 질소 도핑된 그래핀을 수소발생 반응의 촉매로 사용하여 포화전류밀도의 변화 없이 강하게 반응시점이 향상 된 것으로 나타났으며,

단층의 질소 도핑된 그래핀층은 중성 (pH 7)에서 실리콘전극의 산화 방지막으로써 우수한 활용도 또한 증명하였다. 마지막으로, 질도 도핑된 그래핀 양자 시트를 표면적이 넓은 실리코 나노 와이어 전극의 촉매로 사용하여 수소 생성 반응을 분석하였고, 그 결과 광전기화학적 수소 생생 반응의 우수한 촉매로써의 활용을 선보였다. 이것은 현재까지 탄소 기반의 광전기화학반응의 촉매로의 연구결과보다 뛰어난 태양광에너지를 수소에너지로 변화하는 효율을 보였다.

Part 2, 산화그래핀의 산소 기능기가 리튬-황 배터리 성능향상에 미친 영향을 연구하기 위하여, 리튬-황 배터리 양극물질로 산화 그래핀을 황물질과 코어쉘 구조를 합성하였다. 나아가 구조와 산소기능기의 역할을 모두 연구하기 위해, 산소 기능기가 다량 함유된 나노 사이즈형태의 그래핀 양자 점을 합성하여 황 입자를 밀도있게 감싸는 구조를 형성하였다. 이것은 전자 전달에 유리한 구조를 보였으며, 액상의 리튬폴리설파이드의 손실을 막아주었다. 배터리 성능 평가 후, 표면 분석을 통하여 C-S (탄소-황) 결합이 형성된것을 확인 할 수 있었으며 밀도범함수 이론을 통하여 다양한 산소 기능기와 폴리설파이드가 반응하여 C-S결합을 형성할 수 있음을 확인 하였다. 마지막으로, 질도도핑된 탄소 양자점을 사용한 리튬-황 배터리의 우수한 용량 및 율속특성에 대한 메카니즘 연구를 철저히 전기화학적 분석을 통하여 규명하였다.

따라서, 본 학위논문은 질소 혹은 산소로 기능화된 그래핀 혹은 그래핀 양자점을 합성하고 이를 수소 발생 반응과 리튬-황 배터리에 적용한 연구결과를 제시하였다. 본 내용은 *Energy Environ. Sci.* 8, 1329 (2015), *Adv. Mater.* 26, 3501 (2014), *Energy Environ. Sci.* 6, 3658 (2013), and Nanoscale (DOI:10.1039/c5nr01951f) 저널에 등재된 내용을 포함하고 있다.

주요어: 그래핀, 그래핀 양자 시트, 그래핀 양자 점, 수소 발생 반응, 촉매, 리튬-황 배터리, C-S 결합, 나노-사이즈 황

학 번: 2012-30873

이학박사학위논문

Synthesis of Graphene Quantum Dots for Energy Applications

기능화된 그래핀 나노재료의 합성 및 에너지 저장으로의 응용

2015 년 8 월

서울대학교 대학원

화학부 물리화학 전공

문 준 희

Synthesis of Graphene Quantum Dots for Energy Applications

그래핀 양자점 합성 및 에너지 저장으로의 응용

지도교수: 홍 병 희

이 논문을 이학박사 학위논문으로 제출함

2015년 8월

서울대학교 대학원

화학부 물리화학전공

문준희

문준희의 이학박사 학위논문을 인준함

2015년 8월

위 원 장 장두전 ㊞

부위원장 홍병희 ㊞

위 원 조성표 ㊞

위 원 남좌민 ㊞

위 원 박재성 ㊞

Ph. D. Thesis

Synthesis of Graphene Quantum Dots for Energy Applications

Supervisor: Professor Byung Hee Hong

Major: Physical Chemistry

By Joonhee Moon

Department of Chemistry

Graduate School of Seoul National University

2015

Abstract

Synthesis of Graphene Quantum Dots for Energy Applications

Joonhee Moon

Department of Chemistry

The Graduate School Seoul National University

Recently, with the increased demand in energy resources, great efforts have been devoted to developing advanced energy storage and conversion systems. The increasing consumption and the rapid depletion of fossil fuels has driven the major research focus to exploitation and utilization of renewable energy such as wind energy, tidal energy and solar energy for the past few decades. To provide widespread usage of renewable energies, efficient energy storage and conversion technologies are required. Recently, graphene and graphene-based materials have attracted great attention owing to their unique properties of high mechanical flexibility, large surface area, chemical stability, superior electric and thermal conductivities that render them great choices as alternative electrode materials for electrochemical energy storage systems, i.e., lithium batteries, supercapacitors, water splitting systems, and solar systems.

The specific objectives of my thesis are as follow: (1) this dissertation is the results of an effort to develop the solar-to-hydrogen (STH) conversion efficiency using nitrogen doped graphene and graphene quantum sheets as a catalyst of cathode materials for hydrogen evolution reaction (HER) (2) graphene quantum dots with

oxygen rich functional groups were incorporated into sulfur cathode materials of lithium sulfur battery to enhance the battery performance. The main results of my dissertation research can be summarized as follows.

In Part Ⅰ, firstly, a simple one-step method to prepare nitrogen doped graphene quantum sheets (N-GQSs) was introduced by directly applying nitrogen plasma to as-grown graphene on Cu foil. Secondly, monolayer graphene (Gr) and nitrogen doped graphene (N-Gr) were applied as a catalyst on silicon wafer for HER, which strongly shifted toward the anodic direction without a change in the saturation current density as well as exhibits the strong potential as the passivation layer in neutral pH 7. Finally, N-doped graphene quantum sheets were decorated on an optimized silicon nanowires as a catalyst for the solar-driven HER, which can boost the catalytic activity toward the photoelectrochemical HER. The results showed that the N-GQSs electrodes exhibits higher applied bias photon-to-current efficiency (ABPE) than that of any other carbon-based photoelectrochemical HER catalysts reported to date.

In part Ⅱ, to study the role of oxygen functional groups in improving the cyclability, graphene oxide wrapped on sulfur composites were synthesized and used as a cathode electrode in a lithium sulfur battery (Li-S battery). For Further study on structure and functional groups of cathode electrode, graphene quantum dots with oxygen functional groups is found to promote the structural integration of densely packed carbon black (CB) shells surrounding sulfur particles, which enables faster charge transfer and minimal loss of lithium polysulfides through the tightly packed sulfur-carbon morphology and the carbon-sulfur (C-S) bonding. Finally, the

mechanism study of N-GQDs assisted Li-S battery that leads to the excellent cycling and rate performance were thoroughly investigated by detailed electrochemical analysis guided by theoretical modeling.

This dissertation provides the details of my work on all projects related to synthesize and characterization of functionalized graphene and graphene quantum dots for energy system: hydrogen evolution reaction and lithium sulfur batteries. These contents are reported in *Energy Environ. Sci.* 8, 1329 (2015), *Adv. Mater.* 26, 3501 (2014), *Energy Environ. Sci.* 6, 3658 (2013), and Nanoscale (DOI:10.1039/c5nr01951f).

Keywords: graphene, graphene quantum sheets, graphene quantum dots, hydrogen evolution reaction (HER), catalyst, lithium sulfur battery, C-S bonding, nano-sized sulfur

Student Number: 2012-30873

Contents

List of Figures

Chapter 1

Chapter 2

N-GQS is 4.84 ± 0.06 nm. The insets in e and f show selected area diffraction patterns (SAED) of graphene and N-GQS.

Figure 4. (a) Raman spectra and (b) XPS spectra of as-grown graphene and N-GQS. (c, d) Detailed C 1*s* and N 1*s* XPS peaks of N-GQS. (e) UV-vis absorption spectra of N-GQS in dichloromethane. The inset shows a photograph of the N-GQS solution under 365 nm wavelength UV lamp. (f) Photoluminescence (PL) spectra of the N-GQS for different excitation wavelengths (360~440 nm).

Figure 5. SEM images of (a) bare Si and (b) porous Si. Cyclic Voltammetry (CV) of N-GQS on bare Si and porous Si. (c) Photocurrent density-potential (*J-E*) curves for the lightly boron doped p-Si and p-porous Si electrode deposited with N-GQS. N-GQS was introduced by dry transfer on bare Si and by wet transferred on porous Si. Each CV process was performed at a scan rate of 0.005 Vs^{-1}. (d) Electrochemical activity of N-GQS on a Glassy Carbon (GC) electrode with rotating ring disk system. CV data were corrected by iR compensation.

Figure 5. SERS spectra of 1,4-PDI molecules in (a) Si@Au/1,4-PDI, (b) Si@Au/1,4-PDI/Au and (c) Si@Au/1,4-PDI/Au/1,4-PDI systems. The inset shows the Raman band of silicon wafer at 520 cm^{-1} used as an internal reference.

Figure 6. Schematic presentation of 1,4-PDI molecules trapped between two Au nanoparticles. The red part represents the impermeable area for the additional 1,4-PDI molecules into the gap of Au nanoparticle dimer.

Figure 7. (a) FDTD calculation results of the local field intensity ($|E/E_0|^2$) distributions (logarithmic scale) near Au nanoparticle dimer (diameter = 55 nm, gap distance = 1 nm) excited with (a) a parallel-polarized and (b) a perpendicular-

polarized light (wavelength = 632.8 nm) to the dimer axis. (c) The intensity distribution ($|E/E_0|^4$) in the gap of two Au nanoparticles excited with a parallel-polarized light as a function of distance from the center of the gap.

Figure S1. (a, b) AFM surface morphologies of Cu foils annealed at 1,000˚C. (c, d) AFM images of continuous monolayer graphene film grown on Cu by CVD. (e, f) AFM images of N-GQSs converted from monolayer graphene on Cu after N_2-plasma treatment. Scan sizes, 10 x 10 μm^2 for a, c, and e, 1.5 x 1.5 μm^2 for b, d, and f, respectively.

Figure S2. (a-c) AFM images of monolayer graphene on Cu with varying exposure time to N_2-plasma for 0, 8, and 16 sec, respectively. Scan area, 1.5 x 1.5 μm^2. (d) AFM profile of N_2-plasma treated graphene on Cu corresponding to the red box in c. Scan area, 600 x 600 nm^2.

Figure S3. (a) Schematic illustration and photograph images of hydrogen evolution reaction on N-GQSs/Si photocathode.

Chapter 3

Figure 1. Cyclic Voltammetry (CV) of graphene (Gr), N_2-plasma-treated Gr (NGr), Pt, and Pt with NGr on a Si electrode. (a) Photocurrent density-potential (*J-E*) curves for the lightly boron doped p-Si electrode deposited with Gr and NGr. The plasma treatment on Gr was introduced with high purity N_2 gas for 14 sec, which is called NGr-Si. In case of Pt-Si and Pt-NGr-Si electrodes, Pt nanoparticles were deposited on bare Si and NGr-Si by the electroless deposition method, respectively. (b)

Polarization curves of Gr, and NGr on heavily arsenic doped n^+ type Si electrodes under dark condition. Each CV was performed at a scan rate of 0.05 V/sec.

Figure 2. Electrochemical activity of Gr on Glassy Carbon (GC) electrode. (a) CV curve of GC, Gr on GC, NGr on GC, and Pt on GC from rotating disk electrode system. CV data were corrected by iR compensation. (b) Tafel plots were derived from (a) CV data. The 'b' in the inset (mV/decade) and J_0 (A/cm^2) indicate a Tafel slope and an exchange current density, respectively.

Figure 3. (a) Raman spectra and (b) high resolution XPS spectra of N 1s peak of Gr and NGr. The N 1*s* peak is separated into N1 (398.5 eV), N2 (399.9 eV), and N3 (401 eV) which are labeled by green, blue, and red lines. An inset image in (b) represents schematic of NGr. The gray, green, blue, and red spheres indicate the carbon, pyridinic nitrogen, pyrrolic nitrogen, and quaternary nitrogen atoms, respectively. (c-d) High resolution XPS spectra of Si 2*p* region of bare Si, Gr-Si, and NGr-Si electrodes. XPS spectra of each sample (c) before the chronoamperometry test and (d) after the chronoamperometry test at 0 V *vs.* RHE for 10,000 sec. Narrow-scan data of the Si 2*p* region were collected using pass energy of 40 eV and 0.05 eV/step.

Figure 4. The stability test of bare Si, Gr-Si, and NGr-Si photocathodes. CV of Si photocathodes during 300 cycles with a scan rate of 0.05 V/sec at (a) pH 0 and (b) pH 6.8. Polarization curves of each photoelectrodes shifted negatively vs. RHE as the CV operation increased. (c) Chronoamperometry operation of Si photocathodes. The change of normalized photocurrent density (J/ J_{init}) at 0 V vs. RHE of each photoelectrodes with the increase of time at pH 0 (solid line) and pH 6.8 (dash-dotted

line), respectively. J_{init} is the initial current density in the chronoamperometry operation.

Figure S1. Calibration respect to RHE. Current vs. the applied potential respect to Ag/AgCl reference electrode with using (a) Pt foil for Si PEC cell experiment and (b) Pt wire as the counter electrode for RDE experiment.

Figure S2. Resistance of bare Glassy Carbon (GC), Gr on GC, and NGr on GC. Impedance spectroscopy analysis revealed that the resistances of the bare GC, Gr-GC, NGrGC are 7.1 ohm, 7.2 ohm, and 7.4 ohm respectively. Resistances were measured using iR compensation mode in the electrochemical analyzer (CHI 600D, CH Instruments, Inc.).

Figure S3. The logarithm of the exchange current densities calculated by extrapolation to the x-axis. Compared to the bare GC, Gr and NGr catalysts show the high activity for the HER.

Figure S4. Photoelectrochemical performance of NGr-Si photocathode with variation of the amount of Pt solution. (a) Polarization curves of NGr on Si electrode. Each cyclic voltammetry was performed during 4 cycles at a scan rate of 0.05 V/s. The durations of the plasma treatment on Gr were introduced with high purity N2 gas for 4 sec, 10 sec, 14 sec, and 16 sec. For comparison, cyclic voltammogram of Gr without plasma treatment on Si electrode is presented. (b) Representative data from polarization curves of NGr on Si electrode of Figure S4 a

Figure S5. Surface morphology of monolayer Gr and NGrs. (a) AFM images and (b) Raman characterization of a pristine Gr sample as a function of the exposure time to N_2 plasma and the each image was taken the same area measured by AFM. Numbers

on each figure indicate the exposure time. All figures have a size of 6.5 × 6.5 μm_2 (c) Raman spectra of the samples. Numbers on the left side of the left figure indicate the exposure time. Raman peaks are indexed accordingly.

Figure S6. XPS spectra of Gr and NGr. The C 1*s* is 76.78 atomic weight % (at. %) for Gr and 57.17 at. % for NGr, N 1*s* is 0.00 at. % for Gr and 2.20 at. % for NGr, and O 1*s* is 23.22 at. % for Gr and 40.63 at. % for NGr, respectively.

Figure S7. The change of onset potential of bare Si (black line), Gr-Si (red line), and NGr-Si (blue line) electrodes. The onset potential measured from the first CV sweep was a standard, and the difference between the measured onset potential during the CV cycles and the value of the first sweep was investigated; this difference is defined as ΔE – negative shift. The onset potential was measured with increasing the number of cyclic voltammetry in 1M $HClO_4$ (pH 0, dash dot line) and 0.4 M NaH_2PO_4 and 0.6 M Na_2HPO_4 (pH 6.8, solid line) electrolytes, respectively.

Figure S8. The change of photocurrent density at 0 V vs. RHE of bare Si (black line), Gr-Si (red line), and NGr-Si (blue line) electrodes with the increase of time at (a) pH 0 (1M HClO4) and (b) pH 6.8 (0.6 M NaH_2PO_4 and 0.4 M Na_2HPO_4), respectively. At pH 0, NGr-Si electrode shows a spiky plot during a chronoamperometry test because hydrogen bubbles stick to hydrophobic surfaces until sudden bursts occur.

Figure S9. The stability test of bare Si, Gr-Si, and NGr-Si photocathodes. CV results of Si photocathodes during 300 cycles with a scan rate of 0.05 V/sec at (a) pH 0, (b) pH 3.8, and (c) pH 6.8. Polarization curves of each photoelectrodes were shifted negatively vs. RHE as the number of cycles increased.

Figure S10. The stability test of bare Si, Gr-Si, and NGr-Si photocathodes. CV results of Si photocathodes during 300 cycles with a scan rate of 0.05 V/sec at (a) pH 0, (b) pH 3.8, and (c) pH 6.8. Polarization curves of each photoelectrodes were shifted negatively vs. RHE as the number of cycles increased.

Figure S11. Chronoamperometry test of bare Si, NGr-Si, and Pt-NGr-Si photocathodes at pH 6.8. (a) The change of photocurrent density at 0 V *vs.* RHE of bare Si (black line), NGr-Si (red line), and Pt-NGr-Si (blue line) electrodes with the increase of time at pH 6.8. (b) The change of normalized photocurrent density (J/ Jinit) at 0 V *vs.* RHE of each photoelectrodes with the increase of time at pH 6.8.

Chapter 4

Figure 1. Schematic of N-doped graphene quantum sheets (N-GQSs) decorated on a Si nanowire (SiNW) photocathode electrode. Photons absorbed by the SiNWs generate minority carriers (electrons), which drift to the semiconductor/electrolyte interface, where $2H^+$ is reduced to H_2; the N-GQSs serve as electrocatalysts for hydrogen production. The gray, green, blue, and red spheres in the schematic of N-GQSs represent the carbon, pyrrolic nitrogen, quaternary nitrogen, and pyridinic nitrogen atoms, respectively. The average diameter of the N-GQSs is 5 nm, as determined from a TEM image.

Figure 2. SEM images of SiNW arrays on p-silicon substrate obtained by metal assisted chemical etching method. (a) Cross-section and (b) top-view. (c) Dark-field TEM images of N-GQSs on p-SiNWs. (d) High-resolution TEM image shows Moiré pattern created by N-GQS in silicon lattices.

Figure 3. Cyclic voltammograms of N-doped graphene quantum sheets (N-GQSs) on silicon photocathodes. (a) Photocurrent density-potential (*J-E*) curves for a lightly boron-doped planar p-Si electrode and Si nanowire deposited with N-GQSs. The Si nanowire was fabricated using a metal-catalyzed electroless method. (b) Polarization curves of N-GQS on heavily arsenic-doped n^+-type Si electrodes under dark conditions.

Figure 4. Electrochemical activity of graphene monolayer and N-GQSs on glassy carbon (GC) electrodes in a rotating disk electrode system. (a) Cyclic voltammograms (CV) of a graphene monolayer on GC, N-GQSs on GC, Pt/C on GC. CV data obtained compensating for ohmic drop (iR) losses are also plotted (dashed curves). (b) Tafel plots derived from the CV data in (a).

Figure 5. Summary of the experimental data for Si and glassy carbon (GC) electrodes. (a) The photoelectrochemical performance of p-type Si-based photoelectrodes. 'Onset potential' and 'ABPE' indicate the potential at -1 mA/cm^2 *vs.* RHE and the applied bias photon-to-current efficiency, respectively; 'bare' indicates the performance of the bare electrode without deposited catalyst. (b) Electrochemical performance of N-GQSs on GC electrode and other HER catalysts determined using rotating disk electrode system. J_0 indicates that the exchange current density. References can be found in the supporting information (Tables S2 and S3).

Figure 6. Comparison of the electrochemical activity of Si nanowire and N-GQSs on Si nanowire. (a) Mott-Schottky plots from capacitance measurement as a function of potential *vs.* RHE under dark condition. (b) Nyquist plot for Si

nanowire and N-GQSs on Si nanowire at 0 V *vs.* RHE under dark condition. (c) The transient curve of the photocurrent from Si nanowire and N-GQSs on Si nanowire when the light was turned on and turned off at 0 V vs. RHE.

Figure S1. (a) AFM image of nitrogen plasma treated GQSs on Cu foil. Scan size, 600 x 600 nm^2. (b) TEM image of N-GQSs. (c) Histogram showing the size distribution of N-GQSs. (d) Raman spectra of graphene (black) and N-GQSs (red) and (e) detailed N 1*s* XPS spectra of N-GQSs. (f) UV-vis absorption of the N-GQSs in dichloromethane. The inset shows a photograph of the N-GQSs solution under 365 nm wavelength UV lamp.

Figure S2. SEM mapping images of N-GQSs decorated on Si nanowires. (a,b) Colour images of all displayed with three elements; C (red), Si (green), and O (blue).

Figure S3. (a) Bright-field and (b) dark-filed TEM images of N-GQSs dispersed on p-SiNWs. (c) Selected area diffraction patterns (SAED) gives p-SiNWs are well etched toward [001] direction. GQS pattern is hardly observed due to the strong silicon lattice.

Figure S4. Photoelectrochemical performance of Si photocathode (a) Polarization curves of various Si electrodes without depositing any catalyst. Si nanowire were made by metal-catalyzed electroless method. Each of the etching time is 20 min, 30 min, 120 min, and 180 min. Each cyclic voltammetry was performed during 2 or 4 cycles at a scan rate of 5 mV/s. (b) Polarization curves of various Si electrodes deposited with N-GQSs catalyst.

Figure S5. SEM images of cross-sectional views of p-type (100) Si wafers etched in 5 M HF and 0.015 M $AgNO_3$ solution at different etching times. The etching times

are (a) 20 min, (b) 30 min, (c) 120 min, and (d) 180 min.

Figure S6. (a) Schematic illustration and photograph images of hydrogen evolution reaction on N-GQSs/Si photocathode

Figure S7. Calibration respect to RHE. Current vs. the applied potential respect to Ag/AgCl reference electrode with using (a) Pt foil for Si PEC cell experiment and **(b)** Pt wire as the counter electrode for rotating disk electrode (RDE) experiment.

Chapter 5

Figure 1. Introduction to the Li/S battery. (a) The theoretical energy density of different rechargeable battery systems based on active materials only. The units are Wh kg^{-1} and Wh L^{-1} for gravimetric and volumetric energy density, respectively. M = $Ni_{1/3}Mn_{1/3}Co_{1/3}$ for the $LiMO_2$–graphite system. For projected $LiMO_2$–silicon cell, the specific capacity for the cathode and anode are 250 and 3000 mAh g^{-1}, respectively. The density is 4.8 g cm^3 for $LiMO_2$, and the capacity per volume is 2200 mAh L^{-1} for silicon after considering the necessary space for volume expansion. (b) The voltage profile and chemistry of sulfur cathode in the organic electrolyte.

Chapter 6

Figure 1. (a) Schematic illustration and (b) scanning electron microscopy (SEM) image of GO-S/CB composites. (c) Transmission electron microscopy (TME) image and (d) high resolution TEM image of GO-S/CB. (e) Scanning-TEM (STEM) image and (f-h) C, S, and O energy-dispersive S-ray spectroscopy (EDS) maps of the GO-S/CB composites.

Figure 2. (a) FTIR spectra of GO-S/CB and S/CB. The peaks correspond to the various functional groups in GO-S/CB and S/CB. (b) O 1*s* XPS spectra and (c) Raman spectra of GO-S/CB and S/CB.

Figure 3. X-ray diffraction (XRD) patterns and Thermogravimetric analysis (TGA). (a) XRD spectra of S/CB and GO-S/CB on Al foil current collector and (b) TGA spectra collected in N_2 atmosphere with a heating rate of 10℃/min showing the S content of the GO-S electrodes.

Figure 4. Electrochemical characterization of S/CB and GO-S/CB cathodes. Voltage profiles for (a) S/CB and (b) GO-S/CB plotted from 1^{st} to 20^{th} cycles at 0.5 *C*. (c) Cycling performance and (d) Coulombic efficiency of S/CB and GO-S/CB at 0.5 C for 100 cycles.

Figure 5. Cyclic Voltammetry peaks of (a) S/CB and (b) GO-S/CB cathodes at 0.03 mVs^{-1} scan rate.

Figure 6. (a) Rate performance and (b) Coulombic efficiency of S/CB and GO-S/CB composites from 0.1 *C* up to 1 *C*.

Figure 7. Electrochemical Impedance Spectroscopy (EIS) plots of S/CB and GO-S/CB (a) before and (b) after cycles. The symmetry cell of Li metal is plotted in Fig. (a) grey dots.

Figure S1. SEM images of (a) GO-S/CB and (b) S/CB composites. The insets show the magnified images of GO-S/CB and S/CB, respectively.

Figure S2. (a) Fourier transform infrared spectroscopy (FTIR) spectra of CB and GO. Strong peaks attributed to the characteristic vibrational mode of oxygen functional groups. X-ray photoelectron spectroscopy of CB and GO. (b) C 1*s* peaks

and (c) O 1*s* peaks.

Chapter 7

Figure 1. Material characterization of GQDs-S/CB and S/CB composites. a,b, High-resolution TEM images of GQDs. The inset in Fig. 2b shows a histogram of the GQDs size distribution. c, FT-IR spectra of GQDs and CB. The peaks in this figure correspond to the various functional groups in the GQDs and CB. SEM images of d, GQDs-S, and g, GQDs-S/CB. e, HRTEM images of the GQDs-S composites and GQD pattern (yellow circle). A Moiré pattern (red circle) is clearly visible in these TEM images, which is created by a superposition of the GQDs and S crystalline lattices, and f, Raman spectrum of GQDs-S composites, which shows that the GQDs are formed on the sulphur particles. The strong peaks at 218.16 and 472.75 cm^{-1} arise from sulphur, and the D (disorder) and G (graphitic) peaks arise from the GQDs. Schematic diagrams show the structure, h, and the magnified structure, i, of GQDs-S/CB.

Figure 2. Schematic diagrams and SEM images of S/CB and GQDs-S/CB in a Li-S battery. a,b, Schematic configuration of S/CB and GQDs-S/CB employed as a cathode in a Li-S battery. The sulphur (yellow) is wrapped with carbon black (S/CB) and compactly covered with graphene quantum dots and carbon black (GQDs-S/CB), respectively. Polysulphides were dissolved into solvent and the color changed to orange. c,d, SEM images of GQDs-S/CB and S/CB.

Figure 3. Electrochemical properties of S/CB and GQDs-S/CB electrodes. a, Schematic illustration of the discharge profile of a conventional Li-S battery. High

order-polysulphides (S_n^{2-}, n=8-4) and low order-polysulphides (S_n^{2-}, n=2-1) are abbreviated as HO-PSs and LO-PSs. The onset potential (*U*) and the capacity (*Q*) in the dissolution and precipitation regime are noted, which facilitates the analysis of the electrochemical properties of each sample. b, Rate performance of the GQDs-S/CB and S/CB at 0.1 *C* to 10 *C*. c, cycling performance and Coulombic efficiency at 0.5 *C* of both samples for 100 cycles. d,f, Onset potential as a function of cycle number and e,g, capacity as a function of rate and capacity as a function of cycle number.

Figure 4. High resolution C 1*s* X-ray photoemission spectroscopy (XPS) and computational calculations a, S and GQDs-S composites before cycling. b, C 1*s* and c, S 2*p* high resolution spectra of the S/CB and GQDs-S/CB electrodes after 20 cycles. Each spectrum was fitted with functions corresponding to different valencies of carbon and sulphur (dashed line) and the sum of those fitted curves (red line) is consistent with the raw data (black solid line). d, C 1*s* spectra of CB and GQDs/CB electrodes in Li_2S_8 catholyte. e, Raman spectra showing C-S bond formation within the samples. f, XRD spectra of GQDs/CB and CB electrodes in in a Li_2S_8 catholyte. g, A plot of the relative energies for the reactant and product in binding of polysulphides to GQDs, versus the sulphur chain length. The functional groups on GQDs enhance the binding of polysulphides to the carbon due to the substitution of -OH (C-OH) to Sn^{2-}. Yellow, red, white, and gray represents S, O, H, and C atoms, respectively.

Figure 5. TEM and SEM images of nano-sized sulphur on GQDs electrode in Li_2S_8 catholyte after 20 cycles. a,TEM image of nano-sized sulphur in GQDs materials.

The aggregate seen in the TEM is mainly comprised of GQDs, and sulphur is identified as the small darker particles. b, GQDs (yellow circle) covered on nano-sized sulphur particles, c, HRTEM image that shows the lattice fringes of the nano-sized sulphur and GQDs. d, The FFT image of the HRTEM image in c. The two bright spots represent Bragg spots for the sulphur particles, and the other spots are GQDs Bragg spots. e, SEM image of the GQDs electrode in the catholyte after cycling. f-h, C, S, and O energy-dispersive X-ray (EDX) spectroscopy maps of the GQDs electrode.

Figure S1. Scanning electron microscopy and energy-dispersive X-ray spectroscopy characterization of the GQDs-S composites. SEM images of the GQS-S composites, and C, S, and O EDX maps of the GQDs-S composites.

Figure S2. Scanning transmission electron microscopy and EDX characterization of the GQDs-S/CB composites. TEM images of the GQS-S/CB composites, and C, S, and O EDX maps of the GQDs-S/CB composites.

Figure S3. X-ray diffraction (XRD) patterns and Thermogravimetric analysis (TGA). XRD of sulphur, GQDs-S, and GQDs-S/CB composites a, and TGA collected in N_2 atmosphere with a heating rate of 10℃/min b, the S content of the cathode.

Figure S4. X-ray photoelectron spectroscopy of S/CB, and GQDs-S/CB particles. a, C 1*s* peaks, b, S 2*p* peaks, and c, O 1*s* peaks of S/CB and GQDs-S/CB particles.

Figure S5. a, Cycling performance and b, discharge profile of GQDs-S/CB, modified S/CB, and S/CB at 0.05 *C* for 100 cycles. The GQDs-S/CB electrode shows superior cycle retention compared to S/CB and modified S/CB, which indicates that

the surfactant alone does not prevent dissolution of the sulphide discharge-products into the electrolyte.

Figure S6. Charge-discharge profiles of a, S/CB and b, GQDs-S/CB at 0.5 *C* for 100 cycles.

Figure S7. Rate performance of a, S/CB and b, GQDs-S/CB from 0.1 *C* up to 10 *C*.

Figure S8. Relative ratios of dissolution/precipitation regime capacity (Q_2/Q_1). a, Cycling performance up to 100 cycles. b, Rate performance from 0.1 *C* to 10 *C*.

Figure S9. Electrochemical impedance spectroscopy (EIS). Lithium/sulphur cells a, as-prepared, b, fully charged, and c, discharged state after 20 cycles. Insets show the high-frequency range. The equivalent circuit model used to analyze the Nyquist plots d, charge-discharge states.

Figure S10. High resolution C 1*s* X-ray photoelectron spectroscopy a,b, C 1 *s* spectrum of the S/CB and GQDs-S/CB electrodes after 20 cycles in the di scharged state. Each spectrum has been fitted with peaks for different bonde d carbon (dashed line) and the sum of the fitting curves (red line) is consist ent with the raw data (black solid line).

Figure S11. SEM images of GQDs-S/CB and S/CB cathode electrodes after electrochemical cycling. a,b, GQDs-S and S electrodes after cycling.

Figure S12. SEM images and Raman spectra of lithium anodes after cycling against S/CB and GQDs-S/CB electrodes. a,d, SEM images after 20 cycles. b,e, Sulphur energy-dispersive X-ray spectroscopy maps. c,f, Raman spectra. The S peaks are assigned to 156, 221, 473 cm^{-1}, Li_2S to 378 cm^{-1}, and S^{2-} to 746 cm^{-1} (ref. 2). No peaks are present in the cell containing GQDs-S/CB.

Figure S13. High resolution S 2*p* X-ray photoelectron spectroscopy and cycl e performance. a,b, S 2*p* spectrum of the CB and GQDs electrodes, in the charge state, after 20 cycles. These electrodes were cycled in the Li_2S_8 cath olyte. Each spectrum was fitted with functions corresponding to different valencies of sulphur (dashed line) and the sum of these fitted curves (red line) is consistent with the raw data (black solid line). c, Cycle retention of GQDs/CB and CB el ectrodes in Li_2S_8 catholyte over 100 cycles.

Figure S14. The relative energies for the reactant and product in binding of polysulphides to GQDs. The functional groups enhance the binding of polysulphides to carbon due to substitution of –OH (C-COOH) for S_n^{2-}. Yellow, red, white, and gray represents S, O, H, and C atoms, respectively.

Figure S15. TEM images of nano-sized sulphur on a CB electrode in Li_2S_8 catholyte after 20 cycles. a, Bright field STEM image of the CB electrode. b-d, Energy-dispersive X-ray spectroscopy maps of C, S, and O of the CB electrode in the Li_2S_8 catholyte. e, SEM image of the CB electrode in the Li_2S_8 catholyte after cycling. f-h, C, S, and O EDX maps of the GQDs electrode.

Figure S16. HRTEM (high-resolution transmission electron microscopy) images of nano-sized sulphur on GQDs electrode in Li_2S_8 catholyte after 20 cycles. a, TEM image of nano-sized sulphur in the GQD electrode. b, The FFT of the selected region in image, a. The ring pattern of graphene quantum dots. c, Magnification of nano-sized sulphur in image a shows the lattice fringes of sulphur and GQDs. d, The FFT of the selected area in image, c.

List of Tables and Schemes

Chapter 1

Chapter 2

Chapter 3

Chapter 4

Chapter 7

Table S1. Summary of XPS quantitative values of each elements in Figure S4

Table S2. Summary of numerical values of each component (U_1, U_2, Q_1, Q_2, and Q_{total}) with selected cycles for S/CB at 0.5 *C*

Table S3. Summary of numerical values of each component (U_1, U_2, Q_1, Q_2, and Q_{total}) with selected cycles for GQDs-S/CB at 0.5 *C*

Table S4. Summary of numerical values of each component (U_1, U_2, Q_1, Q_2, and Q_{total}) with various C-rates for S/CB

Table S5. Summary of numerical values of each component (U_1, U_2, Q_1, Q_2, and Q_{total}) with various C-rates for GQDs-S/CB

Chapter 1

General Introduction

Hydrogen evolution reaction

The hydrogen production from water under solar energy is considered as one of renewable energy sources and important environmental-issues. However, the development of efficient photoelectrodes and related co-catalyst for water splitting is still challenges in hydrogen production. Considering the thermodynamic potential, a single-component semiconductor with a higher band gap than 1.23V can simultaneously generate hydrogen and oxygen gas from water as well as its band structure is in their proper positions. However, overall water splitting by one single-component semiconductor is still hampered by the poor kinetics in although several semiconductor have band-edge positions that are appropriate for the photoelectrochemical reduction of water. Overcoming this kinetic limitation requires a stronger driving force. Until now, the solar-to-hydrogen conversion efficiency of single-component semiconductor is still under 5%[1], which stimulates photoelectrochemical cells to be separated as cathode and anode electrodes as well as co-catalyst for water splitting also became one of the most important and challenging issues for photoelectrochemical hydrogen production. A critical requirement for outstanding catalysts in a photoelectrochemical cell is not only the ability to boost the kinetics of a chemical reaction but also durability against electrochemical and photoinduced degradation.[12]

General description of HER and catalyst for HER

The oxidation reaction in the electrolysis of water is:[12]

$O_2 + 4e^- + 4H^+ \leftrightarrow 2H_2O$ $E_{anodic} = 1.23\ V - 0.059(pH)\ V\ (vs.\ NHE)$ (1)

while the reduction reaction is:

$4e^- + 4H^+ \leftrightarrow 2H_2$ $E_{cathodic} = 0\ V - 0.059(pH)\ V\ (vs.\ NHE)$ (2)

Where, NHE is the Normal Hydrogen Energy and the standard potential is dependent on pH ($E_{half} = E - 0.059(pH)$ vs NHE). In these two equations, the thermodynamic potential of water splitting ($E^o_{cell} = 1.23V$) is observed by subtracting (2) from (1). Kinetically, however, when a voltage of 1.23V is applied, electrolysis occurs with difficulty, which results in no current flow. In this situation, additional potential is needed to drive a reaction at a certain rate, which is called overpotential, η. Meanwhile, if a current of i_c flows at the cathode, the same current of i_a must flow at the anode to complete the circuit. Because of this, both electrodes (anode and cathode) need the overpotential. Figure 1 shows current to potential curve for the water-splitting reaction. The red line and blue line indicates oxidation and reduction reaction of water electrolysis, respectively. The overpotential at the cathode and anode is written η_c and η_a, respectively. Therefore, total applied potential, E_{appl}, is:[12]

$$E_{appl}=1.23V+\eta_c+\eta_a \quad (3)$$

Higher overpotential requires higher total applied voltage. Using an electrocatalyst for water splitting can reduce the overpotential required for electrolysis of water.

The hydrogen evolution reaction can be written as:

$$H^+ + e^- \rightarrow 1/2H_2 \quad (4)$$

Its standard potential is 0 V vs. NHE and the potential is dependent on pH (E = 0 V – 0.059(pH) vs NHE). Mechanistically, for the HER in acidic solution, the following possible reaction steps have been suggested.[16]

$$H_3O^+ + e^- \rightarrow H_{ads} + H_2O \quad (5)$$

$$H_{ads} + H_3O^+ + e^- \rightarrow H_2 + H_2O \quad (6)$$

$$H_{ads} + H_{ads} \rightarrow H_2 \quad (7)$$

where H_{ads} is the adsorbed hydrogen atom on the surface. Eq. (5) is a discharge step (the Volmer reaction), eq. (6) is a desorption step (the Heyrovsky reaction), and eq. (7) is a recombination step (the Tafel reaction). Therefore, two different pathways for HER can occur. A combination of eq. (5) and (7) step is known as the Volmer-Tafel mechanism. In this mechanism, protons from the solution are discharged on the surface, forming adsorbed hydrogen atoms. Then, two adjacent adsorbed hydrogen atoms combine to form molecular hydrogen. The combination of eq. (5) and (6) is known as the Volmer-Heyrovsky mechanism. A proton from the electrolyte solution is discharged on the catalyst surface to form an adsorbed hydrogen atom. This step is followed by combination with another proton and electron to form molecular hydrogen. However, for the reaction to proceed at a sufficient rate, it needs to be catalyzed on an electrode surface. Possible candidates for an HER catalyst include various metals such as Pt, Pd, and Ru as well as metal oxide, carbon, and enzymes with active centers. Using Pt catalyst for HER, equations (8) – (10) can be described as follows:[2]

$$Pt + H^+ + e- \rightarrow H\text{-}Pt \qquad \text{Volmer reaction} \quad (8)$$

$2(H\text{-}Pt) \rightarrow H_2 + 2Pt$ Tafel reaction (9)

$H\text{-}Pt + H^+ + e^- \rightarrow H_2 + Pt$ Heyrovsky reaction (10)

HER activity of the catalyst can be characterized by representative parameters; the exchange current density and the bond energy of hydrogen adsorbed to the catalyst.[3] During hydrogen evolution, a current I can be described as:[4]

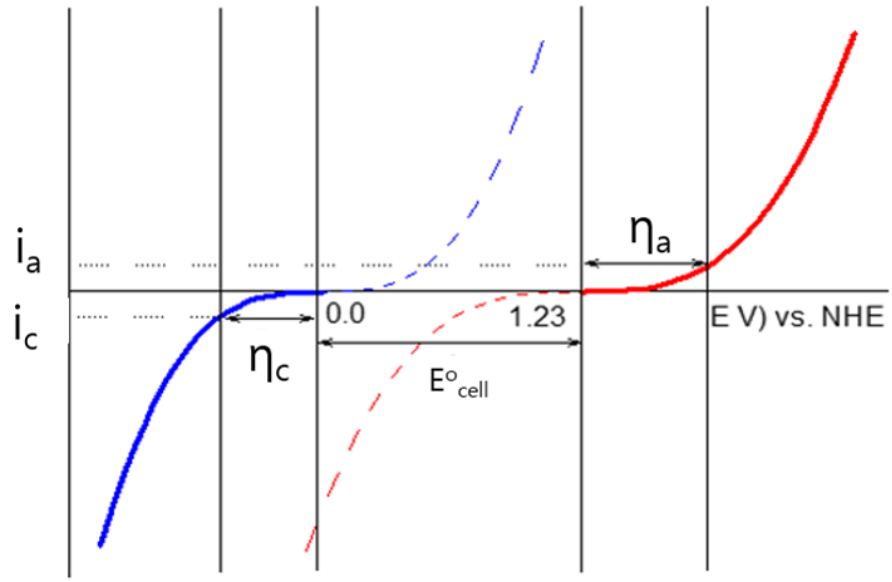

Figure 1. Schematic of the current to potential curve of water splitting reaction

Carbon based HER electrocatalysts

The design of the carbon-based catalysts can represent an important research direction in the search for non-precious, environmentally benign, and corrosion resistant catalysts. In particular, graphene possesses excellent transmittance and superior intrinsic carrier mobility,[5] thus there have been several attempts to use graphene as a catalyst. It has been reported that the reduced graphene oxide (rGO) containing catalytic active materials exhibited an improved activity in HERs as well as oxygen evolution reactions (OERs) or oxygen reduction reactions (ORRs).[6] However, in most cases, the role of carbon materials is limited to an electrical conducting substrate or a supporter that enhances the performance of other decorated active catalysts. Recently, new possibilities have been investigated that monolayer graphene acts as an electrocatalyst for efficient HER.[7] Uk Sim et al., reported that monolayer graphene acts as a catalyst for hydrogen evolution reaction on Si-electrode and boost their catalytic activity by plasma treatment in N_2-ambient.[7] Plasma treatment induces the abundant defects and the incorporation of nitrogen atom in graphene structure, which can act as catalytic sites on graphene. Monolayer graphene containing nitrogen impurities exhibits a remarkable increase in the exchange current density and leads to significant anodic shift of the onset current from a Si-electrode. The electro-catalytic activity of the carbon-based catalyst was much lower than other metal-based catalysts, but the HER

activity of carbon catalyst has increased gradually. The J_0 of monolayer graphene is also comparable to that of the other non-noble metal catalyst, nanoparticulate MoS_2.[7,8,9] J_0 can be accurately calculated by considering the number of active sites. For example, the J_0 of MoS_2 for the HERs is experimentally measured to be 1.3×10^{-7} to 3.1×10^{-7} $A/cm^2_{geometric}$.[9]Active sites of MoS_2 nanoparticle for HER are known to be edge sites of MoS_2 nanoparticle.[10] For the direct site-to-site comparison between MoS_2 nanoparticle and Pt catalyst, T. Jaramillo *et al*. have measured an exchange current per site of MoS_2 combined with STM analysis.[9] The exchange current per site is then multiplied by the site density of Pt for a fair comparison to the transition metal catalyst, resulting in the exchange current density of 7.9×10^{-6} A/cm^2. This value is still similar to exchange current density of monolayer graphene (2.7×10^{-6} A/cm^2). To sum up, while the representative carbon-based catalyst, graphene, has the catalytic activity for HER, the identification and quantification of the active sites of the single monolayer graphene should be further investigated for comparative study.

Recently, a metal-free carbon catalyst doped with nitrogen and phosphorous showed good activity for HER (Figure 2 (c) - (d)). Co-activated N and P heteroatom, which is adjacent to C atom in the graphene matrix, could affect its valence orbital energy levels to enhance reactivity for HER. Graphitic-carbon nitride with nitrogen-doped graphene also shows enhanced

HER activity with similar low overpotential and Tafel slope compared to some well-developed metallic catalysts. Through the density functional theory calculations, it is known that intrinsic chemical and electronic coupling of graphitic C_3N_4 and N-doped graphene synergistically promotes the proton adsorption and reduction kinetics. Table 1 summarizes a selection of experimental values of exchange current for the hydrogen evolution on carbon-based catalysts.

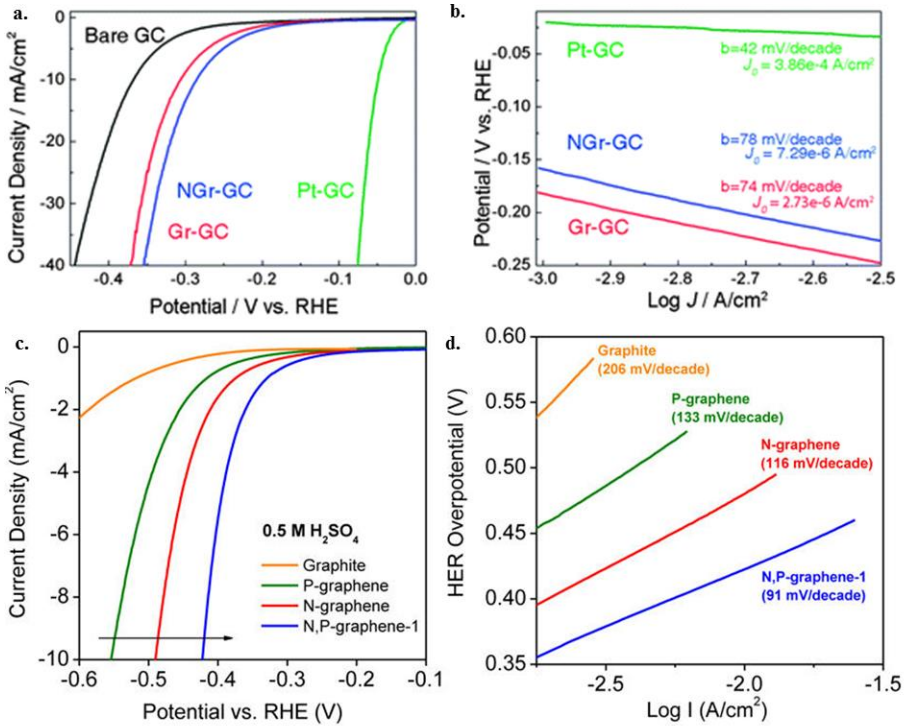

Figure 2. Electrochemical properties and chemical structure of graphene based electrodes (a) CV curve of GC, Gr on GC, NGr on GC, and Pt on GC from a rotating disk electrode system. (iR corrected) (b) Tafel plots were derived from (a) CV data. (c, d) HER polarization curves and the corresponding Tafel plots of N- and/or P-doped graphene electrocatalysts. Reprinted with permission (a), (b) from ref. Copyright 2013 The Royal Society of Chemistry and (c), (d) from ref. [116] Copyright 2014 American Chemical Society.

Catalyst/Substrate (adhesive)	Loading method	Electrolyte	Activity			Ref. (Year)
			Tafel Slope (mV/dec)	TOFs (S^{-1})	Exchange current –log(j_0) (A/cm^2)	
Monolayer graphene	CVD grown graphene	1M HClO4	(75)	N/A	7.57	(2013)
N doped Gr	Annealing mixed precursors	0.5M H_2SO_4 0.1M KOH	(116) (143)	N/A	7.15 9.93	(2014)
P doped Gr	Annealing mixed precursors	0.5M H_2SO_4 0.1M KOH	(133) (159)	N/A	8.05 10.79	(2014)
N,P doped Gr	Annealing mixed precursors	0.5M H_2SO_4 0.1M KOH	(91) (145)	N/A	6.62 9.40	(2014)
g-C_3N_4@NG/GC (Nafion)	Exfoliation & Polycondensation	0.5M H_2SO_4	(51.5)	N/A	6.46	(2014)

Table 1. Selection of experimental values of Tafel slope and exchange current for the hydrogen evolution on carbon based catalyst system. Loading method and electrolyte used are described.

References

1. A. Kudo, Y. Miseki, *Chemical Society Reviews* **2009**, *38*, 253-278.
2. J. Larminie, A. Dicks, M. S. McDonald, *Fuel cell systems explained, Vol. 2*, Wiley New York, **2003**.
3. H. Wolfschmidt, O. Paschos, U. Stimming, in *Fuel Cell Science*, John Wiley & Sons, Inc., **2010**, pp. 1-70.
4. B. E. Conway, G. Jerkiewicz, *Electrochimica Acta* **2000**, *45*, 4075-4083.
5. K. Novoselov, A. K. Geim, S. Morozov, D. Jiang, M. K. I. Grigorieva, S. Dubonos, A. Firsov, *Nature* **2005**, *438*, 197-200.
6. aY. Liang, Y. Li, H. Wang, J. Zhou, J. Wang, T. Regier, H. Dai, *Nature Mater.* **2011**, *10*, 780-786; bJ.-D. Qiu, G.-C. Wang, R.-P. Liang, X.-H. Xia, H.-W. Yu, *J. Phys. Chem. C* **2011**, *115*, 15639-15645; cQ. Xiang, J. Yu, M. Jaroniec, *Chem. Soc. Rev.* **2012**, *41*, 782-796.
7. U. Sim, T.-Y. Yang, J. Moon, J. An, J. Hwang, J.-H. Seo, J. Lee, K. Y. Kim, J. Lee, S. Han, B. H. Hong, K. T. Nam, *Energy Environ. Sci.* **2013**, *6*, 3658-3664.
8. J. Kibsgaard, Z. Chen, B. N. Reinecke and T. F. Jaramillo, *Nat Mater*, **2012**, 11, 963-969.
9. T. F. Jaramillo, K. P. Jørgensen, J. Bonde, J. H. Nielsen, S. Horch, I. Chorkendorff, *Science* **2007**, *317*, 100-102.
10. Y. Li, H. Wang, L. Xie, Y. Liang, G. Hong, H. Dai, *Journal of the American Chemical Society* **2011**, *133*, 7296-7299.
11. Y. Zheng, Y. Jiao, L. H. Li, T. Xing, Y. Chen, M. Jaroniec, S. Z. Qiao, *ACS Nano* **2014**, *8*, 5290-5296.
12. U. Sim, K. Jin, S. Oh, D. Jeong, J. Moon, J. Oh, K. T. Nam, *Handbook of Clean Energy Systems*, 2015.

Part Ⅰ

N-doped Graphene for Hydrogen Evolution Reaction (HER)

Chapter 2

One-step synthesis of N-doped graphene quantum sheets from monolayer graphene by nitrogen plasma

Introduction

Recently, graphene quantum dots (GQDs) has been attracting much attention in bioimaging, light-emitting, and photovoltaic applications[1–3] due to its unique optical properties depending on size and functional edge as well as the accessibility to solution chemistry.[4–6] This has stimulated tremendous efforts to develop various synthesizing methods such as hydrothermal cutting,[7] patterning by nanolithography,[8] and electrochemical scissoring of graphene sheets,[9] as well as bottom up synthesis by wet chemistry to produce GQDs with different sizes and functionalities.[6] Usually, these methods require strongly acidic environment or time-consuming multi-step processes, which is a drawback for more efficient synthesis of high-quality GQDs. Moreover, in order to be used for various optoelectronic and energy applications, GQDs often need to be fabricated as a thin-film structure on a solid interface. However, the GQDs in aqueous solvent are hardly processible because they are unstable in aqueous environment. In addition, preparing GQD films from aqueous dispersion is challenging because spin coating or drop-casting method doesn't provide enough control over thickness and uniformity as well as it requires rigid and flat surface rather than flexible or conformal substrates. Plasma treatment is one of the facile ways to tune the intrinsic properties of graphene, and previously, oxygen plasma was applied to prepare chemically functionalized graphene showing uniform photoluminescence and Raman spectral changes originated from its defective structures.[10,11] On the other hand, chemical doping is an effective way to tune the optical, chemical, and electronic properties of graphene.[12] Likewise, the band-gap of GQDs can be engineered by changing size, shape, edge-, and surface

functionalities,[6,13,14] leading to tunable photoluminescence with higher intensity. In particular, the functional modification with nitrogen could offer more active sites needed for higher catalytic activities, which is important for various energy applications.[9] Herein, we introduce a simple one-step method to prepare large-scale N-doped GQSs by directly applying nitrogen plasma to as-grown graphene on Cu, which can be transferred as a film like layer or easily dispersed in an organic solvent. Moreover, we confirm that the N-GQSs transferred on flat Si and porous Si can be a good photoelectrochemical catalyst for hydrogen evolution reaction (HER). Atomic force microscopy (AFM) and transmission electron microscopy (TEM) images show that the average size of N-GQSs is 4.84 nm, and the substitution of carbon with nitrogen is evidenced by Raman spectroscopy and X-ray photoelectron spectroscopy (XPS). The unique optical properties of N-GQSs were confirmed by absorption and photoluminescence spectra, showing strong emission with the maximum wavelength of 430 nm when excited by 365 nm radiation source (Xe lamp).

Experimental

Synthesis of graphene quantum sheets

In the first step of graphene synthesis, a copper foil was put into a quartz reactor in the CVD system and then heated to 1000℃ with flowing H_2 at 70 mTorr. Additionally, the sample was annealed for 20 min without changing the condition. The gas mixture of H_2 and CH_4 was flowed with rates of 5 and 50 SCCM for 30 min under 8 Torr. Finally, the sample was rapidly cooled down to room temperature with flowing H_2. After growth, in order to remove graphene on one of the sides of Cu foil, graphene on Cu was placed into the plasma chamber (SNTEK). The chamber pressure was pumped down to 50 mTorr, and O_2 gas was introduced into the chamber by applying a radio-frequency (13.56 MHz) forward power of 100 W for 10 s. In addition, to make N-GQS on the front side of Cu, low density N_2-plasma was produced by applying 10 W power. The N_2 flow rate was 20 SCCM and the working pressure of the chamber was 120 mTorr. Under these conditions, the N_2 plasma treatments were performed for 14 s to test the electrochemical reaction of the graphene surface. Finally, poly(methyl methacrylate) (PMMA) was spincoated on graphene and then copper foil was removed in 0.1 M ammonium persulfate solution. After washing with deionized water, the graphene was transferred onto the Si substrate and then PMMA was removed in acetone for 30 min.

Characterization

Raman spectra were obtained with a Renishaw micro-Raman spectroscope with an excitation wavelength of 514.5 nm, an Ar laser. The spot diameter was approximately 2 mm with a 50x objective lens. The oxygen plasma treatment (SNTEK) was carried out with a 100 W radio-frequency (rf) power for 13 s under 140 mTorr and the nitrogen plasma was accelerated with a 10 W rf power for several exposure times (14 s) under 120 mTorr. XPS spectra were collected by AXIS Ultra DLD (Kratos. Inc) using a monochromatic Al K (1486.6 eV), 150 W source at Korea Basic Science Institute (KBSI). Narrow-scan data were collected using a pass energy of 40 eV and 0.05 eV per step.

Calibration with respect to relative hydrogen electrode

The Ag/AgCl/3 M NaCl electrode (BASi) was used as the reference electrode. Pt foil (2 cm x 2 cm x 0.1 mm, 99.997% purity, Alfa Aesar) was used as the counter electrode. In the case of RDE experiment, Pt wire (0.1 mm diameter, Dr Bob's cell) was used as the counter electrode. It was carefully calibrated with respect to the reversible hydrogen electrode (RHE) in an aqueous 1 M perchloric acid solution (Sigma Aldrich) with high purity H_2 saturation at 25℃. The RHE was calibrated to between -0.201 V and -0.203 V vs. the Ag/AgCl reference electrode. The potential was controlled using a potentiostat (CHI 600D, CH Instrument) at a scan rate of 5 mV s^{-1}.

Results and Discussion

First, the monolayer graphene was synthesized by using 10 × 10 cm^2 Cu foils as catalytic substrates in 1000℃ quartz reactor with flowing 50 sccm CH_4 and 5 sccm H_2 for 30 min under 8 Torr.[13] Next, the N-GQSs were prepared by irradiating nitrogen plasma (10 W RF power with varying exposure time under 120 mTorr) to as-grown CVD graphene on Cu as shown in Figure 1. Finally, the N-GQSs were transferred using conventional polymer-assisted dry-transfer methods on a target substrate after removing Cu by 0.1 M aqueous ammonium persulphate etchant.[15] Alternatively, the floating N-GQSs after removing Cu without PMMA can be dispersed into common organic solvent such as dichloromethane using solvent extraction techniques.

The AFM images in Figure 2 a-d show the gradual increase of surface roughness with increasing nitrogen plasma treatment time, indicating that the as-grown graphene on Cu is directly converted N-GQSs. The AFM height profile of N_2-plasma treated graphene for 16 sec shows the average height of 1.64 ± 0.06 nm (Figures S1 and S2).

Figure 3 a-b show the N-GQSs film directly transferred from Cu to a SiO_2 substrate after coating with poly(methyl methacrylate) (PMMA) layer. The PMMA can be easily removable by acetone. Figure 3 c-d show the N-GQDs drop-cased ontoa SiO_2 substrate from the suspension in dichloromethane. The atomic structures of N-GQSs were investigated by high-resolution transmission electron microscopy (HRTEM) as shown in Figure. 3e-g. The sample was prepared by drop-drying the N-GQSs solution on a graphene-supported TEM grid.[16]

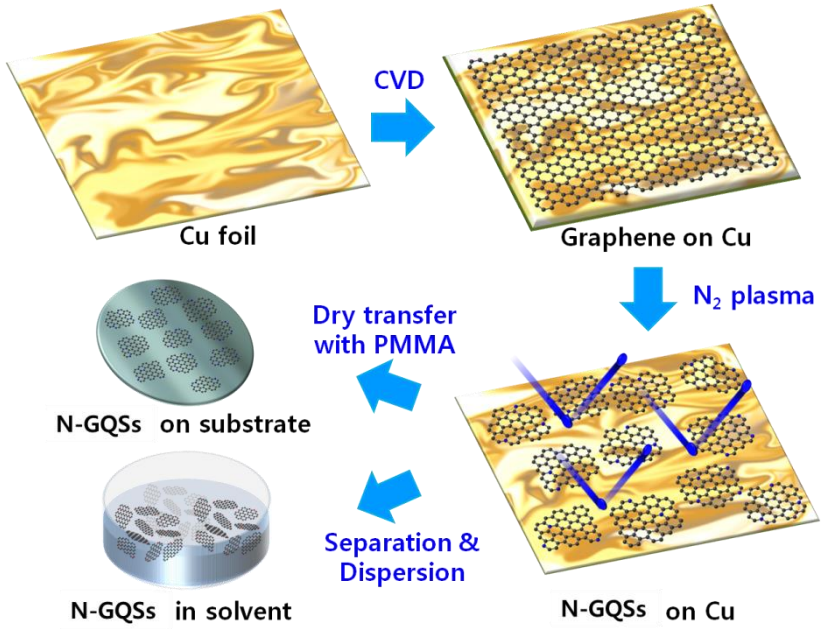

Figure 1. Schematic illustration of N-GQSs fabrication processes.

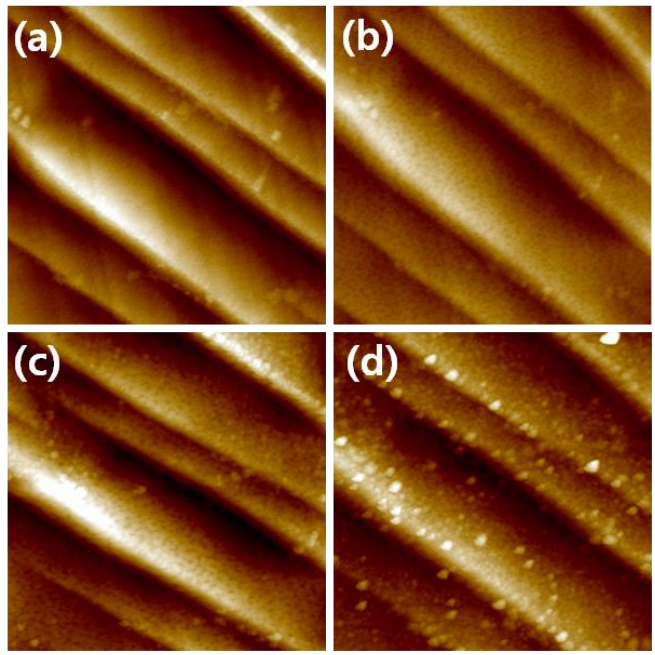

Figure 2. (a-d) AFM images of graphene on Cu surface after exposure to nitrogen plasma for 0, 2, 4, and 6 sec, respectively. Scan sizes, 1.5 x 1.5 μm^2. The AFM images were obtained from a fixed position.

Most of N-GQSs show a size distribution from 3 to 7 nm with an average value of 4.84 nm (Figure 3 h). The clear atomic lattice structure shown in Figure 3 g indicates that the N-GQSs are highly crystalline.

After exposure to nitrogen plasma, the D peaks related structural defects at the edges of graphene were signifi cantly increased in Raman spectra (Figure 4 a).[17,18] On the other hand, the shift of D and 2D peaks indicates that the graphene is doped with nitrogen atoms.[19] X-ray photoelectron spectroscopy (XPS) measurements were performed to determine the chemical composition of N-GQSs (Figure 4 b-d). No N 1*s* peak was observed in monolayer graphene. The strong C 1*s* peak at 284.8 eV corresponding to sp^2 carbon indicates that the conjugated honeycomb lattices are mostly maintained after N_2-plasma treatment. We suppose that the oxygen related sub peaks such as C-O (286.6 eV), C=O (288.3 eV), and O-C=O (289 eV) are originated from the reaction of unstable N-GQS edges or defects with oxygen when exposed to air. The C-N bond peak at 285.2 eV in C 1*s* spectrum (Figure 4 c) as well as the pridinic (398.5 eV) and pyrrolic (399.9 eV) peaks in N 1*s* spectrum (Figure 4 d) indicate that nitrogen-to-carbon ratio is ～2.7%. The UV-vis absorption spectrum of the N-GQSs shows an absorption band with a peak maximum (λ_{max}) at 270 nm (Figure 4 e). The PL spectrum exited at 370 nm shows a strong peak at λ_{max} = 430 nm. Thus, the N-GQDs emitted intense blue luminescence under 365 nm wavelength irradiation by UV lamp (Figure 4 e, inset). We found that the λ_{max} in PL spectra is almost invariable with varying excitation wavelength from 360 nm to 420 nm.

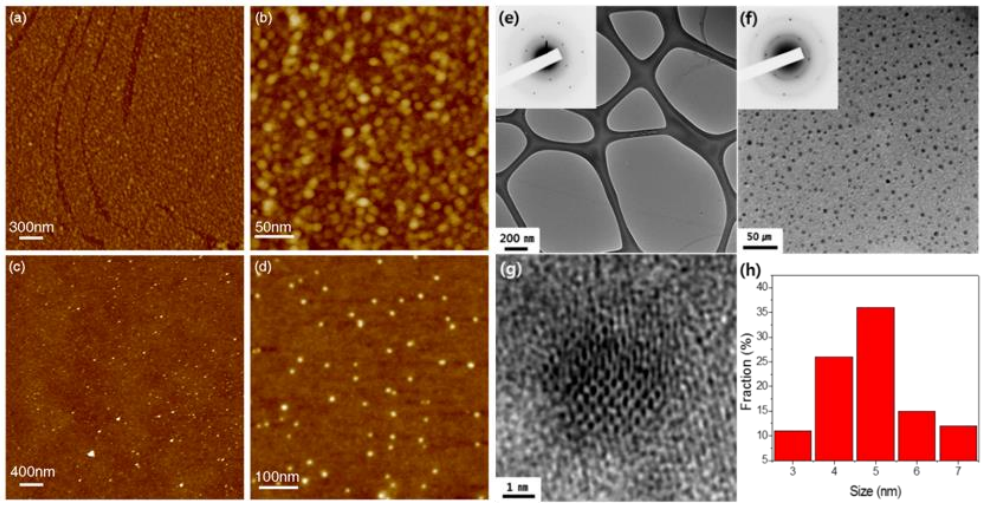

Figure 3. (a, b) AFM images of the N-GQSs transferred to a SiO_2 substrate using polymer-support layer (PMMA). (c, d) AFM images of N-GQS drop-casted from solution to a SiO_2 substrate. Scan sizes, 10 x 10 m^2 for a and c, 1.5 x 1.5 m^2 for b and d, respectively. See Supporting Information of detailed AFM analyses (Figure. S1 and S2). (e) TEM image of monolayer graphene supported by holely carbon grids. (f, g) Low and high-resolution TEM images of N-GQSs on a graphene-supported grid. (h) Histogram showing the size distribution of N-GQS and the average size of N-GQS is 4.84 ± 0.06 nm. The insets in e and f show selected area diffraction patterns (SAED) of graphene and N-GQS.

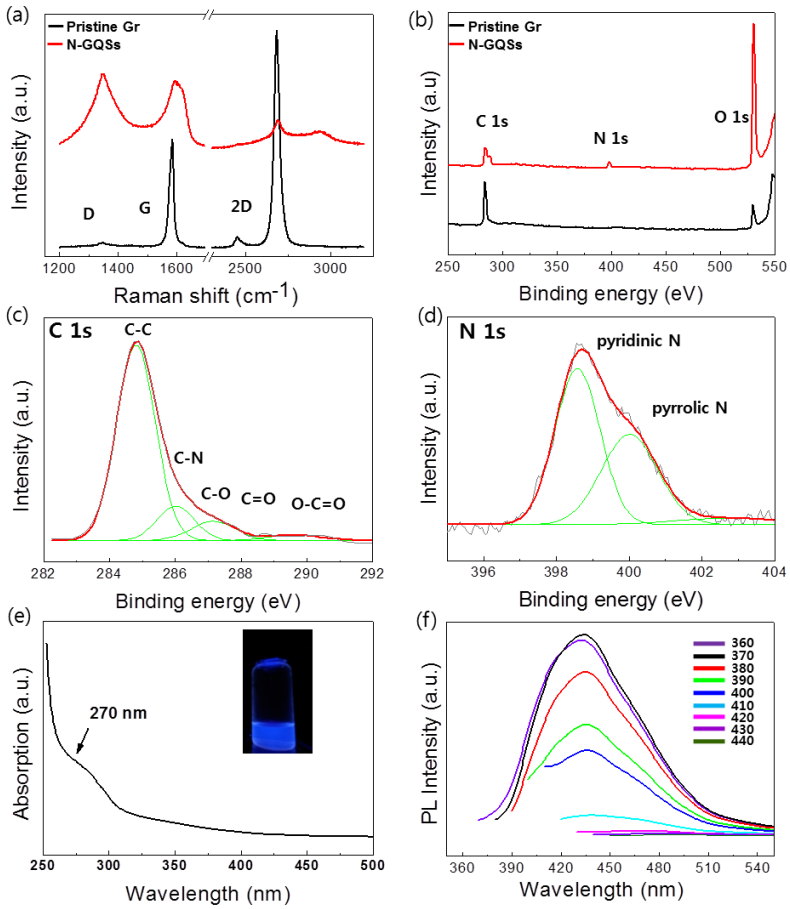

Figure 4. (a) Raman spectra and (b) XPS spectra of as-grown graphene and N-GQS. (c, d) Detailed C 1*s* and N 1*s* XPS peaks of N-GQS. (e) UV-vis absorption spectra of N-GQS in dichloromethane. The inset shows a photograph of the N-GQS solution under 365 nm wavelength UV lamp. (f) Photoluminescence (PL) spectra of the N-GQS for different excitation wavelengths (360~440 nm).

Recently, graphene based catalyst becomes an attractive candidate for photoelectrochemical reaction.[20,21] **Figure 5** demonstrates the catalyst application of N-GQSs on a flat bare Si and a porous Si substrates for hydrogen production. The scanning electron microscopy (SEM) images in Figure 5 a-b show the cross section of a bare Si and a porous Si and each inset shows the top-view of the sample. To evaluate the photocathodic behavior, N-GQSs were loaded on a bare Si with the dry transfer and on a porous Si with the solution drop-casting. The photocurrent density was measured as potential sweep from 0.4 V to –0.8 V *vs*. Reversible Hydrogen Electrode (RHE) in a three electrode cell. A light source of a 300 W Xe lamp (100 mW cm^{-2}) with an Air Mass 1.5 Global condition filter was illuminated on the samples in an aqueous 1 M perchloric acid solution (pH 0) (Figure S3). Interestingly, the N-GQSs exhibit the superior catalytic activity for HER. As shown in Figure 5 c, the photocurrent density-potential (*J*–*E*) curve of N-GQSs/bare Si dramatically is shifted approximately ~0.35 V toward positive potential compared to that of the bare Si as well as the onset potential of N-GQSs also positively shifted by 0.29 V (Table S1). Compared to bare Si, porous Si exhibits enhanced limiting current density and positive shift of onset potential ascribed to light trapping effect. In N-GQSs on a porous Si substrate, the positive shift in 0.09 V of the onset potential also shows higher activity for HER compared to that of a porous Si. Figure 5 d shows the electrocatalytic activity of N-GQSs, CV curves of the samples were obtained without illumination with rotating disk electrode (RDE) system. For the working electrode, N-GQSs were transferred to a glassy carbon tip which is inert in aqueous solution. The *J*–*E* curves were swept from 0.1 V to –0.35 V and the onset potential were

obtained –5 mA cm^{-2} of HER current density of as-grown graphene and N-GQSs (Table S1). The onset potential of N-GQSs is –0.22 V with respect to RHE, which has positive shift by 0.07 V compared to that of as-grown graphene. This result is similar to the photoelectrochemical behavior of the *J*–*E* curves, a positive shift in the overall *J*–*E* curve induced by N-GQSs. From the above results, we conclude that the N-GQSs show the superior electrocatalytic effect for hydrogen production when combined with Si photocathodes with arbitrary morphologies.

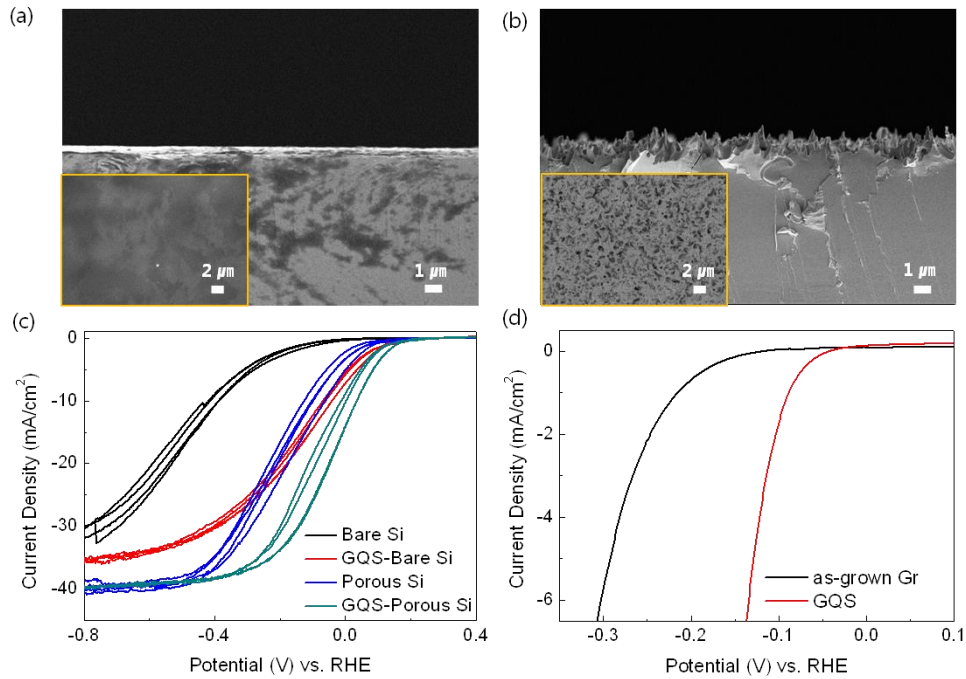

Figure 5. SEM images of (a) bare Si and (b) porous Si. Cyclic Voltammetry (CV) of N-GQS on bare Si and porous Si. (c) Photocurrent density-potential (*J-E*) curves for the lightly boron doped p-Si and p-porous Si electrode deposited with N-GQS. N-GQS was introduced by dry transfer on bare Si and by wet transferred on porous Si. Each CV process was performed at a scan rate of 0.005 Vs^{-1}. (**d**) Electrochemical activity of N-GQS on a Glassy Carbon (GC) electrode with rotating ring disk system. CV data were corrected by iR compensation.

Conclusions

In summary, we have demonstrated the formation of N-doped GQSs from as-grown monolayer graphene on Cu using nitrogen plasma. Various spectroscopic analyses including AFM, TEM, XPS, Raman, and PL indicate the direct formation of high-quality N-GQSs from CVD graphene. The N-GQSs can be transferred onto an arbitrarily shaped photocathode surface to enhance the catalytic activity for photoelectrochemical hydrogen evolution, which would be also useful for various display, energy, and biological applications.

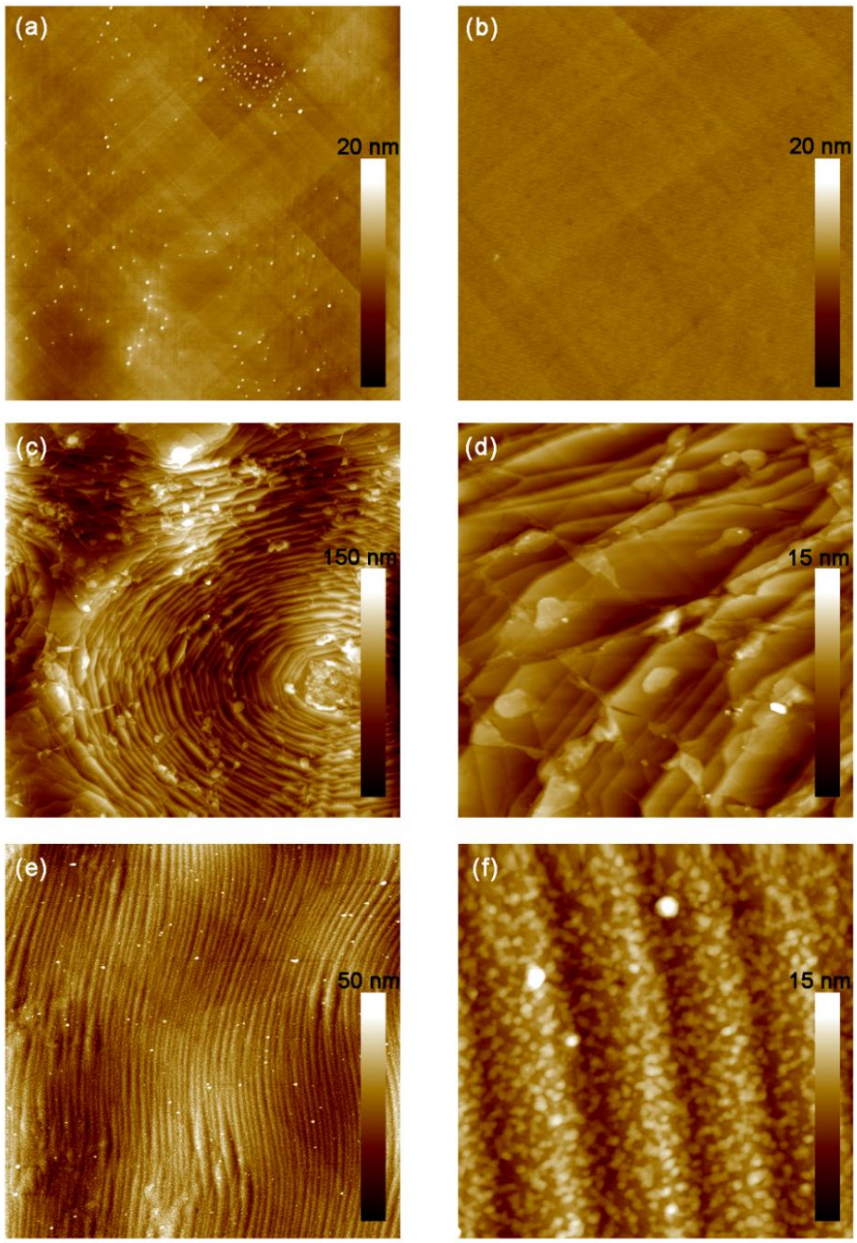

Figure S1. (a, b) AFM surface morphologies of Cu foils annealed at 1,000˚C. (c, d) AFM images of continuous monolayer graphene film grown on Cu by CVD. (e, f) AFM images of N-GQSs converted from monolayer graphene on Cu after N_2-plasma treatment. Scan sizes, 10 x 10 μm^2 for a, c, and e, 1.5 x 1.5 μm^2 for b, d, and f, respectively.

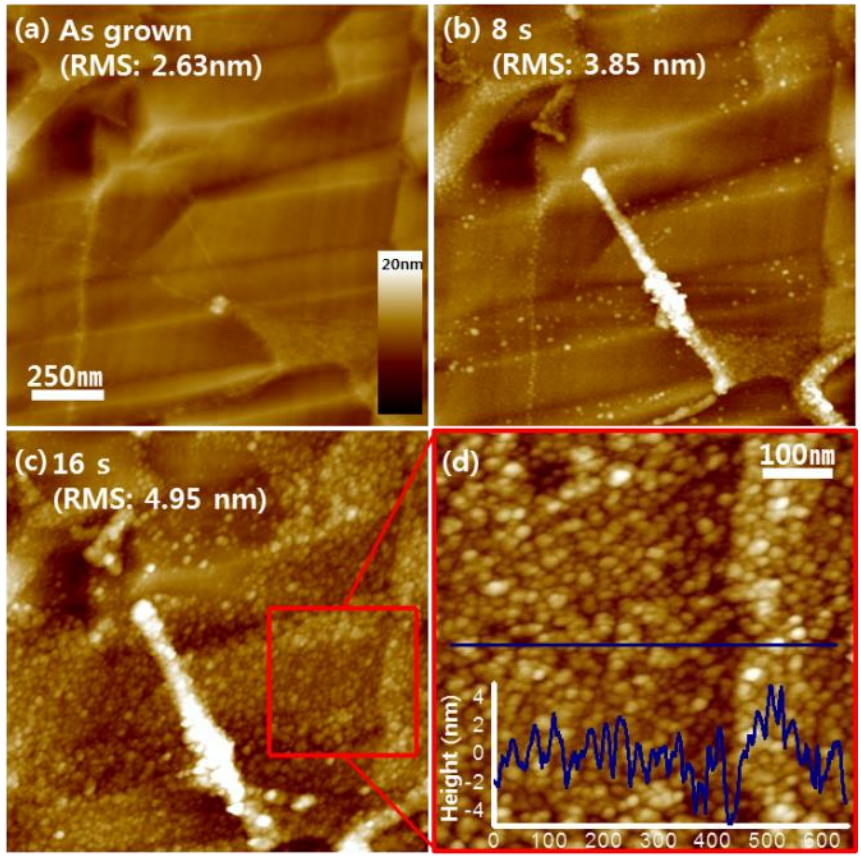

Figure S2. (a-c) AFM images of monolayer graphene on Cu with varying exposure time to N_2-plasma for 0, 8, and 16 sec, respectively. Scan area, 1.5 x 1.5 μm^2. (d) AFM profile of N_2-plasma treated graphene on Cu corresponding to the red box in c. Scan area, 600 x 600 nm^2.

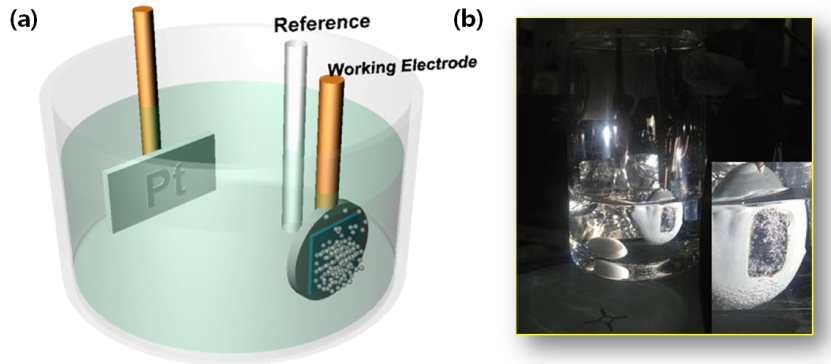

Figure S3. (a) Schematic illustration and photograph images of hydrogen evolution reaction on N-GQSs/Si photocathode.

Table S1. Summary of the experimental data for Si and glassy carbon (GC) electrodes.

condition	Electrode	Onset potential [E (V) at -1mA/cm^2]	[E (V) at -5mA/cm^2]
Under illumination (p type Si)	Bare Si	-0.17	-0.29
	Porous Si	0.07	-0.03
	GQS monolayer Si	0.12	0.01
	GQS solution-porous Si	0.16	0.08
RDE (Glassy carbon) under dark condition	Bare Si	-0.24	-0.33
	As grown Gr-Si	-0.21	-0.29
	GQS-Si	-0.08	-0.22

This value was calculated from the consideration of the following reference; Y. W. Chen, J. D. Prange, S. Dühnen, Y. Park, M. Gunji, C. E. Chidsey and P. C. McIntyre, Nature Mater., 2011, 10, 539-544.

References

1. X. Geng, L. Niu, Z. Xing, R. Song, G. Liu , M. Sun, G. Cheng, H. Zhong, Z. Liu, Z. Zhang, L. Sun, H. Xu, L. Lu, L. Liu, *Adv. Mater.* **2010**, *22*, 638.
2. D. I So , B. W. Kwon, D. H. Park, W. Seo, Y. Yi, B. Adgadi, C. Lee, W. K. Choi, *Nature Nanotech*. **2012**, *7*, 465.
3. a) J. K. Kim , M. J. Park , S J. Kim , D. H. Wang , S.-P. Cho , S. Bae , J. H. park , B. H. Hong , *Acs Nano* **2013** , *7* , 7207 ; b) X. Yan , X. Cui , B. Li , L. Li , *Nano Letters* **2010**, *10*, 1869.
4. S. Kim, S. W. Hwang, M. Kim, D. Y. Shin, D. H. Shin, C. O. Kim, S. B. Yang, J. H. Park, E. Hwang, S. Choi, G. Ko, S. Sim, C. Sone, H. J. Choi, S. Bae, B. H. Hong, *Acs Nano* **2012**, *6*, 8203.
5. S. H. Jin, D. H. Kim, G. H. Jun, S. H. Hong, S. Jeon, *ACS Nano* **2013**, *7*, 1239.
6. X. Yan, X. Cui, L. Li, *J. Am. Chem. Soc.* **2010**, *132*, 5944.
7. D. Pan, J. Zhang, Z. Li, M. Wu, *Adv. Mat.* **2010**, *22*, 734.
8. J. Lee, K. Kim, W. I. Park, B. Kim, J. H. Park, T. Kim, S. Bong, C. Kim, G. Chae, M. Jun, Y. Hwang, Y. S. Jung, S. Jeon, *Nano Letters* **2012**, *12*, 6078.
9. Y. Li, Y. Zhao, H. Cheng, Y. Hu, G. Shi, L. Dai, L. Qu, *J. Am. Chem. Soc.* **2012**, *134*, 15.
10. T. Gokus, R. R. Nair, A. Bonetti, M. Bohmler, A. Lombardo, K. S. Novoselov, A. K. Geim, A. C. Ferrari, A. Hartschuh, *ACS Nano* **2009**, *3*, 3963.
11. D. C. Kim, D.-Y. Jeon, H.-J. Chung, Y. Woo, J. K. Shin, S. Seo, *Nanotechnology* **2009**, *20*, 375703.
12. C. Hu, Y. Liu, Y. Yang, J. Cui, Z. Huang, Y. Wang, L. Yang, H. Wang, Y. Xiao, J. Rlong, *J. Mater. Chem. B* **2013**, *1*, 39.
13. X. Yan, B. Li, X. Cui, K. Wei, L. Li, *J. Phys. Chem. Lett.* **2011**, *2*, 1119.
14. H. Tetsuka, R. Asahi, A. Ngoya, K. Okamoto, I. Tajima, R. Ohta, A. Okamoto, *Adv. Mater.* **2012**, *24*, 5333.
15. S. Bae, H. Kim, Y. Lee, X. Xu, J. Park, Z. Yi, J. Balakrishnan, T. Lei, H. R. Kim, Y. I. Song, Y. Kim, K. S. Kim, B. Ozyilmaz, J. Ahn, B. H. Hong, S. Iijima, *Nature Nanotech*. **2010**, *5*, 574.

16. S. Horischi, T. Gotou, M. Fujiwara, *Appl. Phys. Lett.* **2004**, *84*, 2403.
17. A. C. Ferrari, J. C. Meyer, V. Scardaci, C. Casiraghi, M. Lazzeri, F. Mauri, S. Piscanec, D. Jiang, K. S. Novoselov, S. Roth, A. K. Geim, *Phys. Rev.* **2006**, *97*, 187401.
18. a) A. Ferrari, J. Robertson, *Phys. Rev. B* **2001**, *64*, 075414; b) C. Casiraghi, S. Pisana, K. S. Novoselov, A. K. Geim, A. C. Ferrari, *Appl. Phys. Lett.* **2007**, *91*, 233108.
19. L. G. Bulusheva, A. V. Okotrub, I. A. Kinloch, A. G. Kurenya, A. G. Kudashov, X. Chen, H. Song, *Phys. Stat. Sol. (b)* **2008**, *245*, 1971.
20. U. Sim, T. Yang, J. Moon, J. An, J. Hwang, J. Seo, J. Lee, K. Y. Kim, X. Han, B. H. Hong, K. T. Nam, *Energy Environ. Sci.* **2013**, *6*, 3658.
21. A. C. Nielander, M. J. Bierman, N. Petrone, N. C. Strandwitz, S. Ardo, F. Yang, J. Hone, N. S. Lewis, *J. Am. Chem. Soc.* **2013**, *135*, 17246.

Chapter 3

N-doped monolayer graphene catalyst on silicon photocathode for hydrogen production

Introduction

The discovery of efficient catalysts represents one of the most important and challenging issues for the implementation of photoelectrochemical hydrogen production.[1] A critical requirement for outstanding catalysts in a photoelectrochemical cell (PEC) is not only the ability to boost the kinetics of a chemical reaction but also durability against electrochemical and photoinduced degradation.[2] Generally, precious metals, such as platinum, exhibit superior performance in these requirements; however, the unavoidable weaknesses of precious metals are the economic aspects because of the high-price.[1] Therefore, there has been an intense search for efficient, durable, and inexpensive alternative catalysts.[2,3] Here, we demonstrate that monolayer graphene can catalyze the hydrogen evolution reaction (HER); thus, monolayer graphene can enhance the performance of silicon (Si) photocathodes through a significant decrease in the overpotential. The catalytic activity can be improved in N-doped and defect-abundant graphene that was prepared by treatment with N_2 plasma. Furthermore, surface passivation with a transparent monolayer graphene catalyst allows the Si photocathode to work efficiently and stably in neutral water by suppressing oxidation.

A PEC is the most promising system to sustainably produce hydrogen fuel; a PEC requires semiconductor photoelectrodes that generate electron–hole pairs with absorbed photons and stimulate charge transfer to a semiconductor–aqueous interface.[1] To improve the kinetics of charge transfer, heterogeneous catalysts are added to the surface of a semiconductor.[4] Many attempts to develop highly efficient catalysts have had limited success; the development of an earth-abundant catalyst

that operates at pH 7 with a low overpotential is still a challenge.[2,5] In PEC, negative effects from catalysts should be considered: (1) reflection by the overlaid catalyst, (2) an unfavorable band structure such as a Schottky barrier (3) photocorrosion, and (4) recombination sites at the interface.[6,7] Therefore, to design catalysts for photoelectrochemical water splitting, the optical properties, stability and interfacial issues must be comprehensively considered. The design of carbon-based catalysts represents an important research direction in the search for non-precious, environmentally benign, and corrosion resistant catalysts. Especially, graphene possesses excellent transmittancy and superior intrinsic carrier mobility;[8] thus there have been several attempts to use graphene as a catalyst. It has been reported that reduced graphene oxide (rGO) containing catalytic active materials exhibited improved activity in HERs, oxygen evolution reactions (OERs), and oxygen reduction reactions (ORRs).[9–11] However, in most cases, the role of carbon materials is limited to an electrical conducting substrate or a support that enhances the performance of other decorated active catalysts. In this study, we investigated new possibilities for monolayer graphene as an electrocatalyst for efficient HER and found that nitrogen doping and defects achieved through treatment with N_2 plasma improved the catalytic activity. To the best of our knowledge, there is no prior report on the application of monolayer graphene to hydrogen production.

As a proof of concept, the Si photocathode was employed to investigate the catalytic activity of graphene and the effect of nitrogen doping in photoelectrochemical HER. Si is the most promising photocathode material due to the small band gap of 1.12 eV and precise controllability;[12] however, it cannot be

durably operated in aqueous electrolytes because of surface oxidation.[13] Therefore, passivation of Si surface is essential for the durable operation of the Si photocathode in neutral water.[13] Monolayer graphene on Si acts as a passivation layer against surface oxidation without attenuating the photon incidence.

Experimental

Synthesis of graphene

A monolayer graphene was grown on Cu foil by chemical vapor deposition (CVD) and then transferred to a SiO_2 surface. In the first step of graphene synthesis, a copper foil was put into a quartz reactor in the CVD system and then heated to 1000 ℃ with flowing H_2 at 70 mTorr. Additionally, the sample was annealed for 20 min without changing the condition. The gas mixture of H_2 and CH_4 was flowed with rates of 5 and 50 SCCM for 30 min under 8 Torr. Finally, the sample was rapidly cooled down to room temperature with flowing H_2. After growth, in order to remove graphene on one of the sides of Cu foil, graphene on Cu was placed into the plasma chamber (SNTEK). The chamber pressure was pumped down to 50 mTorr, and O_2 gas was introduced into the chamber by applying a radio-frequency (13.56 MHz) forward power of 100 W for 10 s. In addition, to make vacancy sites and N-doping graphene on the front side of Cu, low density N_2-plasma was produced by applying 10 W power. The N_2 flow rate was 20 SCCM and the working pressure of the chamber was 120 mTorr. Under these conditions, the plasma treatments were performed with various exposure times from 0 to 16 s of N_2 plasma to test the electrochemical reaction of the graphene surface. Finally, poly(methyl methacrylate) (PMMA) was spincoated on graphene and then copper foil was removed in 0.1 M ammonium persulfate solution. After washing with deionized water, the graphene was transferred onto the Si substrate and then PMMA was removed in acetone for 30 min.

Preparation of Si photocathode

In order to establish an ohmic contact between copper wire and the unpolished side (back side) of the Si wafer, a gallium–indium eutectic alloy was incorporated followed by the silver paste. The epoxy was used to insulate and protect the back contact of Si except for the intended illumination area (0.25 cm^2) of the Si front side. Gr was transferred to the Si surface from Cu foil. PMMA was spin-coated on Gr and then the copper foil was removed in an ammonium persulfate solution. After washing with deionized water, Gr was transferred onto the Si substrate and then PMMA was removed in acetone for 30 min. Electrochemical measurements Electrochemical measurements were performed in a three-electrode cell using an electrochemical analyzer (CHI 600D, CH Instruments, Inc.). Pt foil was used as the counter electrode and Ag/AgCl/3 M NaCl electrode was used as the reference electrode. The reference electrode was carefully calibrated with respect to RHE in an aqueous 1 M perchloric acid solution with high purity H_2 saturation at 25℃ (Fig. S1†). The RHE was calibrated to between -0.201 V and -0.203 V *vs.* the Ag/AgCl reference electrode. To evaluate the photoelectrochemical behavior, visible light from a 300 W Xe lamp was illuminated onto the substrate with the light intensity of 100 mW cm^{-2} using an Air Mass 1.5 Global condition glass filter. The RDE system was purchased from EG&G PARC Inc and Glass Carbon tip for RDE measurement (dia. 3 mm) was purchased from BASi. The Pt catalyst mixed with 5 wt% Nafion was synthesized from the literature method.16 The Pt catalyst ink of 10 uL was loaded on GC and dried at 110℃. RDE measurement was performed at a rotating speed of 1000 rpm with a scan rate of 5 mV s^{-1}.

Calibration with respect to relative hydrogen electrode

The Ag/AgCl/3 M NaCl electrode (BASi) was used as the reference electrode. Pt foil (2 cm x 2 cm x 0.1 mm, 99.997% purity, Alfa Aesar) was used as the counter electrode. In the case of RDE experiment, Pt wire (0.1 mm diameter, Dr Bob's cell) was used as the counter electrode. It was carefully calibrated with respect to the reversible hydrogen electrode (RHE) in an aqueous 1 M perchloric acid solution (Sigma Aldrich) with high purity H_2 saturation at 25℃. The RHE was calibrated to between -0.201 V and -0.203 V vs. the Ag/AgCl reference electrode (Fig. S1†). Since the potential difference between Ag/AgCl and RHE is dependent on electrolyte pH, temperature, and so on, the potential was carefully measured before each set of measurement and the measurement was conducted at least three times for each condition. The potential was controlled using a potentiostat (CHI 600D, CH Instrument) at a scan rate of 5 mV s^{-1}.

Characterization

Raman spectra were obtained with a Renishaw micro-Raman spectroscope with an excitation wavelength of 514.5 nm, an Ar laser. The spot diameter was approximately 2 mm with a 50 x objective lens. The oxygen plasma treatment (SNTEK) was carried out with a 100 W radio-frequency (rf) power for 13 s under 140 mTorr and the nitrogen plasma was accelerated with a 10 W rf power for several exposure times (0 to 16 s) under 120 mTorr. XPS spectra were collected by AXIS Ultra DLD (Kratos. Inc) using a monochromatic Al K (1486.6 eV), 150 W source at Korea Basic Science Institute (KBSI). Narrow-scan data were collected using a pass energy of 40 eV and 0.05 eV per step.

Results and Discussion

Monolayer graphene (Gr) was grown on Cu foil through chemical vapor deposition (CVD) and was transferred to p-type Si wafer. To evaluate the photocathodic behavior of Gr loaded on a Si (Gr-Si) electrode, a current density measurement was performed as the potential was swept from 0.4 V to -1.0 V vs. Reversible Hydrogen Electrode (RHE) in a three electrode cell. A light source of a 300 W Xe lamp illuminated the Si photoelectrode with a light intensity of 100 mW/cm^2 with an Air Mass 1.5 Global condition filter in an aqueous 1 M perchloric acid solution (pH 0).

In measurements of the photoelectrochemical performance, Gr exhibites catalytic activity for HER. As shown in Figure 1a, the current density of the bare Si increases gradually from -0.2 V vs. curve is shifted by approximately 0.2 V toward the positive potential. The onset potential is defined as the potential at the photocurrent density of -1 mA/cm^2. The onset potential of Gr-Si is 0.01 V vs. RHE, and this potential is a positive shift by 0.18 V compared to that of bare Si (-0.17 V vs. RHE). Figure 1b also shows dark current densities of heavily arsenic doped n^+ type Si electrodes. In the dark condition, the positive shift in 0.14 V of the onset potential (-0.49 V vs. RHE for Gr-Si) also shows higher activity for HER compared to that of the bare Si (-0.63 V vs. RHE). This result indicates that monolayer Gr acts as an effective catalyst for HER on the Si photocathode.

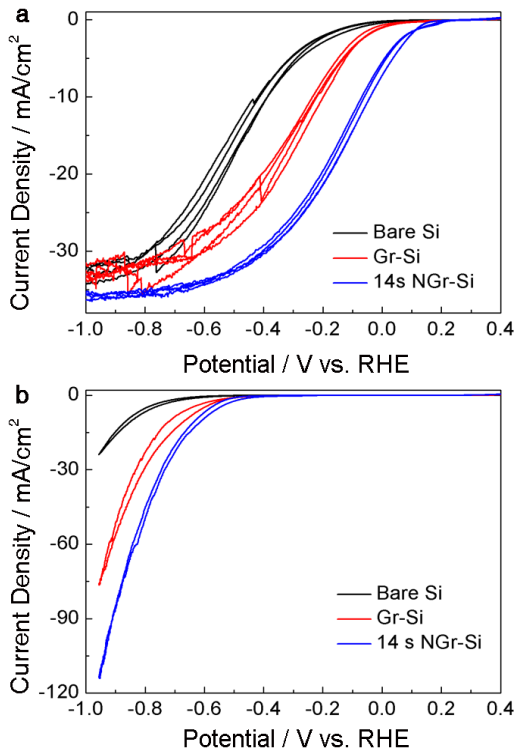

Figure 1. Cyclic Voltammetry (CV) of graphene (Gr), N_2-plasma-treated Gr (NGr), Pt, and Pt with NGr on a Si electrode. (a) Photocurrent density-potential (*J-E*) curves for the lightly boron doped p-Si electrode deposited with Gr and NGr. The plasma treatment on Gr was introduced with high purity N_2 gas for 14 sec, which is called NGr-Si. In case of Pt-Si and Pt-NGr-Si electrodes, Pt nanoparticles were deposited on bare Si and NGr-Si by the electroless deposition method, respectively. (b) Polarization curves of Gr, and NGr on heavily arsenic doped n^+ type Si electrodes under dark condition. Each CV was performed at a scan rate of 0.05 V/sec.

To investigate the electrocatalytic activity of Gr, we measured cyclic voltammetry (CV) without illumination with a rotating disk electrode (RDE). To fabricate the working electrode, Gr was transferred to a glassy carbon (GC) tip that is inert in aqueous solution. As shown in Figure 2a, in *J-E* curves of the RDE measurements, the current density from the electrolysis of water exponentially increases after the onset as the potential is swept from 0 V to -0.5 V. To compare the onset potential for the HER in the RDE system, the potential to attain -5 mA/cm^2 of HER current density was measured for bare GC and for Gr-GC. The potential to attain -5 mA/cm^2 of HER current density is -0.33 V for the bare GC. Similar to the behavior of the photocurrent response for the Gr-Si electrode, a positive shift in the overall J-E curve is also observed for Gr-GC. The potential for Gr-GC at -5 mA/cm^2 is -0.28 V vs. RHE; this potential is shifted positive by 50 mV compared to that for the bare GC. This result means that the Gr monolayer has electrocatalytic activity for HER regardless of substrate materials.

To quantitatively gain more insight into the catalytic activity of Gr, the *J-E* curves in Figure 2a is converted into a plot of the potential as a function of the logarithm of *J*; this plot is called a Tafel plot. The measured potentials are corrected for the ohmic potential drop (iR) losses that originated from the resistance of the interface between the substrate and the electrolyte. Analyzing the impedance spectroscopy reveals that the resistances of the bare GC and Gr-GC are 7.1 and 7.2 ohm, respectively (Figure S2). The Tafel plot provides two parameters to estimate the electrocatalytic activity: the Tafel slope and the exchange current density. The Tafel slope is defined to be a measure of the

potential increase required to increase the resulting current by 1 order of magnitude.[14] The bare GC shows a Tafel slope of 85 mV/decade, and Gr-GC exhibited a 9 mV/decade lower Tafel slope (74 mV/decade) than that of bare GC. For the comparison with the well-known catalyst, Pt particles were deposited on GC and the electro-catalytic activity was analysed. The applied potential to obtain -5 mA/cm^2 is -0.04 V vs. RHE, that is shifted positively by 0.24 V compared to that of Gr-GC. The Tafel slope of Pt-GC is 42 mV/decade, which is a 32 mV/decade lower than that of Gr-GC. In case of 2D MoS_2 catalyst, the potential to attain -5 mA/cm^2 is -0.19 V vs. RHE and the Tafel slope was 60 mV/decade when deposited as a mixture with Nafion on GC.[15]

The Tafel slope is an inherent property of the catalyst that is determined by the rate-limiting step for HER. Mechanistically, for the HER in acidic solution, the following possible reaction steps have been suggested:[16]

$$H_3O^+ + e^- \rightarrow H_{ads} + H_2O \quad (1)$$

$$H_{ads} + H_3O^+ + e^- \rightarrow H_2 + H_2O \quad (2)$$

$$H_{ads} + H_{ads} \rightarrow H_2 \quad (3)$$

where H_{ads} is the adsorbed H. (1) is a discharge step (the Volmer reaction), (2) is a desorption step (the Heyrovsky reaction), and (3) is a recombination step (the Tafel reaction). The value of the Tafel slope also relates to the adsorbed hydrogen coverage (θ_H) on the surface of electrode. If the recombination of adsorbed hydrogen (the Tafel reaction) is the rate-determining step for the HER and if the coverage is very high ($\theta_H \approx 1$), the measured Tafel slope is 30 mV/decade. However, if the electrochemical desorption step (the Heyrovsky reaction) is the

rate-determining step, a Tafel slope of 40 ~ 118 mV/decade is measured and is dependent of the value of θ_H (0 ~ 1).[17] The observed Tafel slope of ~80 mV/decade in the current work indicates that the kinetics of the HER on bare GC and Gr-GC electrodes is determined by the Heyrovsky reaction because θ_H has an intermediate value.

The exchange current density (J_0) is defined to be the current density at zero overpotential. The catalytic effect originates from improving the rate of charge transfer at the interface between the electrode and electrolyte or from lowering the activation energy barrier for a chemical reaction; these catalytic effects are represented by J_0. The higher J_0 indicates that electron transfer or the adsorption/desorption of protons at the electrode/electrolyte can occur more easily with a lower kinetic barrier. From the Tafel plot, J_0 can be obtained by extrapolating the plot in Figure 2b and extracting the current density at 0 V vs. RHE. The Gr-GC electrode shows an enhanced J_0 of 2.73×10^{-6} A/cm^2, which is higher than the J_0 of bare GC (1.63×10^{-6} A/cm^2) (Figure S3). The J_0 of the monolayer Gr is also compared with that of the nanoparticulate MoS_2. The accurate J_0 can be calculated by considering the number of active sites. For example, the J_0 of MoS_2 for the HERs is experimentally measured to be 1.3×10^{-7} to 3.1×10^{-7} A/cm$^2_{geometric}$.[18] Active sites of MoS_2 nanoparticle for HER are known to be edge sites of MoS_2 nanoparticle.[16,18] For the direct site-to-site comparison between MoS_2 nanoparticle and Pt catalyst, T. Jaramillo *et al*. have measured an exchange current per site of MoS_2 combined with STM analysis.[18] The exchange current per site is then multiplied by the site density of Pt for a fair comparison

to the transition metal catalyst, resulting in the exchange current density of 7.9×10^{-6} A/cm^2. This value is still similar to exchange current density of Gr (2.7×10^{-6} A/cm^2). We are currently investigating to identify and quantify the active sites of the single monolayer Gr. From the Tafel analysis, Gr has the catalytic activity for the HER compared to that of the nanoparticulate MoS_2.

The catalytic activity of Gr can be further enhanced by generating more active sites. We expected that treatment with N_2 plasma would induce nitrogen doping and abundant defects in graphitic carbon structure and that these doping and defect sites could be catalytic sites for the HER. In a previous study, Dai's group showed that introducing nitrogen dopants and defect sites in a CNT-Gr composite facilitated an improvement in electrocatalytic activity for ORR.[19] The surface of the as-grown Gr on Cu foil was modified with a N_2 plasma in a reactive ion etcher (RIE), and the catalytic activities of the N_2-plasma-treated Gr (NGr) were measured for various durations of the plasma treatment.

The N_2-plasma treatment improved the catalytic activity of Gr. We optimized the duration of the plasma treatment, and obtained the best-performing Gr at the duration of 14 sec (Figures 1a and S4). As shown in Figure 1a, an additional positive shift of the onset potential is observed for NGr under illumination. The onset potential for NGr-Si is 0.12 V vs. RHE, and this onset potential is enhanced by more than 0.11 V compared to that for Gr-Si. In comparison to bare Si with the onset of -0.17 V vs. RHE, the onset potential is shifted positively by 0.29 V. The more significant enhancement by Gr and NGr is detected at a current density of -10 mA/cm^2. To obtain -10 mA/cm^2 of

photocurrent, potentials of -0.42 V, -0.21 V, and -0.04 V vs. RHE are needed for bare Si, Gr-Si, and NGr-Si, respectively. The potential for -10 mA/cm^2 is shifted to the anodic direction by 0.38 V for NGr-Si compared with bare Si. The cathodic current from NGr-Si rises rapidly at potentials more negative than the onset potential and at current densities less than -5 mA/cm^2. In the dark condition, NGr-Si also shows the positive shift in 50 mV (-0.44 V vs. RHE) compared to the Gr-Si (Figure 1b), which results in the photovoltage of 0.56 V by depositing NGr on bare Si (Table S1). For comparing the catalytic activity of NGr with that of the best catalyst, the CV of Si with electroless-deposited Pt (Pt-Si) is also measured (Figure S5). The onset of Pt-Si is 0.24 V vs. RHE, and the potential to obtain -10 mA/cm^2 is 0.11 V vs. RHE, which is the positive shift in 0.12 V vs. RHE compared to that of the NGr-Si electrode. NGr-Si is also compared to the Si electrode decorated with an earth abundant catalyst, Ni.[20] The Ni-Si electrode shows solar-to-hydrogen (STH) conversion efficiency of 0.4% with the onset potential of 0.34 V vs. RHE and *J* at 0 V vs. RHE of 10 mA/cm^2. NGr-Si shows the onset potential (0.12 V vs. RHE) and *J* at 0 V vs. RHE (-5.5 mA/cm^2). Consequently, the STH conversion efficiency (+0.16%) is achieved by using the NGr catalyst (Table S1). The NGr-Si is also compared with Si electrode with MoS_2 catalyst. The Photocurrent density at 0 V vs. RHE of NGr on the Si electrode is much higher (-5.5 mA/cm^2) than the reported value of MoS_2(approximately -0.5 mA/cm^2).[21]

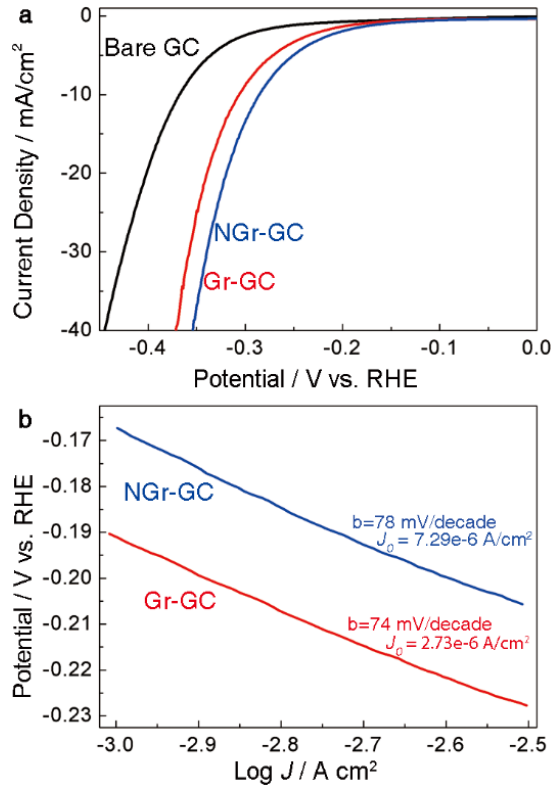

Figure 2. Electrochemical activity of Gr on Glassy Carbon (GC) electrode. (a) CV curve of GC, Gr on GC, NGr on GC, and Pt on GC from rotating disk electrode system. CV data were corrected by iR compensation. (b) Tafel plots were derived from (a) CV data. The 'b' in the inset (mV/decade) and J_0 (A/cm^2) indicate a Tafel slope and an exchange current density, respectively.

An additional positive shift in the onset potential by NGr is also observed in the RDE measurements. The potential to attain current density of -5 mA/cm^2 is -0.26 V vs. RHE; this value is 70 mV larger than that of the bare GC (-0.33 V vs. RHE) and is 20 mV larger than that of the Gr-GC (-0.28 V vs. RHE). The improvement in the catalytic activity with NGr is also confirmed by the comparison of J_0 in the Tafel plot (Figure 2b). The J_0 of NGr-GC is 7.29×10^{-6} A/cm^2, which is approximately 2.8 times of Gr-GC. This is a comparable value with that of the nanoparticulate MoS_2 (7.9×10^{-6} A/cm^2).[18]

In Figure 3, we describe the changes in chemical states of Gr after N_2 plasma treatments of various durations. AFM images for the surface of NGr with N_2 treatment for 14 sec show that plenty of defects and edges were generated in the Gr, while that of monolayer Gr was smooth (Figure S7). In the Raman spectra (Figure 3a), the generation of defects and edges by the N_2 treatment is also identified. In the Raman spectra of pristine Gr, the D peak is due to the breathing modes of six-atom rings, which comes from transverse optical phonons around *K* or *K′* point in the first Brillouin zone. It involves an intervalley double resonance process. The absence of a significant D peak is the evidence of the good crystallization of the single Gr layer. Normally, the D peak is negligibly weak in pristine Gr, but the peak still exists approximately 2% of the G peak. However, after the plasma treatment, the intensity of the D peak significantly increases and the D′ peak at ~1620 cm^{-1} is activated by intravalley double resonance process, i.e., connecting two points belong to the same cone around *K* or *K′*. Moreover, the D + G combination mode at ~2950 cm^{-1} requires defects for

its activation.[22] Thus, these changes in the Raman spectra indicate the formation of abundant edge and defective sites in NGr.

Additionally, the spectral features of monolayered Gr are observed in the Raman spectra. Before the plasma treatment, the G to 2D intensity ratio of ~0.5 and a symmetric 2D band are found at ~1580 cm^{-1} and at ~2670 cm^{-1}.[23] These features are caused by the G band from the in-plane vibrational mode and the 2D band from double resonance scattering, respectively.[24,25] Thus, they can be observed when Gr is successfully formed in a single-layer.

The plasma treatment induces not only the formation of many defect sites but also nitrogen doping in Gr. The chemical states of the nitrogen dopant were identified from the high resolution N 1*s* spectra from X-ray photoelectron spectroscopy (XPS, Figure 3b and S8). No obvious distinct nitrogen peak is observed for Gr, whereas nitrogen peaks for NGr are observed at pyridinic (398.5 eV), pyrrolic (399.9 eV), and a small number of quaternary nitrogen (401 eV) sites with a concentration of ~ 2.2 at.%. Inset in Figure 3b shows a schematic diagram of the bonding configurations for nitrogen in NGr. The passivation effect of Gr was also investigated. CV of Si photocathodes was measured during 300 cycles with a scan rate of 0.05 V/sec (Total operation time of each electrodes is about 20,000 sec) in pH 0 and pH 6.8. As shown in Figure 4a and 4b, CV curves of all electrodes shift negatively vs. RHE as the CV cycle increases, but bare Si shows the largest negative shift even in much lower cycles. As a key parameter determining the passivation performance of Gr and NGr against the surface oxidation of Si, the changes in onset potentials were

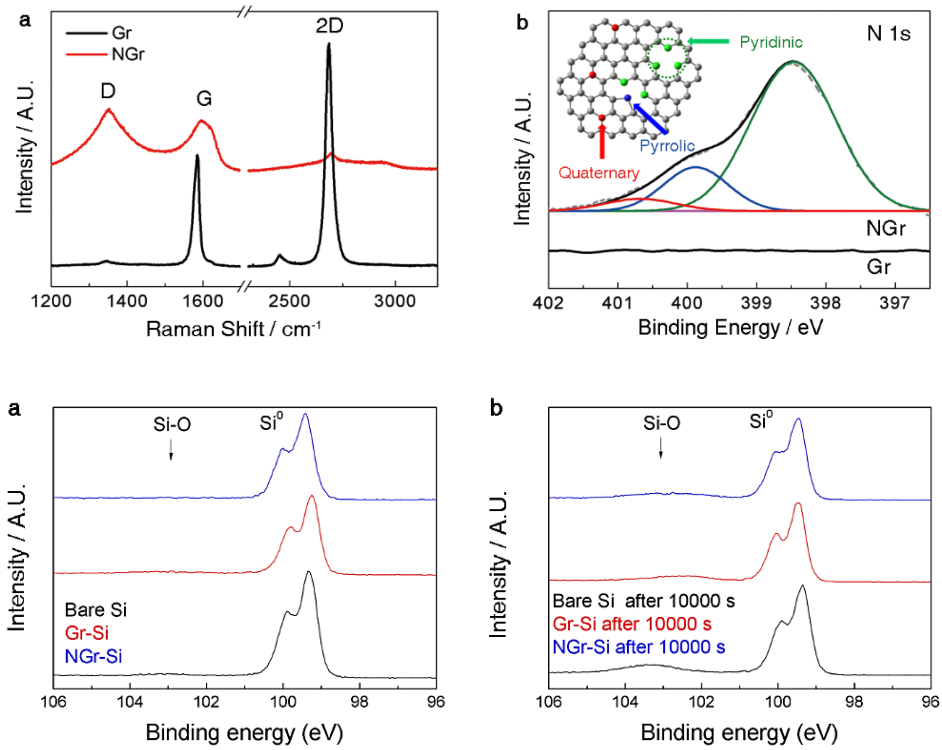

Figure 3. (a) Raman spectra and (b) high resolution XPS spectra of N 1s peak of Gr and NGr. The N 1*s* peak is separated into N1 (398.5 eV), N2 (399.9 eV), and N3 (401 eV) which are labeled by green, blue, and red lines. An inset image in (b) represents schematic of NGr. The gray, green, blue, and red spheres indicate the carbon, pyridinic nitrogen, pyrrolic nitrogen, and quaternary nitrogen atoms, respectively. (c-d) High resolution XPS spectra of Si 2*p* region of bare Si, Gr-Si, and NGr-Si electrodes. XPS spectra of each sample (c) before the chronoamperometry test and (d) after the chronoamperometry test at 0 V *vs.* RHE for 10,000 sec. Narrow-scan data of the Si 2*p* region were collected using pass energy of 40 eV and 0.05 eV/step.

measured (Figure S9). At pH 0, the Gr-Si and NGr-Si electrodes shows only shifts in the onset potential of 0.1 V and 0.035 V, respectively, while the onset potential of the bare Si electrode shifts negatively by 0.38 V within 100 cycles (Figure S9). At pH 6.8, both the Gr-Si and NGr-Si electrodes shows the negative shift of less than 0.24 V in the onset potential, whereas the onset potential of the bare Si sharply decreases and is saturated at a value of approximately -1.1 V vs. RHE within only 30 cycles.

A chronoamperometray test of the bare Si, Gr-Si, and NGr-Si was also performed at 0 V vs. RHE (Figure S10) and the current densities normalized by their initial values were displayed as a function of time in Figure 4c. Gr-Si and NGr-Si also shows the suppressed degradation of the performance in the photocurrent density compared to that of the bare Si at both pH 0 and pH 6.8 condition. The performance of the bare Si completely fails only after 1,000 sec (Figure 4c and S10) at pH 6.8. The NGr-Si electrode maintains more than 30% of the normalized current and -4.8 mA/cm^2 (pH 0) even at 10,000 sec. Thus, from the change of the onset potential and current density at 0 V vs. RHE, it is known that Gr and NGr suppresses the degradation of the photoelectrochemical performance by the oxidation of Si surface.

To confirm the passivation effect of Gr and NGr on Si surface, the surface state of Si was investigated before and after the chronoamperometry test at 0 V vs. RHE for 10,000 sec. (Figure S14). XPS spectra of bare Si, Gr-Si, and NGr-Si were measured in the Si $2p_{3/2}$ region. The Si peak can be assigned at 99.3 eV, and SiO_2 peak can be assigned at 103.3 eV.[26] From XPS spectra of bare Si, the peak

of Si-O increases after the chronoamperometry test. In case of Gr-Si and NGr-Si samples, after the long-term test, there is only slight increase in the Si-O peak. These results indicate that graphene suppresses the oxidation of Si surface during the photoelectrolysis.

To further enhance the electro-catalytic activity of Gr, Pt nanoparticles were electrodeposited onto the NGr-Si (Pt-NGr-Si). We also expected that the passivation effect of Gr to suppress the Si oxidation during the photoelectrolysis could make the synergistic advantage with other catalysts. As a proof of concept, Pt was chosen to investigate those effects. The catalytic activity of Pt-NGr-Si was significantly enhanced compared to that of NGr-Si as shown in Figure S5. From a CV measurement, the onset of Pt-NGr-Si is 0.35 V vs. RHE at -1 mA/cm^2, and the potential to reach -10 mA/cm^2 is 0.25 V vs. RHE. The STH conversion efficiency is increased to 3.05 %. As expected, the long-term stability was also achieved by combining Pt and Gr as demonstrated in Figure S12 and Figure S13. The chronoamperometry test showed that Pt-NGr-Si is maintained the stable current density of -4.7 mA/cm^2 and -4.0 mA/cm^2 respectively at pH 3.8 and 6.8 even after 8,000 sec.

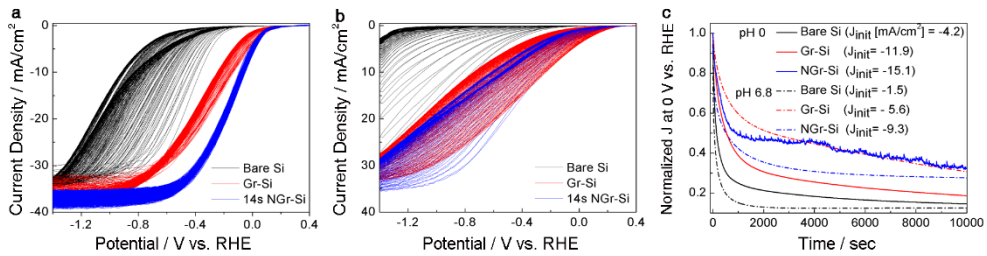

Figure 4. The stability test of bare Si, Gr-Si, and NGr-Si photocathodes. CV of Si photocathodes during 300 cycles with a scan rate of 0.05 V/sec at (a) pH 0 and (b) pH 6.8. Polarization curves of each photoelectrodes shifted negatively vs. RHE as the CV operation increased. (c) Chronoamperometry operation of Si photocathodes. The change of normalized photocurrent density (J/ J_{init}) at 0 V vs. RHE of each photoelectrodes with the increase of time at pH 0 (solid line) and pH 6.8 (dash-dotted line), respectively. J_{init} is the initial current density in the chronoamperometry operation.

Conclusions

We have presented the N-doped monolayer graphene catalyst that enhanced the PEC performance of a Si-photocathode. The onset potential for photocurrent from the Si was significantly shifted toward the anodic direction without a change in the saturation current density. NGr has excellent catalytic activity for photoelectrochemical HER on the Si photocathode and is the passivation layer that maintains higher onset potential and current density even at neutral pH. Our approach in this study exploits a strategy to develop metal-free carbon-based catalysts with high efficiency and durability for solar-driven hydrogen fuel production.

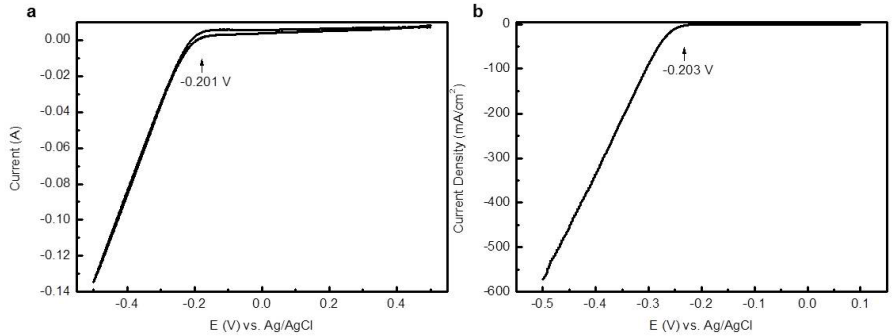

Figure S1. Calibration respect to RHE. Current vs. the applied potential respect to Ag/AgCl reference electrode with using (a) Pt foil for Si PEC cell experiment and (b) Pt wire as the counter electrode for RDE experiment.

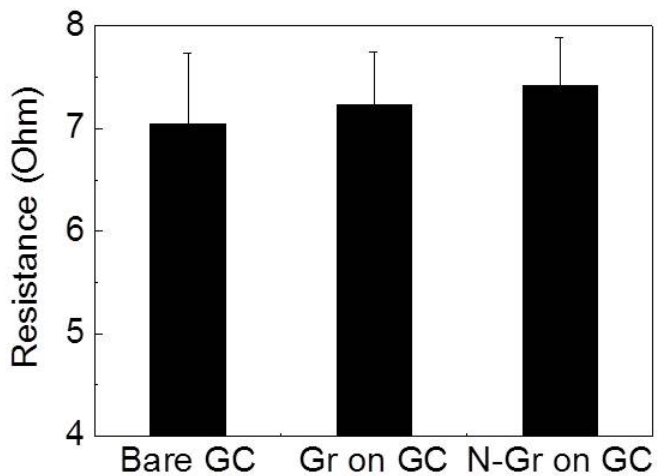

Figure S2. Resistance of bare Glassy Carbon (GC), Gr on GC, and NGr on GC. Impedance spectroscopy analysis revealed that the resistances of the bare GC, Gr-GC, NGrGC are 7.1 ohm, 7.2 ohm, and 7.4 ohm respectively. Resistances were measured using iR compensation mode in the electrochemical analyzer (CHI 600D, CH Instruments, Inc.).

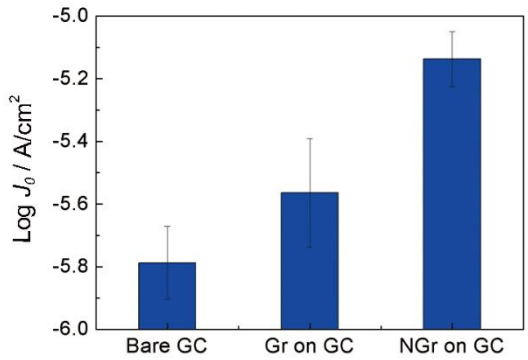

Figure S3. The logarithm of the exchange current densities calculated by extrapolation to the x-axis. Compared to the bare GC, Gr and NGr catalysts show the high activity for the HER.

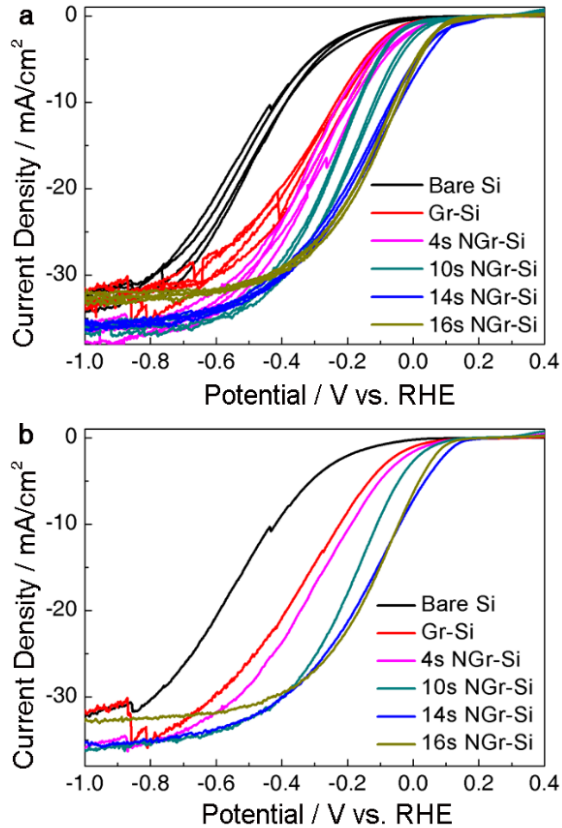

Figure S4. Photoelectrochemical performance of NGr-Si photocathode with variation of the amount of Pt solution. (a) Polarization curves of NGr on Si electrode. Each cyclic voltammetry was performed during 4 cycles at a scan rate of 0.05 V/s. The durations of the plasma treatment on Gr were introduced with high purity N2 gas for 4 sec, 10 sec, 14 sec, and 16 sec. For comparison, cyclic voltammogram of Gr without plasma treatment on Si electrode is presented. (b) Representative data from polarization curves of NGr on Si electrode of Figure S4 a

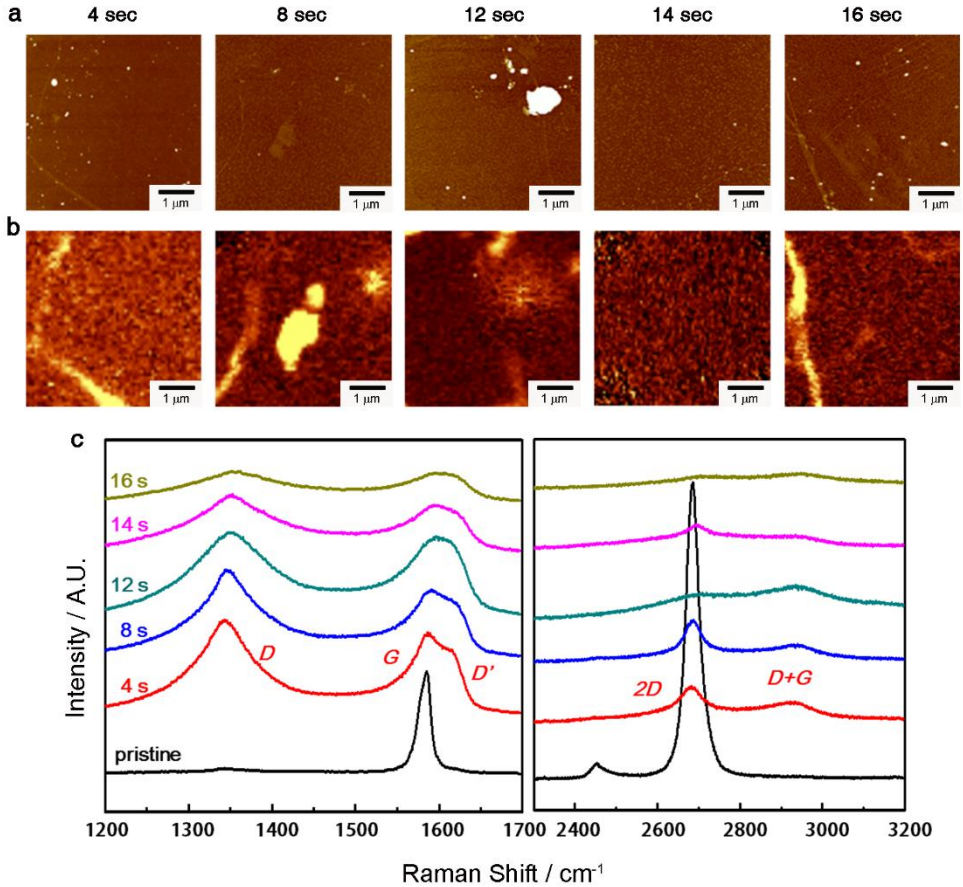

Figure S5. Surface morphology of monolayer Gr and NGrs. (a) AFM images and (b) Raman characterization of a pristine Gr sample as a function of the exposure time to N_2 plasma and the each image was taken the same area measured by AFM. Numbers on each figure indicate the exposure time. All figures have a size of 6.5 × 6.5 μm_2 (c) Raman spectra of the samples. Numbers on the left side of the left figure indicate the exposure time. Raman peaks are indexed accordingly.

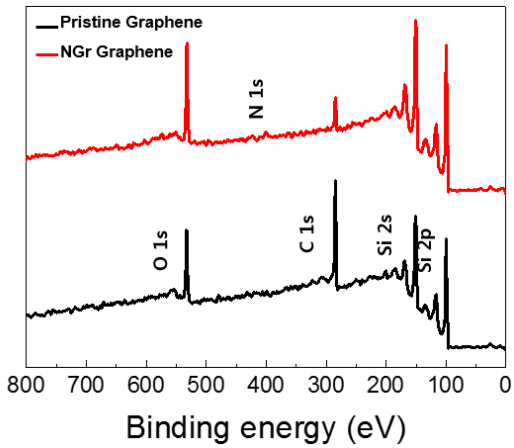

Figure S6. XPS spectra of Gr and NGr. The C 1*s* is 76.78 atomic weight % (at. %) for Gr and 57.17 at. % for NGr, N 1*s* is 0.00 at. % for Gr and 2.20 at. % for NGr, and O 1*s* is 23.22 at. % for Gr and 40.63 at. % for NGr, respectively.

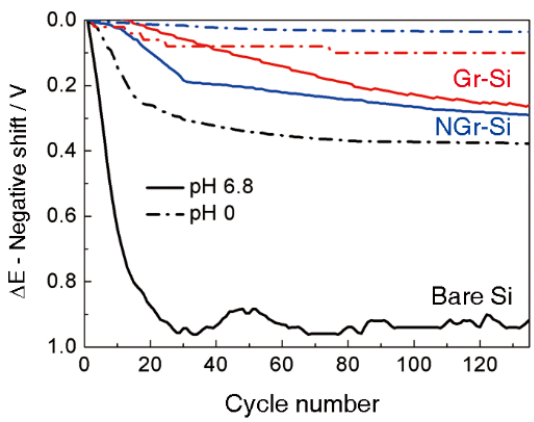

Figure S7. The change of onset potential of bare Si (black line), Gr-Si (red line), and NGr-Si (blue line) electrodes. The onset potential measured from the first CV sweep was a standard, and the difference between the measured onset potential during the CV cycles and the value of the first sweep was investigated; this difference is defined as ΔE – negative shift. The onset potential was measured with increasing the number of cyclic voltammetry in 1M $HClO_4$ (pH 0, dash dot line) and 0.4 M NaH_2PO_4 and 0.6 M Na_2HPO_4 (pH 6.8, solid line) electrolytes, respectively.

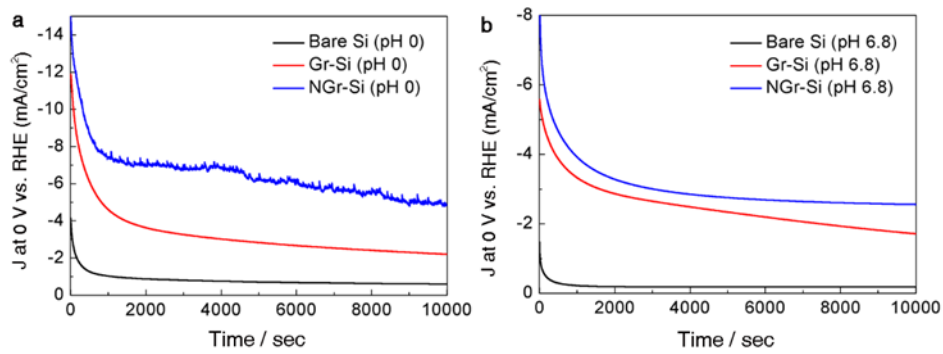

Figure S8. The change of photocurrent density at 0 V vs. RHE of bare Si (black line), Gr-Si (red line), and NGr-Si (blue line) electrodes with the increase of time at (a) pH 0 (1M HClO4) and (b) pH 6.8 (0.6 M NaH_2PO_4 and 0.4 M Na_2HPO_4), respectively. At pH 0, NGr-Si electrode shows a spiky plot during a chronoamperometry test because hydrogen bubbles stick to hydrophobic surfaces until sudden bursts occur.

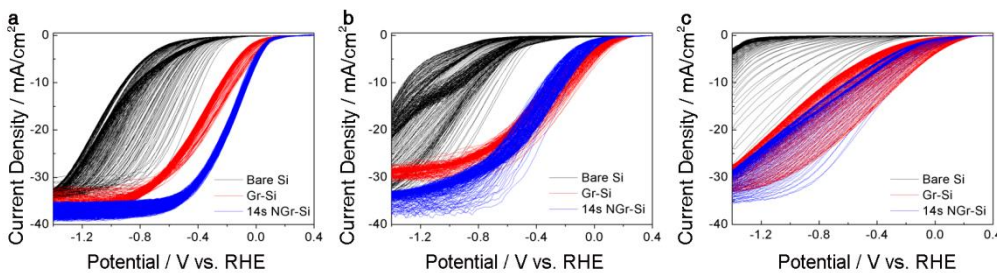

Figure S9. The stability test of bare Si, Gr-Si, and NGr-Si photocathodes. CV results of Si photocathodes during 300 cycles with a scan rate of 0.05 V/sec at (a) pH 0, (b) pH 3.8, and (c) pH 6.8. Polarization curves of each photoelectrodes were shifted negatively vs. RHE as the number of cycles increased.

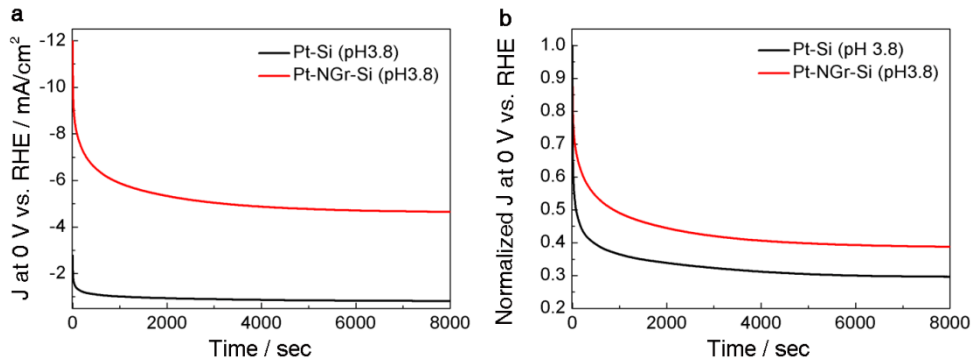

Figure S10. The stability test of bare Si, Gr-Si, and NGr-Si photocathodes. CV results of Si photocathodes during 300 cycles with a scan rate of 0.05 V/sec at (a) pH 0, (b) pH 3.8, and (c) pH 6.8. Polarization curves of each photoelectrodes were shifted negatively vs. RHE as the number of cycles increased.

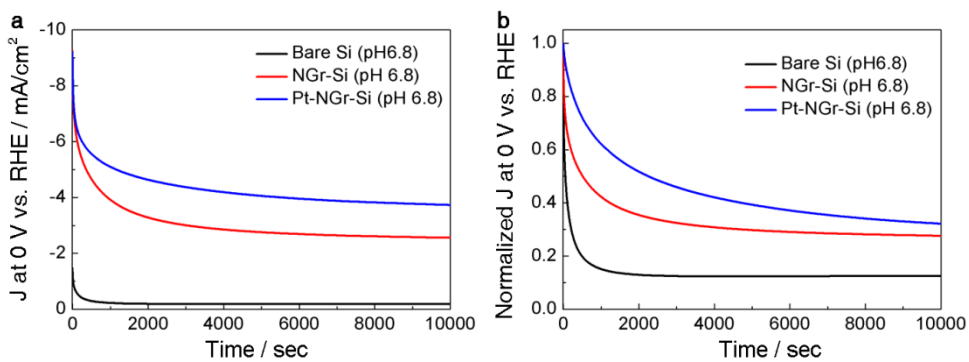

Figure S11. Chronoamperometry test of bare Si, NGr-Si, and Pt-NGr-Si photocathodes at pH 6.8. (a) The change of photocurrent density at 0 V *vs.* RHE of bare Si (black line), NGr-Si (red line), and Pt-NGr-Si (blue line) electrodes with the increase of time at pH 6.8. (b) The change of normalized photocurrent density (J/ Jinit) at 0 V *vs.* RHE of each photoelectrodes with the increase of time at pH 6.8.

Table S1. Summary of the experimental data for Si and Glassy Carbon (GC) electrodes.

Condition	Electrode	Onset potential [E (V) at -1 mA/cm^{-2}]	E (V) at -5 mA/cm^{-2}	E (V) at -10 mA/cm^{-2}	Solar-to-Hydrogen Conversion Efficiency (%)
Under illumination (p type Si)	Bare Si	-0.17	-0.29	-0.42	0.02
	Gr--Si	0.01	-0.13	-0.21	0.04
	14s NGr-Si	0.12	0.02	-0.04	0.16
	Pt-Si	0.24	0.16	0.11	1.19
	Pt-NGr-Si	0.35	0.29	0.25	3.05
Under dark condition (n^+ type Si)	Bare Si	-0.63	-0.78	-0.85	
	Gr-Si	-0.49	-0.61	-0.69	
	14s NGr-Si	-0.44	-0.55	-0.62	
Photovoltage*	Bare Si	0.46			
	Gr-Si	0.50			
	14s NGr-Si	0.56			
RDE (GC) under dark condition	Bare GC	-0.24	-0.33	-0.37	
	Gr-GC	-0.18	-0.28	-0.31	
	14s NGr-GC	-0.16	-0.26	-0.29	
	Pt-GC	-0.02	-0.04	-0.05	

The photovoltage is defined as the difference between the onset potential under the dark and illumination condition. This value was calculated from the consideration of the following reference; Y. W. Chen, J. D. Prange, S. Dühnen, Y. Park, M. Gunji, C. E. Chidsey and P. C. McIntyre, Nature Mater., 2011, 10, 539-544. (Ref. 5 in the main article)

References

1. A. Heller, E. Aharon-Shalom, W. A. Bonner and B. Miller, *J. Am. Chem. Soc.*, 1982, **104**, 6942-6948.
2. Y. Hou, B. L. Abrams, P. C. K. Vesborg, M. E. Björketun, K. Herbst, L. Bech, A. M. Setti, C. D. Damsgaard, T. Pedersen, O. Hansen, J. Rossmeisl, S. Dahl, J. K. Nørskov and I. Chorkendorff, *Nature Mater.*, 2011, **10**, 434-438.
3. S. Y. Reece, J. A. Hamel, K. Sung, T. D. Jarvi, A. J. Esswein, J. J. H. Pijpers and D. G. Nocera, *Science*, 2011, **334**, 645-648.
4. A. Kudo and Y. Miseki, *Chem. Soc. Rev.*, 2009, **38**, 253-278.
5. Y. W. Chen, J. D. Prange, S. Dühnen, Y. Park, M. Gunji, C. E. Chidsey and P. C. McIntyre, *Nature Mater.*, 2011, **10**, 539-544.
6. R. N. Dominey, N. S. Lewis, J. A. Bruce, D. C. Bookbinder and M. S. Wrighton, *J. Am. Chem. Soc.*, 1982, **104**, 467-482.
7. U. Sim, H.-Y. Jeong, T.-Y. Yang and K. T. Nam, *J. Mater. Chem. A*, 2013, **1**, 5414-5422.
8. K. Novoselov, A. K. Geim, S. Morozov, D. Jiang, M. K. I. Grigorieva, S. Dubonos and A. Firsov, *Nature*, 2005, **438**, 197-200.
9. Y. Liang, Y. Li, H. Wang, J. Zhou, J. Wang, T. Regier and H. Dai, *Nature Mater.*, 2011, **10**, 780-786.
10. J.-D. Qiu, G.-C. Wang, R.-P. Liang, X.-H. Xia and H.-W. Yu, *J. Phys. Chem. C*, 2011, **115**, 15639-15645.
11. Q. Xiang, J. Yu and M. Jaroniec, *Chem. Soc. Rev.*, 2012, **41**, 782-796.
12. M. G. Walter, E. L. Warren, J. R. McKone, S. W. Boettcher, Q. Mi, E. A. Santori and N. S. Lewis, *Chem. Rev.*, 2010, **110**, 6446-6473.
13. F.-M. Liu, B. Ren, J.-W. Yan, B.-W. Mao and Z.-Q. Tian, *J. Electrochem. Soc.*, 2002, **149**, G95-G99.
14. A. J. Bard and L. R. Faulkner, *Electrochemical methods: fundamentals and applications*, Wiley, New York, 1980.
15. J. D. Benck, Z. Chen, L. Y. Kuritzky, A. J. Forman, and T. F. Jaramillo, *ACS Catal*., 2013, **2**, 1916-1923

16. Y. Li, H. Wang, L. Xie, Y. Liang, G. Hong and H. Dai, *J. Am. Chem. Soc.*, 2011, **133**, 7296-7299.
17. B. Conway and B. Tilak, *Electrochim. acta*, 2002, **47**, 3571-3594.
18. T. F. Jaramillo, K. P. Jørgensen, J. Bonde, J. H. Nielsen, S. Horch and I. Chorkendorff, *Science*, 2007, 317, 100-1024075-4083.
19. Y. Li, W. Zhou, H. Wang, L. Xie, Y. Liang, F. Wei, J.-C. Idrobo, S. J. Pennycook and H. Dai, *Nature Nanotech.*, 2012, **7**, 394-400.
20. J. R. McKone, E. L. Warren, M. J. Bierman, S. W. Boettcher, B. S. Brunschwig, N. S. Lewis and H. B. Gray, *Energy Environ. Sci*., 2011, **4**, 3573-3583.
21. P. D. Tran, S. S. Pramana, V. S. Kale, M. Nguyen, S. Yang Chiam, S. K. Batabyal, L. H. Wong, J. Barber, and J. Loo, *Chem. Eur. J.*, 2012, **18**, 13994-13999.
22. L. G. Cancado, A. Jorio, E. H. Martins, F. Stavale, C. A. Achete, R. B. Capaz, M. V. O. Moutinho, A. Lombardo, T. S. kulmala, and A. C Ferrari, *Nano Letters*, 2011, **11**, 3190.
23. A. Ferrari and J. Robertson, *Phys. Rev. B*, 2001, **64**, 075414.
24. C. Casiraghi, S. Pisana, K. S. Novoselov, A. K. Geim and A. C. Ferrari, *Appl. Phys. Lett.*, 2007, 91, 233108.
25. X. Li, W. Cai, J. An, S. Kim, J. Nah, D. Yang, R. Piner, A. Velamakanni, I. Jung, E. Tutuc, S. K. Banerjee, L. Colombo and R. S. Ruoff, *Science*, 2009, **324**, 1312-1314.
26. C.D. Wagner, W. M. Riggs, L. E. Davis, J. F. Moulder and G. E. Muilenberg, *Handbook of X-ray Photoelectron Spectroscopy*, Perkin-Elmer Corporation, USA, 1979.

Chapter 4

N-doped graphene quantum sheets on silicon nanowire photocathodes for hydrogen production

Introduction

The development of sustainable energy sources is an urgent issue because of the current level of energy consumption.[1] Renewable and sustainable energy sources must be developed because the present energy sources have several disadvantages such as CO2 emission and limited deposits of fossil fuels.[2] Photoelectrochemical hydrogen production using solar energy represents an important and environmentally friendly technology with no carbon emissions.[3] The development of efficient and cheap photoelectrodes for water splitting is one of the fundamental challenges in hydrogen production.[4] Despite the intriguing advances in controlling the nanostructural interface and newly discovered material compositions for photoelectrodes, sluggish kinetic issues associated with a high overpotential remain some of the most difficult issues that need to be resolved.[5,6] Intense research into efficient, durable, and inexpensive hydrogen evolution reaction (HER) catalysts has been undertaken to solve the kinetic problem.[7–10] In general, precious metals such as platinum exhibit superior performance as HER catalysts; however, the unavoidable disadvantage of precious metals is their high cost.[11] A critical requirement for producing outstanding catalysts in a photoelectrochemical cell is not only the ability to boost the kinetics of the electrochemical reaction but also the ability to resist electrochemicaland photoinduced degradation. Herein we demonstrate that the combination of controlling a nanostructure of the photoelectrode and using a carbon-based hydrogen evolution catalyst represents a significant step toward enhancing the applied bias photon-to-current efficiency (ABPE). In the present work, a 430 mV decrease in overpotential was achieved using graphene quantum sheets on a silicon

nanowire, which exhibited an enhanced effect comparable to that of platinum catalysts. Furthermore, the current density at the reversible potential *vs.* a reversible hydrogen electrode (RHE) exhibited a 101-fold enhancement relative to the current density achieved with planar silicon substrates. The thermodynamic potential of water splitting is 1.23 V, which is observed by subtracting the reduction reaction and oxidation reaction in the photoelectrochemical reaction of water. At the anode, the oxidation reaction in the electrolysis of water is:

$$O_2 + 4e^- + 4H^+ \leftrightarrow 2H_2O, \quad E_{anodic} = 1.23\ V - 0.059(pH)\ V\ (vs.\ NHE) \quad (1)$$

whereas the reduction reaction at the cathode is:

$$4e^- + 4H^+ \leftrightarrow 2H_2, \qquad E_{cathodic} = 0\ V - 0.059(pH)\ V\ (vs.\ NHE) \qquad (2)$$

where, NHE is the normal hydrogen electrode and the standard potential is dependent on pH ($E_{half} = E - 0.059(pH)$ vs NHE). Kinetically, however, when a voltage of 1.23 V is applied, electrolysis is difficult to induce, which results in no current flow. In this situation, a higher potential, which is referred to as the overpotential, η, is needed to drive the reaction at a certain rate. Moreover, if a current i_c flows at the cathode, a current i_a of the same magnitude must flow at the anode to complete the circuit, which requires the overpotential at both electrodes. The overpotentials at the cathode and anode are denoted as η_c and η_a, respectively. Therefore, the total applied potential, E_{appl}, is

$$E_{appl} = 1.23\ V + \eta_c + \eta_a \qquad (3)$$

A higher overpotential requires a higher total applied voltage. Using an electrocatalyst for water splitting can reduce the overpotential required for the electrolysis of water.

In an effort to reduce the overpotential for the water splitting reaction, various catalysts have been deposited onto photoelectrode materials. Previously reported HER catalysts include pure metals, metal composites/alloys, compounds such as nonmetallic elements, and molecular catalysts.[4,5,12-16] Among metal-based catalysts, Pt, Pd, and Ru are near the top of the volcano plot, exhibiting high catalytic activity toward the HER.[7] For example, Pt nanoparticles on p-type Si nanowires in aqueous electrolyte solutions can enhance the onset potential by approximately 0.42 V.[17] In view of economic issues, recent progress has been concentrated on the incorporation of metal nanoparticles into earth-abundant elements rather than on the use of noble metals alone.[11] Nonprecious metal catalysts and catalysts that are abundant in nature have also exhibited high activity toward the HER. Binary structures such as MoS_2, Mo_2N, Mo_2C, and Ni_2P and bimetallic compounds such as Co-Mo-N and Ni-Mo have been suggested as catalysts with high HER activity.[12,18-21] However, the rigorous and precise tuning of the composition of $A_xB_yM_z$ compounds, controlling the active sites in catalysts for the HER, and nanostructuring make optimization of the properties of catalysts for the HER difficult. Moreover, when deposited with catalysts, the saturation current density and the current density at a reversible potential vs. RHE significantly decrease because of light scattering by catalysts on the surface of the photoelectrodes.

To solve the problems associated with previously developed catalysts, carbon-based catalysts may represent an important research direction in the search for low-cost, environmentally friendly, and corrosion-resistant catalysts.

Among carbon-based catalysts, graphene, in particular, possesses excellent transmittance and superior intrinsic carrier mobility; thus, several attempts have been made to use graphene as a catalyst.[22] Co-activated N and P heteroatoms adjacent to C atoms in the graphene matrix can affect such catalysts' valence orbital energy levels and thereby enhance their reactivity toward the HER.[23] Graphitic-carbon nitride combined nitrogen-doped graphene also exhibits enhanced HER activity, with HER properties similar to those of well-established metallic catalysts.[24] Reduced graphene oxide containing catalytic active materials has exhibited improved activity in oxygen reduction reactions and oxygen evolution reactions as well as in the HER.[25-28] However, in most cases, the role of carbon materials is limited to an electrically conducting substrate or a supporter that increases the HER activity of other decorated active catalysts. Recently, we suggested that monolayer graphene deposited onto a planar Si electrode acts as an efficient HER electrocatalyst and that N_2 plasma treatment enhances its catalytic activity.[29] In this study, we further investigated N_2-plasma-treated graphene quantum sheets deposited on the Si nanowire photocathodes as efficient HER electrocatalyst.

Controlling the surface structure of Si represents another important approach to improving photoelectrochemical performance. Si, one of the most abundant elements in the Earth's crust, can be used both as a photocathode and a photoanode for photochemical water splitting because its bandgap (1.12 eV) allows for the absorption of a significant portion of the solar spectrum.[30,31] However, the small band bending between the conduction band edge and the H^+/H_2 redox level of aqueous

electrolytes limits the photoelectrochemical performance of Si relative to that of Si/non-aqueous solvent systems.[5] The application of an external potential or the use of catalysts is necessary for efficient operation under solar irradiation. To overcome this problem, a porous structure or a nanostructure can increase the current density of Si photoelectrodes by increasing the number of effective reaction sites between the Si semiconductor and the liquid electrolyte junction as well as by reducing the reflection of incident light.[6,32] A nanowire structure can increase the efficiency due to the orthogonalization of the direction of incident light absorption and charge carrier collection.[33] Therefore, the combination of an optimized Si nanowire photocathode and a graphene quantum sheet catalyst can boost the catalytic activity toward the photoelectrochemical HER.

Experimental

Synthesis of graphene quantum sheets

A copper foil (10 × 10 cm^2) was inserted into a quartz tube and then heated to 1,000℃ min with flowing 5 sccm H_2. After reaching 1,000℃, the sample was annealed for 20 min under the same condition. The gas mixture of 50 sccm CH_4 and 5 sccm H_2 was flowed for 30 min at a pressure of 8 Torr. After growth, the monolayer graphene on back-side of copper was removed by oxygen plasma (100 W RF power, 12 sec). Next, the N-GQSs were prepared by being irradiate with nitrogen plasma (10 W RF power, 12 sec) to graphene on front-side of copper foil. Finally, the N-GQSs were floated on a 0.1 M ammonium persulfate etchant to remove the Cu substrate. After the Cu was removed, the floating N-GQSs were dispersed in a common organic solvent such as dichloromethane by solvent extraction.[48]

Preparation of Si nanowire (SiNW) photocathode

Boron-doped (p-type) single-crystal Si wafers (4-inch diameter, 500-mm thickness, doped to achieve a resistivity of 10-15 cm, oriented along the (100) plane were purchased from Namkang Co. Ltd. $AgNO_3$ powder (99.5%) and HF (48–51 wt%) were purchased from Sigma Aldrich, and concentrated nitric acid solution (70 wt%) was purchased from Daejung Chemical. The wafers were cut into 1 cm^2 pieces and successively cleaned in acetone, 2-propanol and deionized water for 10 min under sonication.

Each of the Si nanostructures was fabricated by the metal-catalyzed electroless etching method in a 20 mL aqueous solution of $AgNO_3$ (0.015 M) and HF (5 M) for

an etching times of 20 min, 30 min, 120 min, or180 min (Figure S5). Excess Ag residues that could be contaminated during the electroless etching were removed by washing with 70% nitric acid solution for two hours.

A SiNW photocathode was fabricated by establishing an ohmic contact at the back side of a Si substrate. After a native oxide layer was removed on the Si surface using HF, gallium-indium eutectic alloy was loaded onto the surface, followed by the application of silver conductive paste a copper wire; the resulting assembly was then dried at 100ºC. To insulate and protect the back contact of the Si substrate, epoxy was applied over the entire sample except for the area that was illuminated on the front side. After the bare Si cell was fabricated, N-GQSs were transferred onto the Si surface via drop-casting.

Electrochemical measurements

Photoelectrochemical measurements were performed in a three-electrode cell using an electrochemical analyzer (CHI 760E, CH Instruments, Inc.). Schematic illustration and photograph images of hydrogen evolution reaction on N-GQSs/Si photocathode are shown in Figure S6. Pt foil and Pt wire were used as the counter electrode, and a Ag/AgCl/3 M NaCl electrode was used as the reference electrode. The reference electrode was carefully calibrated with respect to RHE at 25℃ in an aqueous 1 M perchloric acid solution saturated with high purity H_2. The RHE was calibrated to between -0.201 V and -0.203 V vs. the Ag/AgCl reference electrode (Figure S7). To evaluate the photoelectrochemical behavior, visible light from a 300 W Xe lamp was illuminated onto the substrate with a light intensity of 100 mW/cm^2 using a glass Air Mass 1.5 Global filter. For the

electrochemical study, the Rotating Disk Electrode (RDE) system was purchased from PINE, Inc., and a glass carbon tip was used for the RDE measurements (dia. 5 mm). For comparison, 10 uL of Pt catalyst ink mixed with 5 wt% Nafion was loaded onto the GC and dried at 110^{o}C. RDE measurements were performed at a rotation speed of 1,000 rpm and at a scan rate of 5 mV/sec.

Characterization

Raman spectra were collected using a Renishaw micro-Raman spectrometer with an excitation wavelength of 514.5 nm emitted from an Ar laser. The spot diameter was ~2 μm, and a 50× objective lens was used. Oxygen plasma treatment (SNTEK) was carried out at a radio-frequency (rf) power of 100 W for 13 sec under a pressure of 140 mTorr for back side of graphene on Cu and the nitrogen plasma was accelerated at an rf power of 10 W over an exposure time of 12 sec under a pressure of 120 mTorr on graphene.

Results and Discussion

Measurements of photoelectrochemical performance show that N-doped graphene quantum sheets (N-GQSs) on a Si photoelectrode exhibit catalytic HER activity. Fig. 1 shows a schematic of hydrogen production on N-GQSs on Si nanowire arrays (SiNWs) in an acid solution under irradiation. Photons absorbed by the SiNWs generate minority carriers (electrons), which drift to the semiconductor/electrolyte interface where $2H^+$ is reduced to H_2; the N-GQSs serve as electrocatalysts for hydrogen production. In the schematic of the N-GQSs, gray, green, blue, and red spheres represent carbon, pyrrolic nitrogen, quaternary nitrogen, and pyridinic nitrogen atoms, respectively, based on high resolution X-ray photoelectron spectrum (XPS) measurements. The transmission electron microscopy (TEM) image and a size-distribution histogram indicate that the average diameter of the N-GQSs is 5 nm (Fig. S1). N-GQSs were transferred to p-type silicon nanowires via drop-casting. The N-GQSs were converted from monolayer graphene on Cu foil using nitrogen plasma. After exposure to nitrogen plasma, the nano-sized GQSs were distributed on the Cu foil and were subsequently characterized by atomic force microscopy (AFM); the strong D peak of the sheets, which is related to the structural defects at the edges of graphene, was identified in the Raman spectrum. In addition, the doping of the GQSs with ~2.9% nitrogen was determined by the N 1*s* XPS spectrum, and the UV-vis absorption spectrum of the N-GQSs revealed an absorption band with a peak at 275 nm, as shown in Fig. S1. The well-aligned SiNW arrays serve as an anti-reflector that enhances light absorption in the structure and increases the overall surface area; the N-GQSs act as electrocatalysts for hydrogen evolution.

The top-view and cross-sectional scanning electron microscopy (SEM) images of the N-GQSs on SiNWs are shown in Fig. 2a and b. The SiNWs exhibited an average diameter of ~400 nm, and lengths of up to ~5 μm. To determine the crystallinity, orientation, and morphology of the N-GQSs on SiNWs, TEM analyses were performed. The selected area electron diffraction pattern, with an incident beam axis of [11-0] (Fig. S3), indicated that a single-crystalline SiNW was well aligned along the [001] direction; the thickness fringes, brightness and dark line pattern indicate that the SiNW was etched as a column with angled edges, as shown in Fig. 2c. Moreover, the N-GQSs, which measured approximately 7 nm in diameter, were uniformly placed on the SiNWs, as indicated by dark-field TEM imaging (Fig. 2c); moreover, the formation of the N-GQSs was verified by high-resolution TEM (HRTEM). The HRTEM image shows the Moiré pattern created by the superposition of the mismatched crystalline lattices of the N-GQSs and SiNWs, as shown in Fig. 2d. The lattice plane spacing of p-Si was observed to be 3.1 Å, which corresponds to the silicon (100) plane (JCPDS, no. 24-1402). The Moiré pattern (6.2 Å) indicates mixed translational and rotational geometry. The corresponding spacing of the fringes was calculated as follows:[34]

$$a_m = (a_{GQS} \times a_{Si}) / \sqrt{a_{GQS}^2 + a_{Si}^2 - 2a_{GQS}a_{Si}\cos(\alpha_{GQS} - \alpha_{Si})} \quad (4)$$

where a_m is the *d*-spacing of the Moiré pattern, a_{GQS} is the *d*-spacing of the N-GQS, and a_{si} is the *d*-spacing of Si. On the basis of Eq. (4), the placement of an N-GQS on a SiNW with a 20 degree tilt was verified by the relation between the Moiré fringe spacing and the Si lattice plane.

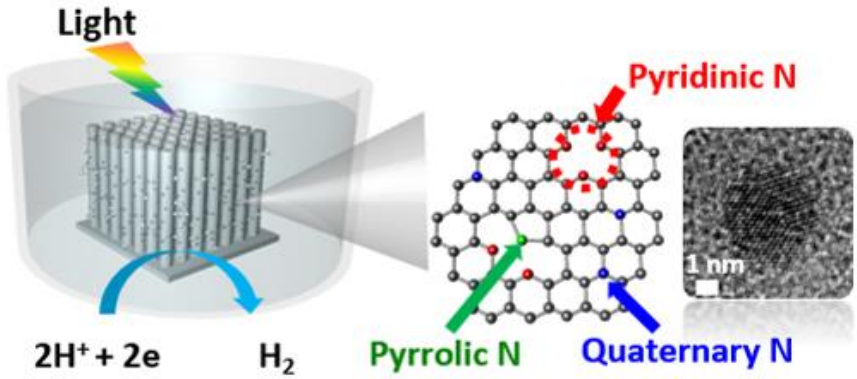

Figure 1. Schematic of N-doped graphene quantum sheets (N-GQSs) decorated on a Si nanowire (SiNW) photocathode electrode. Photons absorbed by the SiNWs generate minority carriers (electrons), which drift to the semiconductor/electrolyte interface, where $2H^+$ is reduced to H_2; the N-GQSs serve as electrocatalysts for hydrogen production. The gray, green, blue, and red spheres in the schematic of N-GQSs represent the carbon, pyrrolic nitrogen, quaternary nitrogen, and pyridinic nitrogen atoms, respectively. The average diameter of the N-GQSs is 5 nm, as determined from a TEM image.

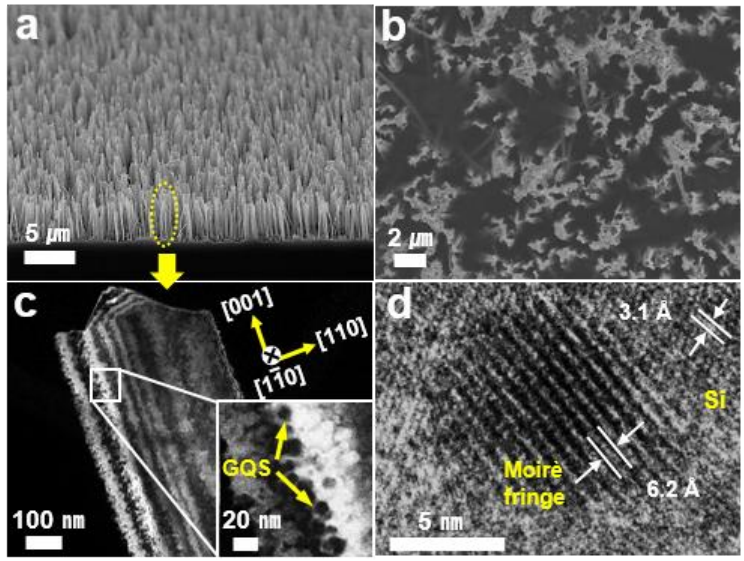

Figure 2. SEM images of SiNW arrays on p-silicon substrate obtained by metal assisted chemical etching method. (a) Cross-section and (b) top-view. (c) Dark-field TEM images of N-GQSs on p-SiNWs. (d) High-resolution TEM image shows Moiré pattern created by N-GQS in silicon lattices.

To investigate the dependence of Si photoelectrode on its nanostructure, Si substrates of various nanostructures were fabricated by silver metal-assisted chemical etching.[35] Normal boron-doped p-type (100) Si substrates were immersed in an aqueous solution of 0.015 M silver nitrate and 5 M hydrofluoric acid. Continuous Si oxidation by the galvanic reduction of Ag^+ ions and the ensuing dissolution of silicon oxide by HF resulted in the [100] directional etching of the Si substrates. The etching time was varied among 20 min, 30 min, 120 min, and 180 min. Depending on the etching time, different Si nanostructures were observed as characterized by SEM (Figure S5). When the etching time was shorter than 120 min, a porous nanostructure was observed. The transition of the surface structure from a porous to a nanowire structure occurred when the Si substrates were etched for 120 min. After this stage, the length of the nanowires was observed to increase with increasing etching time. Representative images of the SiNWs are shown in Figures 2a and 2b.

For the evaluation of the photocathodic behavior of the nanostructured Si electrodes, the current density was measured as the potential was swept from 0.4 V to -1.0 V *vs.* RHE in a three-electrode cell. A 300 W Xe lamp illuminated the Si photoelectrode with a light intensity of 100 mW/cm^2 through an Air Mass 1.5 Global filter in an aqueous 1 M perchloric ($HClO_4$) acid solution (pH 0). Because the applied potential of the Si working electrode was negative (cathodic), the magnitude of the current density increased and saturated at a specific value of the applied potential. The current density at the saturation point is called the limiting current density or the saturation current density. As shown in Figure 3a

and Figure S4, the current density of the planar Si continued to increase until the length of the nanowires reached 5 μm as the surface became increasingly nanostructured. The limiting current density of bare planar Si was approximately -33 mA/cm^2. The surface area of the nanostructured Si substrate was greater than that of the planar structure. The reflectance of incident light could be reduced by the nanostructured Si surface. Although the surface of planar Si reflects approximately one quarter of incident light, photon absorption is enhanced at the nanostructured surface because of its low reflectance. Nanostructured silicon wires have been reported to exhibit a light trapping effect,[36] which can enhance the current level for hydrogen production when the length of the Si nanowires is optimized to exhibit strong broadband optical absorption.[37] The nanowire structure also has the advantage of inducing the orthogonalization of light absorption and charge-carrier collection.[33] Thus, the minority carriers generated by incident solar light can move to the lateral side of each nanowire and participate in the hydrogen evolution reaction more quickly than in the planar structure. To calculate the photovoltage of the Si photoelectrode, the dark current density was also measured. The photovoltage is defined as the difference between the onset potential under the dark and illuminated conditions. Figure 2b shows the dark current densities of representative Si electrodes. The dark current density of the nanostructured electrodes was also greater than that of the planar Si substrate. The nanostructured photoelectrode (0.59 V of photovoltage) exhibited a positive shift in photovoltage of 0.13 V relative to that of the planar Si electrode (0.46 V of photovoltage) as shown in Table S1.

In measurements of the photoelectro-catalytic performance, N-GQSs on SiNWs exhibited catalytic activity toward the HER. As shown in Figure 3a, the current density of the N-GQSs/planar Si structure increased gradually from -0.2 V *vs.* RHE and was saturated at approximately -35 mA/cm^2 below -0.8 V *vs.* RHE at negative applied potentials. This current density is higher than that of planar Si without N-GQSs. Interestingly, measurements of the N-GQSs/planar Si structure showed that the overall current density-potential (*J-E*) curve was shifted by approximately 0.2 V toward positive potentials compared to that of planar Si without N-GQSs. The onset potential is defined as the potential at a photocurrent density of -1 mA/cm^2. The onset potential of N-GQSs/planar Si was 0.13 V *vs.* RHE, representing a positive shift of 0.30 V compared to the onset potential of bare Si (-0.17 V *vs.* RHE). Figure 3b also shows the dark current densities of the heavily arsenic-doped n^+-type Si electrodes. In the dark condition, the positive shift in the onset potential of 0.21 V (-0.44 V *vs.* RHE for N-GQSs/planar Si) also shows higher than that of planar Si (-0.63 V vs. RHE for planar Si).

When incorporated into the nanostructured photoelectrode system, the N-GQSs exhibited much higher catalytic activity than that of the planar photoelectrode system. The onset potential of the N-GQSs/Si nanowire electrode was 0.26 V *vs.* RHE, which is 0.09 V higher than that of the Si nanowire without a catalyst (0.17 V *vs.* RHE). Both the increased onset potential and the current density at the reversible potential (0 V *vs.* RHE) showed an enhanced ABPE of 2.29%, which is greater than that of the bare Si nanowire system (0.91%). ABPE is the applied bias photon-to-current efficiency:[38]

$$ABPE = [j_{ph}\ (mA/cm^2) \times (V_{redox} - V_b)\ (V) / P_{in}\ (mW/cm^2)]_{AM\ 1.5\ G} \times 100\ (\%)\ (5)$$

where, j_{ph} is the photocurrent density obtained under an applied bias V_b, V_{redox} is the redox potential for hydrogen production (0 V), V_{bias} is the externally applied bias potential that is often necessary to achieve reasonable photocurrents, and P_{light} is the intensity of the incident light for AM 1.5 G condition (~100 mW/cm^2).The enhanced photocatalytic performance indicates a synergistic effect between the N-GQSs and Si nanowire structures; moreover, the N-GQSs act as effective HER catalysts on the Si photocathode. Compared to previously reported carbon-based catalysts on Si system, the N-GQSs/Si nanowire system exhibits a higher ABPE.

To investigate the electrocatalytic activity of the N-GQSs, we measured cyclic voltammetry using a rotating disk electrode (RDE) system. To fabricate the working electrode, an N-GQSs solution was transferred to a glassy carbon (GC) tip that was inert in an aqueous solution. As shown in Figure 4a, in the *J-E* curves obtained by the RDE measurements, the current density associated with the water splitting reaction exponentially increased after the onset point as the potential was swept from 0.1 V to -0.45 V. For comparison with the potential for the HER in the RDE system, the potential required to attain -5 mA/cm^2 of HER current density was measured for graphene monolayer/GC, N-GQSs/GC, and Pt/GC systems. Also for comparison, the RDE of a graphene monolayer without plasma treatment was measured. The potential required to attain -5 mA/cm^2 of HER current density was -0.32 V *vs.* RHE for the graphene monolayer without plasma treatment. The potential for the N-GQSs/GC electrode at -5 mA/cm^2 was -0.22 V *vs.* RHE; this potential was positively

(anodically) shifted by 100 mV relative to that for the monolayer graphene. This result indicates that the N-GQSs and monolayer graphene exhibit electrocatalytic activity toward the HER.

To gain further quantitative insight into the catalytic activity of the N-GQSs, the *J-E* curves in Figure 4a were converted into plots of the potential as a function of the logarithm of *J*. This potential-log *J* plot is called a Tafel plot. The measured potentials were corrected for the iR losses that originated from the resistance of the interface between the electrode and the electrolyte. Analysis of the impedance spectra revealed that the resistances of the graphene monolayer and N-GQSs/GC were 7.5 and 8.0 Ω, respectively. The Tafel plot provides two parameters for estimating the electrocatalytic activity: the Tafel slope and the exchange current density. The Tafel slope is defined to be a measure of the potential increase required to increase the resulting current by one order of magnitude. The graphene monolayer exhibited a Tafel slope of 75 mV/decade, and the N-GQSs/GC exhibited a slope of 45 mV/decade, 30 mV lower than that of the graphene monolayer. For comparison with a well-known catalyst, Pt particles were deposited onto GC and the electro-catalytic activity of the resulting electrode was measured. The applied potential required to obtain -5 mA/cm^2 was -0.04 V *vs.* RHE, which represents a positive shift of 0.18 V relative to that of the N-GQSs/GC electrode. The Tafel slope of Pt-GC was 42 mV/decade, which is similar to that of the N-GQSs/GC. For previously reported carbon-based catalysts, the potential required to attain -5 mA/cm^2 was -0.5 V *vs.* RHE for N-doped graphene and -0.3 V *vs.* RHE for graphitic C_3N_4,

respectively.[23,24] The Tafel slope was reported to be 116 mV/decade for N-doped graphene and 51.5 mV/decade for graphitic C_3N_4 when deposited as a mixture with Nafion or carbon black on GC, respectively.

The Tafel slope provides an indication of which reaction steps are possible in the HER among the following:[39]

$$H_3O^+ + e^- \rightarrow H_{ads} + H_2O \quad \text{Volmer reaction} \quad (6)$$

$$H_{ads} + H_3O^+ + e^- \rightarrow H_2 + H_2O \quad \text{Heyrovsky reaction} \quad (7)$$

$$H_{ads} + H_{ads} \rightarrow H_2 \quad \text{Tafel reaction} \quad (8)$$

where H_{ads} is adsorbed H, (6) is a discharge step, (7) is a desorption step, and (8) is a recombination step. Considering the adsorbed hydrogen coverage (θ_H) on the surface of an electrode, if the recombination of adsorbed hydrogen (the Tafel reaction) is the rate-determining step for the HER and if the coverage is very high ($\theta_H \approx 1$), the measured Tafel slope will be 30 mV/decade. However, if the electrochemical desorption step (the Heyrovsky reaction) is the rate-determining step, a Tafel slope of 40-118 mV/decade is measured and is dependent of the value of θ_H (0-1).[40] The observed Tafel slope of 45 mV/decade in the present work indicates that the kinetics of the HER on the graphene monolayer/GC and N-GQS/GC electrodes is determined by the Heyrovsky reaction.

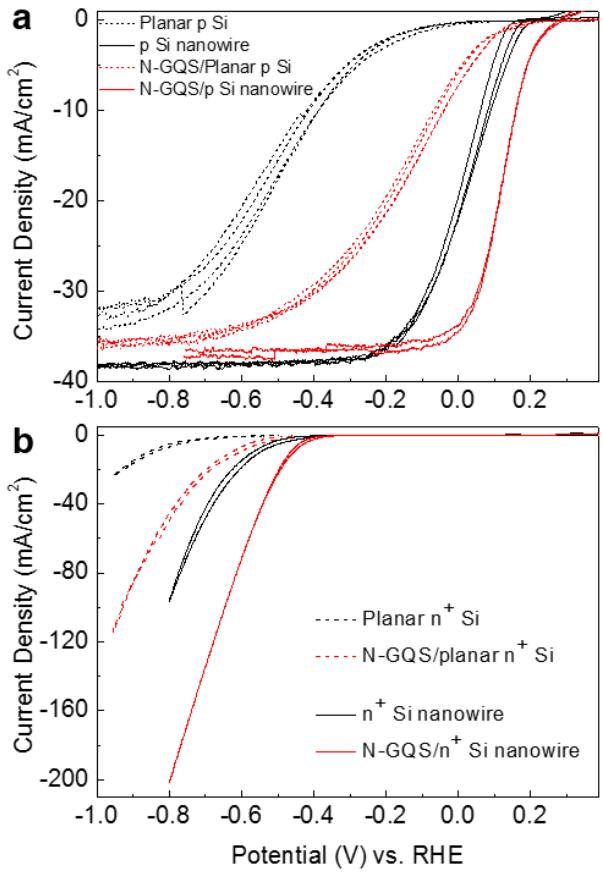

Figure 3. Cyclic voltammograms of N-doped graphene quantum sheets (N-GQSs) on silicon photocathodes. (a) Photocurrent density-potential (*J-E*) curves for a lightly boron-doped planar p-Si electrode and Si nanowire deposited with N-GQSs. The Si nanowire was fabricated using a metal-catalyzed electroless method. (b) Polarization curves of N-GQS on heavily arsenic-doped n^+-type Si electrodes under dark conditions.

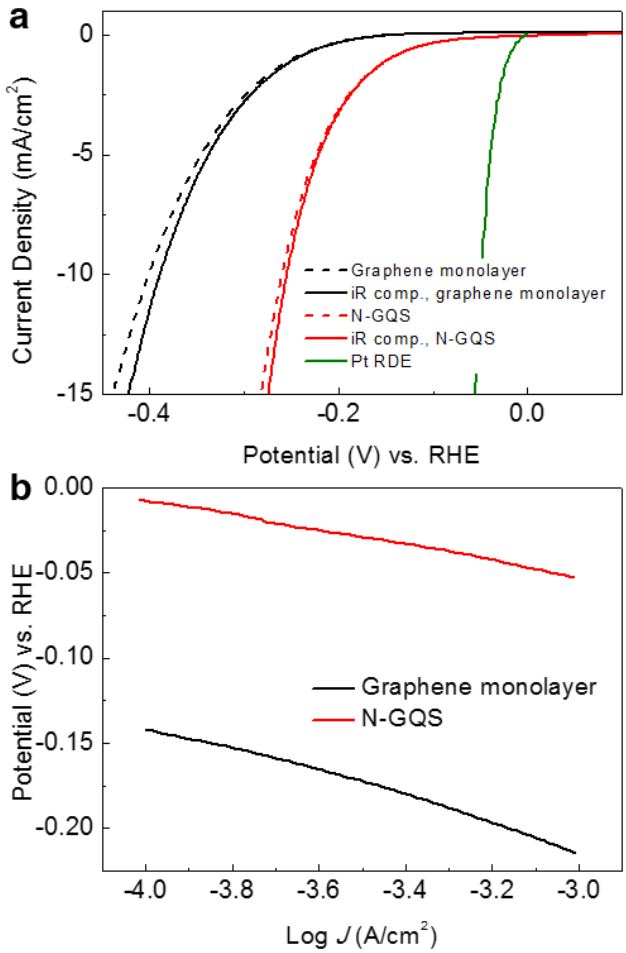

Figure 4. Electrochemical activity of graphene monolayer and N-GQSs on glassy carbon (GC) electrodes in a rotating disk electrode system. (a) Cyclic voltammograms (CV) of a graphene monolayer on GC, N-GQSs on GC, Pt/C on GC. CV data obtained compensating for ohmic drop (iR) losses are also plotted (dashed curves). (b) Tafel plots derived from the CV data in (a).

The exchange current density (J_0) of the N-GQSs catalyst was also analyzed. During hydrogen evolution, the current I can be described the following equation:[7]

$$I=-e(r^{+}-r^{-}) \quad (8)$$

where $r^{+}-r^{-}$ is the net rate of the electron transfer between the oxidation ($4e^{-} + 4H^{+} \leftarrow 2H_2$) and the reduction ($4e^{-} + 4H^{+} \rightarrow 2H_2$) from Eq. (2). The exchange current is the sum of the forward and backward rates when Eq. (2) is in equilibrium. The ability of a given material to catalyze the HER is usually measured by J_0, which is the rate of hydrogen evolution per surface area at the electrode potential when the reaction is at equilibrium. The J_0 is also defined as the current density at zero overpotential. The catalytic effect originates from improvement of the rate of charge transfer at the interface between the electrode and electrolyte or from a decrease in the activation energy barrier for a chemical reaction; these catalytic effects are represented by J_0. A high value of J_0 indicates that electron transfer or the adsorption/desorption of protons at the electrode/electrolyte can occur more easily, with a lower kinetic barrier. The value of J_0 can be obtained by extrapolating the Tafel plot in Figure 4b and extracting the current density at 0 V *vs.* RHE. The N-GQSs/GC electrode exhibited an enhanced J_0 of 7.1×10^{-5} A/cm^2, which was 26.3 times greater than the J_0 of monolayer graphene on GC (2.7×10^{-6} A/cm^2). The J_0 of the N-GQSs was also compared with that of other carbon-based catalysts (Table S3). The reported carbon-based catalysts exhibited a lower J_0 than that of our N-GQSs electrode. In addition, a metal-free carbon catalyst doped with nitrogen and

phosphorous exhibited a J_0 of 2.4×10^{-7} A/cm^2 and a graphitic C_3N_4 catalyst with nitrogen-doped graphene exhibited 3.5×10^{-6} A/cm^2 of J_0.[23,24]

Figure 5 summarizes the experimental data for the Si and GC electrodes. As shown in Figure 5b, our N-GQSs catalyst exhibited a lower Tafel slope and a higher J_0 compared to those of other reported carbon-based HER catalysts. Moreover, considering its role as a co-catalyst on the photoelectrode, the N-GQSs/Si nanowire system exhibited better photoelectrochemical performance in terms of ABPE and onset potential than any other reported catalyst/photoelectrode system (Figure 5a). Using only a non-metal carbon-based catalyst without incorporating a noble catalyst, the ABPE was increased to 2.29% by the combination of the nanostructured photoelectrode and N-GQSs catalyst. The good HER activity of the N-GQSs is attributed to abundant defects introduced by the plasma treatment. Moreover, high-resolution XPS result show that N-sites are classified into pyridinic (2.07 at%), pyrrolic (0.45 at%), and a small number of quaternary nitrogen (0.16 at%), which acts as the good catalytic sites for HER (Figure S1 e). Previous report also suggested that N-doping on graphene could significantly improve the HER by providing additional active sites[23] and theoretical computation shows favorable N-sites for H adsorption.[41] We are under investigation various N-sites with density functional theory for the precise mechanism on HER.

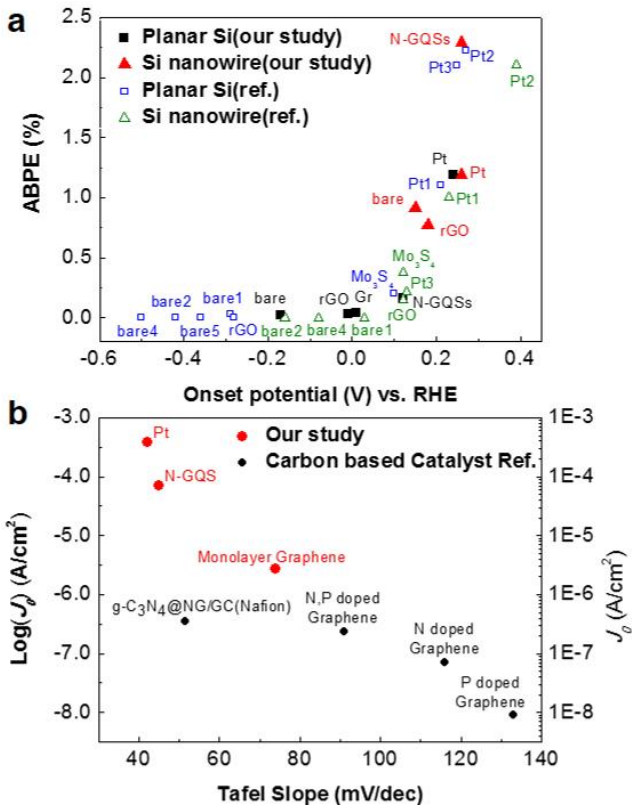

Figure 5. Summary of the experimental data for Si and glassy carbon (GC) electrodes. (a) The photoelectrochemical performance of p-type Si-based photoelectrodes. 'Onset potential' and 'ABPE' indicate the potential at -1 mA/cm^2 *vs.* RHE and the applied bias photon-to-current efficiency, respectively; 'bare' indicates the performance of the bare electrode without deposited catalyst. (b) Electrochemical performance of N-GQSs on GC electrode and other HER catalysts determined using rotating disk electrode system. J_0 indicates that the exchange current density. References can be found in the supporting information (Tables S2 and S3).

To further study the electrochemical performance of the N-GQSs/Si electrode, capacitance, impedance, and transient photoresponse measurements were performed, the results of which are shown in Figure 6. Capacitance measurements of the N-GQSs/Si nanowire and bare Si nanowire electrodes were performed as the potential was swept from 0.6 V to -0.5 V *vs.* RHE in a three-electrode cell without illumination. On the basis of the capacitance results, the flat band potential of the Si nanowire and N-GQSs/Si nanowire electrodes were calculated using the Mott-Schottky relation:[42]

$$1/C_{sc}^2 = 2(E - E_{fb} - kT/e)/(e\varepsilon\varepsilon_0 N) \qquad (9)$$

where C_{sc} is the capacitance of the space charge region, ε is the dielectric constant of the semiconductor, ε_0 is the permittivity of free space, N is the donor density (electron donor concentration for an n-type semiconductor or hole acceptor concentration for a p-type semiconductor), E is the applied potential, and E_{fb} is the flat band potential. Figure 6a shows the typical Mott-Schottky plots for a p-type silicon semiconductor. The donor density was calculated from the slope, and the E_{fb} was determined by extrapolation to a capacitance of zero. On the basis of these relations, the N-GQSs/Si nanowire electrode exhibited an E_{fb} of 0.13 V *vs.* RHE, whereas the E_{fb} of the bare Si nanowires was 0.02 V vs. RHE, as shown in Figure 6a. According to the equation: $E_b = E - E_{fb}$, the applied potential determines the magnitude of band bending (E_b) in the semiconductor and E_{fb}.[43] As E_{fb} increases positively, the absolute value of E_b increases because the applied potential, E is always negative under the cathodic reaction for proton reduction. Higher band bending at the interface between the electrode and electrolyte promotes faster charge

separation of generated electrons and holes.[44] The possibility of charge recombination or surface trapping at sub-band gap energy levels may also be diminished. The higher E_{fb} of the N-GQSs/SiNW electrode relative to that of the bare SiNW electrode appears to have augmented the extent of band bending at the depletion region of the semiconductor near the solid/solution interface because of the relationship between E_b and E_{fb}. Moreover, the doping density of bare SiNW and N-GQSs/SiNW is also calculated from Mott-Schottky relationship. Using the Eq. (9), the bare SiNW shows the donor density of 4.46×10^{15} /cm^3, which corresponds to the resistivity of $10^0 \sim 10^1$ ohm×cm for boron doped p-Si.[45] The N-GQSs/SiNW electrodes shows the donor density of 5.74×10^{15} /cm^3. From the donor density results, N-GQSs deposited on SiNW showed slight increase of the donor density, which might change the electrochemical property at the semiconductor/liquid interface. Zheng *et al.* reported that N dopant adjacent to C atom in a graphene matrix act as an electron acceptor through the analysis of the natural bond orbital population.[23] Likewise, N dopant on GQSs might also act as an active catalytic site for HER.

Impedance measurements were also performed to study the enhanced electrochemical properties of the N-GQSs/SiNW system. Under an illumination intensity of 100 mW/cm^2 with a frequency of 10^3-1 Hz and an amplitude of 5 mV in a three electrode system, electrochemical impedance spectroscopy was performed at 0 V *vs.* RHE. Figure 6b shows a Nyquist plot representing a typical impedance result. In Figure 6b, the N-GQSs/SiNW electrode shows two semicircles that are smaller than those exhibited by the Si nanowire electrode.

On the basis of the results gathered from these two semicircles, two capacitance elements can be assigned: the capacitance of the charge depletion layer in the semiconductor and the capacitance of the double layer at the semiconductor/electrolyte interface. In the high-frequency region, the charge transfer process in the depletion layer of the semiconductor dominates, whereas charge transfer across the double layer at the semiconductor/electrolyte interface is dominant in the low-frequency region.[46] In the case of the N-GQSs/SiNW electrodes, the two semicircles indicating charge transfer processes in the double layers at the solid/solution interface and in the depletion region of the semiconductor are smaller than those of the bare SiNWs. The smaller semicircle in the low frequency range means that the charge transfer resistance of the N-GQSs/SiNW in the double layer is lower than that of bare SiNW. The charge transfer resistance is also related with a kinetic barrier energy for the faradaic reactions across the double.[46] Thus, N-GQSs might promote the faradaic reactions by reducing the charge transfer resistance across the double layer. Similar charge transfer mechanism of the hydrogen production was also reported using reduced graphene oxide catalyst.[28] From the result of smaller semicircle in the high frequency range, the charge transfer resistance of the semiconductor depletion layer in the N-GQSs/SiNW is also lower than that of the bare SiNW. The charge transfer resistance in the semiconductor depletion layer is also correlated with higher photocurrent response because of the higher band bending in the depletion layer.[44, 47]

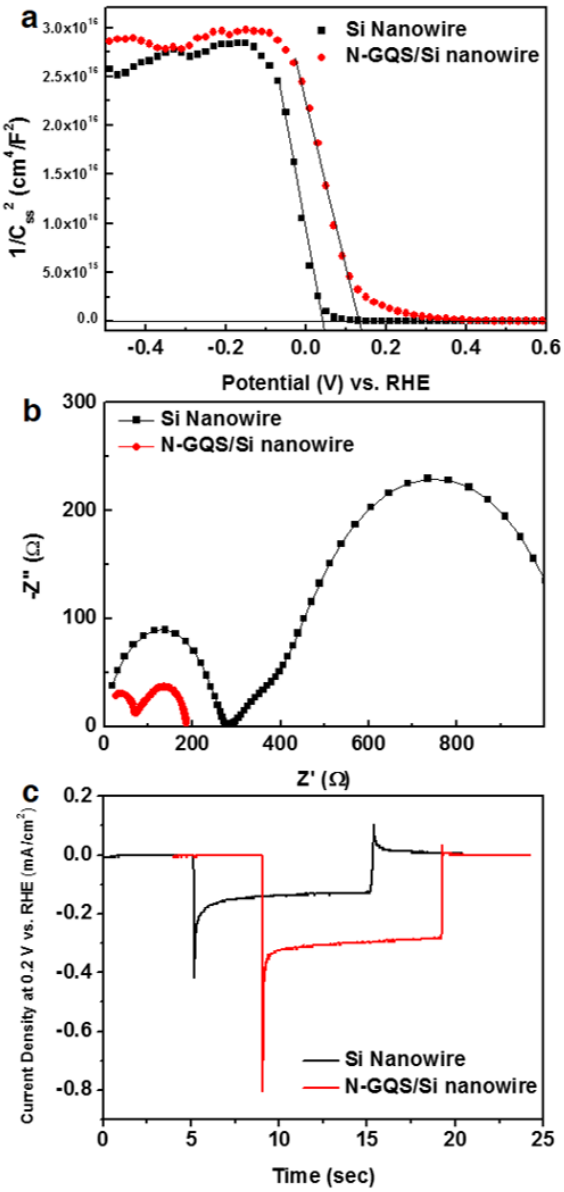

Figure 6. Comparison of the electrochemical activity of Si nanowire and N-GQSs on Si nanowire. (a) Mott-Schottky plots from capacitance measurement as a function of potential *vs.* RHE under dark condition. (b) Nyquist plot for Si nanowire and N-GQSs on Si nanowire at 0 V *vs.* RHE under dark condition. (c) The transient curve of the photocurrent from Si nanowire and N-GQSs on Si nanowire when the light was turned on and turned off at 0 V vs. RHE.

Transient photoresponse measurements were also performed to determine the factors enhancing the photoelectrochemical performance of the N-GQSs/SiNW electrodes; the results are shown in Figure 6c. The transient behavior of the N-GQSs/SiNW and bare Si nanowire electrodes was measured at 0.2 V *vs.* RHE using a chopped illumination system. Figure 6c shows the transient behavior of the N-GQSs/Si and bare Si electrodes without a catalyst. The light was turned on and turned off after 10 sec while the potential was maintained at 0.2 V *vs.* RHE. At the moment of the light was turned on, the current density reached a peak, which is referred to as the initial photocurrent density (J_{in}). The J_{in} values of the N-GQSs/Si nanowire and bare Si nanowire electrodes were -0.80 mA/cm^2 and -0.42 mA/cm^2, respectively. The current density then saturated, and the saturated photocurrent density (J_{st}) under illumination was -0.30 mA/cm^2 for the N-GQSs/Si nanowire electrode and -0.13 mA/cm^2 for the bare Si nanowire electrode. At the moment the light was turned off, the current density again showed an oscillating plot, and the current density at the peaks was designated as J_{off}. The J_{off} values of the N-GQSs/Si nanowire and Si nanowire electrodes were is -0.02 mA/cm^2 and -0.12 mA/cm^2, respectively. The high $J_{st}/J_{in,\ \text{N-GQSs}}$ ratio of 0.375 and small J_{off} of the N-GQS/Si nanowire electrode suggest that fewer carriers were trapped and that less recombination occurred at the surface state of the electrode surface, in comparison with those of the surface state of the bare Si nanowire sample ($J_{st}/J_{in,\ \text{bare}}$ = 0.309). Together, the capacitance and impedance results indicate that the N-GQSs/Si nanowire electrode can contribute to charge separation by inducing favorable band bending and boosting the charge transfer rate, which enhance the electrode's HER performance. To summarize, the

results obtained from the capacitance, impedance, and transient photoresponse measurements indicate that the N-GQSs/SiNW electrode enhances the HER activity by reducing the possibility of charge recombination and lowering the kinetic barriers for the HER at the interface between the Si semiconductor and electrolyte solution.

Conclusions

We fabricated N-doped graphene quantum sheets (N-GQSs) as a catalyst for the solar-driven hydrogen evolution reaction on Si nanowire photocathodes. The onset potential for the Si nanowire photocurrent was significantly shifted toward the anodic direction without a change in the saturation current density. N-GQSs exhibited excellent catalytic activity for the photoelectrochemical HER on Si nanowire photocathodes. The results showed that the N-GQSs electrodes exhibited a ABPE of 2.29%, which is higher than that of any other carbon-based photoelectrochemical HER catalysts reported to date. Our approach in this study involved a strategy for developing metal-free carbon-based catalysts with high efficiency for solar-driven hydrogen fuel production.

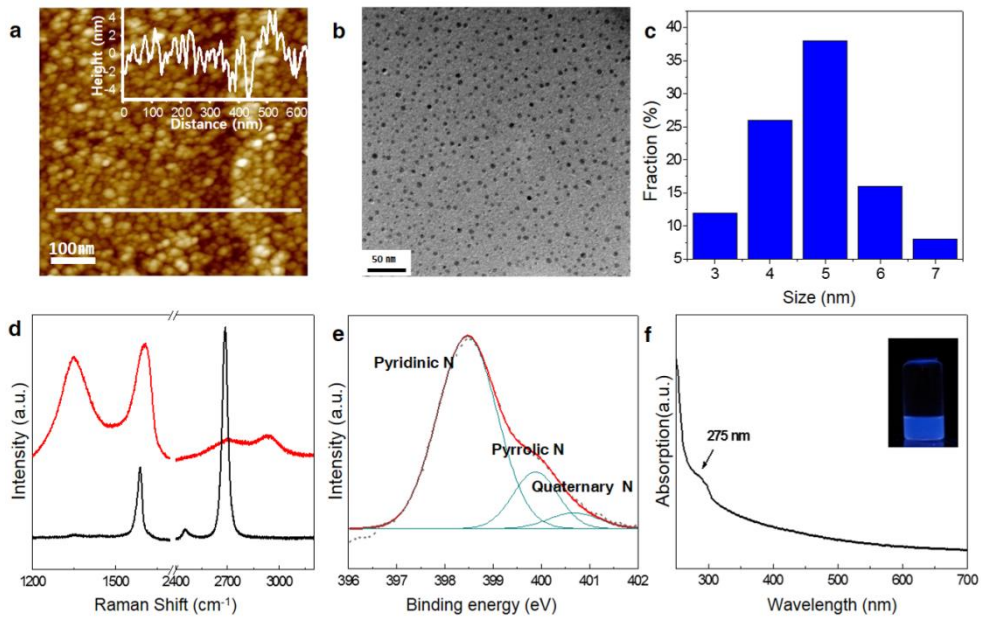

Figure S1. (a) AFM image of nitrogen plasma treated GQSs on Cu foil. Scan size, 600 x 600 nm^2. (b) TEM image of N-GQSs. (c) Histogram showing the size distribution of N-GQSs. (d) Raman spectra of graphene (black) and N-GQSs (red) and (e) detailed N 1*s* XPS spectra of N-GQSs. (f) UV-vis absorption of the N-GQSs in dichloromethane. The inset shows a photograph of the N-GQSs solution under 365 nm wavelength UV lamp.

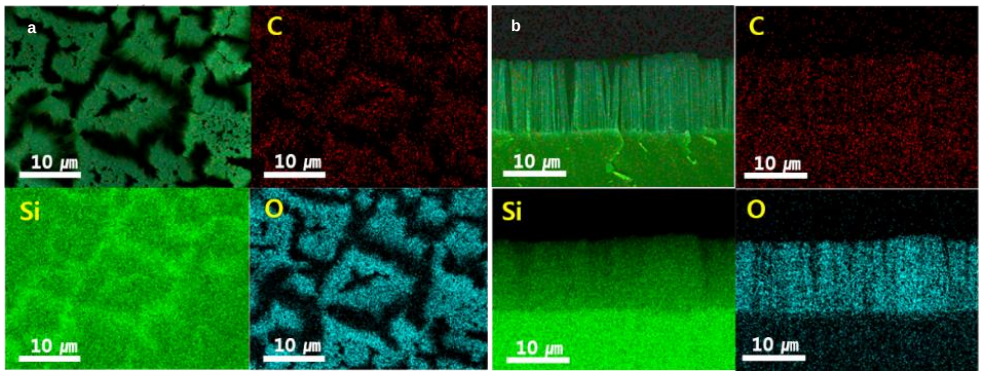

Figure S2. SEM mapping images of N-GQSs decorated on Si nanowires. (a,b) Colour images of all displayed with three elements; C (red), Si (green), and O (blue).

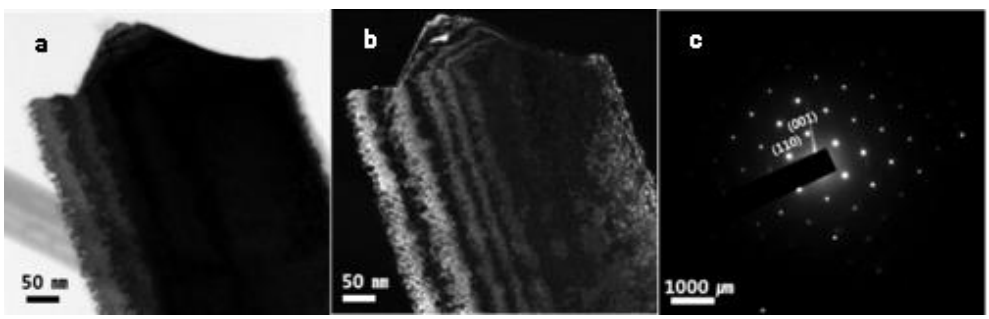

Figure S3. (a) Bright-field and (b) dark-filed TEM images of N-GQSs dispersed on p-SiNWs. (c) Selected area diffraction patterns (SAED) gives p-SiNWs are well etched toward [001] direction. GQS pattern is hardly observed due to the strong silicon lattice.

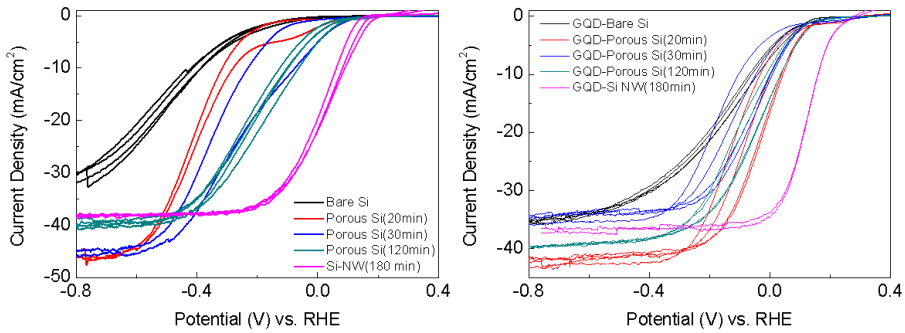

Figure S4. Photoelectrochemical performance of Si photocathode (a) Polarization curves of various Si electrodes without depositing any catalyst. Si nanowire were made by metal-catalyzed electroless method. Each of the etching time is 20 min, 30 min, 120 min, and 180 min. Each cyclic voltammetry was performed during 2 or 4 cycles at a scan rate of 5 mV/s. (b) Polarization curves of various Si electrodes deposited with N-GQSs catalyst.

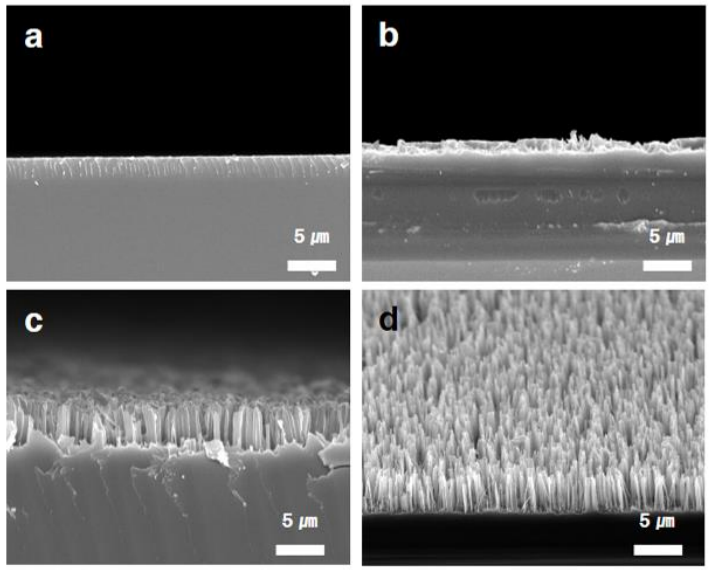

Figure S5. SEM images of cross-sectional views of p-type (100) Si wafers etched in 5 M HF and 0.015 M $AgNO_3$ solution at different etching times. The etching times are (a) 20 min, (b) 30 min, (c) 120 min, and (d) 180 min.

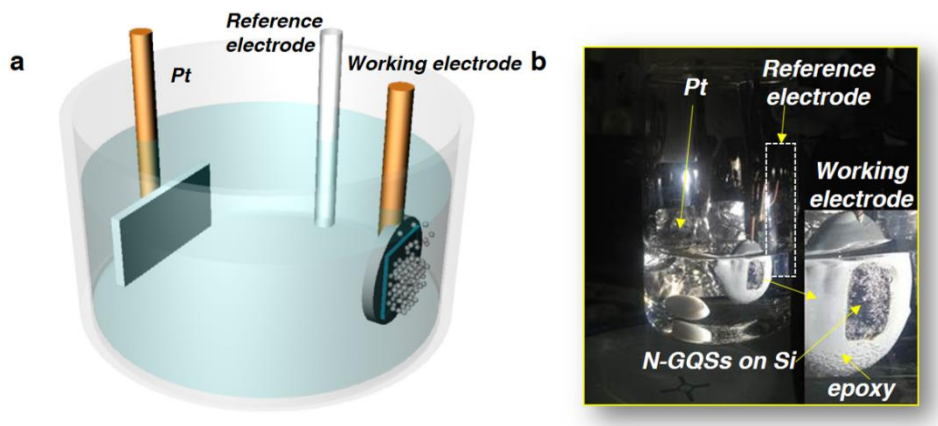

Figure S6. (a) Schematic illustration and photograph images of hydrogen evolution reaction on N-GQSs/Si photocathode

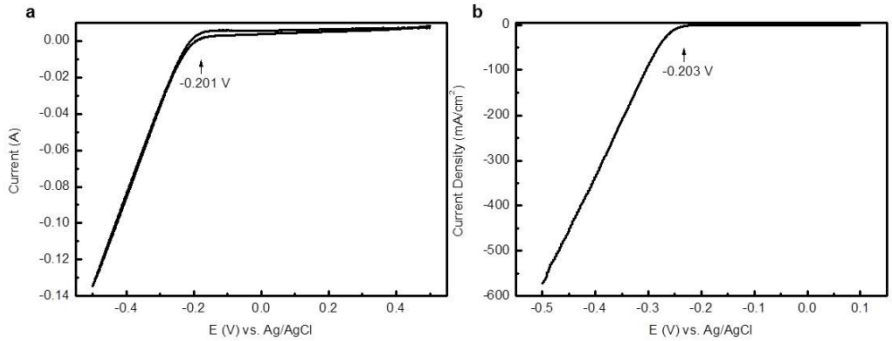

Figure S7. Calibration respect to RHE. Current vs. the applied potential respect to Ag/AgCl reference electrode with using (a) Pt foil for Si PEC cell experiment and (b) Pt wire as the counter electrode for rotating disk electrode (RDE) experiment.

Table S1. Summary of the experimental data of Si and Glassy Carbon (GC) electrodes.

Condition	Electrode	Onset potential [E (V) at -1 mA/cm^2]	E (V) at -5 mA/cm^2	E (V) at -10 mA/cm^2	Current density at reversible potential vs. RHE [mA/cm^2 at 0 V vs. RHE]	ABPE$^{\#}$ (%)
Under illumination (p type Si)	Planar Si	-0.17	-0.29	-0.42	0.34	0.02
	Si NW	0.17	0.12	0.09	21.61	0.91
	N-GQSs/ planar Si	0.13	0.03	-0.04	6.78	0.16
	N-GQSs/ Si NW	0.26	0.19	0.16	34.49	2.29
Under dark condition (n^+ type Si)	Planar Si	-0.63	-0.78	-0.85		
	Si NW	-0.42	-0.51	-0.56		
	N-GQSs/ planar Si	-0.44	-0.55	-0.62		
	N-GQSs/ Si NW	-0.37	-0.42	-0.45		
Photovoltage*	Planar Si	0.46				
	Si NW	0.59				
	N-GQSs/ planar Si	0.57				
	N-GQSs/ Si NW	0.63				
RDE analysis	Graphene/ GC	-0.20	-0.32	-0.37		
	N-GQSs/ GC	-0.11	-0.22	-0.25		
	Pt/GC	-0.02	-0.04	-0.05		

* The photovoltage is defined as the difference between the onset potential under the dark and illumination condition.

ABPE is the applied bias photon-to-current efficiency

Table S2. Summary of the photoelectrochemical data of various catalysts on p-type Si electrodes.

Catalyst	Synthesis and Loading method	Electrolyte	Activity			Ref. (Year)
			Onset Potential vs. RHE (V)	ABPE (%)	E (V) at -5 mA/cm^2	
Planar Si (our study)						
without catalyst (bare)		1M $HClO_4$	-0.17	0.02	-0.42	
Graphene (Gr)	CVD grown graphene & transfer	1M $HClO_4$	0.01	0.04	-0.21	
N-doped graphene quantum sheets (N-GQSs)	CVD grown graphene, plasma treatment, GQSs solution & drop casting	1M $HClO_4$	0.12	0.16	-0.04	
Pt	Nanoparticle by metal catalyzed electroless method	1M $HClO_4$	0.24	1.19	0.11	
Reduced graphene oxide (rGO)	Hummers' method & drop casting	1M $HClO_4$	-0.01	0.03	-0.20	
Si nanowire(our study)						
bare		1M $HClO_4$	0.15	0.91	0.13	
rGO	Hummers' method & drop casting	1M $HClO_4$	0.18	0.77	0.13	
N-GQSs	CVD grown graphene, plasma treatment, GQSs solution & drop casting	1M $HClO_4$	0.26	2.29	0.19	
Pt	Nanoparticle by metal catalyzed electroless method	1M $HClO_4$	0.26	1.19	0.19	
Planar Si(Ref.)						
bare[1]		0.2 M potassium hydrogen phthalate (KHP) with 0.5 M K_2SO_4, buffered to pH 4.5 using KOH.	-0.29*	0.03	-0.423*	[1](2011)
Pt[1]	Nanoparticle by metal catalyzed electroless method		0.21*	1.1	0.15*	
rGO	Hummers' method & drop casting	H_2SO_4 solution containing 0.5 M K_2SO_4 (pH = 1.8)	-0.28*	~0*	-0.49*	[2](2013)
bare[2]		H_2SO_4 and 0.5 M K_2SO_4 (pH 1)	-0.42*	~0*	-0.55*	[3](2012)
Pt[2]	Nanoparticle by metal catalyzed		0.27*	~2.22*	0.2*	

	electroless method					
Pt[3]	Nanoparticle by metal catalyzed electroless method	0.5 M aq. K_2SO_4 adjusted to pH ~ 2 using H_2SO_4	0.25*	2.1	0.2*	[4](2011)
bare[4]		1M $HClO_4$	-0.5*	~0*	-0.07*	[5](2011)
Mo_3S_4	Molecular cluster synthesis & drop casting		0.1*	~0.2*	0.04*	
bare[5]		0.5M H_2SO_4	-0.36*	~0*	-0.54*	[6](2011)
Si nanowire(Ref.)						
bare[1]		0.2 M KHP with 0.5 M K_2SO_4, buffered to pH 4.5 using KOH.	0.03	0	N/A	[1](2011)
Pt[1]	Nanoparticle by metal catalyzed electroless method		0.23*	1	0.16*	
bare[2]	Nanoparticle by metal catalyzed electroless method	H_2SO_4 and 0.5 M K_2SO_4 (pH 1)	~-0.16*	~0*	~-0.3*	[3](2012)
Pt[2]			~0.39*	~2.1*	~0.33*	
Pt[3]	Nanoparticle by metal catalyzed electroless method	0.5 M aq. K_2SO_4 adjusted to pH ~ 2 using H_2SO_4	0.13*	0.21	0.04*	[4](2011)
bare[4]		1M $HClO_4$	-0.08*	~0*	-0.22*	[5](2011)
Mo_3S_4	Molecular cluster synthesis & drop casting		0.12*	~0.38*	0.08*	
rGO	Hummers' method & drop casting	H_2SO_4 solution containing 0.5 M K_2SO_4 (pH = 1.8)	0.12*	0.15*	-0.04*	[2](2013)

*: Values were measured and extrapolated by our group referring to the figures and data from the references. The onset potential is defined as the potential at a photocurrent density of -1 mA/cm^2.

Table S3. Summary of the electrochemical data of RDE system for various catalysts on GC electrodes.

Catalyst/Substrate (adhesive)	Loading method	Electrolyte	Activity			Ref. (Year)
			Tafel Slope (mV/dec)	Exchange current J_0 (A/cm^2)	Exchange current $\log(J_0)$ (A/cm^2)	
Our Study						
Monolayer Graphene	CVD grown graphene	1M $HClO_4$	74	2.7E-6	-5.57	
N-GQSs	CVD grown graphene and plasma treatment	1M $HClO_4$	45	7.1E-5	-4.15	
Pt	Annealing from mixed precursors	1M $HClO_4$	42	3.86E-4	-3.41	
Carbon based catalyst (Ref.)						
N doped Graphene	Annealing from mixed precursors	0.5M H_2SO_4	116	7.04E-8	-7.15	[7](2014)
P doped Graphene	Annealing from mixed precursors	0.5M H_2SO_4	133	8.97E-9	-8.05	[7](2014)
N, P doped Graphene	Annealing from mixed precursors	0.5M H_2SO_4	91	2.4E-7	-6.62	[7](2014)
graphitic-C_3N_4@N-graphene/glassy carbon (Nafion)	Exfoliation & Polycondensation	0.5M H_2SO_4	51.5	3.5E-7	-6.46	[8](2014)

References

1. J. R. McKone, E. L. Warren, M. J. Bierman, S. W. Boettcher, B. S. Brunschwig, N. S. Lewis and H. B. Gray, Energy & Environmental Science, 2011, 4, 3573-3583.
2. Z. Huang, P. Zhong, C. Wang, X. Zhang and C. Zhang, ACS Applied Materials & Interfaces, 2013, 5, 1961-1966.
3. I. Oh, J. Kye and S. Hwang, Nano Letters, 2011, 12, 298-302.
4. S. W. Boettcher, E. L. Warren, M. C. Putnam, E. A. Santori, D. Turner-Evans, M. D. Kelzenberg, M. G. Walter, J. R. McKone, B. S. Brunschwig, H. A. Atwater and N. S. Lewis, Journal of the American Chemical Society, 2011, 133, 1216-1219.
5. Y. Hou, B. L. Abrams, P. C. K. Vesborg, M. E.Björketun, K. Herbst, L. Bech, A. M. Setti, C. D. Damsgaard, T. Pedersen, O. Hansen, J. Rossmeisl, S. Dahl, J. K. Nørskov and I. Chorkendorff, Nat Mater, 2011, 10, 434-438.
6. J. Oh, T. G. Deutsch, H.-C. Yuan and H. M. Branz, Energy & Environmental Science, 2011, 4, 1690- 1694.
7. Y. Zheng, Y. Jiao, L. H. Li, T. Xing, Y. Chen, M. Jaroniec and S. Z. Qiao, ACS Nano, 2014, 8, 5290- 5296. 8. Y. Zheng, Y. Jiao, Y. Zhu, L. H. Li, Y. Han, Y. Chen, A. Du, M. Jaroniec and S. Z. Qiao, Nat Commun, 2014, 5.

References

1. J. A. Turner, *Science*, 2004, **305**, 972–974.
2. N. S. Lewis and D. G. Nocera, *Proc. Natl. Acad. Sci.* U. S. A., 2006, **103**, 15729–15735.
3. M. G. Walter, E. L. Warren, J. R. McKone, S. W. Boettcher, Q. Mi, E. A. Santori and N. S. Lewis, *Chem. Rev.*, 2010, **110**, 6446–6473.
4. T. R. Cook, D. K. Dogutan, S. Y. Reece, Y. Surendranath, T. S. Teets and D. G. Nocera, *Chem. Rev.*, 2010, **110**, 6474–6502.
5. S. W. Boettcher, E. L. Warren, M. C. Putnam, E. A. Santori, D. Turner-Evans, M. D. Kelzenberg, M. G. Walter, J. R. McKone, B. S. Brunschwig, H. A. Atwater and N. S. Lewis, *J. Am. Chem. Soc.*, 2011, **133**, 1216–1219.
6. U. Sim, H.-Y. Jeong, T.-Y. Yang and K. T. Nam, *J. Mater. Chem. A*, 2013, **1**, 5414–5422.
7. J. K. Nørskov, T. Bligaard, A. Logadottir, J. R. Kitchin, J. G. Chen, S. Pandelov and U. Stimming, *J. Electrochem. Soc.*, 2005, **152**, J23–J26.
8. T. F. Jaramillo, J. Bonde, J. Zhang, B.-L. Ooi, K. Andersson, J. Ulstrup and I. Chorkendorff, *J. Phys. Chem. C*, 2008, **112**, 17492–17498.
9. Y. Hou, A. B. Laursen, J. Zhang, G. Zhang, Y. Zhu, X. Wang, S. Dahl and I. Chorkendorff, *Angew. Chem., Int. Ed.*, 2013, **52**, 3621–3625.
10. Y. Yan, B. Xia, Z. Xu and X. Wang, *ACS Catal.*, 2014, **4**, 1693–1705.
11. C. Chen, Y. Kang, Z. Huo, Z. Zhu, W. Huang, H. L. Xin, J. D. Snyder, D. Li, J. A. Herron, M. Mavrikakis, M. Chi, K. L. More, Y. Li, N. M. Markovic, G. A. Somorjai, P. Yang and V. R. Stamenkovic, *Science*, 2014, **343**, 1339–1343.
12. J. R. McKone, E. L. Warren, M. J. Bierman, S. W. Boettcher, B. S. Brunschwig, N. S. Lewis and H. B. Gray, *Energy Environ. Sci.*, 2011, **4**, 3573–3583.
13. B. Marsen, B. Cole and E. L. Miller, *Sol. Energy Mater. Sol. Cells*, 2008, **92**, 1054–1058.
14. M. W. Kanan, Y. Surendranath and D. G. Nocera, *Chem. Soc. Rev.*, 2009, **38**, 109–114.
15. A. Kudo and Y. Miseki, *Chem. Soc. Rev.*, 2009, **38**, 253–278.

16. J. Ran, J. Zhang, J. Yu, M. Jaroniec and S. Z. Qiao, *Chem. Soc. Rev.*, 2014, **43**, 7787–7812.
17. I. Oh, J. Kye and S. Hwang, *Nano Lett.*, 2011, **12**, 298–302.
18. D. H. Youn, S. Han, J. Y. Kim, J. Y. Kim, H. Park, S. H. Choi and J. S. Lee, *ACS Nano*, 2014, **8**, 5164–5173.
19. R. K. Shervedani and A. Lasia, *J. Electrochem. Soc.*, 1998, **145**, 2219–2225.
20. B. Cao, G. M. Veith, J. C. Neuefeind, R. R. Adzic and P. G. Khalifah, *J. Am. Chem. Soc.*, 2013, **135**, 19186–19192.
21. S. Chen, J. Duan, Y. Tang, B. Jin and S. Zhang Qiao, *Nano Energy*, 2015, **11**, 11–18.
22. K. S. Novoselov, A. K. Geim, S. V. Morozov, D. Jiang, M. I. Katsnelson, I. V. Grigorieva, S. V. Dubonos and A. A. Firsov, *Nature*, 2005, **438**, 197–200.
23. Y. Zheng, Y. Jiao, L. H. Li, T. Xing, Y. Chen, M. Jaroniec and S. Z. Qiao, *ACS Nano*, 2014, **8**, 5290–5296.
24. Y. Zheng, Y. Jiao, Y. Zhu, L. H. Li, Y. Han, Y. Chen, A. Du, M. Jaroniec and S. Z. Qiao, *Nat. Commun.*, 2014, **5**.
25. Y. Liang, Y. Li, H. Wang, J. Zhou, J. Wang, T. Regier and H. Dai, *Nat. Mater.*, 2011, **10**, 780–786.
26. J.-D. Qiu, G.-C. Wang, R.-P. Liang, X.-H. Xia and H.-W. Yu, *J. Phys. Chem. C*, 2011, **115**, 15639–15645.
27. Q. Xiang, J. Yu and M. Jaroniec, *Chem. Soc. Rev.*, 2012, **41**,782–796.
28. Z. Huang, P. Zhong, C. Wang, X. Zhang and C. Zhang, *ACS Appl. Mater. Interfaces*, 2013, **5**, 1961–1966.
29. U. Sim, T.-Y. Yang, J. Moon, J. An, J. Hwang, J.-H. Seo, J. Lee, K. Y. Kim, J. Lee, S. Han, B. H. Hong and K. T. Nam, *Energy Environ. Sci.*, 2013, **6**, 3658–3664.
30. Y. Hou, B. L. Abrams, P. C. K. Vesborg, M. E. Bj¨orketun, K. Herbst, L. Bech, A. M. Setti, C. D. Damsgaard, T. Pedersen, O. Hansen, J. Rossmeisl, S. Dahl, J. K. Nørskov and I. Chorkendorff, *Nat. Mater.*, 2011, **10**, 434–438.
31. Y. W. Chen, J. D. Prange, S. D¨uhnen, Y. Park, M. Gunji, C. E. D. Chidsey, P. C. McIntyre, *Nat. Mater.*, 2011, **10**, 539–544.

32.J. Oh, T. G. Deutsch, H.-C. Yuan and H. M. Branz, *Energy Environ. Sci.*, 2011, **4**, 1690–1694.

33.B. M. Kayes, H. A. Atwater and N. S. Lewis, *J. Appl. Phys.*, 2005, **97**.

34.D. B. Williams, Carter and C. Barry, Transmission Electron Microscopy, Springer, 2009.

35. K. Peng, H. Fang, J. Hu, Y. Wu, J. Zhu, Y. Yan and S. Lee, Chem.–Eur. J., 2006, **12**, 7942–7947.

36.E. Garnett and P. Yang, *Nano Lett.*, 2010, **10**, 1082–1087.

37.L. Tsakalakos, J. Balch, J. Fronheiser, M.-Y. Shih, S. F. LeBoeuf, M. Pietrzykowski, P. J. Codella, B. A. Korevaar, O. V. Sulima, J. Rand, A. Davuluru and U. Rapol, *J. Nanophotonics*, 2007, **1**, 013552.

38.Z. Chen, T. F. Jaramillo, T. G. Deutsch, A. Kleiman-Shwarsctein, A. J. Forman, N. Gaillard, R. Garland, K. Takanabe, C. Heske, M. Sunkara, E. W. McFarland, K. Domen, E. L. Miller, J. A. Turner and H. N. Dinh, *J. Mater. Res.*, 2010, **25**, 3–16.

39.L. R. F. Allen and J. Bard, John Wiley & Sons, Inc., 2001, 864.

40.B. E. Conway and G. Jerkiewicz, *Electrochim. Acta*, 2000, **45**, 4075–4083.

41.Y. Fujimoto and S. Saito, *J. Appl. Phys.*, 2014, **115**, 153701.

42.A. W. Bott, *Curr. Sep.*, 1998, **17**, 87–91.

43.K. Gelderman, L. Lee and S. W. Donne, *J. Chem. Educ.*, 2007, **84**, 685.

44.N. S. Lewis, *J. Electrochem. Soc.*, 1984, **131**, 2496–2503.

45.R. E. Hummel, Electronic Properties of Materials, Springer, 4th edn, 2011.

46.D. Merki, H. Vrubel, L. Rovelli, S. Fierro and X. Hu, *Chem. Sci.*, 2012, **3**, 2515–2525.

47.T. Lopes, L. Andrade, H. A. Ribeiro and A. Mendes, Int. *J. Hydrogen Energy*, 2010, **35**, 11601–11608.

48.J. Moon, J. An, U. Sim, S.-P. Cho, J. H. Kang, C. Chung, J.-H. Seo, J. Lee, K. T. Nam and B. H. Hong, *Adv. Mater.*,2014, **26**, 3501–3505.

Part Ⅱ

Oxygen-rich functionalized graphene for lithium sulfur battery

Chapter 5

General introduction of lithium sulfur battery

Lithium sulfur battery

Rechargeable batteries with superior performance are desired to solve imminent energy and environmental issues.[1–3] Lithium ion batteries have become dominant in the market as the state-of-the-art energy storage devices in portable and smart devices, such as cell phone, cameras and laptops, due to high energy density and log cycle life. However, the specific capacity and energy density become insufficient to meet the increased energy-demanding applications including electric vehicles and grid-level energy storage.[4,5] To solve these challenges, many researchers try to find an advanced batteries system with superior performance over current technologies.

The Li/S battery is an attractive and promising candidate among emerging battery technologies.[6] The concept of utilizing elemental sulfur as a cathode electrode material was introduced by Herbet and Ulam in 1960s.[7,8] In Li/S battery cell, elemental sulfur and lithium are used as the positive and negative electrodes, respectively, and the overall reaction during discharge can be described as

$$S_8 + 16Li^+ + 16e \rightarrow 8Li_2S \text{ (cathode)}$$

$$16Li \rightarrow 16Li^+ + 16e^- \text{ (anode)}$$

Sulfur and lithium have theoretical specific capacities of 1673 and 3861 mAh g^{-1}, respectively and the average voltage of the full cell is 2.15 V. The Li/S battery system supply a theoretical energy density of 2500 Wh kg^{-1} or 2800 Wh L^{-1},[4,9] which is 5 times higher than that of current lithium ion batteries (500 Wh kg^{-1}), as shown in Figure 1a.

The common Li/S battery architecture is comprised of a positive electrode of sulfur, carbon additives and binder, and a metallic lithium anode separated by an

organic electrolyte. In the organic liquid electrolyte. Figure 1b shows a typical charge-discharge profile in a Li/S cell. During the discharge process, two voltage plateaus at 2.4 and 2.15 V, which corresponded to the reduction of high-order lithium polysulfides (Li_2S_x, $4 \leq x$) and low-order lithium polysulfide (Li_2S_x, $x \leq 4$), are observed. During charging cycle, two plateaus at 2.2 and 2.5 V appear. Based on the phase transition mechanism, the discharge procedure goes through two stages.[10,11] The reaction of elemental sulfur with Li forms high-order lithium polysulfide, which dissolve in the liquid electrolyte.

$$S_8 + 2Li^+ + 2e^- \rightarrow Li_2S_8$$

$$3Li_2S_8 + 2Li^+ + 2e^- \rightarrow 4\,Li_2S_6^-$$

$$Li_2S_8 + 2Li^+ + 2e^- \rightarrow 2Li_2S_4$$

In the second steps, insoluble Li_2S_2 and Li_2S are formed and they precipitate out at the cathode. The corresponding voltage is lower, as indicated by the long plateau at 2.1 V.

$$Li_2S_4 + 2Li^+ + 2e^- \rightarrow 2Li_2S_2$$

$$Li_2S_2 + 2Li^+ + 2e^- \rightarrow 2Li_2S$$

The reaction of first plateau has fast or moderate kinetics, while the second reaction of converting Li_2S_2 to Li_2S is difficult and is impeded by slow solid-state diffusion. Consequently, the voltage drops rapidly once Li_2S covers the whole electrode, resulting in the termination of discharge. The summary of the reaction sequence of the sulfur cathode and the corresponding electrochemical profile is shown in Figure 1b.

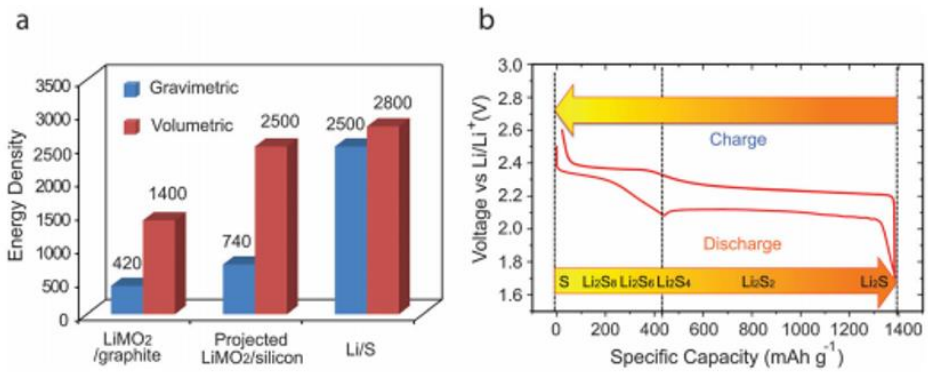

Figure 1. Introduction to the Li/S battery. (a) The theoretical energy density of different rechargeable battery systems based on active materials only. The units are Wh kg^{-1} and Wh L^{-1} for gravimetric and volumetric energy density, respectively. M = $Ni_{1/3}Mn_{1/3}Co_{1/3}$ for the $LiMO_2$–graphite system. For projected $LiMO_2$–silicon cell, the specific capacity for the cathode and anode are 250 and 3000 mAh g^{-1}, respectively. The density is 4.8 g cm^3 for $LiMO_2$, and the capacity per volume is 2200 mAh L^{-1} for silicon after considering the necessary space for volume expansion. (b) The voltage profile and chemistry of sulfur cathode in the organic electrolyte. This is referred by Yi's group.

Previous challenges and Studies

Rechargeable Li/S batteries have significant attention when considering the high specific energy density and low price. However, there is still have challenges to commercialize. The first problem is related to the volume change of sulfur particles during battery operation. Sulfur has a density of 2.03 g cm^3, while Li_2S (low-order polysulfide) is lighter (1.66 g cm^3), which leads to the volume expansion (80%) when sulfur is fully converted to Li_2S. This volume change causes fast capacity fading due to the pulverized structure of active materials. Second, the poor electrical conductivity of sulfur (10^{-28} $S \cdot cm^{-1}$) and Li_2S ($\geq 10^{14}$ ohm·cm),[12] which results in sluggish kinetics of the sulfur cathode. Moreover, the ionic insulating nature of sulfur leads to low active material utilization. Once a thin low-order polysulfide layer completely covers the whole electrode, further lithiation will be largely hampered and the voltage decreases rapidly. Third, the polysulfides are intermediates produced during the electrochemical reduction of sulfur which are highly soluble in the electrolyte. These soluble species diffused from the sulfur cathode to the lithium anode driven by the concentration and gradually passivating the anode. The low-order polysulfide can move back to the cathode and oxidized to high-order polysulfide. This parasitic process takes place continuously, creating an internal "shuttle" phenomenon. The polysulfide shuttle usually leads to an irreversible loss of sulfur in cathode, which results in low Coulombic efficiency.[4,9,14] and fast capacity fading. Moreover, the dissolution and precipitation process alters the morphology of the cathode in each cycle, which induces strain inside the electrode and degrades the cycle life.[13] Besides challenges related to the sulfur cathode, the use of lithium metal

anodes results in safety concerns and energy density penalties due to the use of excess lithium;[15,16] these concerns warrant careful examination in the future.

To solve these challenges, many researches have been focused on the rational design of the electrode structure. Based on previous reports in the past several years, the ideal sulfur electrode structure should have the following characteristics:[17,18] first, sufficient space for sulfur volumetric expansion during battery operation; second, small dimensions of the active material to avoid pulverization; third, short transport pathways for both electrons and Li ions for high capacity and power capability; forth, physically and chemically trapping the high-order polysulfide; fifth, additional electrolyte additives to cover the lithium surface to minimize the shuttle effect. These characteristics allow to develop various sulfur structures which can be divided into several categories, such as graphene-sulfur composites, nano-sized carbon-sulfur composites, conductive polymer-sulfur composites, etc.

References

1. J. M. Tarascon and M. Armand, *Nature*, 2001, **414**, 359-367.
2. M. Armand and J.-M. Tarascon, *Nature*, 2008, **451**, 652-657.
3. M. S. Whittingham, *Chem. Rev.*, 2004, **104**, 4271-4301.
4. X. L. Ji and L. F. Nazar, *J. Mater. Chem.*, 2010, **20**, 9821-9826.
5. M. Z. Jacobson, *Energy Environ. Sci.*, 2009, **2**, 148-173.
6. P. G. Bruce, S. A. Freunberger, L. J. Hardwick and J.-M. Tarascon, *Nat. Mater.*, 2012, **11**, 19-30.
7. D. Herbert and J. Ulam, U.S. Patent, 3043896, 1962.
8. J. R. Birk and R. K. Steunenberg, *Adv. Chem. Ser.*, 1975, 186-202.
9. Y. V. Mikhaylik and J. R. Akridge, *J. Electrochem. Soc.*, 2004, **151**, A1969-A1976
10. K. Kumaresan, Y. Mikhaylik and R. E. White, *J. Electrochem. Soc.*, 2008, **155**, A576-A582.
11. H. Yamin and E. Peled, *J. Power Sources*, 1983, **9**, 281-287.
12. Y. Yang, G. Y. Zheng, S. Misra, J. Nelson, M. F. Toney and Y. Gui, *J. Am. Chem. Soc.*, 2012, **134**, 15387-15394.
13. R. Elazari, G. Salitra, Y. Talyosef, J. Grinblat, C. ScordilisKelley, A. Xiao, J. Affinito and D. Aurbach, *J. Electrochem. Soc.*, 2010, **157**, A1131-A1138.
14. S. Joongpyo, K. A. Striebel and E. J. Cairns, *J. Electrochem. Soc*., 2002, **149**, A1321-A1325.
15. C. Brissot, M. Rosso, J. N. Chazalviel and S. Lascaud, *J. Power Sources*, 1999, **81**, 925-929.
16. X. H. Liu, L. Zhong, L. Q. Zhang, A. Kushima, S. X. Mao, J. Li, Z. Z. Ye, J. P. Sullivan and J. Y. Huang, *Appl. Phys. Lett.*, 2011, **98**, 183107
17. G. Zheng, Y. Yang, J. J. Cha, S. S. Hong, and Y. Cui, *Nano Lett.*, 2011, **11**, 4462-4467.
18. Y. Yang, G. Zheng, and Y. Cui, *Chem. Soc. Rev.* 2013, **42**, 3018-3032.

Chapter 6

An electrochemical approach to graphene oxide coated sulfur for long cycle life

Introduction

There has been a growing demand for studies on eco-friendly and alternative energy sources to replace fossil fuels and natural gas. Lithium-based rechargeable batteries with both high volume and gravimetric energy have received significant attention as green power sources for portable electronics including mobile phones and laptops.[1-3] However, state-of-the-art lithium rechargeable battery systems must be substantially improved to satisfy the ever-increasing energy demands of current electric vehicles for both high energy and power density.[1-3] The low specific capacity of cathode materials (~ 150 mAh/g for layered oxides and ~ 170 mAh/g for $LiFePO_4$) compared to those of the anode materials (370 mAh/g for graphite and 4200 mAh/g for silicon[4]) has spurred many researchers to develop new high capacity cathode materials.

Among many candidates, sulfur is one of the most promising materials that can overcome the aforementioned issues. Elemental sulfur has a theoretical specific capacity of 1675 mAh/g,[5,6] which is approximately five times higher than that of conventional $LiCoO_2$ cathode materials. Furthermore, sulfur has other noticeable advantages[7] as its resource is abundant, and it is inexpensive and environmentally friendly. These advantages are expected to play pivotal roles in commercializing as a next generation battery system that has a high specific energy.

However, the poor electronic conductivity of elemental sulfur (~1×10^{-30} S/cm at room temperature) limits its utilization as an active material for sulfur

electrodes[8]. During charging and discharging, the sulfur cathode is converted into lithium polysulfides (Li_2S_8, Li_2S_6, Li_2S_4 2.15-2.4 V and Li_2S_2, Li_2S ≤2.1 V)[8,9] dissolved in liquid organic electrolytes and deposited on lithium metal electrodes and separators, which causes irreversible loss of polysulfides. Recently, Y. V. Mikhaylik *et al.* reported that high order polysulfides generated at the sulfur electrode in charge state diffuse to the lithium anode where they react directly with the lithium metal in a parasitic reaction to recreate the low order polysulfides. Those species diffuse back to the surfur cathode to regenerate the higher forms of polysulfide, thus creating a shuttle mechanism.[10] These losses of an active material leads to low Coulombiv efficiency, poor rechargeability, and rapie fading of the capacity.[8-12] Thus, extensive research studies have been conducted in an attempt to overcome the above mentioned problems. In fact, the effots have been focuesed on enhancing the electrical conductivity of sulfur by combinding it with various conducting materials such as porous carbon,[13-15] one dimensional carbon,[16,17] graphene oxide (GO),[18-20] and conductive polymers.[21] In particular, the GO-based materials showed enhanced electrochemical properties because GO-sulfur composites are capable of preventing the shuttle of polysulfides. However, the role of oxygen functional groups in such improvement has still not been completely understood yet.

In this work, GO wrapped sulfur (GO-S) composites were prepared and decorated with carbon black (CB), and then utilized as a cathode electrode in a lithium sulfur battery (Li-S battery). The structural properties of the cathode electrode were characterized *via* transmission electron microscopy (TEM), scanning

electron microscopy (SEM), and Raman spectroscopy. In addition, the chemical properties were determined by using Fourier transform infrared spectroscopy (FTIR) and X-ray photoelectron spectroscopy (XPS). The cyclic performance and Coulombic efficiency was analysed using various electrochemical measurement techniques.

Experimental

Synthesis: GO used in this paper was synthesized by Hummer's method.[22] Graphite power (10 g) was prepared in a flask in an ice bath. 7.6 g $NaNO_3$ was added into the flask which was filled with 338 ml H_2SO_4 under stirring condition until homogenized. In addition, 45 g of $KMnO_4$ was gradually put into the system over 1 h under magnetic stir. The solution was removed from the ice bath after 2 h and was further stirred for 5 days. Then viscous slurry was obtained and then added to 600 ml aqueous solution over 1 h and H_2O_2 (30 wt.%) (5 ml) was added into the mixture with stirring system over 1 day. The brown colour mixture was rinsed with deionized water using centrifuge system for several times. Finally, the GO aqueous solution was obtained and dried with vacuum evaporator.[17]

GO (~4 mg/ml) was dispersed in deionized water and sonicated for 1 h. GO has hydrophilic properties from oxygen functional group, which made GO was easily dispersed in water. In order to increase the conductivity of the core-shell material, carbon black nanoparticles (Super P, ~ 40 nm in diameter, CB, 40 mg) were loaded on the graphene oxide (GO) by simple sonication method. The mixture in the flask was sonicated for 1 h for a homogeneous suspension. For GO-S/CB composites, 1.5 g of $Na_2S_2O_3$ powder was dissolved in 250 ml deionized water and hydrochloric acid was added to the solution with a magnetic stirring, which turns to be yellow colour from sulfur. To decorate GO/CB on sulfur particles, Triton TX-100 aqueous solution was poured into the flask while the system was heated up to ~ 70°C in an oil bath. After 20 min at ~ 70°C, the

prepared GO/CB suspension was added into the flask and kept for 20 min under vigorous magnetic stirring. Then, the system was cooled down to room temperature and the resultant product was collected and rinsed several times by centrifuge. The product was dried in a vacuum system.

Cell Assembly and Electrochemical Measurement: The GO-S composites were mixed with Super P (type of carbon black) and polyvinyldifluoride (PVDF), with mass ration of 60:20:20, in N-Methylpyrrolidone (NMP) solvent to produce electrode slurry. The slurry was loaded onto a current collector, an aluminium foil, using a doctor blade technique, and then dried for 3 h to form a working electrode. After dehydration, it was pressed by a roll press machine and then, it was dried again for 12 h. The loading level of total material was ~ 1-1.2 mg/cm^2. 2032 type coin cells were used for the battery type and Li metal foil for the counter electrode. The electrolyte was 1.0 M lithium bis-trifluoro-methane sulfonylimide (LITFSI) in 1,3-dioxolane (DOL) and 1,2-dimethoxyethane (DME) (volume ratio 1:1). In addition, it should be noted that $LiNO_3$ was used as an additive in the electrolyte to enhance the cycle stability of the Li-S cell. The coin cells were assembled in an Ar-filled glove box. The galvanostatic charge-discharge experiment was performed with a WBC3000 cycler (WonA Tech, Korea) at room temperature (RT). The coin cells were cycled at a constant current density of 835 mA/g (0.5 *C*) on cycling performance or various constant current density from 0.1 *C* to 1 *C* on rate performance with the voltage range of 1.7-2.8 V *vs.* Li/Li$^+$. All the specific capacity values were based on the mass of elemental sulfur. The Cyclic voltammetry (CV) was operated from 1.5 V to 3.0 V at 0.03

mV/s scan rate, which can be converted to the constant current of 0.1 *C*-rate. The Electrochemical Impedance Spectroscopy (EIS) was recorded by applying an AC voltage of 0.005 V in the frequency range from 100,000 to 0.05 Hz.

Material Characterization: The charge-discharge capacity of the Li-S cell was calculated by the sulfur content of the electrode matrix and the weight ratio of sulfur to carbon in the composite electrode was measured by thermogravimetric analysis (TGA: SDT Q600). TGA measurements were conducted in a nitrogen atmosphere from room temperature to 600°C at a heating rate of 5°C/min. X-ray diffraction pattern was obtained using High Power XRD from Rigaku Corp. with Cu K_α radiation (λ) 0.15418 nm (model: D-MAX2500-PC). The diffraction data was recorded in the 2θ range of 20-80° with a step of 4°/min. To determine the surface morphology, field-emission scanning electronic microscopy (FE-SEM) was performed (AURIGA, Carl Zeiss).

Results and Discussion

The GO-S/CB composites were synthesized with a help of surfactants in order to increase the surface affinity between GO and sulfur. The surfactant is also useful to control the grain size in a manner similar to that of conventional sulfur particles. The GO contained both hydrophobic aromatic and hydrophilic regions which interact with carbon black (Super P, average particle size ~50 nm, CB), and polysulfides, respectively. The schematic illustration in Fig. 1(a) shows a sulfur particle tightly packed with GO sheets. The SEM images of GO-S/CB show a few micron-sized sulfur particles well covered with GO and CB (Fig. 1(b) and Fig. S1(a)), while the surface of the sulfur particles are partially exposed in the S/CB electrode as shown in Fig. S1(b). The fringes and Moiré patterns in the TEM images (Figs. 1(c,d)) imply that the sulfur particles are compactly wrapped with GO and CB. The corresponding GO-S/CB composites were characterized using scanning transmission electron microscopy (STEM) and energy dispersive X-ray spectroscopy (EDS). The elemental EDS mapping for carbon (orange), sulfur (blue), and oxygen (magenta) clearly shows that GO-S/CB forms a core-shell structure with oxygen-rich functional groups (Figs. 1(e-h)).

The surfaces of the GO-S/CB and the S/CB electrodes were characterized *via* Fourier transform infrared spectroscopy (FTIR), X-ray photoelectron spectroscopy (XPS), and Raman spectroscopy, as shown in Fig. 2. The FTIR spectrum of GO-S/CB shows various configurations of oxygen in the structure including the vibration modes of -OH, C=O, C-O, and C-O-C at 3434 cm^{-1}, 1725 cm^{-1}, 1024–1180 cm^{-1}, and

1200 cm^{-1}, respectively; the peak at 1629 cm^{-1} results from the sp^2-hybridized C=C in-plane stretching.[23] Moreover, the O 1*s* spectra obtained from XPS exhibit significantly higher intensity of the peak at 533.0 eV (C-OH) in GO-S/CB, compared to that of the S/CB. These results noticeably match with the FTIR and XPS spectra of each carbon material (GO and CB) as shown in Fig. S2. The Raman spectra exhibit typical of carbon peaks; i.e., two strong peaks at 1350 cm^{-1} for the D band and at 1590 cm^{-1} for the G band, which stem respectively from structural defects and the in-plane vibrational mode.[24] The Raman spectrum in the inset of Fig. 2(c) shows a peak corresponding to sulfur only.[25] The sulfur peak was not observed for both samples, implying that the sulfur particles are surrounded by carbon materials.

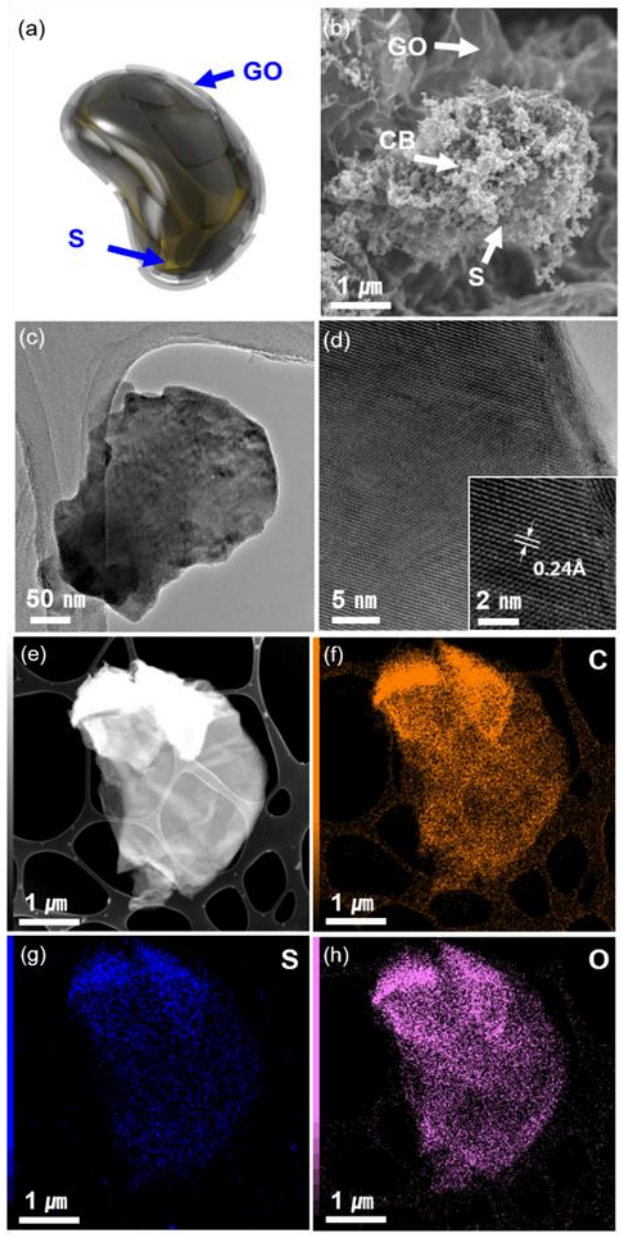

Figure 1. (a) Schematic illustration and (b) scanning electron microscopy (SEM) image of GO-S/CB composites. (c) Transmission electron microscopy (TME) image and (d) high resolution TEM image of GO-S/CB. (e) Scanning-TEM (STEM) image and (f-h) C, S, and O energy-dispersive S-ray spectroscopy (EDS) maps of the GO-S/CB composites.

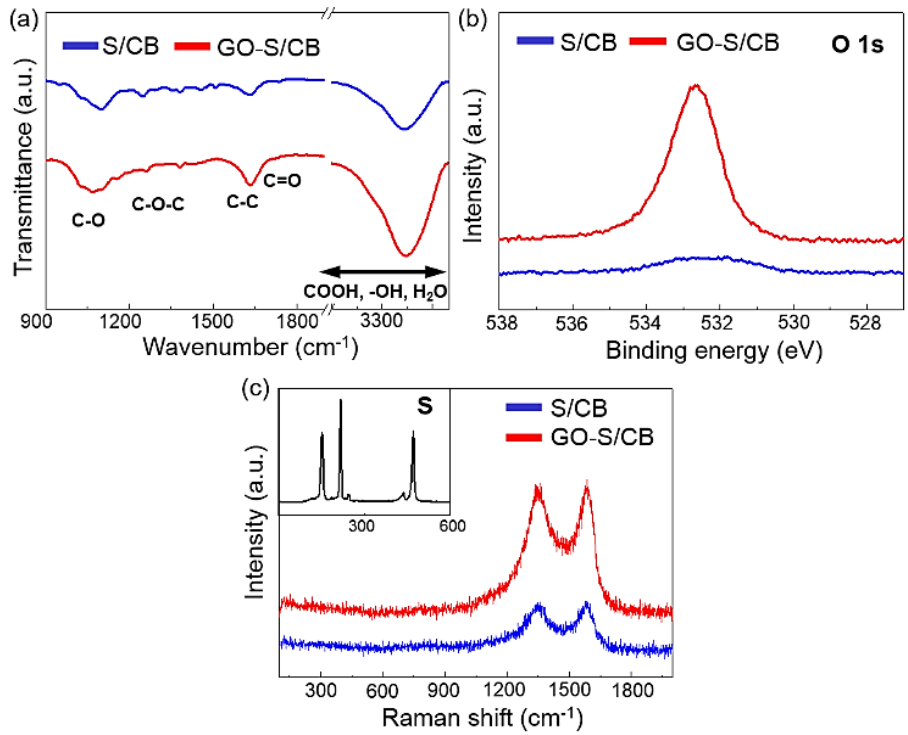

Figure 2. (a) FTIR spectra of GO-S/CB and S/CB. The peaks correspond to the various functional groups in GO-S/CB and S/CB. (b) O 1*s* XPS spectra and (c) Raman spectra of GO-S/CB and S/CB.

Figure 3(a) shows the X-ray diffraction (XRD) patterns measured from the S/CB and GO-S/CB composites on the Al foil. The positions of the peaks corresponding to sulfur particles all occurred at the standard Bragg position of the orthorhombic phase with the space group Fddd (JCPDS 24-0733: S_8)[26] and no traces of other impurities were detected. The amount of GO in the GO-S composite was quantified *via* TGA analysis. Fig. 3(b) represents the TGA results of the GO-S composite from 40 to 600℃ under a nitrogen atmosphere, and the weight loss was shown approximately up to 84wt.%. The loss of the sulfur-conducting material composite results mainly from the evaporation of sulfur at temperatures of ~170-250℃. Furthermore, the continuous and steady weight loss of the second stage above 370°C is estimated to be 6 wt.%. The sulfur content of the GO-S composite was adjusted to 90 wt.% during the preparation process.

Fig. 4(a) and (b) show conventional charge-discharge profiles of the S/CB and the GO-S/CB as a lithium sulfur battery. The cell is discharged and charged at 0.5 C rate (835 mA/g) for 20 cycles, which is sufficient for revealing variations and tendencies in the electrochemical behavior. In the discharge profiles, two-step plateaus were generated at 2.4 V and 2.1 V due to the dissolution of sulfur to soluble high-order polysulfide and the precipitation of low-order polysulfide to lithium sulfide (Li_2S_8, Li_2S_6, Li_2S_4 2.15-2.4 V and Li_2S_2, Li_2S ≤2.1 V).[8,9] In this paper, we designated three regions, Q_1, Q_2 and ΔV, which facilitate the explanation of the electrochemical properties of GO-S/CB cathode electrode. Q_1 and Q_2 indicate

capacity of the dissolution and the precipitation regions, respectively and the ΔV means of overpotential between discharge and charge reactions.

In the Q_1 region, the sulfur particles as reactants are initially dissolved into electrolyte, and then, the reactants are reduced to the long-chain sulfides (S_n^{2-},n=8-4) in the liquid phase (dissolved state). In this regime, the lithium/polysulfide ions can easily move, leading to the fast kinetics of the reaction. However, those liquid mechanism leads to irreversible loss of soluble polysulfides due to diffusion from the polysulfide into the bulk electrolyte.[9] In the Q_2 region, long-chain polysulfides are converted to short-chain polysulfides (S_n^{2-},n=4-1), and then finally produced the lithium sulfide (Li_2S) (precipitated state); the kinetics of this reaction are sluggish owing to the formation of lithium polysulfides, driving the high reversible cycle retention of capacity.[9] In charge processes, the reverse reactions aforementioned occur. Q_1, Q_2, and ΔV provide insight into the origins of the unique reaction mechanism of the materials. The GO-S/CB exhibits the constant Q_1 capacity retention with increasing cycle number, while the capacity of S/CB is continuously fading due to irreversible loss of polysulfide, which represents that GO can play a key role in reserving polysulfides.

Moreover, the slowly decreasing Q_2 value of the GO-S/CB, compared to the rapidly decreasing value of S/CB indicates that GO provides reversible reaction sites with polysulfide. Previous studies assert that the oxygen-rich carbon matrix promotes the interaction of carbon with sulfides.[18,19,27] Thus, we believe that the increased electrochemical performance of GO stems from physical wrapping and chemical surface modification. The cycling performance and Coulombic efficiency

of S/CB and GO-S/CB composites were measured at 0.5 *C* rate (1 *C* rate = 1,675 mA/g) for 100 cycles, as shown in Figs. 4(c) and (d); respective initial capacities of 1003.5 mAh/g and 1142.7 mAh/g were obtained for S/CB and GO-S/CB at the first cycle. At the relatively fast *C*-rate, GO as a conducting agent supports electrical contact with sufur, which shows the discharge capacities of ~723.7 mAh/g (GO-S/CB) and ~307.3 mAh/g (S/CB) at 100th cycle, respectively. The fading capacity of the S/CB may be attributed to its Coulombic efficiency, i.e., the S/CB exhibits a low charge/discharge ratio in the initial cycle, but the Coulombic efficiency increased gradually due to the shuttle mechanism stemming from the irreversible loss of the polysulfide into electrolyte. This loss indicates that the structure of the S/CB does not trap the soluble polysufide.[10]

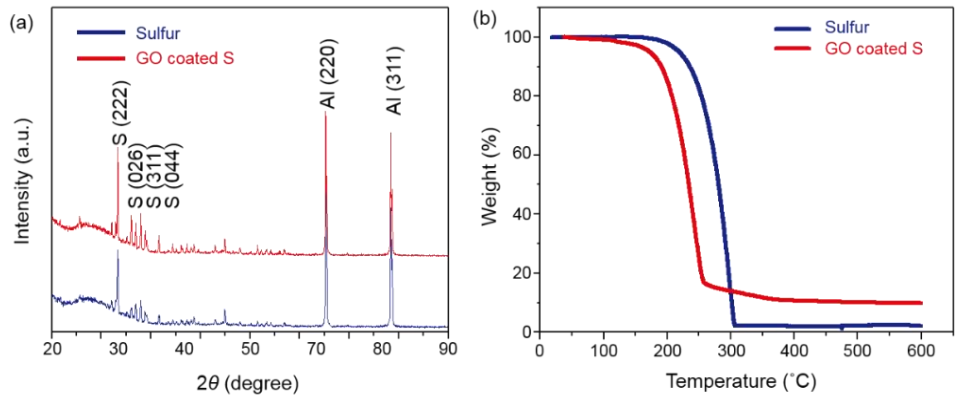

Figure 3. X-ray diffraction (XRD) patterns and Thermogravimetric analysis (TGA). (a) XRD spectra of S/CB and GO-S/CB on Al foil current collector and (b) TGA spectra collected in N_2 atmosphere with a heating rate of 10℃/min showing the S content of the GO-S electrodes.

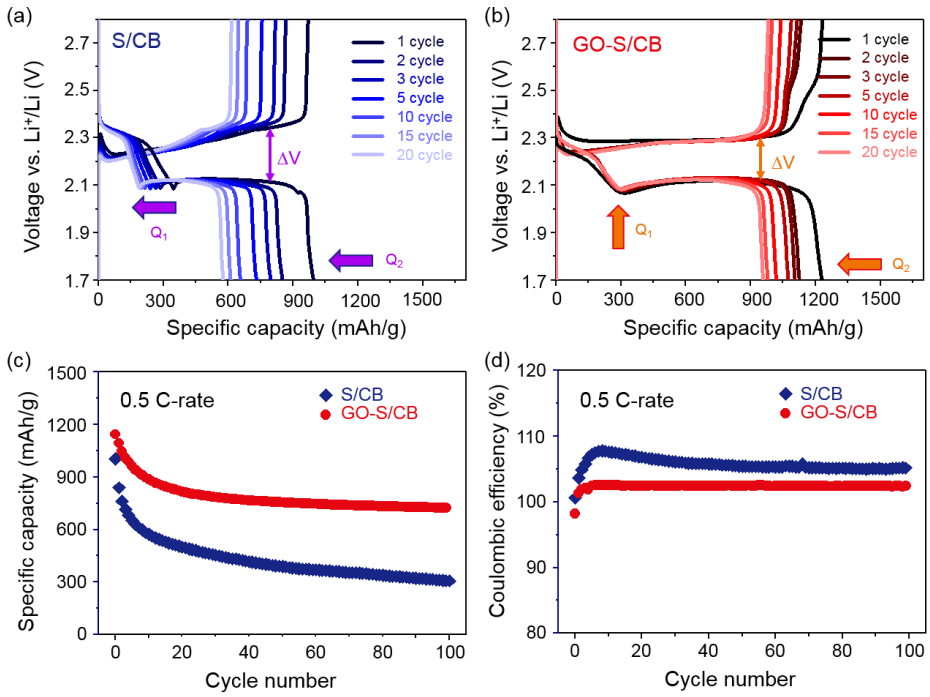

Figure 4. Electrochemical characterization of S/CB and GO-S/CB cathodes. Voltage profiles for (a) S/CB and (b) GO-S/CB plotted from 1st to 20th cycles at 0.5 *C*. (c) Cycling performance and (d) Coulombic efficiency of S/CB and GO-S/CB at 0.5 *C* for 100 cycles.

The overpotential (ΔV) was estimated from the reaction potential of the charge/discharge profile (Figs. 4(a and b)). In Fig. 5, the cyclic voltammetry (CV) results provide a detailed view of the reaction potential including that of the oxidized and reduced polysulfides. To exclude the effect of mass transfer of an ion in the electrolyte, a scan rate of CV at 0.03 mVs^{-1} was converted to the approximately 0.1 *C* rate. Moreover, to facilitate electrochemical analysis, we designated the first and second reactions of the anodic and cathodic scan as O_2 and O_1, and R_1 and R_2, respectively; i.e. solid-state sulfur (S_8) is converted to polysulfide in R_1 region and liquid-state sulfide forms solid-state sulfur in the O_1 area. In the R_2 and O_2 regions, liquid-state sulfide is converted to solid Li_2S, and Li_2S is dissolved in polysulfide, respectively. The R_2 of S/CB and GO-S/CB exhibits similar reaction potential. In contrast, the R_1 reaction of GO-S/CB exhibits a 0.3 V higher potential shift than that of S/CB, indicative of the superior electrical contact between sulfur and the conducting agent. In the anodic scan, however, the O_1 and O_2 peaks of GO-S/CB are shifted toward more negative potentials than those of S/CB. This phenomenon is consistent with the improved electrical contact of GO-S/CB, while the increased hysteresis of charge/discharge of S/CB stems from electrical contact loss. In addition, the higher intensity and sharper peaks of GO-S/CB indicate better reaction kinetics at each step, compared to those of the S/CB.

Rate capability tests were conducted at various *C*-rates (0.1 *C* to 1 *C*), as shown in Fig. 6. The GO-S/CB exhibits superior stability of rate performance in the higher *C*-rate condition, which concurs with the Coulombic efficiency

resulting from the irreversible loss of dissolved polysulfide with increasing current. On the other hand, the Coulombic efficiency of S/CB is significantly influenced by the constant current scale in Fig. 6(b). After a rate of 1 *C*, the Coulombic efficiency is still sharply reduced even after recovery up to 0.1 *C*, which implies that the severe active-material loss at high constant results from an unstable structure. This result also indicates that the accumulated sulfide has a significant influence on the successive cycling performance; i.e., the so-called shuttle phenomena. Thus, our results suggest that GO improves the electrical conductivity and physical stability of the cathode materials during battery operation.

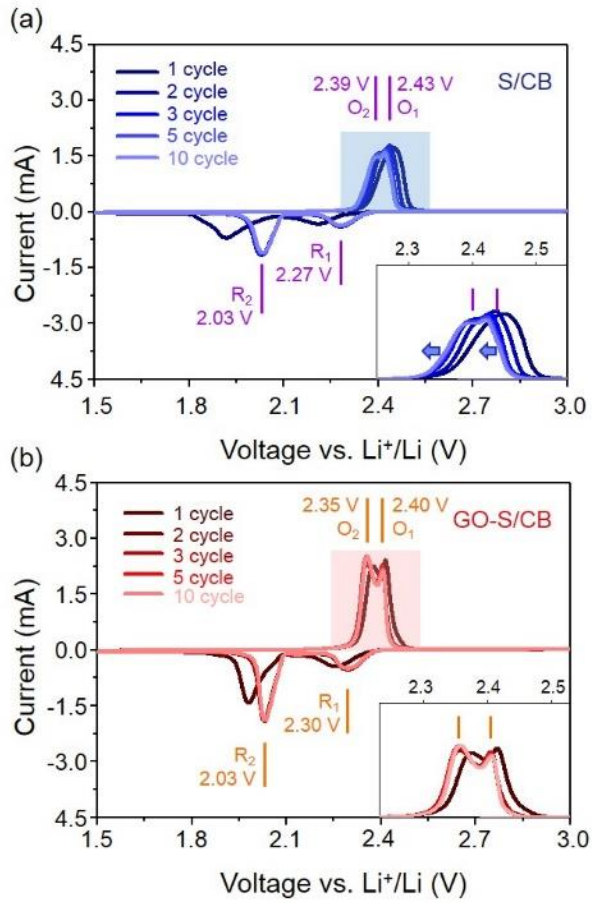

Figure 5. Cyclic Voltammetry peaks of (a) S/CB and (b) GO-S/CB cathodes at 0.03 mVs^{-1} scan rate.

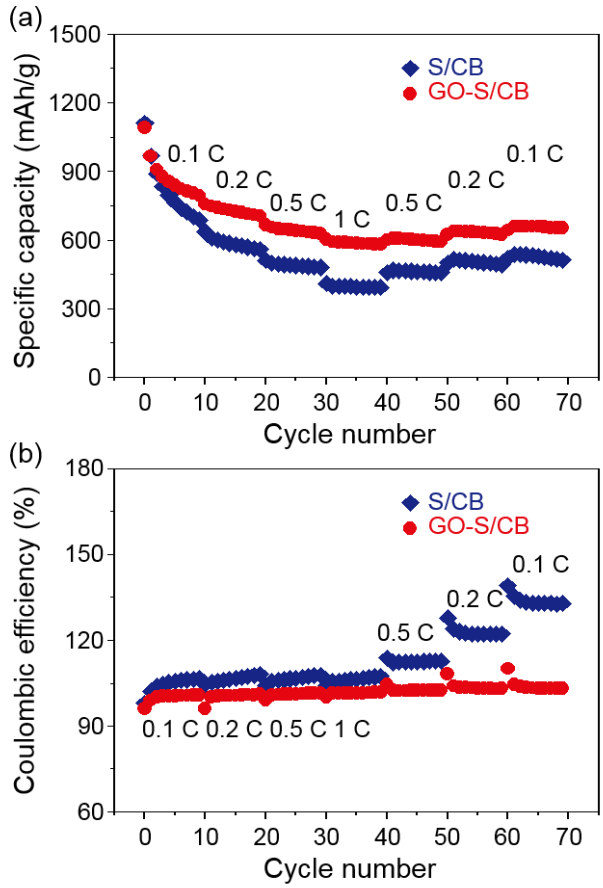

Figure 6. (a) Rate performance and (b) Coulombic efficiency of S/CB and GO-S/CB composites from 0.1 *C* up to 1 *C*.

The electrochemical impedance spectroscopy (EIS) spectra (Fig. 7) represents the structural stability and electrical conductivity of the cathode electrodes before and after battery operation. The Nyquist plots are composed of a semi-circle in the high-frequency region, which is related to contact and charge transfer resistance, and a short inclined line in the low-frequency regions; this line results from ion diffusion in the cathode.[29] In order to measure the precise EIS property of the cathode electrode, a symmetric type cell with lithium metal is positioned in a parallel configuration (grey dots), and the effect of lithium metal on the EIS spectra was determined. Prior to cycling, the semi-circle corresponding to GO-S/CB is smaller than its S/CB counterpart. This indicates that the electrical conductivity of the former is higher than that of the latter. Moreover, after battery operation, the diameters of both semi-circles increase owing to the formation of a passivation layer, increased resistance of the electrolyte, modified surface roughness, and so forth. The semi-circle corresponding to GO-S/CB is, however, still smaller than that of S/CB, which indicates that the GO aid in increasing the conductivity and structural stability during battery operation.

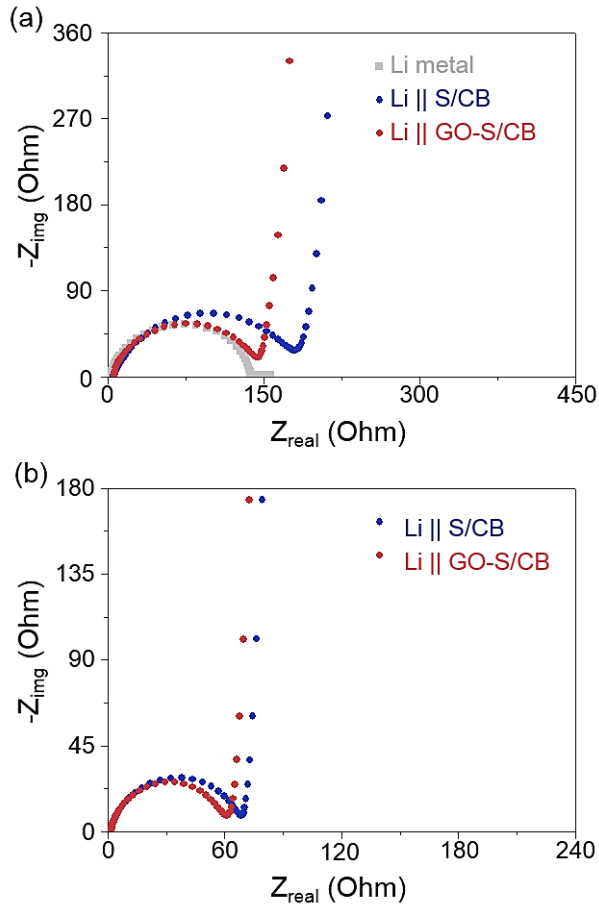

Figure 7. Electrochemical Impedance Spectroscopy (EIS) plots of S/CB and GO-S/CB (a) before and (b) after cycles. The symmetry cell of Li metal is plotted in Fig. (a) grey dots.

Conclusions

In summary, we have synthesized GO-S/CB composites that micron-sized sulfur particles are encapsulated by GO sheets. The structural properties and chemical properties of GO-S/CB composites were characterized by various microscopic and spectroscopic techniques. Various electrochemical analyses were conducted to elucidate the role of GO that has rich oxygen functional groups and its effect on the electrochemical properties. The charge-discharge profiles revealed the significantly enhanced cycling and rate performance of the GO-S/CB electrode, indicating that GO plays a key role in trapping dissolved polysulfide and in improving electronic conductivity. Moreover, the Columbic efficiency of the GO-S/CB electrode prevents capacity fading stemming from the dissolution and precipitation of polysulfide, and also promotes homogeneous electron flows. In addition, EIS spectra indicate that the GO-S/CB electrode has a higher electrical conductivity before/after battery cycling than the S/CB electrode, implying that the structure of the GO-S/CB electrode is maintained during battery operation. Thus, we expect that the incorporation of GOs would make an important step forward to the practical applications of Li-S batteries in the future.

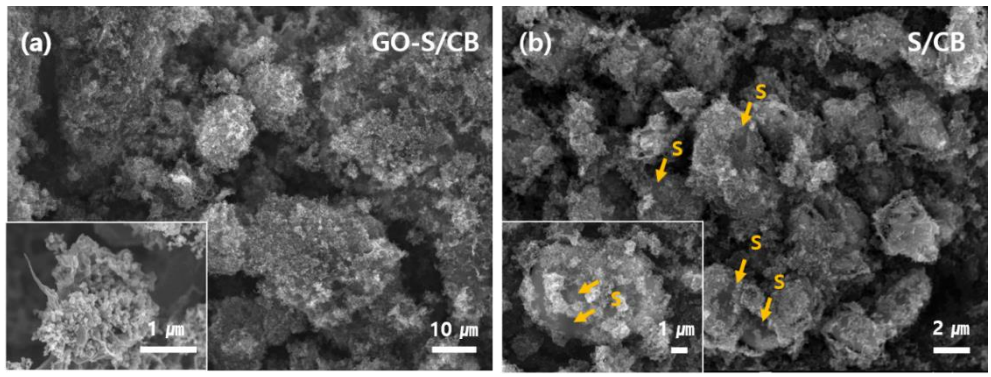

Figure S1. SEM images of (a) GO-S/CB and (b) S/CB composites. The insets show the magnified images of GO-S/CB and S/CB, respectively.

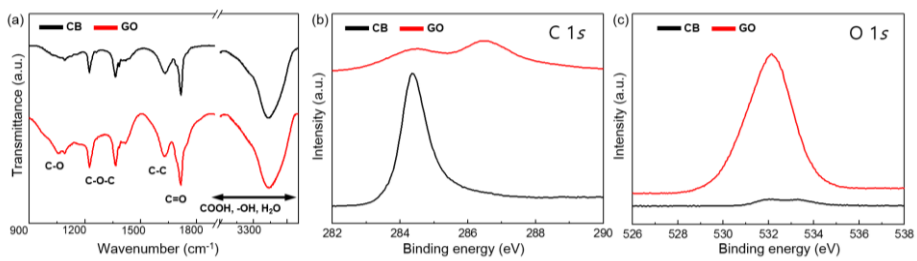

Figure S2. (a) Fourier transform infrared spectroscopy (FTIR) spectra of CB and GO. Strong peaks attributed to the characteristic vibrational mode of oxygen functional groups. X-ray photoelectron spectroscopy of CB and GO. (b) C 1*s* peaks and (c) O 1*s* peaks.

References

1. N. Choi, Z. Chem, S. A. Freunberger, X. Ji, Y.-K. Sun, K. Amine, G. Yushin, L. F. Nazar, J. Cho and P. G. Bruce, *Angew. Chem., Int. Ed.*, 2012, **51**, 9994.

2. Y.-K. Sun, Z. Chen, H.-J. Noh, D.-J. Lee, H.-G. Jung, Y. Ren, S. Wang, C. S. Yoon, S.-T. Myung and K. Amine, *Nat. Mater.*, 2012, **11**, 942.

3. M. Armand and J.-M. Tarascon, *Nature*, 2008, **451**, 652.

4. C. K. Chan, H. Peng, G. Liu, K. McIlwrath, X. F. Zhang, R. A. Huggins and Y. Cui, *Nat. Nanotechnol.*, 2008, **3**, 31.

5. J. Kim, D.-J. Lee, H.-G. Jung, Y.-K. Sun, J. Hassoun and B. Scrosati, *Adv. Funct. Mater.*, 2013, **23**, 1076.

6. J. Wang, J. Yang, C. Wan, K. Du, J. Xie and N. Xu, *Adv. Funct. Mater*. 2003, **13**, 487.

7. W. J. Chung, J. J. Griebel, E. T. Kim, H. Yoon, A. G. Simmonds, H. J. Ji, P. T. Dirlam, R. S. Glass, J. J. Wie, N. A. Nguyen, B. W. Guralnick, J. Park, A. Somogy, P. Theato, M. E. Mackey, Y.-E. Sung, K. Char and J. Pyun, *Nat. Chem.*, 2013, **5**, 518.

8. Y. Yang, G. Zheng and Y. Cui, *Chem. Soc. Rev.*, 2013, **42**, 3018.

9. Y.-S. Su, Y. Fu, T. Cochell and A. Manthiram, *Nat. Commun.*, 2013, **4**, 2985.

10. Y. V. Mikhaylik and J. R. Akridge, *J. Electrochem. Soc.*, 2004, **151**, A1969.

11. R. Elazari, G. Salitra, A. Garsuch, A. Panchenko and D. Aurbach, *Adv. Mater.*, 2011, **23**, 5641.

12. S. S. Zjang and J. A. Read, *J. Power Sources*, 2012, **200**, 77.

13. C. D. Liang, N. J. Dudney and J. Y. Howe, Chem. Mater., 2009, 21, 4724.

14. N. Jayaprakash, J. Shen, S. S. Moganity, A. Corona and L. A. Archer, *Angew. Chem., Int. Ed.*, 2011, **50**, 5904.

15. J. L. Wang, J. Yang, J. Y. Xie, N. X. Xu and Y. Li, *Electrochem. Commun.*, 2002, **4**, 499.

16. G. Zheng, Y. Yang, J. J. Cha, S. S. Hong and Y. Cui, *Nano Lett.*, 2011, **11**, 4462.

17. W. Ahn, K.-B. Kim, K.-N. Jung, K.-H. Shin and C.-S. Jin, *J. Power Sources*, 2012, **202**, 394.

18. H. Wang, Y. Yang, Y. Liang, J. T. Robinson, Y. Li, A. Jackson, Y. Cui and H. Dai, *Nano Lett.*, 2011, **11**, 2644.

19. L. Ji, M. Rao, H. Zheng, L. Zhang, Y. Li, W. Duan, J. Guo, E. J. Cairns and Y. Zhang, *J. Am. Chem. Soc.*, 2011, **133**, 18522.

20. J. Liu, Y. L. Cao, X. L. Li, I. A. Aksay, J. Lemmon, Z. M. Nie and Z. G. Yang, *Phys. Chem. Chem. Phys.*, 2011, **13**, 7660.

21. C. D. Dimitrakopoulos and P. R. L. Malenfant, *Adv. Mater.*, 2002, **14**, 99.

22. W. S. Hummers Jr. and R. E. Offeman, *J. Am. Chem. Soc.*, 1958, **80**, 1339.

23. M. Acik, G. Lee, C. Mattevi, A. Pirkle, R. M. Wallace, M. Chhowalla, K. Cho and Y. Chabal, *J. Phys. Chem. C*, 2011, **115**, 19761.

24. L. G. Cancado, K. Takai, T. Enoki, M. Endo, Y. A. Kim, H. Mizusaki, A. Jorio, L. N. Coelho, R. Magalhäes-Paniago and M. A. Pimenta, *Appl. Phys. Lett.*, 2006, **88**, 163106.

25. J.-T. Yeon, J.-Y. Jang, J.-G. Han, J. Cho, K. T. Lee and N.-S. Choi, J. *Electrochem. Soc.*, 2012, **159**, A1308.

26. Joint Committee in Powder Diffraction Standards (JCPDS), International Center of Diffraction Data, Swarthmore, PA.

27. X. Ji, K. T. Lee and L. F. Nazar, *Nat. Mater.*, 2009, **8**, 500.

28. J. Brückner, S. Thieme, H. T. Grossmann, S. Dörfler, H. Althues and S. Kaskel, *J. Power Sources*, 2014, **268**, 82.

29. Z. Dung, Z. Zhang, Y. Lai, J. Liu, J. Li and Y. Liu, *J. Electrochem. Soc.*, 2013, **160**, A553.

Chapter 7

Graphene Quantum Dots: Induces C-S Bonding Suitable for High Sulphur/Shulphide Utilization

Introduction

Rechargeable lithium ion batteries (LIBs) are widely used for various applications such as portable devices, bio-medical implants, and electric vehicles because of their high energy and power density [1-4]. However, current LIBs based on graphite-transition metal oxide electrode couples have nearly reached a ceiling in their storage capability due to their electrical and crystal structural limitations. Therefore, breakthroughs with new energy storage systems that can surpass current performance barrier of LIBs should be brought about in a timely manner. Recently, systems that can operate by electrochemical transformation of sulphur (S_8) to lithium sulphide (Li_2S) have attracted great attention because elemental lithium and sulphur can be directly utilized as an anode and a cathode, respectively[5]. Sulphur (S_8) generated from petroleum refinement[6] is an ideal choice for a cathode due to its low cost, environmental friendliness, and high theoretical specific capacity (1,675 mAh/g, 16 electron process) when it is fully transformed to Li_2S (refs 6-9). However, three main barriers limit the efficient use of sulphur as a cathode: the deleterious electrochemically induced volume expansion of lithiated from S_8 to Li_2S (~80%), the poor electronic conductivity of S_8 (~1×10^{-30} S/m) and Li_2S (~1×10^{-14} S/m), and the irreversible loss of intermediate LiPSs into the electrolyte[5,10,11]. This loss of LiPSs during cycling is responsible for the poor cycle stability, low sulphur utilization, and polysulphide-shuttle mechanism[5]. To overcome these problems, various carbonaceous materials have been integrated into the sulphur cathode matrix to take advantage of their physical properties to prevent LiPSs dissolution into the electrolyte[12-14], sorption properties[15-17], and high electronic conductivity[18-19]. In

particular, graphene oxide (GO)-sulphur composites have been reported as a new approach to prevent the loss of LiPSs by adsorption and wrapping properties of GO (refs 20-23). However, these systems were found to have poor structural integrity[24] between S and GO, which allows LiPSs to be readily lost by repeated electrochemical cycling. Furthermore, these studies focused on the characteristics of as-prepared GO-S composites, which limits understanding of the role of functional groups during battery operation.

Herein, we introduce nano-sized GQDs (an average particle size of ~4 nm) with oxygen functional groups[25-27] that assemble with sulphur and carbon black (CB) to form a tightly packed structure, which provides fast charge conduction pathways while minimizing the irreversible loss of LiPSs. Oxygen functional groups also serve to preserve dissolved LiPSs by the formation of C-S bonds (the so called sulphiphilic property), as confirmed by density functional theory (DFT) calculations, whereby high sulphur/sulphide utilization is achieved even at high current densities. In order to study the mechanism of the enhanced electrochemical performance, the contribution of dissolution and precipitation to the electrochemical performance was carefully considered.

Experimental

Synthesis of graphene quantum dots.

Carbon fibers were placed into a mixture of H_2SO_4 and HNO_3. The solution was sonicated for 2 h, and then stirred for 24 h. The solution was then refluxed at 90℃ for 48 h with vigorous stirring. The mixture was cooled and diluted with deionized water, and the pH was adjusted to 8 with Na_2CO_3. The final product was dialyzed for 5 days and then filtered. Finally, the GQDs aqueous solution was concentrated.

Synthesis of GQDs-S composites.

1.5 g of $Na_2S_2O_3$ powder (Sigma-Aldrich) was dissolved in 250 ml deionized water, and this solution was stirred with 10 ml hydrochloric acid. The GQDs-S core-shell composites were synthesized by heating up to ~80℃, and then added 10 ml Triton TX-100 (Sigma-Aldrich, average mol wt.% 625) to the solution for 20 min. The prepared GQDs (80 mg in 20 ml D.I. water) solution was added and vigorously stirred in this flask for 20 min. A carbon black suspension (40 mg in 20 ml D.I. water) was then injected into this mixture and was stirred vigorously for 30 minutes. Then, the solution was cooled to room temperature and the collected products were rinsed several times. Finally the GQDs-S/CB composites were dried under vacuum evaporator.

Cell fabrication and electrochemical measurement.

The electrodes were fabricated from slurries that contained 60 wt.% sulphur, 20 wt.% conducting agents and 20 wt.% polyvinylidene fluoride (pvdf) binder dispersed in N-methyl-2-pyrrolidone (2 ml). The prepared slurry was cast onto an aluminum foil using a doctor blade method. The prepared electrodes were transferred to an Ar-filled

glove box and were assembled in a 2032 type coin cell. The mass loading of all samples was ~1 mg of active material. The electrolyte was 1.0 M LiTFSI (lithium bis-trifluoromethanesulfonimide) and 0.1 M $LiNO_3$ (lithium nitrate) with DOL (dioxolane) and DME (dimethyl ether) 1:1 volume ratio (Panax Etec, Korea). The separator was supplied from SK Innovation Corporation (Korea), and lithium metal was used as a counter electrode. Electrochemical properties were measured with a WBCS3000 cycler (Won-A Tech, Korea). The voltage window for electrochemical measurements was fixed between 1.7 – 2.8 V vs. Li^+/Li (all the voltages below are vs. Li^+/Li). The Carbon or GQDs electrodes were fabricated similarly to the aforementioned procedures from slurries that contained 80 wt.% contents of carbon (carbon-only, and carbon black:GQDs=1:1) and 20 wt.% polyvinylidene fluoride (pvdf) binder dispersed in N-methyl-2-pyrrolidone (2 ml). Li_2S_8 catholyte was prepared by using Li_2S and S_8 powders which were inserted into the same electrolyte condition according to the stoichiometric ratio. In order to analyze the cycled electrodes the coin cells were opened in an Ar-filled glove box. All the samples were analyzed after rinsing with copious amounts of DOL/DME.

Characterization.

XRD was performed on a (Rigaku, D-MAX2500-PC) operating with Cu Ka radiation (λ=1.5406 Å) at 40 kV and 200 mA. TEM was performed on a (JEOL JEM-2100F). XPS was performed on a AXIS Ultra DLD (Kratos.Inc) using a 150 W monochromatic Al K (1486.6 eV) source at the Korea Basic Science Institute (KBSI). High resolution data was collected using a pass energy of 40 eV and 0.05 eV step. Raman spectra was obtained with a Renishaw micro-Taman spectroscope with an

excitation wavelength of 514.5 nm. The spot diameter was approximately 2 μm.

Computational methods.

We carried out density functional theory (DFT) calculations for optimizing structures and analyzing frequencies. Conventional B3LYP exchange-correlation functional[39] was used for the DFT calculations. B3LYP is a hybrid-GGA exchange-correlation functional, which means size-consistency problem can't be considered. To more precisely describe the anion systems, we used a 6-31++G(d) basis set which added diffuse functions to all atoms. All structures in this paper are optimized which is confirmed by frequency analysis. GAUSSIAN 09 package[40] is used for all calculations.

Results and Discussion

To study the physical/chemical properties of GQDs, various microscopic and spectroscopic analytical tools were employed. High resolution transmission electron microscope (HRTEM) images were collected to study the morphology of the GQDs (Figs. 1a and 1b). The GQDs are highly crystalline and show an average size of 4.11 (±0.55) nm (the inset of Fig. 1b). Oxygen-rich functional groups on the edge of the GQDs where non-bonding carbons exist were identified by Fourier-transform infra-red (FTIR) spectroscopy (Fig. 1c). Strong peaks attributed to the characteristic vibrational modes of oxygen functional groups (–OH at 3,434 cm^{-1}, C=O at 1,725 cm^{-1}, C-O in 1,024-1,180 cm^{-1}, and C-O-C at 1,200 cm^{-1}) can be observed in GQDs, while the peak at 1,629 cm^{-1} results from sp^2-hybridized C=C (in-plane stretching)[28]. These oxygen-functional groups of GQDs can strongly bond to sulphur *via* electrostatic interaction.

The GQDs-S composites were prepared by GQDs and S that is chemically reduced from $Na_2S_2O_3$. It should be noted that surface of sulphur was mediated by a surfactant (see the details in the Method section). The scanning electron microscopy (SEM) and TEM images in Figs. 1d and 1e show the morphology of the GQDs-S. Several micron-sized sulphur particles are homogeneously coated with GQDs. The uniform distribution of GQDs on the sulphur surface is confirmed by energy dispersive X-ray spectroscopy (EDX) mapping of C, O, and S (Fig. S1). The graphitic characteristic of GQDs-S was established by Raman spectroscopy (Fig. 1f), where the peaks for carbon (D and G at 1,350 and 1,590 cm^{-1}, ref. 29) and sulphur (the four characteristic peaks below 600 cm^{-1})[30] can be clearly resolved.

The GQDs-S/carbon black (CB, average particle size of ~50 nm) composite structures were prepared from GQDs-S and CB *via* van der Waals interaction[20]. Experimental details can be found in the Methods section. The SEM image of GQDs-S/CB, Fig. 1g, presents that CBs are tightly bound to the GQDs-S composites. Scanning transmission electron microscopy (STEM)-EDX was used to determine the compositional distribution of C, O, and S in the GQDs-S/CB composite and shows that C, O, and S is homogeneously distributed throughout the composite structure (Fig. S2). X-ray diffraction (XRD) analysis of the GQDs-S/CB composite structures reveals high S crystallinity and phase purity (Fig. S3a) and the composition of GQDs-S/CB was estimated by thermogravimetric analysis (TGA) (Fig. S3b) to be 70 : 20 : 10 (wt.%) in S : CB : GQD. X-ray photoelectron spectroscopy (XPS), Fig. S4, analyzed the surface of the GQDs-S/CB composite and the results of the quantitative analysis are displayed in Table S1. The XPS results indicate higher intensity of C=O (286.7 eV in C 1*s* and 530.9 eV in O 1*s*) and C-OH (533 eV in O 1*s*) for GQDs-S/CB compared to S/CB due to the surfactant and oxygen functional group of the GQDs[31]. Meanwhile negligible S 2*p* signal was detected since the GQDs-S are covered with CB in the GQDs-S/CB structure (see S 2*p* in GQDs-S/CB *vs*. S/CB). The schematic illustration in Figs. 1h and 1i, shows the GQDs distributed on a sulphur particle, which can strongly bond to CB, leading to a densely coated GQDs-S/CB composite structure.

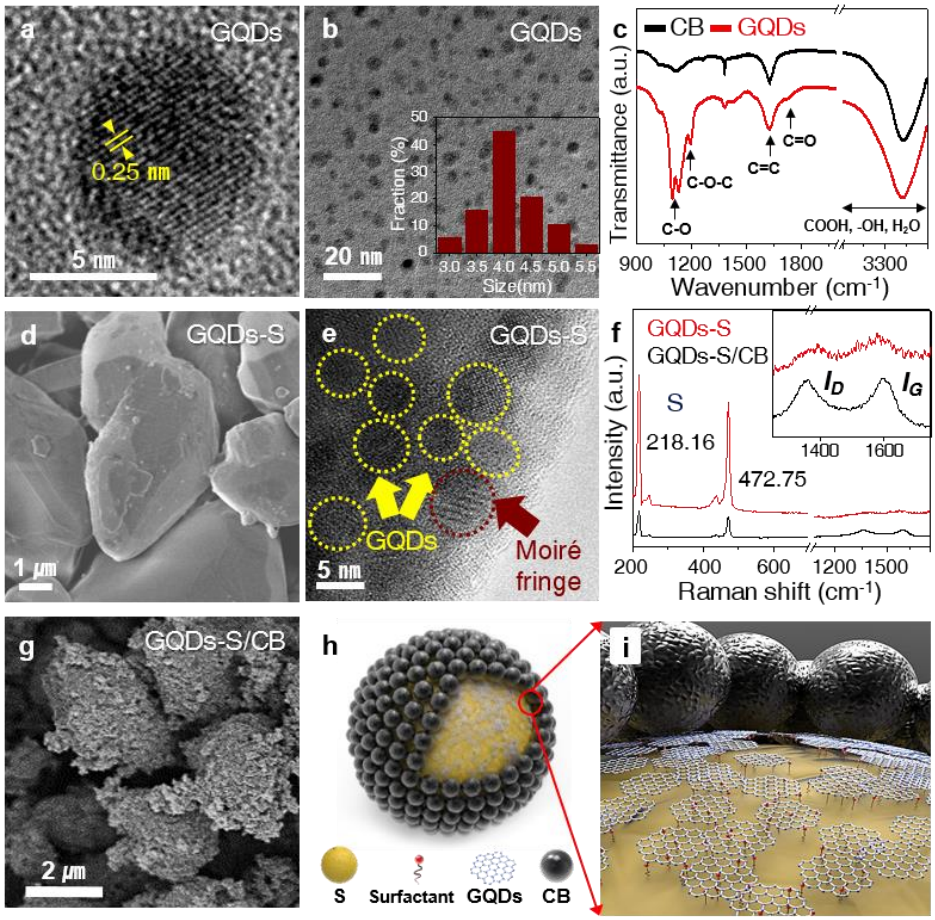

Figure 1. Material characterization of GQDs-S/CB and S/CB composites. a,b, High-resolution TEM images of GQDs. The inset in Fig. 2b shows a histogram of the GQDs size distribution. c, FT-IR spectra of GQDs and CB. The peaks in this figure correspond to the various functional groups in the GQDs and CB. SEM images of d, GQDs-S, and g, GQDs-S/CB. e, HRTEM images of the GQDs-S composites and GQD pattern (yellow circle). A Moiré pattern (red circle) is clearly visible in these TEM images, which is created by a superposition of the GQDs and S crystalline lattices, and f, Raman spectrum of GQDs-S composites, which shows that the GQDs are formed on the sulphur particles. The strong peaks at 218.16 and 472.75 cm^{-1} arise from sulphur, and the D (disorder) and G (graphitic) peaks arise from the GQDs. Schematic diagrams show the structure, h, and the magnified structure, i, of GQDs-S/CB.

The schematic illustration in Fig. 2a depicts a conventional Li-S battery, where the anode is made of a metallic lithium, and the cathode is a composite of sulphur and CB. The structure of the cathode has a large impact on the irreversible loss of LiPSs into the electrolyte during battery operation. Herein, GQDs are introduced at the S/CB cathode, as shown in Fig. 2b. The GQDs contain both hydrophobic aromatic and hydrophilic defect regions, which can interact with CBs (ref. 20) and S_8, respectively. Scanning electron microscopy (SEM) images (Figs. 2c and 2d) confirm that the GQDs-S/CB composite electrodes are densely packed with CBs, which should increase electrochemical performance by highly preserving LiPSs in the geometric structure of GQDs-S/CB, while the surface of the sulphur particles are partially exposed in S/CB electrode. The exposure of S_8 to the electrolyte leads to the severe loss of electrochemically generated LiPSs followed by the degradation of the electrochemical performance.

The discharge profile in Fig. 3a illustrates a schematic model of possible reaction pathways that occur in a conventional Li-S battery. In the upper plateau region, elemental sulphur (S_8) is gradually reduced to the soluble sulphide anion (S_8^{2-}). Then, continuous reduction leads to the conversion of dissolved S_8^{2-} to S_n^{2-} (n = 6, 4) [32]. Since these high-order LiPSs (HO-LiPSs, (S_n^{2-}, n=8-4)) reactions are generated in the liquid electrolyte, the loss of active materials can occur simultaneously with this electrochemical reaction. The summation of the upper plateau and slope regions can be defined as the dissolution regime. Once the composition of S_4^{2-} is reached, low-order LiPSs (LO-LiPSs, (S_n^{2-}, n=2-1)) are converted to Li_2S through the reduction of S_4^{2-} (lower plateau region, defined as

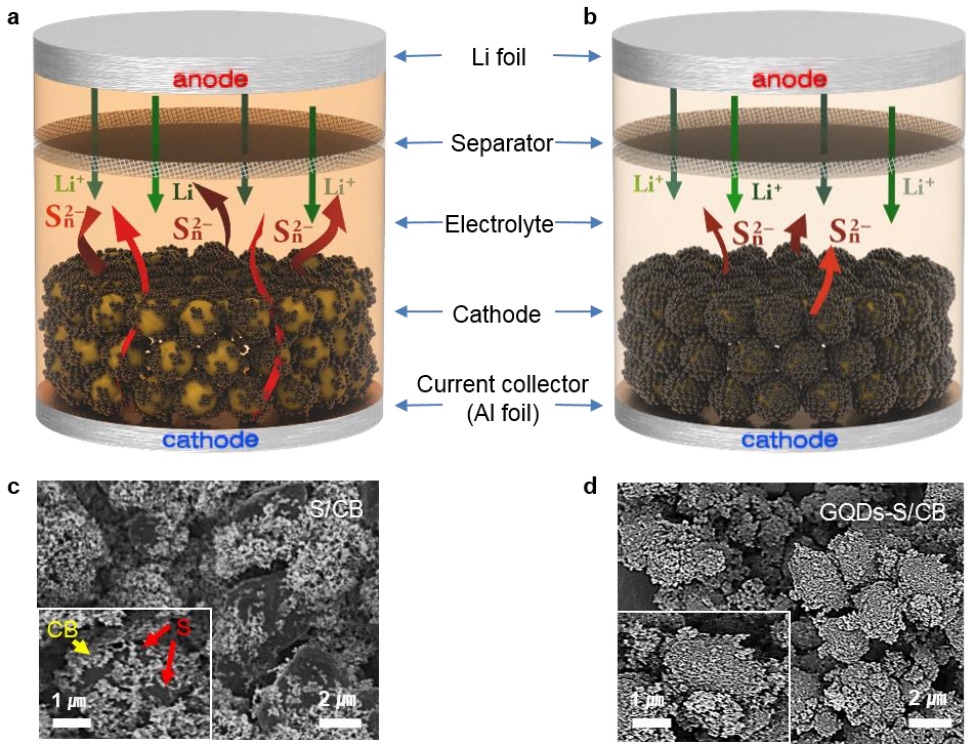

Figure 2. Schematic diagrams and SEM images of S/CB and GQDs-S/CB in a Li-S battery. a,b, Schematic configuration of S/CB and GQDs-S/CB employed as a cathode in a Li-S battery. The sulphur (yellow) is wrapped with carbon black (S/CB) and compactly covered with graphene quantum dots and carbon black (GQDs-S/CB), respectively. Polysulphides were dissolved into solvent and the color changed to orange. c,d, SEM images of GQDs-S/CB and S/CB.

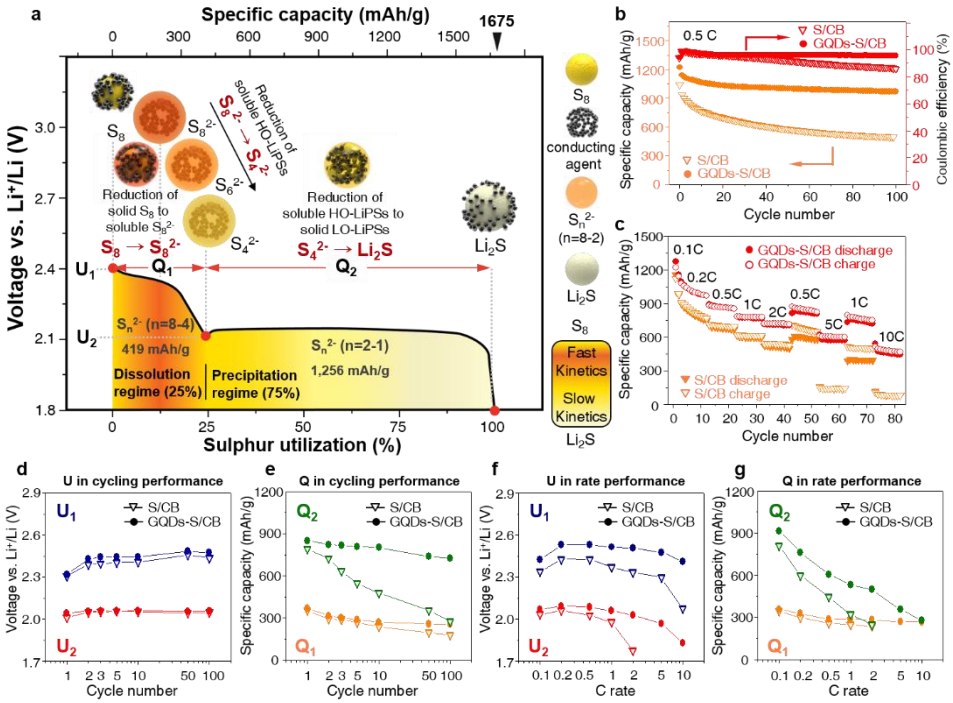

Figure 3. Electrochemical properties of S/CB and GQDs-S/CB electrodes. a, Schematic illustration of the discharge profile of a conventional Li-S battery. High order-polysulphides (S_n^{2-}, n=8-4) and low order-polysulphides (S_n^{2-}, n=2-1) are inscribed the HO-PSs and LO-PSs as abbreviation. The onset potential (*U*) and the capacity (*Q*) in the dissolution and precipitation regime are noted, which facilitates the analysis of the electrochemical properties of each sample. b, Rate performance of the GQDs-S/CB and S/CB at 0.1 *C* to 10 *C*. c, cycling performance and Coulombic efficiency at 0.5 *C* of both samples for 100 cycles. d,f, Onset potential as a function of cycle number and e,g, capacity as a function of rate and capacity as a function of cycle number.

precipitation regime). Finally, Li_2S results from the complete reduction of S_8, which induces ~80% (compared to S_8) theoretical volume expansion. Representative points U_1, U_2, Q_1, and Q_2 are marked in the profile, where U_1 and U_2 indicate the onset reaction potentials of the dissolved and precipitated species, respectively, while Q_1 and Q_2 are the capacities corresponding to dissolution and precipitation regime, respectively. Q_1 is 419 mAh/g estimated from the reaction, S_8 (*s*) + $4Li^+ + 4e^- \leftrightarrow 2Li_2S_4$ (*l*). Meanwhile, Q_2 is 1,256 mAh/g which is achieved by the reduction of higher order to lower order polysulphides, $2Li_2S_4$ (*l*) + $12Li^+ \leftrightarrow 8Li_2S$ (*s*). Four parameters (U_1, U_2, Q_1, and Q_2) and the Q_2/Q_1 ratio (= 3) will be evaluated to understand the battery performance[32].

The cycling performance was tested at 0.5 *C*-rate (1 *C* = 1,675 mA/g assuming the reaction, $S_8 + 16Li^+ + 16e^- \leftrightarrow 8Li_2S$) in Fig. 3b. GQDs-S/CB composites exhibit superior cyclability and Coulombic efficiency compared to S/CB. A discharge capacity of ~1,000 mAh/g was achieved after 100 cycles while S/CB showed only 459.57 mAh/g. The capacity *vs*. voltage profiles at selected cycles are presented in Fig. S6. The electrochemical properties of modified sulphur (surfactant coated sulphur) covered with CBs were also measured to study the effect of the surfactant on the electrochemical performance (Fig. S5). Modified S/CB exhibits lower initial capacity but slightly better retention than S/CB because the surfactant on the surface of S partially protect the loss of HO-LiPSs (refs 15,20). Figure 3c presents the rate capabilities of GQDs-S/CB and S/CB from 0.1 *C* to 10 *C* (see Fig. S7 for the capacity *vs*. voltage profiles at the different rate steps). The GQDs-S/CB shows excellent rate properties in comparison with S/CB. In Fig. S8, a capacity of 540.17 mAh/g at 10 *C*

was achieved (42% *vs*. capacity at *C*/10) in GQDs-S/CB. In contrast, only 120.35 mAh/g was achieved at 10 *C* (10% *vs*. that at *C*/10) in S/CB.

The onset potentials (U_1 and U_2) and capacities (Q_1 and Q_2) of GQDs-S/CB and S/CB are presented in Figs. 3d-3g, which were derived from the capacity *vs*. voltage profiles (Figs. S6 and S7). These values are tabulated in Tables S2-5. Firstly, these parameters are studied to analyse the electrochemical differences between GQDs-S/CB and S/CB. In the first cycle, U_1 of GQDs-S/CB is 2.33 V, which is slightly higher than that of S/CB, 2.31 V, owing to the lowered interface resistance. The better carbon coverage in GQDs-S/CB leads to faster electron transfer kinetics (Fig. 3d). Electrochemical impedance spectroscopy (EIS) quantified the interfacial resistance, as shown in Fig. S9. The radius of the smaller sized semi-circle (100 kHz – 1 Hz) is proportional to summation of the initial resistance and the charge transfer resistance (R_{int} + R_{ct}) based on the equivalent circuit in Fig S9a (ref. 33). The U_2 value is also slightly higher in GQDs-S/CB, which indicates that HO-LiPSs are easily reduced to LO-LiPSs. After the first cycle, a slight increase of U_1 and U_2 was observed for both samples due to the decrease in overpotential resulting from the rearrangement of micron-sized sulphur[33]. U_1 and U_2 of both GQDs-S/CB and S/CB follow the same trend during 100 cycles which confirms that there is no significant change of onset potential after the first cycle.

In contrast, Q_1 and Q_2 show quite different behaviour as shown in Fig. 3e. For the first cycle, higher Q_1 and Q_2 are observed in GQDs-S/CB (Q_1 = 370.9 mAh/g and Q_2 = 853.24 mAh/g) compared to the S/CB (Q_1 = 354.86 mAh/g and Q_2 = 793.35 mAh/g) due to the enhanced electrical contact by the densely packed sulphur-carbon

structure. However, the Q_2/Q_1 ratios are low in both GQDs-S/CB (Q_2/Q_1 = 2.30) and S/CB (Q_2/Q_1 = 2.24). Such low Q_2/Q_1 ratio for the first cycle can be attributed to the irreversible initial loss of HO-LiPSs, inefficient precipitation of LO-LiPSs, and electrolyte decomposition was followed by formation of solid electrolyte interphase (SEI). Q_1 and Q_2 values gradually decrease with extended cycling in S/CB. While the Q_1 values show relatively slow decay, severe fading of Q_2 is observed, which indicates the precipitation reaction is highly impeded by the loss of active sites. Whereas, the Q_1 and Q_2 values are maintained for GQDs-S/CB even after 100 cycles through minimized loss of active species and preservation of active sites for facile reactions. The Q_2/Q_1 ratios in GQDs-S/CB are found to be 2.94 and 2.81, at the 10th cycle and the 100th cycle, respectively, which are close to the theoretical value (=3), while Q_2/Q_1 ratios of S/CB are 1.96 and 1.55, at the 10th and 100th cycle, respectively. Such high Q_2/Q_1 ratios strongly support that the redox reaction between S_8 and Li_2S can occur very reversibly owing to highly efficient electrode structure driven by GQDs. The GQDs can aid in capturing the PSs during the electrochemical reaction, which will be discussed in detail later. In addition, the EIS study, Fig. S9 b,c, and associated discussion to support PSs capture by GQDs can be found in supplemental section.

The U_1 and U_2 values are also derived from the rate capability tests as shown in Fig. 3f. The GQDs-S/CB electrode shows slightly higher U_1 and U_2 values than S/CB at a relatively low rate (< 0.2 *C*). However, the U_1 and U_2 values of the S/CB electrodes significantly decrease at a rate above the 0.5 *C* rate while the U_1 and U_2 values of the GQDs-S/CB electrodes remain more stable. The higher U_1 and U_2 in

GQDs-S/CB confirm that the GQDs increase the electrical conductivity of the material, whereby overpotentials that are required to initiate the dissolution (U_1) and precipitation (U_2) reactions are decreased. It should be noted that the tendency of U_1 and U_2 are similar because these values are related to the electrical contact of S_8 and HO-LiPSs, respectively. On the contrary, different behaviours are observed in Q_1 and Q_2, particularly, under the higher current density as shown in Fig. 3g. The reaction kinetics for formation of HO-LiPSs is fast; thus, Q_1 is less affected by high current density[34]. However, a significant decrease is revealed in Q_2 at higher current density, which is attributed to the slow reduction due to the low electrical conductivity of LO-LiPSs or limited reaction sites. The Q_2/Q_1 ratios in S/CB are 2.36 and 1.27, at 0.1 *C* and 2 *C* rate, respectively, while higher Q_2/Q_1 ratios, 2.55 (at 0.1 *C*) and 1.75 (at 2 *C*), can be achieved in GQDs-S/CB. The larger Q_2/Q_1 ratio in GQDs-S/CB indicate superior capacity retention is available through the facile charge transfer and preserved reaction sites, which leads to faster reaction kinetics of LO-LiPSs (higher Q_2) as well as lower overpotential (higher U_1 and U_2).

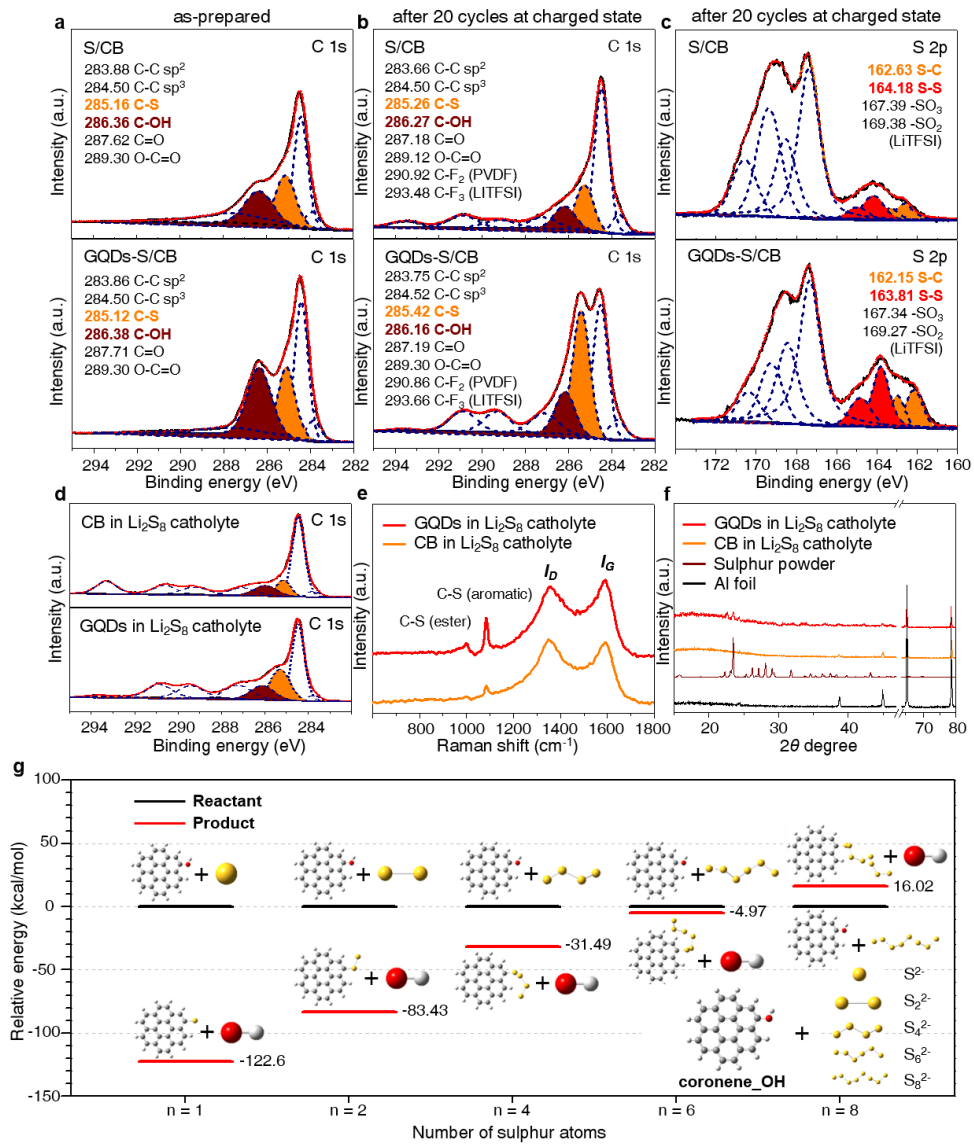

Figure 4. High resolution C 1*s* X-ray photoemission spectroscopy (XPS) and computational calculations a, S and GQDs-S composites before cycling. b, C 1*s* and c, S 2*p* high resolution spectra of the S/CB and GQDs-S/CB electrodes after 20 cycles. Each spectrum was fitted with functions corresponding to different valencies of carbon and sulphur (dashed line) and the sum of those fitted curves (red line) is consistent with the raw data (black solid line). d, C 1*s* spectra of CB and GQDs/CB electrodes in Li_2S_8 catholyte. e, Raman spectra showing C-S bond formation within

the samples. f, XRD spectra of GQDs/CB and CB electrodes in in a Li_2S_8 catholyte. g, A plot of the relative energies for the reactant and product in binding of polysulphides to GQDs, versus the sulphur chain length. The functional groups on GQDs enhance the binding of polysulphides to the carbon due to the substitution of -OH (C-OH) to Sn^{2-}. Yellow, red, white, and gray represents S, O, H, and C atoms, respectively.

The chemical bonding states of S/CB and GQDs-S/CB electrodes were characterized by XPS (Fig. 4a-c). The C 1*s* spectra of the as-prepared electrodes (Fig. 4a) exhibit peaks at 283.8 eV and 284.5 eV attributed to sp^2 and sp^3 hybridized carbons[35], respectively, while the peak at 285.3 eV corresponds to C-S bonding[36]. The peak at 286.2 eV is assigned to C-OH bonding, which is more intense in the GQDs-S/CB than S/CB because the GQDs have a high density of OH surface functional groups. The two peaks that correspond to carbonyl and carboxyl groups are located at 287.0 eV and 289.0 eV, respectively. The C 1*s* spectra of the S/CB electrode obtained from the charged and discharged stages, after the 20th cycle (Figs. 4b and S10), shows negligible intensity loss for the C-OH (286.27 eV) and C-S (285.26 eV) peaks. However, for the GQDs-S/CB electrode, the hydroxyl peak (286.2 eV) decreases noticeably while a C-S peak (285.4 eV) becomes prominent in the charged state. The change in the bonding nature indicates that hydroxyl groups in the GQDs can facilitate the formation of C-S bonds during cycling. These C-S bonds can provide the reaction sites to fully reduce HO-LiPSs to LO-LiPSs, thus the Q_2/Q_1 ratio is stable at ~2.9 even after 100 cycles as shown in Fig. S8. The C-F_2 peak at ~291.0 eV and C-F_3 peak at ~293.0 eV are originated from the binder (polyvinylidene fluoride, PVDF) and electrolyte salt (lithium bis(trifluoromethane)-sulfonimide , LiTFSI), respectively[37].

The S 2*p* spectra in Fig. 4c, collected after 20 cycles, also support the formation of C-S bonding discussed above. The C-S bonding peak (162.63 eV) in S 2*p* is assigned to a lower binding energy than the S-S (164.0 eV) bonding[26], which has correlated with C-S bonding in C 1*s* peak. The intensity in the GQDs-S/CB electrode

is higher than that in the S/CB. The S-S bonding peaks at ~164.0 eV are ascribed to the crystalline sulphur in the electrode[31]. The higher S-S peak intensity of GQDs-S/CB compared to S/CB indicates that more elemental sulphur is formed by adsorption of sulphur onto the GQDs. The adsorption processes prevents irreversible loss of the active material into the electrolyte by formation of nano-sized sulphur that is chemically favorable to bond to the GQDs as discussed later. The peaks at 167.0 eV and around 170.0 eV are attributed to sulphate, SO_2, from LiTFSI (ref. 37) and oxidized polysulphide species, SO_3, respectively.

The SEM images, Fig. S11 and S12, of both anodes and cathodes after 20 cycles, respectively, were taken of GQDs-S/CB and S/CB electrodes. Due to the thick SEI layer formation, the SEM images of the cathodes, Fig. S11, show flattened morphologies. Interestingly, homogenous surfaces can be observed in GQDs-S/CB, while, segregation of carbon is observed in the CB/S electrode. . This morphological difference is driven by the tightly packed structure of GQDs-S/CB during battery operation. A clean surface is observed on the GQDs-S/CB anode while the CB/S anode exhibits S and Li_2S particles on the surface (as confirmed by EDX and Raman spectroscopy as shown in Fig. S12). These sulphur and LiPSs deposits result from the loss of active materials from the cathode side during repeated cycling.

To further investigate the intrinsic surface interaction at the interface between GQDs and CB, GQDs/CB and CB electrodes without sulphur were prepared and electrochemically cycled in Li_2S_8 catholyte (Fig. 4d). The cycle retention of GQDs/CB is over 90% during 100 cycles while CB exhibits a capacity retention below 80% (Fig. S13c). After cycling the GQDs/CB electrode, the C 1*s* and S 2*p*

XPS spectra (Figs. 4d and S13a,b) show higher S-S and C-S peaks compared with CB. Furthermore, Raman peaks for C-S aromatic bonding at 1,086 cm^{-1} and for C-S esteric bonds at 997 cm^{-1} are more intense for the GQDs/CB electrodes[38]. The carbon peaks at 1,590 cm^{-1} and 1,350 cm^{-1} are assigned to the G and D bands of carbon, respectively (Fig. 4e). XRD of the GQDs/CB electrodes also confirms nano-sized crystalline sulphur (Fig. 4f), which strongly supports that PSs are adsorbed on the oxygen functional groups of GQDs. DFT calculations were performed to clarify the formation of C-S bonding between the GQDs and sulphur species. The calculation is based on the following reaction:

$$\text{coronene\_OH} + S_n^{2-} \rightarrow (\text{coronene\_}S_n)^- + OH^- \qquad (n=1, 2, 4, 6, 8)$$

This model is used to represent the terminal edges of the GQDs (ref. 39), with one of the edges replaced by a hydroxyl group, "coronene_OH." A coronene is a polycyclic aromatic hydrocarbon comprising six peri-fused benzene rings with the chemical formula of $C_{24}H_{12}$. The relative energies calculated by DFT for the reactants and products indicate that replacing the terminal hydroxyl group by a sulphur dianion results in a lower energy state. The relative energies are shown in Fig. 4g, where it is clear that the energies of the product decrease when sulphur dianions are replaced with the terminal hydroxyl group. The lower energy of the products (S_n^{2-}, n = 1, 2, 4, and 6) can provide a driving force for the reaction, thereby the formation of C-S bonds are favourable. However, the small sulphur dianions normally exist in the form of a solid crystal combined with lithium cations, such as Li_2S that cannot easily participate in C-S bonding[5]. In addition, sulphur dianions

become unstable as the sulphur chain length is shortened due to the Coulombic repulsion. Meanwhile, large sulphur dianion chains (n>6) tend to disassemble into smaller chains[40]. Thus, it is speculated that the major participants in the reaction are S_2^{2-}, S_4^{2-} and S_6^{2-} ions. In addition, the same DFT calculation was performed for carboxyl group terminated coronene (coronene_COOH) (Fig. S14), showing similar results toacoronene_OH group. Our results highlight the crucial role in the formation of C-S bonds through terminal oxygen-functional groups present on the edge of GQDs.

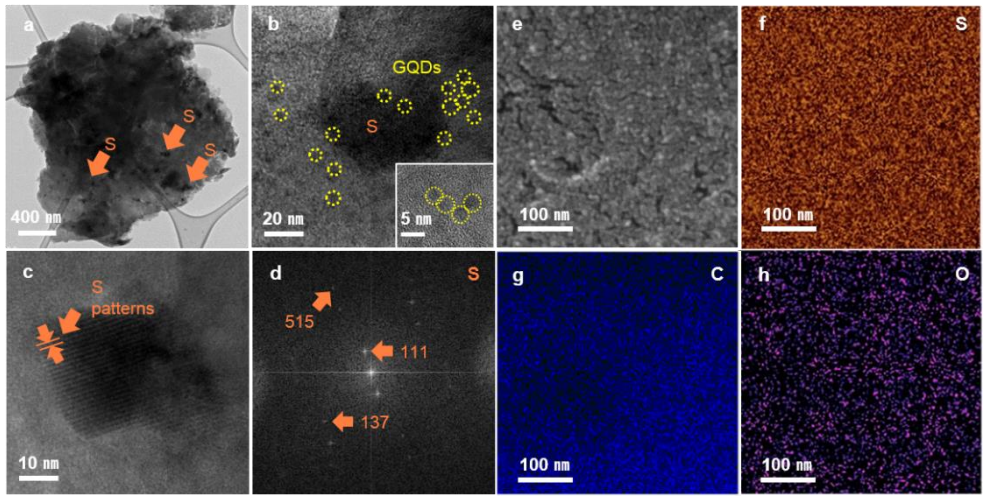

Figure 5. TEM and SEM images of nano-sized sulphur on GQDs electrode in Li_2S_8 catholyte after 20 cycles. a,TEM image of nano-sized sulphur in GQDs materials. The aggregate seen in the TEM is mainly comprised of GQDs, and sulphur is identified as the small darker particles. b, GQDs (yellow circle) covered on nano-sized sulphur particles, c, HRTEM image that shows the lattice fringes of the nano-sized sulphur and GQDs. d, The FFT image of the HRTEM image in c. The two bright spots represent Bragg spots for the sulphur particles, and the other spots are GQDs Bragg spots. e, SEM image of the GQDs electrode in the catholyte after cycling. f-h, C, S, and O energy-dispersive X-ray (EDX) spectroscopy maps of the GQDs electrode.

TEM images were obtained from the GQDs/CB and CB electrodes after 20 (dis)charge cycles in Li_2S_8 catholyte. While only a small number of sulphur particles were observed on the CB electrode (Fig. S15), many nano-sized sulphur particles can be observed on the GQD electrode in Figs. 5a-d. Nano-sized sulphur particles were covered with GQDs, which was confirmed by their lattice fringes corresponding to (111) planes. In addition, the indices of bright spots on the fast Fourier transform (FFT) image indicate sulphur is single crystalline and crystallizes in the orthorhombic structure of the alpha phase (JCPDS, No. 08-0247)[41]. The broad ring patterns in the FFT image indicate the presence of multiple GQDs with different orientations in Fig. S16. The SEM-EDX analysis of the GQDs also indicates that nano-sized sulphur particles are adsorbed onto the GQDs (Figs. 5e-h). On the other hand, the CB electrode contains a low sulphur density (Fig. S15.) This observation implies that the oxygen functional groups in the GQDs induce preferred nucleation of sulphur onto the GQDs. Thus, sulphur can easily be adsorbed/desorbed on the GQDs as predicted by the aforementioned DFT calculation.

Conclusion

In summary, we have designed GQDs-S/CB composites as a high-performance cathode material for Li-S batteries. The nano-sized GQDs induce a tightly packed structure *via* charge interaction with S and CB, which results in enhanced conductivity by shortened electron conduction paths. Furthermore, C-S bonding is generated *in-situ* during the operation of the battery, which originates from the high functional-edge density of the GQDs. Thus, loss of active materials into the electrolyte is minimized. The adsorption of nano-sized sulphur particles onto the GQD interfaces by C-S bonding was confirmed by TEM, and further supported by XPS and Raman analysis and DFT calculations. The GQDs-S/CB composites significantly improve cycling and rate performances, with high reversible capacities at both high and low current density. This excellent cycling behavior was demonstrated through the analysis of discharge profiles. We believe that our results provide a new avenue for material scientists to tailor oxygen-rich functional groups of nano-sized carbon for the application in various batteries.

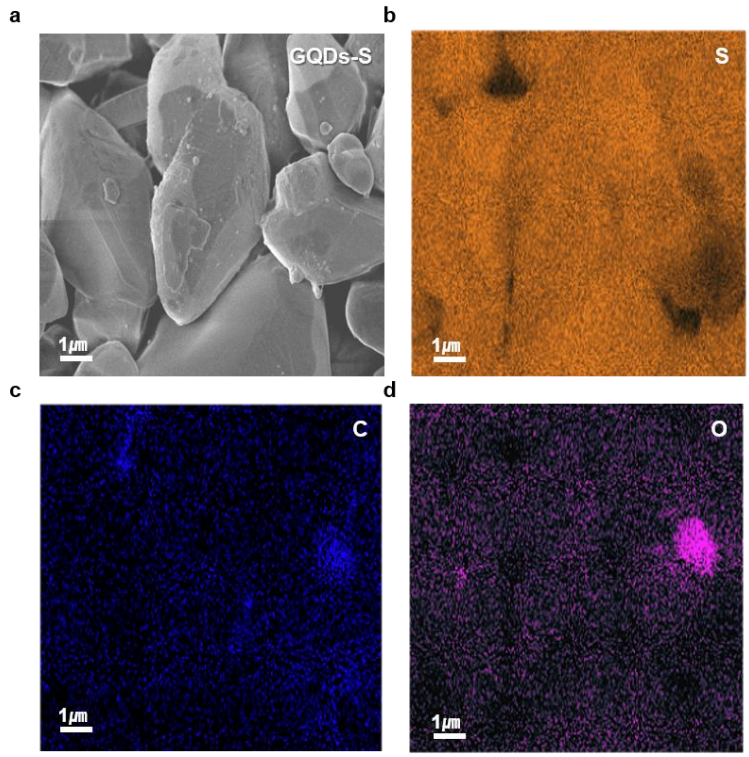

Figure S1. Scanning electron microscopy and energy-dispersive X-ray spectroscopy characterization of the GQDs-S composites. SEM images of the GQS-S composites, and C, S, and O EDX maps of the GQDs-S composites.

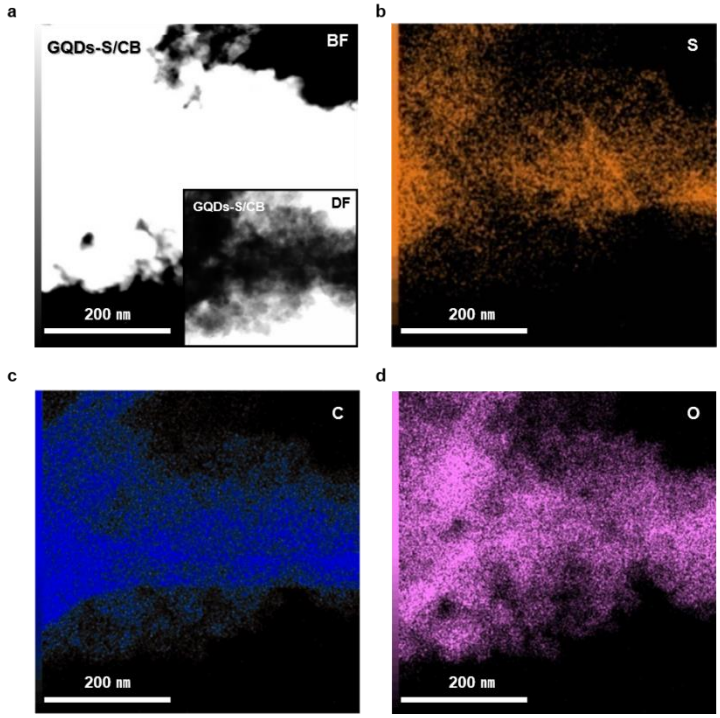

Figure S2. Scanning transmission electron microscopy and EDX characterization of the GQDs-S/CB composites. TEM images of the GQS-S/CB composites, and C, S, and O EDX maps of the GQDs-S/CB composites.

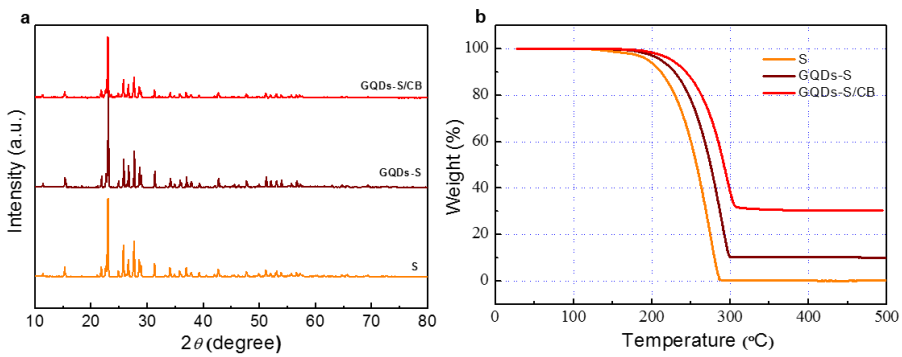

Figure S3. X-ray diffraction (XRD) patterns and Thermogravimetric analysis (TGA). XRD of sulphur, GQDs-S, and GQDs-S/CB composites a, and TGA collected in N_2 atmosphere with a heating rate of 10℃/min b, the S content of the cathode.

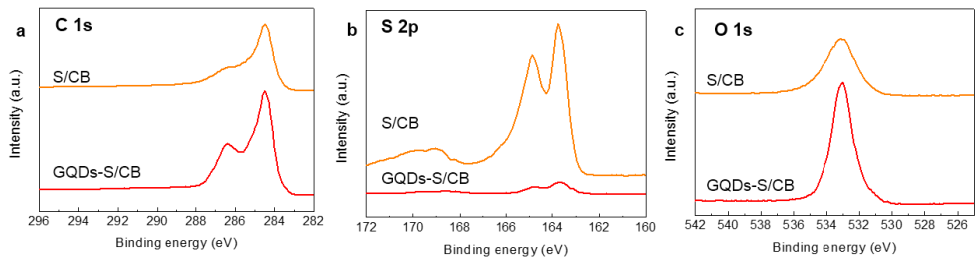

Figure S4. X-ray photoelectron spectroscopy of S/CB, and GQDs-S/CB particles. a, C 1*s* peaks, b, S 2*p* peaks, and c, O 1*s* peaks of S/CB and GQDs-S/CB particles.

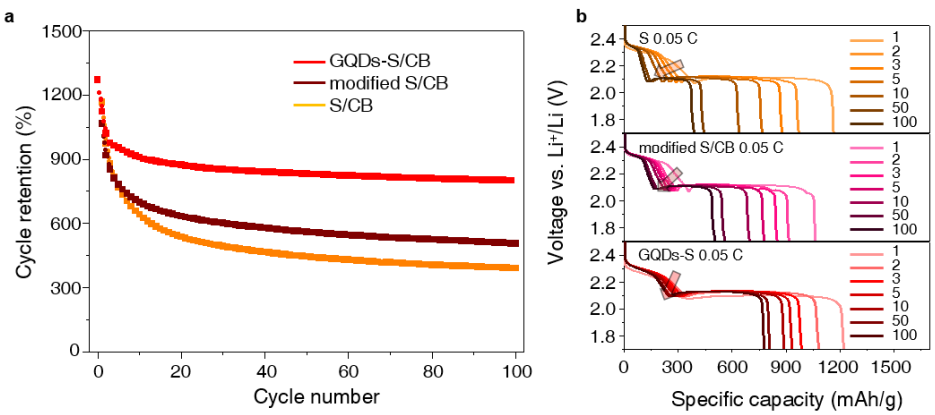

Figure S5. a, Cycling performance and b, discharge profile of GQDs-S/CB, modified S/CB, and S/CB at 0.05 *C* for 100 cycles. The GQDs-S/CB electrode shows superior cycle retention compared to S/CB and modified S/CB, which indicates that the surfactant alone does not prevent dissolution of the sulphide discharge-products into the electrolyte.

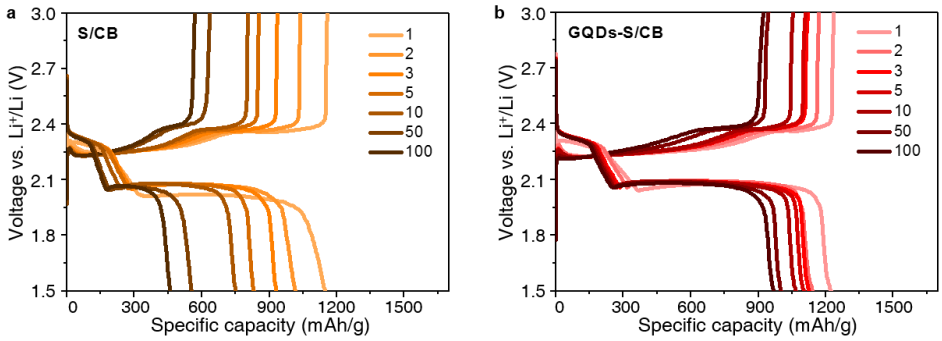

Figure S6. Charge-discharge profiles of a, S/CB and b, GQDs-S/CB at 0.5 *C* for 100 cycles.

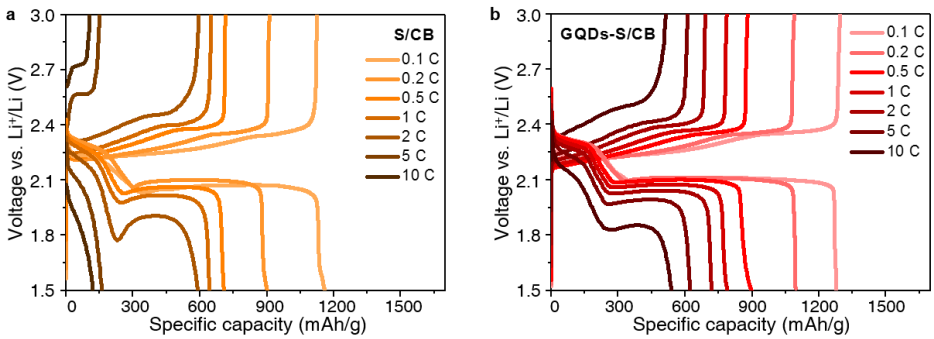

Figure S7. Rate performance of a, S/CB and b, GQDs-S/CB from 0.1 *C* up to 10 *C*.

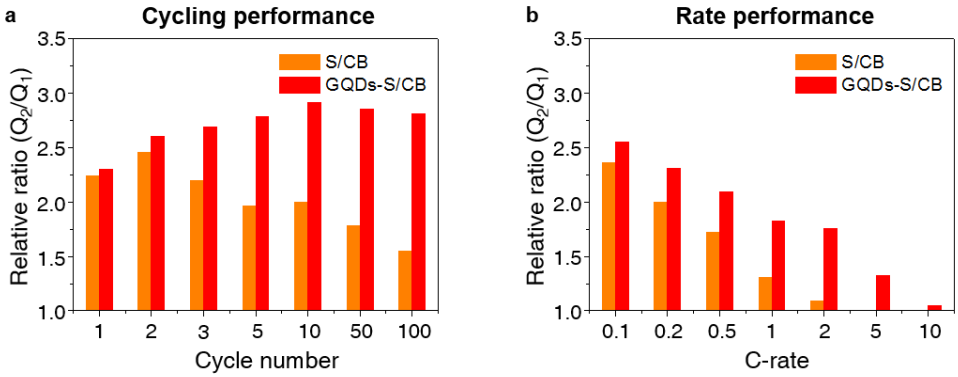

Figure S8. Relative ratios of dissolution/precipitation regime capacity (Q_2/Q_1). a, Cycling performance up to 100 cycles. b, Rate performance from 0.1 *C* to 10 *C*.

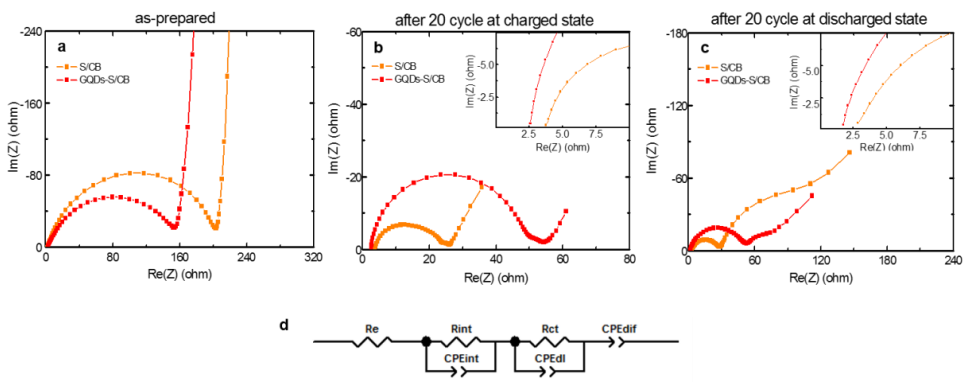

Figure S9. Electrochemical impedance spectroscopy (EIS). Lithium/sulphur cells a, as-prepared, b, fully charged, and c, discharged state after 20 cycles. Insets show the high-frequency range. The equivalent circuit model used to analyze the Nyquist plots d, charge-discharge states.

Electrochemical impedance spectroscopy (EIS) was used to analyze the interfacial resistance of the active material, the solution, and the carbon conducting agents, as shown in Fig. S9. The Warburg element (WO) is converted to a CPE_{diff} term while the other terms were fixed for the fitting process. The constant phase element (CPE) is normally used in modelling impedance data in place of a capacitor to compensate for non-ideal behaviour of the electrode (e.g. roughness or porosity at the electrode surface, ideal semi-circle n=1). R_e is relative to the resistance of the electrolyte, and the ratio R_{int}/CPE_{int} is related to the resistance and capacitance of the interphase contact of the sulphur electrode. In a Nyquist diagram R_e occurs in the high frequency (HF) region (100 kHZ-1kHz). In middle frequency (MF) (1kHz–1Hz) region, the ration R_{ct}/CPE_{dl} is related to the charge transfer resistance and capacitance at the interface between the active materials, the conducting agent, and the electrolyte. The term CPE_{diff}, the diffusion impedance, related to the Li-ion diffusion process, occurs in low frequency (LF, 1Hz-100mHz)[1]. EIS was also performed in the charged/discharged states at the 20th cycle, Figs. S9b and S9c, to examine the conductivities of both electrodes in these states. At high frequency (> 100 Hz), where the EIS response is associated with Rint/Cint, the GQDs-S/CB shows a larger semi-circle compared to that of S/CB owing to the higher concentration of active material. Despite the higher population of active materials, the GQDs-S/CB electrodes exhibit a smaller semi-circle than S/CB at intermediate frequency region (100 Hz – 1 Hz). This semi-circle is related to Rct/Cdl, which suggests that the GQDs-S/CB electrode has higher structural stability and lower electrical resistance compared to the S/CB electrode. These observations support that the GQDs-S/CB prohibit dissolution of HO-LiPSs into the electrolyte and facilitate electron transfer between the conducting agent and active materials.

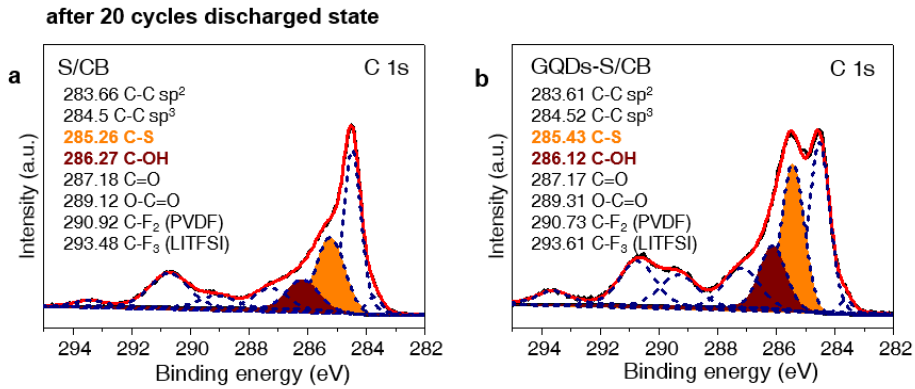

Figure S10. High resolution C 1*s* X-ray photoelectron spectroscopy a,b, C 1*s* spectrum of the S/CB and GQDs-S/CB electrodes after 20 cycles in the discharged state. Each spectrum has been fitted with peaks for different bonded carbon (dashed line) and the sum of the fitting curves (red line) is consistent with the raw data (black solid line).

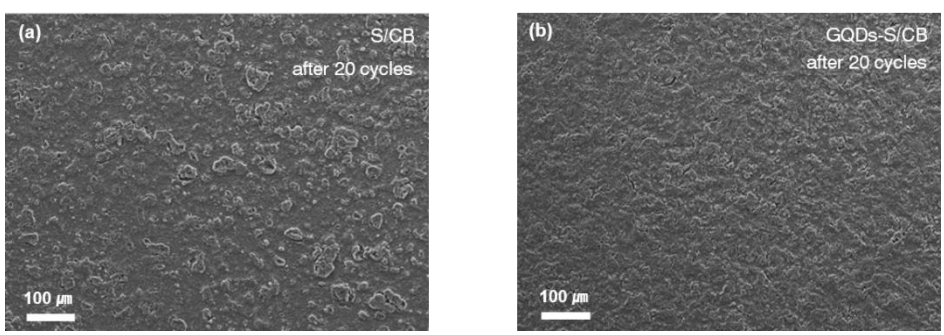

Figure S11. SEM images of GQDs-S/CB and S/CB cathode electrodes after electrochemical cycling. a,b, GQDs-S and S electrodes after cycling.

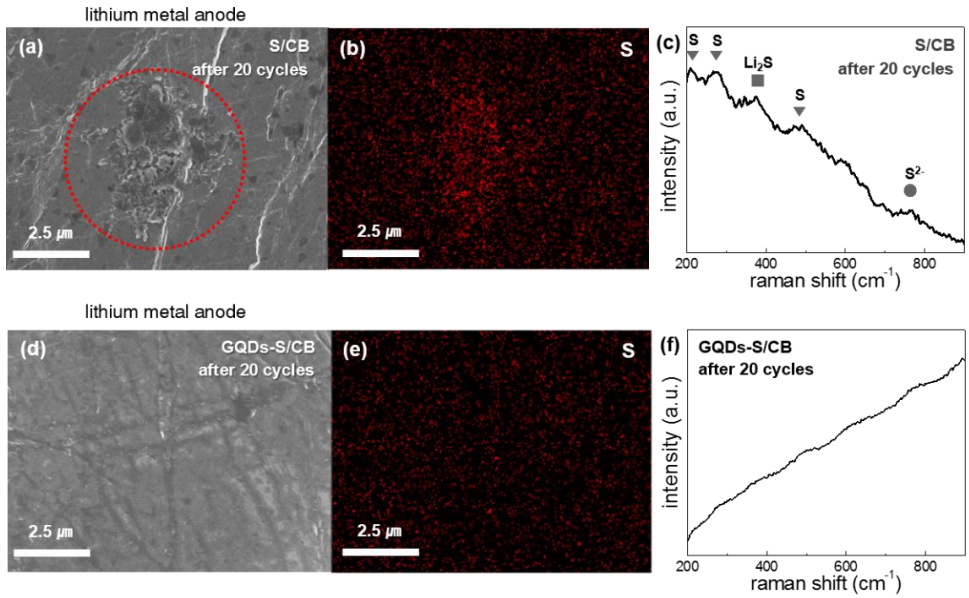

Figure S12. SEM images and Raman spectra of lithium anodes after cycling against S/CB and GQDs-S/CB electrodes. a,d, SEM images after 20 cycles. b,e, Sulphur energy-dispersive X-ray spectroscopy maps. c,f, Raman spectra. The S peaks are assigned to 156, 221, 473 cm^{-1}, Li_2S to 378 cm^{-1}, and S^{2-} to 746 cm^{-1} (ref. 2). No peaks are present in the cell containing GQDs-S/CB.

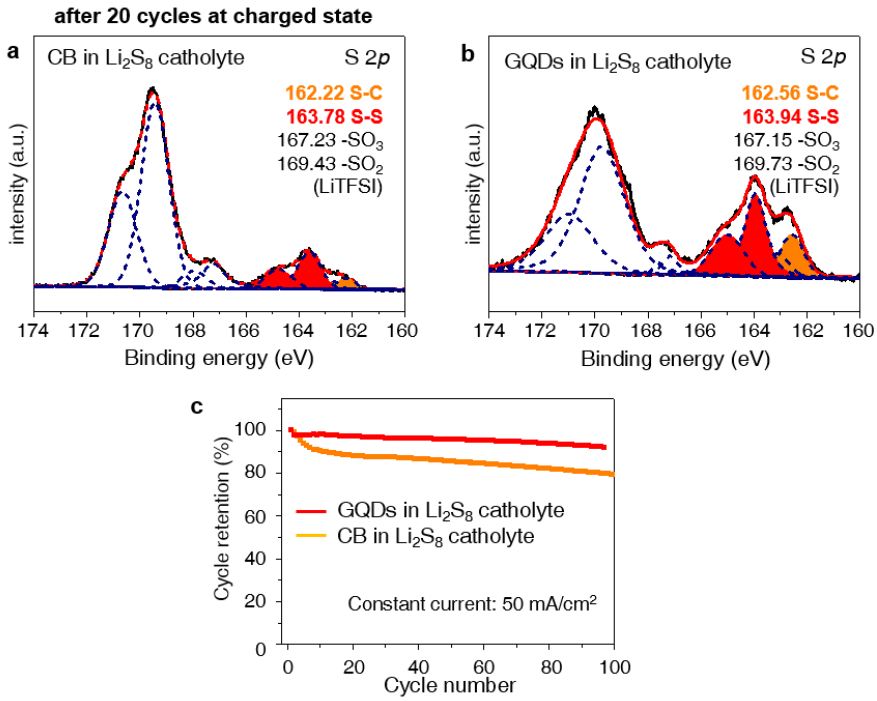

Figure S13. High resolution S 2*p* X-ray photoelectron spectroscopy and cycl e performance. a,b, S 2*p* spectrum of the CB and GQDs electrodes, in the charge state, after 20 cycles. These electrodes were cycled in the Li_2S_8 cath olyte. Each spectrum was fitted with functions corresponding to different valencies of sulphur (dashed line) and the sum of these fitted curves (red line) is consistent with the raw data (black solid line). c, Cycle retention of GQDs/CB and CB el ectrodes in Li_2S_8 catholyte over 100 cycles.

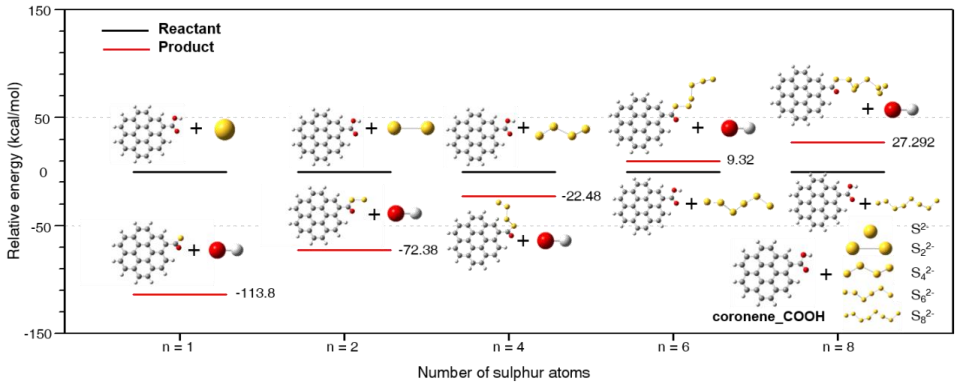

Figure S14. The relative energies for the reactant and product in binding of polysulphides to GQDs. The functional groups enhance the binding of polysulphides to carbon due to substitution of –OH (C-COOH) for S_n^{2-}. Yellow, red, white, and gray represents S, O, H, and C atoms, respectively.

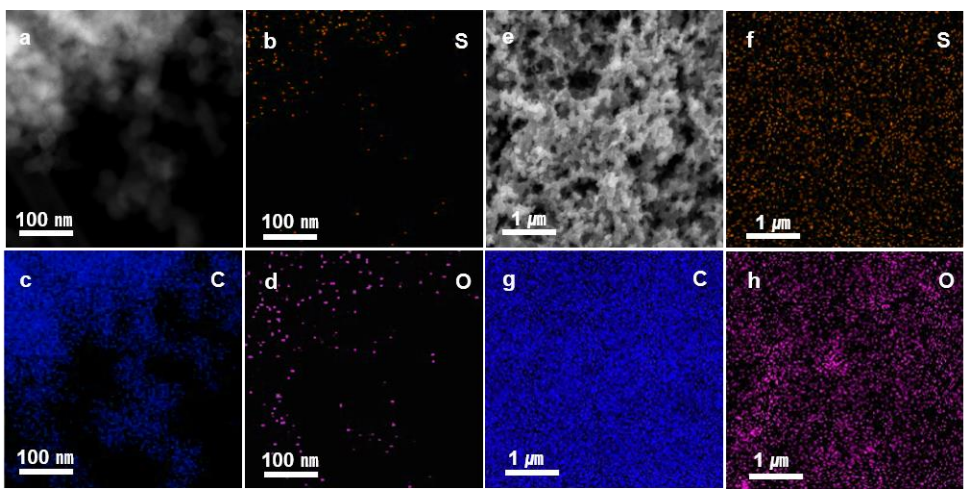

Figure S15. TEM images of nano-sized sulphur on a CB electrode in Li_2S_8 catholyte after 20 cycles. a, Bright field STEM image of the CB electrode. b-d, Energy-dispersive X-ray spectroscopy maps of C, S, and O of the CB electrode in the Li_2S_8 catholyte. e, SEM image of the CB electrode in the Li_2S_8 catholyte after cycling. f-h, C, S, and O EDX maps of the GQDs electrode.

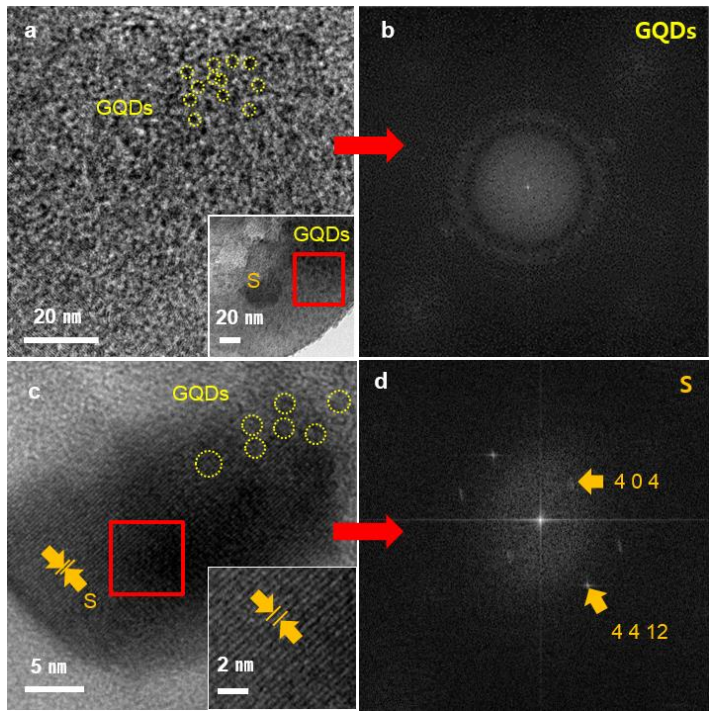

Figure S16. HRTEM (high-resolution transmission electron microscopy) images of nano-sized sulphur on GQDs electrode in Li_2S_8 catholyte after 20 cycles. a, TEM image of nano-sized sulphur in the GQD electrode. b, The FFT of the selected region in image, a. The ring pattern of graphene quantum dots. c, Magnification of nano-sized sulphur in image a shows the lattice fringes of sulphur and GQDs. d, The FFT of the selected area in image, c.

References

1. Armand, M. and Tarascon, J. -M. Building better batteries. *Nature* **451,** 652-657 (2008).
2. Goodenough, J. B., Park, K. -S. The Li-ion rechargeable battery: a perspective. *J. Am. Chem. Soc.***135**, 1167-1176 (2013).
3. Marom, R., et al. A review of advanced and practical lithium battery materials. *J. Mater. Chem.* **21**, 9938-9954 (2011).
4. Cabana, J., et al. Beyond intercalation-based Li-ion batteries: the state of the art and challenges of electrode materials reacting through conversion reactions. *Adv. Mater.* **22**, E170-E192 (2010)
5. Manthiram, A., Fu, Y. and Su, Y.-S. Challenges and prospects of lithium-sulphur batteries. *Acc. Chem. Res.* **46**, 1125-1134 (2013).
6. Chung, W. J., Griebel, J. J., et al. The use of elemental sulfur as an alternative feedstock for polymeric materials. *Nat. Chem.* **5**, 518-524 (2013).
7. Bruce, P. G., Freunberger, S. A., Hardwick, L. J., Tarascon, J. -M. Li-O_2 and Li-S batteries with high energy storage. *Nat. Mater.* **11**, 19-29 (2012).
8. Choi, N. -S., et al. Challenges facing lithium batteries and electrical double-layer capacitors capacitors. *Angew. Chem. Int. Ed.* **51**, 9994-10024 (2012).
9. Simmonds, A. G., Griebel, J. J., Park, J., et al. Inverse vulcanization of elemental sulfur to prepare polymeric electrode materials for Li-S batteries. *ACS Macro Letters* **3**, 229-232 (2014).
10. Mikhaylik, Y. V., Akridge, J. R., Polysulfide shuttle study in the Li/S battery system, *J. Electrochem. Soc.*, **151**, A1969-A1976 (2004).
11. Elazari, R., Salitra, G., Garsuch, A., Panchenko, A., Aurbach, D. Sulphur-impregnated activated carbon fiber cloth as a binder-free cathode for rechargeable Li-S batteries. *Adv. Mater.* **23**, 5641-5644 (2011).
12. Su, Y. and Manthiram, A. Lithium-sulphur batteries with a microporous carbon paper as a bifunctional interlayer. *Nat. Comm.* **3** 1166-1171 (2012).
13. Zhang, C., et al. Confining sulfur in double-shelled hollow carbon spheres for lithium-sulfur batteries. *Angew. Chem. Int. Ed.* **51**, 9592-9595 (2012).

14. Zhou, G. and et al. A graphene-pure sulfur sandwich structure for ultrafast long-life lithium-sulfur batteries. *Adv. Mater.* **26**, 625-631 (2014).
15. Ji, X., Lee, K. T., and Nazar, L. F. A Highly ordered nanostructured carbon-sulphur cathode for lithium-sulphur batteries. *Nat. Mater.* **8**, 500-506 (2009).
16. Xin, S. et al. Smaller sulphur molecules promise better lithium-sulphur batteries. *J. Am. Chem. Soc.* **134**, 18510-18513 (2012).
17. Schuster, J., He, G. et al. Spherical ordered mesoporous carbon nanoparticle with high porosity for lithium-sulphur batteries. *Angew. Chem. Int. Ed.* **51**, 3591-3595 (2012).
18. Ji, L., Aloni, S., Wang, L., Cairns, E. J., Zhang, U. Porous carbon nanofiber-sulphur composite electrodes for lithium/sulphur cells. *Energy Environ. Sci.* **4**, 5053-5059 (2011).
19. Guo, J., Xu, Y., and Wang, C. sulphur-impregnated disordered carbon nanotubes cathode for lithium sulphur batteries. *Nano Letters* **11,** 4288-4294 (2011).
20. Wang, H. et al. Graphene–wrapped sulphur particles as a rechargeable lithium-sulphur battery cathode material with high capacity and cycling stability. *Nano Letters* **11**, 2644-2647 (2011).
21. Ji, L., Rao, M. et al. Graphene oxide as a sulphur immobilizer in high performance lithium/sulphur cells. *J. Am. Chem. Soc.* **133**, 18522-18525 (2011).
22. Zu, C., Manthiram, A. Hydroxylated graphene-sulphur nanocomposites for high-rate lithium-sulphur batteries. *Adv. Energy Mater.* **3**, 1008-1012 (2013).
23. Evers, S., Nazar, L. F. Graphene-enveloped sulphur in a one pot reaction: a cathode with good coulombic efficiency and high practical sulphur content. *Chem. Commun.* **48,** 1233-1235 (2012).
24. Fu, Y. and Manthiram, A. Orthorhombic bipyramidal sulphur coated with polypyrrole nanolayers as a cathode material for lithium-sulfur batteries. *J. Phsy. Chem. C* **116**, 8910-8915 (2012).
25. Peng, J. et al. Graphene quantum dots derived from carbon fibers. *Nano Letters* **12**, 844-846 (2012).

26. Ritter, K. A., Lyding, J. W. The influence of edge structure on the electronic properties of graphene quantum dots and nanoribbons. *Nat. Mater.* **8**, 235-242 (2009).
27. Pan, D., Zhang, J., Li, Z., Wu, M. Hydrothermal route for cutting graphene sheets into blue-luminescent graphene quantum dots. *Adv. Mater.* **22**, 734-738, (2010).
28. Acik, M., Lee, G., Mattevi, C, Pirkle, A., Wallace, R. M., et al. The role of oxygen during thermal reduction of graphene oxide studied by infrared absorption spectroscopy. *J. Phys. Chem. C* **115**, 19761-19781 (2011).
29. Gokus, T., Nair, R. R., Bonetti, A., Bohmler, M., Lombardo, A., Noboselov, et al. Making graphene luminescent by oxygen plasma treatment. *ACS Nano* **3**, 3963-3968 (2009).
30. Yeon, J., Jang, J. et al. Raman spectroscopy and X-ray diffraction studies of sulphur composite electrodes during discharge and charge. *J. Electrochem. Soc.* **159**, A1308-A1314 (2012)
31. John F. Moulder, William F. Stickle, Peter E. Sobol, Kenneth D. Bomben. Handbook of X-ray photoelectron spectroscopy (Physical Electronics, Inc., 1995).
32. Su, Y.-S., Fu, Y., Cochell, T., and Manthiram, A. A strategic approach to recharging lithium-sulphur batteries for long cycle life. *Nat. Comm.* **4**, 2985-2992 (2013).
33. Deng, Z., Zhang, Z. et al. Electrochemical impedance spectroscopy study of a lithium/sulphur battery: modelling and analysis of capacity fading. *J. Electrochem. Soc*. **4**, A553-A558 (2013)
34. Bruckner, J., Soren T. et al. Lithium sulphur batteries: influence of C-rate, amount of electrolyte and sulphur loading on cycle performance. *J. Power Sources* **268**, 82-87 (2014).
35. S. Kaciulis Spectroscopy of carbon: from diamond to nitride films. *Surf. Interface Anal.* **44**, 1155-1161 (2012).
36. Kummer, K., Vyalikh, D. V., High-resolution photoelectron spectroscopy of self-assembled mercaptohexanol monolayers on gold surfaces. *J. Electron. Spectrosc. Relat. Phenom.* **163**, 59-64 (2008).

37. Juhye Song, Sung Jun Lee et al. Thermal reactions of lithiated and delithiated sulphur electrodes in lithium-sulfur batteries. *ECS Electrochemistry Letters* **3** (4) A26-A29 (2014).
38. Socrates, G. Infrared and Raman characteristic group frequencies tables and charts: *Sulphur and Selenium compounds* Ch.16 (John Wiley & Sons Ltd, Third edition, 2001).
39. Song, J., Xu. T. et al. Nitrogen-doped mesoporous carbon promoted chemical adsorption of sulphur and fabrication of high-areal-capacity sulphur cathode with exceptional cycling stability for lithium-sulphur batteries. *Adv. Func. Mater*. **24**, 1243-1250 (2014).
40. Berghof, V., Sommerfeld, T., and Cederbaum, L. S. Sulfur cluster dianions. *J. Phys. Chem. A*, **102**, 5100-5105 (1998).
41. Abrahams, S. C. The crystal and molecular structure of orthorhombic sulfur, *Acta Cryst*. **8**, 661-671 (1955).
42. Stephens, P. J., Devlin, F. J., Chabalowski, C. F., Frisch, M. J. Ab Initio calculation of vibrational absorption and circular dichroism spectra using density functional force fields. *J. Phys. Chem.* **98**, 11623-11627 (1994).
43. Gaussian 09, Frisch, M. J., Trucks, G. W., Schlegel, H. B., Scuseria, G. E., et al. Gaussian, Inc., Wallingford CT, 2009.

Abstract (Korean)

최근 에너지 자원에 대한 수요가 증가함에 따라 새로운 에너지 장치 및 변환 시스템 개발에 대한 노력이 끊임 없이 진행되어 왔다. 급격히 증가된 소비 속도와 빠른 화석연료의 고갈은 지난 수십년간 많은 재생에너지, 풍력에너지, 조력에너지, 그리고 태양 에너지에 관한 연구가 집중되게 되었다. 한편, 재생에너지에 대한 폭넓은 사용을 제공하기 위해 효과적인 에너지 장치 및 변환기술 개발이 요구되는 실정이다. 최근 그래핀 및 그래핀 기반 복합물질은 높은 기계적 구부러짐, 넓은 표면적, 우수한 화학적 안정성, 높은 전기 및 열 전도도 특성으로 인해 많은 관심을 받고 있으며, 전기화학적 에너지 저장장치 즉, 리튬 배터리, 슈퍼캐페시터, 물분해 시스템 및 태양광 시스템에 관한 대체 전극 물질로서의 연구되고 있다.

본 학위논문은 다음과 같다. 1장에서는 질소 도핑된 그래핀 및 그래핀 양자시트를 사용하여 수소 생산반응 전극의 촉매로사용하여 우수한 물분해효율 향상에 대한 결과 및 그에 대한 메커니즘을 규명하는 것이다. 2장에서는 산소기능기를 다량 함유하고 있는 나노 사이즈의 그래핀 양자점을 황 물질에 포함하여 코어 셀 구조를 합성하고 이를 리튬 황 배터리의 양극 물질로 활용하여 고성능 및 고용량 배터리를 구현한 연구이다. 본문의 주요 결과는 다음과 같다.

Part 1, 첫째, 화학기상증착법에 의하여 촉매층 상 (구리 박막)에서 형성된 단층 그래핀에 질소 플라즈마를 인가하여 질소 도핑된 그래핀 양자 시트 (N-doped graphene quantum sheet, N-GQSs)를 간단히 제작하는 방법을 처음으로 발견하였다. 둘째, 단층의 질소 도핑된 그래핀을 수소발생 반응의 촉매로 사용하여 포화전류밀도의 변화 없이 강하게 반응시점이 향상 된 것으로 나타났으며,

단층의 질소 도핑된 그래핀층은 중성 (pH 7)에서 실리콘전극의 산화 방지막으로써 우수한 활용도 또한 증명하였다. 마지막으로, 질도 도핑된 그래핀 양자 시트를 표면적이 넓은 실리코 나노 와이어 전극의 촉매로 사용하여 수소 생성 반응을 분석하였고, 그 결과 광전기화학적 수소 생생 반응의 우수한 촉매로써의 활용을 선보였다. 이것은 현재까지 탄소 기반의 광전기화학반응의 촉매로의 연구결과보다 뛰어난 태양광에너지를 수소에너지로 변화하는 효율을 보였다.

Part 2, 산화그래핀의 산소 기능기가 리튬-황 배터리 성능향상에 미친 영향을 연구하기 위하여, 리튬-황 배터리 양극물질로 산화 그래핀을 황물질과 코어쉘 구조를 합성하였다. 나아가 구조와 산소기능기의 역할을 모두 연구하기 위해, 산소 기능기가 다량 함유된 나노 사이즈형태의 그래핀 양자 점을 합성하여 황 입자를 밀도있게 감싸는 구조를 형성하였다. 이것은 전자 전달에 유리한 구조를 보였으며, 액상의 리튬폴리설파이드의 손실을 막아주었다. 배터리 성능 평가 후, 표면 분석을 통하여 C-S (탄소-황) 결합이 형성된것을 확인 할 수 있었으며 밀도범함수 이론을 통하여 다양한 산소 기능기와 폴리설파이드가 반응하여 C-S결합을 형성할 수 있음을 확인 하였다. 마지막으로, 질도도핑된 탄소 양자점을 사용한 리튬-황 배터리의 우수한 용량 및 율속특성에 대한 메카니즘 연구를 철저히 전기화학적 분석을 통하여 규명하였다.

따라서, 본 학위논문은 질소 혹은 산소로 기능화된 그래핀 혹은 그래핀 양자점을 합성하고 이를 수소 발생 반응과 리튬-황 배터리에 적용한 연구결과를 제시하였다. 본 내용은 *Energy Environ. Sci.* 8, 1329 (2015), *Adv. Mater.* 26, 3501 (2014), *Energy Environ. Sci.* 6, 3658 (2013), and Nanoscale (DOI:10.1039/c5nr01951f) 저널에 등재된 내용을 포함하고 있다.

주요어: 그래핀, 그래핀 양자 시트, 그래핀 양자 점, 수소 발생 반응, 촉매, 리튬-황 배터리, C-S 결합, 나노-사이즈 황

학 번: 2012-30873